ELECTROMAGNETIC SCATTERING FROM ROUGH SURFACES COVERED WITH SHORT BRANCHING VEGETATION

by

Tsen-Chieh Chiu

A dissertation submitted in partial fulfillment
of the requirements for the degree of
Doctor of Philosophy
(Electrical Engineering)
in The University of Michigan
1998

Doctoral Committee:

Associate Professor Kamal Sarabandi, Chairperson
Professor Anthony W. England
Associate Professor Brian E. Gilchrist
Professor William R. Kuhn
Professor Fawwaz T. Ulaby

To my parents.

ACKNOWLEDGEMENTS

I am sincerely grateful to professor Kamal Sarabandi. With his intellectual guidance, I was able to go through the biggest challenge so far in my life. I also thank all the professors in my committee for their time and help.

During my study in the Radiation Lab, it seems every time I need help in either experimental or theoretical work, someone is always there for me. I still remember five year ago, when I just came here, prof. Sarabandi took me to the main lab and showed me the dielectric measurement. Dr. Adib Nashashibi patiently taught me my first radar measurement in the anechoic chamber. Mr. Ron Hartikka and Dr. James Stiles gave me the training for the adventurous truck-mounted radar measurement. Mr. Yanni Kouskoulas helped me in the soybean measurement and later in the data processing of the AIRSAR images. Dr. Roger DeRoo and Mr. Bryan Hauck generously taught me and let me use the bistatic facility. And how can I forget that, during one measurement in the winter of 1994, Mr. Eric Li and I were almost frozen to death?

I would also like to thank all my friends in the Rad Lab: Dr. Yicheng Lin, Dr. Juiching Chen, Mr. Daniel Zahn, Mr. Craig Wilson, Dr. Leland Pierce, and Mr. Craig Dobson. My friend, if your name is not listed, you know you are always in my heart.

Finally, I want to thank my family. It has been a long journey. Without them, it would have been a lonely one. May the enlightened one be with them.

TABLE OF CONTENTS

LIST OF FIGURES

Figure

LIST OF TABLES

Table

LIST OF APPENDICES

Appendix

CHAPTER I

INTRODUCTION

1.1 Background

One of the primary concerns in climate studies in the past decades has been soil moisture, because it is an influential parameter in both climatic and hydrologic models. Considerable effort has been made to discover its effects on atmospheric circulation. For example, it has been found that seasonal anomalies of soil wetness have a significant effect on the atmospheric seasonal cycles. In vegetation-covered areas, moisture is available to the atmosphere from both wet foliage (through evaporation) and dry foliage (through transpiration), and is affected by the incoming solar radiation, air vapor pressure deficit, air temperature, and soil moisture. Among these, soil moisture determines the maximum rate of the water extraction from the root zone, and therefore regulates the exchanges of energy and moisture fluxes at the land-air interface. In order to observe the soil-moisture variation, sensors have been mounted on airplane and satellite platforms to collect the radiation and backscatter from the earth surfaces.

Microwave remote sensing has evolved into an important tool for monitoring the atmosphere and surfaces of the earth, because microwave sensors are capable of penetrating clouds and are independent of the sun as a source of illumination.

Microwaves are also able to penetrate more deeply into vegetation than optical waves can. Therefore, soil-moisture retrieval of bare-soil and vegetated ground surfaces has become one of the major applications of microwave remote sensing. With the advent of polarimetric synthetic aperture radar (SAR), which is capable of measuring the magnitude and phase of the scattered field at different polarizations and frequencies, the soil-moisture retrieval from radar scatter measurement has attained significant prominence. While a large amount of data can be collected, there are difficulties in mapping the scattering data correctly into the desired parameters. To accomplish this mapping, a necessary step is to determine the relationship between all parameters to the radar backscatter. Therefore, to retrieve the soil-moisture information from the radar backscatter, it is essential to understand both the quantitative and qualitative aspects of electromagnetic scattering from bare-soil and vegetated ground surfaces.

Many scattering models for random rough surfaces have been developed over the past years [2–5, 10, 11, 29, 33, 70, 72]. Generally, these scattering models consider the rough surfaces as either perfectly conducting surfaces or homogeneous dielectric surfaces. Nevertheless, some scattering models have been developed to investigate the effect of dielectric inhomogeneity. Sarabandi et al. [43] assumes that the rough surface is a collection of dielectric humps above an impedance surface. After deriving the scattering from a single hump, the Monte-Carlo simulation is applied to calculate the scattering from a random rough surface. However, it is time-consuming, and so far is limited to one-dimensional roughness cases.

Fung et al. [12] developed a model which utilizes the matrix doubling method to compute the scattered intensity from surfaces with inhomogeneous underlying dielectric profiles, as shown in Fig. 1.1. The inhomogeneous medium is modeled as stratified layers with smooth or irregular interfaces. The relationship between

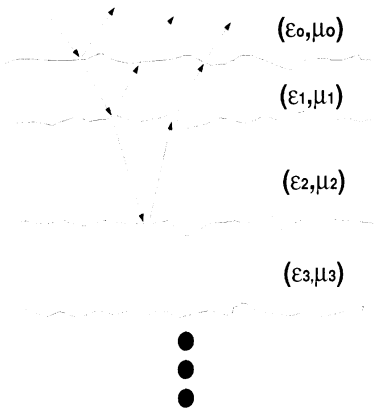

Figure 1.1: The geometry of a multi-layered inhomogeneous medium with irregular interfaces. The arrows represent part of the multiple scattering.

incident intensity, scattered intensity, and transmitted intensity at interfaces can be defined by a phase matrix which can be computed using the bistatic scattering coefficients of the interfaces. Depending on the roughness of the interface, these bistatic scattering coefficients can be calculated using the surface scattering models mentioned earlier. The total scattered intensity can be expressed in terms of the summation of the scattered intensities resulting from the multiple scattering between each layer. When two adjacent interfaces are close, the interaction between both interfaces should be described using near-field expressions. However, the phase matrix used in this technique can only account for far-field interaction. Therefore, this model is appropriate only when the spacing between interfaces is large.

For the vegetated ground, many scattering models have been developed for vegetation components [18, 19, 22, 39, 41, 47, 48, 51, 53] and the simplified vegetation canopies [26, 31, 68, 73, 74]. In the early vegetation scattering models, the vegetation was simplified in terms of a homogeneous random medium and the single scattering theory was applied to account for the scattering and propagation in the random medium [18, 21, 69]. For example, in [69], a forest stand is represented in terms of a two-layer random medium including a crown layer composed of randomly oriented

cylinders and disks representing branches and leaves and a trunk layer containing nearly vertical cylinders representing tree trunks below the crown layer. Although these models are capable of predicting the scattering behavior of vegetation qualitatively, they are incapable of predicting the scattering behavior quantitatively due to their simplifying assumptions. An important feature of a high fidelity scattering model is to preserve the structure of vegetation as different species of vegetation have their own unique structures, which are expected to exhibit their own scattering behaviors. An important effect of the vegetation structure is the coherence effect caused by the relative position of the vegetation particles which produce certain interference pattern. It is shown that the coherence effects caused by the vegetation structure become more significant at lower frequencies [65]. In the remote sensing of vegetation-covered terrain where the underlying soil surface is the target of interest , low microwave frequencies are recommended and therefore the coherence effects must be carefully accounted for. The model developed by Yueh et al. [74] may be among the first to address the coherence effects caused by the vegetation structure. In their scattering model for soybeans, a two-scale branching vegetation structure was constructed, and the scattered fields from particles are added coherently. Hsu et al. [16] develop the scattering model for the pine forest based on radiative transfer theory [62]. In this model, the scattering function of each cluster is calculated by incorporating the phase interference of scattered fields from each component, and therefore, the coherence effect caused by the vegetation structure is accounted for. Lin et al. [23] also proposes a coherent scattering model for forest canopies in which rather realistic tree-like structures are constructed using the fractal theory. In both models, the scattering solutions are formulated using the single scattering theory.

Another important issue in modeling the scattering from vegetation is the effect

of the multiple scattering among vegetation particles. Vegetation particles are usually arranged in clusters within a single plant, such as leaves around end branches and branches around main stems and trunks. Therefore, a vegetation medium may be appropriately considered to be locally dense. In such cases, the near-field multiple scattering is strong and may significantly affect the overall response. To accurately evaluate the near-field interaction, the realistic description of the relative positions and orientations of the vegetation particles and accurate and efficient scattering formulations are required. In the recent years, some advanced scattering solutions that account for the near-field interaction between scatterers have been presented [48,64]. However, vegetation scattering models which can handle the near-field interaction with realistic vegetation structures have not been developed yet. The evaluation of the near-field interaction is usually numerically intensive, considering the huge number of particles in the medium.

1.2 Dissertation Overview

The goal of this study is to develop electromagnetic scattering models for bare-soil and short-vegetation-covered ground surfaces with inhomogeneous dielectric profiles. Natural ground surfaces are rough and their underlying dielectric profiles can be inhomogeneous. Though many rough-surface scattering models have been developed in the past decades, most models are developed for rough surfaces with homogeneous profiles. The other models which account for the dielectric inhomogeneity of the profile are either computationally inefficient (numerical model with Monte-Carlo simulation) or not able to handle the cases in which the inhomogeneous layers are thin (matrix doubling method). In this thesis, a new analytical scattering model for rough surfaces will be developed. This model will be able to handle rough surfaces

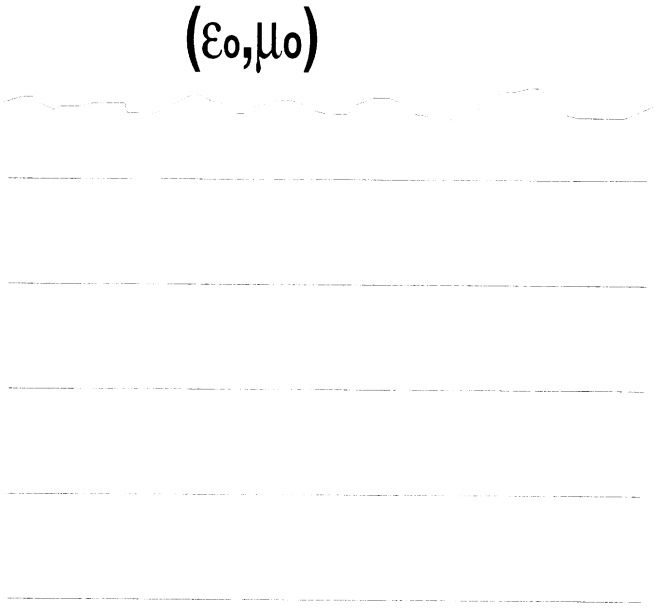

Figure 1.2: The geometry of a multi-layered inhomogeneous medium. Except for the top surface which is rough, all interfaces are flat. The thickness of every layer can be small.

with dielectric profiles shown in Fig. 1.2, which the matrix doubling method can not handle because the top layer can be very thin (an extreme case is that the second interface, which is flat, can touch the lowest point of the top surface).

For the short-vegetation-covered ground surfaces, the focus will be on:

1. Coherence effect of the vegetation structure. In order to account for the effect of the vegetation structure, a computer program has been developed to generate realistic vegetation structures. The statistics of constituent geometries — orientation, shape, dimension, and location — is determined from the ground truth.

2. A rough ground surface. It is practical to model the ground surface as a rough surface. The rough-surface scattering model developed in this thesis is incorporated into the vegetation scattering model.

3. Near-field interaction between the vegetation particle and rough surface. Low-

Figure 1.3: Soybeans.

frequency waves are capable of penetrating the vegetation medium. In this case, this scattering mechanism is significant in relating the radar backscatter to soil moisture.

4. Near-field interaction among the vegetation particles. This mechanism is often ignored in existing models due to its time-consuming and complicated computation. However, it is important in characterizing the scattering behavior of the vegetation.

In this model, soybeans, as shown in Fig. 1.3, are chosen as the target vegetation. Soybeans, are erect branching plants composed of components which can be often found in many vegetation: stems, branches, leaves and fruits (pods) arranged in a very well-defined manner. Hence it is very appropriate for studying the effect of

the vegetation structure on the radar backscatter. Also because of its moderate number of particles, the computation of the second-order near-field interaction is not formidable. From the experimental point of view, the dimensions of soybean plants are small enough to allow for conducting controlled experiments using truck-mounted scatterometers. Due to the uniformity of the plants and underlying soil surface, gathering the ground truth data is rather simple.

In addition to the main goals, a design procedure of a stable passive calibration target for low frequency SAR is proposed. This research is ancillary to the main topic of this thesis but is of great importance to SAR images. In what follows, the structure of this dissertation will be explained.

Chapter 2 presents analytical expressions for the bistatic scattering coefficients of soil surfaces with slightly rough interface and stratified permittivity profile. The scattering formulation is based on a new approach where the perturbation expansion of the volumetric polarization current instead of the tangential fields is used to obtain the scattered field. Basically, the top rough layer is replaced with an equivalent polarization current and using the volumetric integral equation in conjunction with the dyadic Green's function of the remaining stratified half-space medium, the scattering problem is formulated. Closed form analytical expressions for the induced polarization currents to any desired order are derived which are then used to evaluate the bistatic scattered fields up to and including the third order. The analytical solutions for the scattered fields are used to derive the complete second-order expressions for the backscattering coefficients as well as the statistics of phase difference between the scattering matrix elements. Also the theoretical results are compared with the backscatter measurements of rough surfaces with known dielectric profiles and roughness statistics.

In chapter 3, an electromagnetic scattering solution for the interaction between a dielectric cylinder and a slightly rough surface is presented. Taking advantage of a newly-developed technique which utilizes the reciprocity theorem, the difficulty in formulating the secondary scattered fields from the composite target reduces to the evaluation of integrals involving the scattered fields from the cylinder and polarization currents of the rough surface induced by a plane wave. Basically, only the current distribution of isolated scatterers are needed to evaluate the interaction in the far-field region. The scattered field from the cylinder is evaluated in the near-field region using the stationary phase approximation along the direction perpendicular to the cylinder axis. Also the expressions for the polarization current induced within the top rough layer of the rough surface derived from the iterative solution of an integral equation are employed in this chapter. A sensitivity analysis is performed for determining the dependency of the scattering interaction on the target parameters such as surface rms height, dielectric constant, cylinder diameter and length. The accuracy of the theoretical formulation is verified by conducting polarimetric backscatter measurements from a lossy dielectric cylinder above a slightly rough surface.

In chapter 4, the scattering solutions for vegetation particles will be described. Vegetation particles are usually modeled using simple geometries for which the analytical scattering solutions are available. For leaves, due to their small thickness compared to the wavelength in microwave range, the Rayleigh-Gans formulation can be applied. Dielectric cylinders are often used to model vegetation particles such as tree trucks and branches. An exact scattering solution does not exist for cylinders of finite length, but an approximated solution, which assumes the internal field induced within the finite cylinder is the same as that of the infinite cylinder with the

same cross section and dielectric constant, can be used. Generally, in order for this solution to be valid, the ratio of the length to the diameter should be large so that the fringing effects at both ends of the cylinder can be ignored. Also a formulation for the second-order scattering interaction between two Rayleigh-Gans particles is developed using Rayleigh-Gans approach.

Chapter 5 proposes an electromagnetic scattering model for short branching vegetation. With the realistic structures which reasonably describe the relative positions of particles, this model is able to consider the coherence effect due to the phase difference between the scattered fields from different particles, and handle the second-order near-field interaction between particles to which the relative positions and orientation of the particles are essential. The model validation with measurements is also presented. The polarimetric radar backscatter measurements for soybean plants using truck-mounted scatterometers were conducted at L-band and C-band under different soil-moisture conditions. An extensive ground truth collection was also performed to recorded moisture, dielectric constant, and geometry of the soybean plants and rough surface. Thus, the uncertainty which exists when inputing the values of parameters to the model is reduced. This model also demonstrate its ability for estimating the physical parameters and moistures of a soybean field using AIRSAR image data with limited knowledge of the ground truth.

Chapter 6 is concerned with the corner reflectors which is used for the calibration of the SAR. In this paper, a general class of corner reflectors with high aperture efficiency referred to as self-illuminating corner reflectors is introduced whose coherent interaction with their surrounding terrain is minimized and their total surface area is two-thirds of that of a triangular corner reflector having the same maximum RCS. Analytical expressions based on geometrical optics and a new numerical solution

based on near-field physical optics for the RCS of two simple self-illuminating corner reflectors are presented and compared with backscatter measurements. Also the panel geometry for an optimum corner reflector which has the shortest edge length among polygonal self-illuminating corner reflectors is obtained.

CHAPTER II

ELECTROMAGNETIC SCATTERING FROM SLIGHTLY ROUGH SURFACES WITH INHOMOGENEOUS DIELECTRIC PROFILES

2.1 Introduction

The temporal and spatial variations of soil moisture are influential parameters in both climatic and hydrologic models. Soil dielectric constant at microwave frequencies exhibits a strong dependence on the soil's moisture content. At L-band, for example, the real part of the dielectric constant ranges from 3 for dry soil to about 25 for saturated soil. This variation can result in a change on the order of 10 dB in the magnitude of the radar backscatter coefficient [29]. With the advent of polarimetric synthetic aperture radar (SAR), radar remote sensing of soil moisture has attained significant prominence in the past decade. SAR systems are capable of producing a backscatter map of the terrain with high resolution from an airborne or space-borne platform. From the electromagnetic point of view, remote sensing of soil moisture, in the absence of vegetation cover, can be modeled as an inverse scattering problem, where the dielectric constant and surface roughness statistics are to be determined from a set of backscatter measurements.

The problem of wave scattering from random rough surfaces has been the sub-

ject of ongoing research over the past several decades because of its arises in many areas of science and engineering. Generally speaking, the available electromagnetic scattering models can be categorized into three major groups: (1) analytical, (2) empirical, and (3) numerical. The analytical scattering solutions for rough surfaces apply when the roughness dimensions of the surface are either much smaller or much larger than the wavelength. For surfaces with small surface rms height and slope, the small perturbation model (SPM) is the most commonly used formalism [27,33]. In this approach, the surface fields are expanded in terms of a power series in the small roughness parameter and then, using either the Rayleigh hypothesis or the extended boundary condition [1], the expansion coefficients are obtained recursively. The scattering formulations based on SPM exist for dielectric and perfectly conducting rough surfaces. For these surfaces, only first-order expressions for the co-polarized backscattering coefficients and second-order expressions for the cross-polarized backscattering coefficients are reported [62]. On the other hand, if the irregularities of the surface have relatively small slopes and large radii of curvature, the Kirchhoff approximation (KA) can be used [5]. In this approach, the surface fields at a given point are approximated by those of the local tangent plane. In the past two decades, many attempts have been made to extend the validity region of SPM and KA. Among these, three can be mentioned: the phase perturbation method (PPM) [72] and the unified perturbation expansion (UPE) [36] for extending the low-frequency techniques, and the integral equation method (IEM) [10] for extending the high-frequency techniques. In the PPM, the perturbation solution is obtained by expanding the phase of the field instead of the field itself, whereas in the UPE method, the solution is obtained by expanding the field in terms of a parameter (momentum transfer) that remains small over a region larger than the perturbation parameter used in SPM. Scattering

formulation based on PPM and UPM are reported only for one-dimensional rough surfaces. The scattering solution based on IE method is obtained by inserting the KA into the surface field integral equation. This method is significant in that it reduces to the SPM solution, thereby seemingly bridging the gap between the low- and high-frequency solutions [11].

In this chapter, no attempt is made to extend the validity region of the existing methods; instead another practical aspect of the scattering problem is investigated. In most practical situations, the soil moisture content as a function of depth is non-uniform in depth. The soil moisture profile is usually a complex function of soil type, temperature profile, surface evaporation and moisture content [28]. For radar remote sensing of soil moisture, the effect of the inhomogeneity in the complex permittivity of the soil surface on its backscatter must be understood. For this purpose, analytical expressions for the bistatic scattering coefficients of a slightly rough surface with inhomogeneous dielectric profile are derived. Using the classical perturbation expansion of the electric field, a new volumetric integral equation approach is used to obtain the iterative scattering solutions. In what follows, the theoretical formulation for the scattering problem is given and the closed-form complete second order solution for backscattering coefficients and phase-difference statistics are derived. In Section 2.3, the theoretical solution will be compared with experimental backscatter measurements collected using the University of Michigan's bistatic indoor facilities.

2.2 Theoretical Analysis

Consider an inhomogeneous half-space medium with a rough interface as shown in Fig. 1. In the following derivation, it is assumed that the medium is stratified,

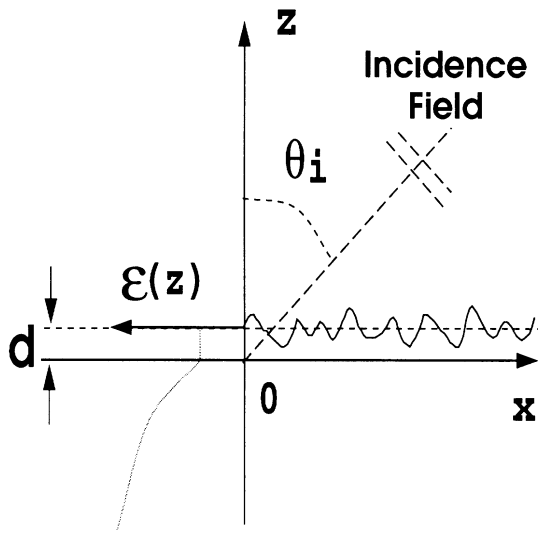

Figure 2.1: An inhomogeneous half-space medium with a rough interface. Left side of this figure shows the dielectric profile.

that is, the relative permittivity is only a function of z, and is given by

$$\epsilon_r(x, y, z) = \epsilon_r(z) \ .$$

Suppose a plane wave is illuminating the rough interface from the upper medium and, with a very high probability, the surface height variation is small compared with the wavelength of the incident wave. To make the solution tractable, the permittivity of the top layer down to a depth of d is considered to be uniform, where -d $<$ $min\{$surface profile$\}$. Denote the surface height profile by the function $z = \triangle f(x, y)$, where $f(x, y)$ is a zero-mean stationary random process with a known autocorrelation function, and $\triangle << \lambda$ is a small constant known as the perturbation parameter. The incident wave can be written as

$$\mathbf{E}^i(\bar{r}) = \mathbf{P}_i \, e^{ik_0 \hat{k}^i \cdot \mathbf{r}} \ ,$$

where $\mathbf{P}_i$ denotes the polarization of the incident wave, $k_0 = \frac{2\pi}{\lambda}$ is the free space propagation constant, and $\hat{k}^i$ is the unit vector along the direction of propagation,

given by

$$\hat{k}^i = \sin\theta_i \cos\phi_i \hat{x} + \sin\theta_i \sin\phi_i \hat{y} - \cos\theta_i \hat{z} \ .$$

In the absence of the top homogeneous rough layer (with thickness d), the incident wave would be reflected at the smooth interface between the free space and the inhomogeneous half space soil medium. The reflected wave can be expressed by

$$\mathbf{E}^r(\bar{r}) = \mathbf{P}_r \, e^{ik_0 \hat{k}^r \cdot \mathbf{r}} \ ,$$

where $\hat{k}^r$ is the direction of propagation of the reflected wave, given by

$$\hat{k}^r = \hat{k}^i - 2(\hat{z} \cdot \hat{k}^i)\hat{z} \ ,$$

and $\mathbf{P}_r$ is the polarization vector of the reflected wave, which can be obtained from

$$\mathbf{P}_r = r_v(\mathbf{P}_i \cdot \hat{v}_i)\hat{v}_r + r_h(\mathbf{P}_i \cdot \hat{h}_i)\hat{h}_r \ .$$

Here r_v and r_h are the Fresnel reflection coefficients, and the horizontal and vertical unit vectors are given by

$$\hat{h}_s = \frac{\hat{k}_s \times \hat{z}}{|\hat{k}_s \times \hat{z}|}, \qquad \hat{v}_s = \hat{h}_s \times \hat{k}_s \ , \tag{2.1}$$

where the subscript s can be i or r for the incident and reflected waves. In presence of the homogeneous rough layer, the incident and reflected waves induce a polarization current within the top dielectric layer which is the source of the scattered field. The polarization current in terms of the total field and the permittivity of the layer is

$$\mathbf{J}(\mathbf{r}) = -ik_0 Y_0(\epsilon - 1)\mathbf{E}^t \ , \tag{2.2}$$

where $Y_0 = \frac{1}{Z_0}$ is the characteristic admittance of the free space, and

$$\mathbf{E}^t = \mathbf{E}^i + \mathbf{E}^r + \mathbf{E}^s \ .$$

The scattered field $\mathbf{E}^s$ can in turn be expressed in terms of the polarization current and is given by

$$\mathbf{E}^s = ik_0 Z_0 \int_{V_{slab}} \bar{\bar{\mathbf{G}}}(\mathbf{r},\mathbf{r}') \cdot \mathbf{J}(\mathbf{r}')\, dv' \ , \tag{2.3}$$

where $\bar{\bar{\mathbf{G}}}(\mathbf{r},\mathbf{r}')$ is the dyadic Green's function of the half-space inhomogeneous medium (in the absence of the top rough layer). Substituting (2.3) into (2.2), the following integral equation for the polarization current can be obtained:

$$\frac{1}{\epsilon - 1}\mathbf{J}(\mathbf{r}) = -ik_0 Y_0(\mathbf{E}^i + \mathbf{E}^r) + k_0^2 \iint_{-\infty}^{\infty} \int_{0}^{d+\triangle f(x',y')} \bar{\bar{\mathbf{G}}}(\mathbf{r},\mathbf{r}') \cdot \mathbf{J}(\mathbf{r}')\, dv' \ . \tag{2.4}$$

An approximate solution for the integral equation can be obtained using a perturbation technique. By breaking the z' integral into two integrals, one with limits from 0 to d and the other with limits from d to $d + \triangle f(x',y')$, and noting $\triangle f(x',y')$ is a small quantity, up to the Nth order in $\triangle$, (2.4) can be written as

$$\begin{aligned}\frac{1}{\epsilon - 1}\mathbf{J}(\mathbf{r}) \simeq & -ik_0 Y_0(\mathbf{E}^i + \mathbf{E}^r) + k_0^2 \iint_{-\infty}^{\infty} \int_{0}^{d} \bar{\bar{\mathbf{G}}}(\mathbf{r},\mathbf{r}') \cdot \mathbf{J}(\mathbf{r}')\, dx'dy'dz' \\ & + k_0^2 \sum_{n=0}^{N-1} \iint_{-\infty}^{\infty} \frac{[\triangle f(x',y')]^{n+1}}{(n+1)!} \frac{\partial^n}{\partial z'^n} \left\{ \bar{\bar{\mathbf{G}}}(\mathbf{r},\mathbf{r}'_d) \cdot \mathbf{J}(\mathbf{r}'_d) \right\} dx'dy' \ ,\end{aligned} \tag{2.5}$$

where $\mathbf{r}'_d = x'\hat{x} + y'\hat{y} + d\hat{z}$. Taking the two-dimensional Fourier transform of both sides of (2.5) and noting that the integrals in x' and y' are of convolution type, it can be shown that

$$\begin{aligned}\frac{1}{\epsilon - 1}\widetilde{\mathbf{J}}(\mathbf{k}_\perp, z) = & -i4\pi^2 k_0 Y_0 \delta(\mathbf{k}_\perp - \mathbf{k}^i_\perp) \left[\mathbf{P}_i e^{-ik^i_z z} + \mathbf{P}_r e^{ik^i_z z} \right] \\ & + k_0^2 \int_0^d \tilde{\bar{\bar{\mathbf{G}}}}(\mathbf{k}_\perp; z, z') \cdot \widetilde{\mathbf{J}}(\mathbf{k}_\perp, z')\, dz' + k_0^2 \sum_{n=0}^{N-1} \sum_{m=0}^{n} \frac{\binom{n}{m} \triangle^{n+1}}{(n+1)!} \\ & \cdot \frac{\partial^m}{\partial z'^m} \tilde{\bar{\bar{\mathbf{G}}}}(\mathbf{k}_\perp; z, d) \cdot \left[\frac{\partial^{n-m}}{\partial z'^{n-m}} \widetilde{\mathbf{J}}(\mathbf{k}_\perp, d) * \bigotimes^{n+1} F(\mathbf{k}_\perp) \right] \ ,\end{aligned} \tag{2.6}$$

where $*$ is the convolution operator, $F(\mathbf{k}_\perp)$ is the Fourier transform of $f(x', y')$, $\overset{n}{\bigotimes}$ represents n-fold self-convolution ($\overset{n}{\bigotimes} F = \overbrace{F * F * \cdots * F}^{n}$), $k_z^i = k_0 \cos\theta_i$, and $\bar{\bar{\mathbf{G}}}(\bar{k}_\perp; z, z')$ is the Fourier transform of the Green's function, given by

$$\bar{\bar{\mathbf{G}}}(\mathbf{k}_\perp; z, z') = -\hat{z}\hat{z}\frac{\delta(z-z')}{k_0^2} + \frac{i}{2k_z}\begin{cases} \left\{\left[r_h\hat{h}(k_z)e^{ik_z z} + \hat{h}(-k_z)e^{-ik_z z}\right]\cdot \hat{h}(-k_z)e^{ik_z z'}\right. \\ \left. + \left[r_v\hat{v}(k_z)e^{ik_z z} + \hat{v}(-k_z)e^{-ik_z z}\right]\cdot \hat{v}(-k_z)e^{ik_z z'}\right\} \\ \qquad\qquad z < z', \\ \left\{\hat{h}(k_z)\left[r_h\hat{h}(-k_z)e^{ik_z z'} + \hat{h}(k_z)e^{-ik_z z'}\right]e^{ik_z z}\right. \\ \left. + \hat{v}(k_z)\left[r_v\hat{v}(-k_z)e^{ik_z z'} + \hat{v}(k_z)e^{-ik_z z'}\right]e^{ik_z z}\right\} \\ \qquad\qquad z > z'. \end{cases}$$

In (2.2), $k_z = \sqrt{k^2 - k_x^2 - k_y^2}$, $\mathbf{k}_\perp = k_x\hat{x} + k_y\hat{y}$, and $\hat{h}(\pm k_z)$ and $\hat{v}(\pm k_z)$ can be obtained from (2.1) with $\hat{k}_s = (k_x\hat{x} + k_y\hat{y} \pm k_z\hat{z})/k_0$.

Since the surface height variations are much smaller than the wavelength ($\triangle << \lambda_0$), the induced polarization current on the top rough layer closely resembles that of a smooth layer with the same dielectric constant and thickness d. Under this assumption, the polarization current may be expanded in terms of a convergent perturbation series in $\triangle$, and is given by

$$\mathbf{J}(\mathbf{r}) = \sum_{n=0}^{\infty} \mathbf{J}_n(\mathbf{r})\triangle^n \ ,$$

where $\mathbf{J}_0(\mathbf{r})$ is the induced polarization current in the unperturbed layer. Then by substituting this expansion into (2.6) and collecting terms of equal powers in $\triangle$, a recursive set of equations for the components of the polarization current can be

obtained, and is given by

$$\frac{1}{\epsilon-1}\tilde{\mathbf{J}}_0(\mathbf{k}_\perp,z) = -i4\pi^2 k_0 Y_0 \delta(\mathbf{k}_\perp-\mathbf{k}_\perp^i)\left[\mathbf{P}_i e^{-ik_z^i z}+\mathbf{P}_r e^{ik_z^i z}\right] + k_0^2\int_0^d \tilde{\tilde{\mathbf{G}}}(\mathbf{k}_\perp;z,z')\cdot\tilde{\mathbf{J}}_0(\mathbf{k}_\perp,z')\,dz' \ , \tag{2.7}$$

$$\frac{1}{\epsilon-1}\tilde{\mathbf{J}}_N(\mathbf{k}_\perp,z) = k_0^2\int_0^d \tilde{\tilde{\mathbf{G}}}(\mathbf{k}_\perp;z,z')\cdot\tilde{\mathbf{J}}_N(\mathbf{k}_\perp,z')\,dz' + k_0^2\tilde{\tilde{\mathbf{G}}}(\mathbf{k}_\perp;z,d)\cdot\tilde{\mathbf{V}}_N \ . \tag{2.8}$$

Here $\tilde{\mathbf{V}}_N$ is the source function for the Nth-order integral equation with a closed form representation

$$\tilde{\mathbf{V}}_N = \sum_{n=0}^{N-1}\sum_{m=0}^{N-n-1}\frac{\binom{N-n-1}{m}(ik_z)^m}{(N-n)!}\cdot\left[\frac{\partial^{N-n-m-1}}{\partial(z')^{N-n-m-1}}\tilde{\mathbf{J}}_n(\mathbf{k}_\perp,d)\right] * \bigotimes^{N-n} F(\mathbf{k}_\perp) \ .$$

The integral equations so obtained are Fredholm integral equations of the second kind, for which analytical solutions can be obtained. Note that the solution of the zeroth-order equation is the source function for the first-order equation and the Nth-order equation has an excitation function which consists of N-1 lower order polarization currents. To solve (2.7), let us first split the integral into two integrals : one over the interval $[0,z]$ and the other over the interval $[z,d]$. Extending the integration limits of the second integral over the entire interval $[0,d]$ by adding and subtracting an integral over the interval $[0,z]$ and noting $\hat{h}(k_z)=\hat{h}(-k_z)$, (2.7) can

be written as

$$\frac{1}{\epsilon-1}\widetilde{\mathbf{J}}_0(\mathbf{k}_\perp,z) = -i4\pi^2 k_0 Y_0 \delta(\mathbf{k}_\perp-\mathbf{k}_\perp^i)\left[\mathbf{P}_i e^{-ik_z^i z}+\mathbf{P}_r e^{ik_z^i z}\right]-\hat{z}\hat{z}\cdot\widetilde{\mathbf{J}}_0(\mathbf{k}_\perp,z)$$
$$+\frac{ik_0^2}{2k_z}\int_0^z\left\{\hat{h}(k_z)\hat{h}(k_z)\left[e^{-ik_z(z'-z)}-e^{ik_z(z'-z)}\right]\right.$$
$$\left.+\left[\hat{v}(k_z)\hat{v}(k_z)e^{-ik_z(z'-z)}-\hat{v}(-k_z)\hat{v}(-k_z)e^{ik_z(z'-z)}\right]\right\}\cdot\widetilde{\mathbf{J}}_0(\mathbf{k}_\perp,z')\,dz'$$
$$+\frac{ik_0^2}{2k_z}\left\{\left[r_h e^{ik_z z}+e^{-ik_z z}\right]\hat{h}(k_z)\hat{h}(k_z)+\left[r_v e^{ik_z z}\hat{v}(k_z)+e^{-ik_z z}\hat{v}(-k_z)\right]\right.$$
$$\left.\hat{v}(-k_z)\right\}\cdot\int_0^d\widetilde{\mathbf{J}}_0(\mathbf{k}_\perp,z')e^{ik_z z'}\,dz' \quad . \tag{2.9}$$

Noting that the second integral in (2.9) is a constant function of z and that the first integral is of convolution type in z, (2.9) is recognized as a vector Volta integral equation that can be solved analytically using the Laplace transformation or Picard's Process of successive approximation [61]. Since the involved integral in (2.9) is explicit in terms of variable $\mathbf{k}_\perp$, it can be shown that $\widetilde{\mathbf{J}}_0(\mathbf{k}_\perp,z)$ is of the form

$$\widetilde{\mathbf{J}}_0(\mathbf{k}_\perp,z) = (2\pi)^2\,\delta(\mathbf{k}_\perp-\mathbf{k}_\perp^i)\,\widetilde{\mathbf{J}}_0(z)\,.$$

The polarization current can be decomposed into its principal components, given by

$$\widetilde{\mathbf{J}}_0(z) = J_{0h}(z)\,\hat{h}(k_z^i)+J_{0t}(z)\,\hat{t}(k_z^i)+J_{0z}(z)\,\hat{z}\quad,$$

where $\hat{t}(k_z^i)=\hat{z}\times\hat{h}(k_z^i)$. Evaluating the inner product of (2.9) with $\hat{h}(k_z^i)$, $\hat{t}(k_z^i)$ and $\hat{z}$, three uncoupled scalar Volta integral equations are obtained. Solutions to the resulted integral equations for the three components of current are of the following forms:

$$J_{0h}(z) = A_h^0\, e^{ik_{1z}^i z} + B_h^0\, e^{-ik_{1z}^i z} \ ,$$

$$J_{0t}(z) = A_v^0\, e^{ik_{1z}^i z} + B_v^0\, e^{-ik_{1z}^i z} \ ,$$

$$J_{0z}(z) = -\frac{k_\rho^i}{k_{1z}} \left\{ A_v^0\, e^{ik_{1z}^i z} - B_v^0\, e^{-ik_{1z}^i z} \right\} \ . \tag{2.10}$$

After a long algebraic manipulation, closed form expressions for the zeroth-order polarization current are obtained

$$J_{0h}(z) = -\,i\,\frac{2k_0 k_z^i}{k_z^i + k_{1z}^i} Y_0\,(\epsilon - 1)\; C_0^h(\mathbf{k}^i, z)\; \left[\mathbf{P}_i \cdot \hat{h}(k_z^i)\right]\; e^{-ik_z^i d} \ ,$$

$$J_{0t}(z) = -\,i\frac{2k_0 k_z^i k_{1z}^i}{k_\rho^i\,(\epsilon k_z^i + k_{1z}^i)} Y_0(\epsilon - 1)\, C_0^v(\mathbf{k}^i, z)\; [\mathbf{P}_i \cdot \hat{z}]\; e^{-ik_z^i d} \ ,$$

$$J_{0z}(z) = -\,i\frac{2k_0 k_z^i}{\epsilon k_z^i + k_{1z}^i} Y_0(\epsilon - 1)\, C_1^v(\mathbf{k}^i, z)\; [\mathbf{P}_i \cdot \hat{z}]\; e^{-ik_z^i d} \ ,$$

where

$$k_{1z}^i = k_0\sqrt{\epsilon - \sin^2\theta_i}\,, \qquad k_\rho^i = k_0 \sin\theta_i\,, \qquad R_h^i = \frac{k_z^i - k_{1z}^i}{k_z^i + k_{1z}^i}\,, \qquad R_v^i = \frac{\epsilon k_z^i - k_{1z}^i}{\epsilon k_z^i + k_{1z}^i}\,,$$

$$C_n^h(\mathbf{k}, z) = \frac{(-1)^n\,(R_h - r_h)\, e^{ik_{1z}z} + (R_h r_h - 1)\, e^{-ik_{1z}z}}{R_h\,(R_h - r_h)\, e^{ik_{1z}d} + (R_h r_h - 1)\, e^{-ik_{1z}d}} \ ,$$

$$C_n^v(\mathbf{k}, z) = \frac{(-1)^n\,(r_v - R_v)\, e^{ik_{1z}z} + (R_v r_v - 1)\, e^{-ik_{1z}z}}{R_v\,(R_v - r_v)\, e^{ik_{1z}d} + (R_v r_v - 1)\, e^{-ik_{1z}d}} \ .$$

The source function of (2.8) can be written as

$$k_0^2 \tilde{\tilde{\mathbf{G}}}(\mathbf{k}_\perp; z, d) \cdot \tilde{\mathbf{V}}_N \triangleq -ik_0 Y_0 \left(\mathbf{q}_{Ni} e^{-ik_z z} + \mathbf{q}_{Nr} e^{ik_z z}\right) \ , \tag{2.11}$$

where

$$\mathbf{q}_{Ni} = \frac{-Z_0 k_0}{2k_z} e^{ik_z d} \cdot \left\{ \left(\hat{h}(k_z) \cdot \tilde{\mathbf{V}}_N\right)\, \hat{h}(k_z) + \left(\hat{v}(-k_z) \cdot \tilde{\mathbf{V}}_N\right) \hat{v}(-k_z) \right\} \ ,$$

$$\mathbf{q}_{Nr} = \frac{-Z_0 k_0}{2k_z} e^{ik_z d} \cdot \left\{ \left(\hat{h}(k_z) \cdot \tilde{\mathbf{V}}_N\right)\, \hat{h}(k_z) + \left(\hat{v}(-k_z) \cdot \tilde{\mathbf{V}}_N\right) \hat{v}(k_z) \right\} \ .$$

Noted that the vector integral equation (2.8) and the source function for the Nth-order polarization current are identical to those of the zeroth-order polarization current, and therefore a similar solution can be easily obtained. By decomposing the

Nth-order polarization current in terms of its three principle components, it can be shown that

$$\widetilde{J}_{Nh}(\mathbf{k}_\perp, z) = \frac{ik_0^2(\epsilon-1)}{k_z + k_{1z}} C_0^h(\mathbf{k}, z) \left[\tilde{\mathbf{V}}_N \cdot \hat{h}(k_z)\right] ,$$
$$\widetilde{J}_{Nt}(\mathbf{k}_\perp, z) = \frac{ik_0 k_{1z}(\epsilon-1)}{\epsilon k_z + k_{1z}} C_0^v(\mathbf{k}, z) \left[\tilde{\mathbf{V}}_N \cdot \hat{v}(-k_z)\right] ,$$
$$\widetilde{J}_{Nz}(\mathbf{k}_\perp, z) = \frac{ik_0 k_\rho(\epsilon-1)}{\epsilon k_z + k_{1z}} C_1^v(\mathbf{k}, z) \left[\tilde{\mathbf{V}}_N \cdot \hat{v}(-k_z)\right] .$$

2.2.1 Scattering Coefficients

Once the polarization current is obtained, the scattered field in region $z > d$ can be obtained from (2.3). Assuming that the surface perturbation is localized and the observation point $\mathbf{r} = r(\sin\theta_s\cos\phi_s\hat{x} + \sin\theta_s\sin\phi_s\hat{y} + \cos\theta_s\hat{z})$ is far from the scatterer, the far field approximation can be used to find the scattered fields. Using the stationary phase approximation in the far fields region, the Green's function is reduced to

$$\bar{\bar{\mathbf{G}}}(\mathbf{r}, \mathbf{r}') = \frac{e^{ik_0 r}}{4\pi r} \left\{ \left[\hat{h}(k_z^s)\hat{h}(k_z^s) r_h^s + \hat{v}(k_z^s)\hat{v}(-k_z^s) r_v^s\right] e^{-i\mathbf{K}^s r'} \right.$$
$$\left. + \left[\hat{h}(k_z^s)\hat{h}(k_z^s) + \hat{v}(k_z^s)\hat{v}(k_z^s)\right] e^{-i\mathbf{k}^s r'} \right\} . \qquad (2.12)$$

Substituting (2.12) and the polarization currents into (2.3) and expanding the integral similar to those used in (2.5), the Nth-order scattered field is given by a power series in $\triangle f(x, y)$ (similar to (2.3)). In this process, the Nth-order scattered field components are found to be

$$\mathbf{E}_N^s(\mathbf{r}) \cdot \hat{h}(k_z^s) = ik_0 Z_0 \triangle^N \frac{e^{ik_0 r}}{4\pi r} e^{-ik_z^s d} \sum_{n=0}^{N-1} \sum_{m=0}^{N-n-1} \frac{\binom{N-n-1}{m} (ik_z^s)^m}{(N-n)!} \left[R_h^s + (-1)^m\right]$$
$$\cdot C_m^h(\mathbf{k}^s, d) \left[\frac{\partial^{N-n-m-1}}{\partial (z')^{N-n-m-1}} \widetilde{\mathbf{J}}_n(\mathbf{k}_\perp^s, d)\right] * \bigotimes^{N-n} F(\mathbf{k}_\perp^s) \cdot \hat{h}(k_z^s) , \qquad (2.13)$$

$$\mathbf{E}_N^s(\mathbf{r})\cdot\hat{v}(k_z^s) = ik_0Z_0\triangle^N \frac{e^{ik_0r}}{4\pi r}e^{-ik_z^sd}\sum_{n=0}^{N-1}\sum_{m=0}^{N-n-1}\frac{\binom{N-n-1}{m}(ik_z^s)^m}{(N-n)!}\Bigg\{\left[R_v^s-(-1)^m\right]$$
$$\cdot C_m^v(\mathbf{k}^s,d)\cos\theta_s\,\hat{t}(k_z^s)+\left[R_v^s+(-1)^m\right]C_{m+1}^v(\mathbf{k}^s,d)\sin\theta_s\,\hat{z}\Bigg\}$$
$$\cdot\left[\frac{\partial^{N-n-m-1}}{\partial(z')^{N-n-m-1}}\widetilde{\mathbf{J}}_n(\mathbf{k}_\perp^s,d)\right]*\bigotimes^{N-n}F(\mathbf{k}_\perp^s)\ . \qquad (2.14)$$

The polarimetric response of a target can be obtained from its complex scattering matrix, defined by

$$\mathbf{E}^s=\frac{e^{ikr}}{r}\bar{\bar{\mathbf{S}}}\,\mathbf{E}^i\ .$$

The elements of the bistatic scattering matrix can simply be computed by setting $\mathbf{P}_i=\hat{h}(k_z^i)$ and $\mathbf{P}_i=\hat{v}(k_z^i)$ in (2.13) and (2.14). For distributed targets, such as rough surfaces, the quantities of interest are the elements of the differential covariance matrix, defined by

$$\sigma_{ijpq}^0=\lim_{A\to\infty}\frac{4\pi}{A}\left\langle S_{ij}S_{pq}^*\right\rangle\ , \qquad i,\,j,\,p,\,q\in\{h,\,v\}\,. \qquad (2.15)$$

Here $\langle\cdot\rangle$ denotes ensemble averaging. These elements are in general complex quantities, except when $i=p$ and $j=q$, in which case the elements are the usual scattering coefficients. In the perturbation analysis, each element of the scattering matrix can be evaluated up to the Nth-order, that is

$$S_{ij}=\sum_{n=1}^{N}S_{ij}^{(n)}\triangle^n\ , \qquad i,\,j\in\{h,\,v\}\,. \qquad (2.16)$$

It turns out that simple expressions for the first-order elements can be obtained and are given by

$$S_{hh}^{(1)} = \frac{k_0^2 k_z^i k_z^s (\epsilon - 1) e^{-i(k_z^i + k_z^s)d}}{\pi (k_z^i + k_{1z}^i)(k_z^s + k_{1z}^s)} C_0^h(\mathbf{k}^s, d) C_0^h(\mathbf{k}^i, d) \cos(\phi_s - \phi_i) F(\mathbf{k}_\perp^s - \mathbf{k}_\perp^i) , \tag{2.17}$$

$$S_{hv}^{(1)} = \frac{k_0 k_z^i k_z^s k_{1z}^i (\epsilon - 1) e^{-i(k_z^i + k_z^s)d}}{\pi (\epsilon k_z^i + k_{1z}^i)(k_z^s + k_{1z}^s)} C_0^h(\mathbf{k}^s, d) C_0^v(\mathbf{k}^i, d) \sin(\phi_s - \phi_i) F(\mathbf{k}_\perp^s - \mathbf{k}_\perp^i) , \tag{2.18}$$

$$S_{vh}^{(1)} = \frac{k_0 k_z^i k_z^s k_{1z}^s (\epsilon - 1) e^{-i(k_z^i + k_z^s)d}}{\pi (\epsilon k_z^s + k_{1z}^s)(k_z^i + k_{1z}^i)} C_0^h(\mathbf{k}^i, d) C_0^v(\mathbf{k}^s, d) \sin(\phi_s - \phi_i) F(\mathbf{k}_\perp^s - \mathbf{k}_\perp^i) , \tag{2.19}$$

$$S_{vv}^{(1)} = \frac{k_z^i k_{1z}^i (\epsilon - 1) e^{-i(k_z^i + k_z^s)d}}{\pi (\epsilon k_z^i + k_{1z}^i)(\epsilon k_z^s + k_{1z}^s)} \left[-k_z^s k_{1z}^s C_0^v(\mathbf{k}^s, d) C_0^v(\mathbf{k}^i, d) \cos(\phi_s - \phi_i) + \frac{\epsilon k_z^s k_\rho^s k_\rho^i}{k_{1z}^i} \cdot C_1^v(\mathbf{k}^s, d) C_1^v(\mathbf{k}^i, d) \right] F(\mathbf{k}_\perp^s - \mathbf{k}_\perp^i) . \tag{2.20}$$

In these expressions $F(\mathbf{k}_\perp^s - \mathbf{k}_\perp^i)$ is the only indeterministic factor and therefore the elements of the differential covariance matrix can easily be obtained by noting that

$$\lim_{A \to \infty} \frac{1}{A} \left\langle \left| \triangle F(\mathbf{k}_\perp^s - \mathbf{k}_\perp^i) \right|^2 \right\rangle = W(\mathbf{k}_\perp^s - \mathbf{k}_\perp^i) , \tag{2.21}$$

where $W(\mathbf{k}_\perp)$ is the power spectral density of the surface.

To examine the validity of the first-order results, a special case is considered. In the case of backscattering ($\mathbf{k}_\perp^s = -\mathbf{k}_\perp^i$) and for a homogeneous profile where $R_v = r_v$ and $R_h = r_h$, the first-order backscattering coefficients are given by

$$\begin{aligned}
\sigma_{hhhh}^0 &= \frac{4}{\pi} k_0^4 \cos^4 \theta_i \left| R_h^i \right|^2 W(-2\mathbf{k}_\perp^i) , \\
\sigma_{vvvv}^0 &= \frac{4}{\pi} \cos^4 \theta_i \left| \frac{(k_1^2 - k_0^2)(k_{1z}^2 + k_1^2 \sin^2 \theta_i)}{(k_{1z}^i + \epsilon k_z^i)^2} \right|^2 W(-2\mathbf{k}_\perp^i) , \\
\sigma_{hvhv}^0 &= \sigma_{vhvh}^0 = 0 ,
\end{aligned}$$

which are in agreement with the results reported in the literature [62]. Before we proceed with the higher order scattering solutions, the following observations are in

order. The analysis is simplified if we assume that the surface height profile $f(x,y)$ is a Gaussian random field. There is some evidence that this assumption is reasonable for some surfaces of practical importance [29]. Since Fourier transformation is a linear operation, $F(\mathbf{k}_\perp)$ is also Gaussian. It is well known that the following identities hold for a zero-mean jointly Gaussian random vector $\{X_1, \ldots, X_n\}$:

$$\langle X_i X_j X_k \rangle = 0 \ , \tag{2.22}$$

$$\langle X_i X_j X_k X_l \rangle = \langle X_i X_j \rangle \langle X_k X_l \rangle + \langle X_i X_k \rangle \langle X_j X_l \rangle + \langle X_i X_l \rangle \langle X_j X_k \rangle \ . \tag{2.23}$$

On the other hand, it can be shown that

$$S_{ij}^{(1)} \propto F(\mathbf{k}_\perp^s - \mathbf{k}_\perp^i) \ , \tag{2.24}$$

$$S_{ij}^{(2)} \propto \int_{-\infty}^{\infty} d\mathbf{k}_\perp \, F(\mathbf{k}_\perp^s - \mathbf{k}_\perp) F(\mathbf{k}_\perp - \mathbf{k}_\perp^i) \, I_{ij}^{(2)}(\mathbf{k}_\perp) \ , \tag{2.25}$$

$$S_{ij}^{(3)} \propto \iint_{-\infty}^{\infty} d\mathbf{k}_\perp d\mathbf{k}'_\perp \, F(\mathbf{k}_\perp^s - \mathbf{k}_\perp) F(\mathbf{k}_\perp - \mathbf{k}'_\perp) F(\mathbf{k}'_\perp - \mathbf{k}_\perp^i) \, I_{ij}^{(3)}(\mathbf{k}_\perp, \mathbf{k}'_\perp) \ , \tag{2.26}$$

where $I_{ij}^{(2)}$ and $I_{ij}^{(3)}$ are functions of polarization currents (see (2.17)$\sim$(2.20) and Appendix A). For the evaluation of the covariance matrix, we confine our interest in perturbation terms up to $\triangle^4$. Substituting (2.24)$\sim$(2.26) in (2.16) and then using (2.22), the elements of covariance matrix simplify to

$$\left\langle S_{ij} S_{pq}^* \right\rangle \approx \left\langle S_{ij}^{(1)} S_{pq}^{(1)*} \right\rangle \triangle^2 + \left[\left\langle S_{ij}^{(2)} S_{pq}^{(2)*} \right\rangle + \left\langle S_{ij}^{(1)} S_{pq}^{(3)*} \right\rangle + \left\langle S_{ij}^{(3)} S_{pq}^{(1)*} \right\rangle \right] \triangle^4 . \tag{2.27}$$

Noting that property (2.22) is valid for any odd number of random variables, the elements of covariance matrix are only functions of even power of $\triangle$. Therefore the next higher order of approximation in calculation of $\left\langle S_{ij} S_{pq}^* \right\rangle$ can be obtained by inclusion of products of the first and the fifth, the second and the fourth, and the third-order scattering terms. However, evaluation of high-order scattered fields such

as fourth and fifth order are rather complex and tedious. Noting that $\triangle$ is a small quantity compared to the wavelength, the benefit of inclusion of $\triangle^6$ term is not significant. This argument cannot be used for the second order solution ($\triangle^4$ term), since this term is the dominant factor for some important scattering parameters such as cross-polarized backscattering coefficient and co-polarized degree of correlation.

The scattering matrix elements up to third order are derived. These expressions are very lengthy and are included in the Appendix A. Using these expressions in (2.27), the elements of the covariance matrix can be obtained. The ensemble averaging process can be carried out easily using (2.23), and

$$\triangle^2\langle F(\mathbf{k}_\perp)F^*(\mathbf{k}'_\perp)\rangle = \triangle^2\langle F(\mathbf{k}_\perp)F(-\mathbf{k}'_\perp)\rangle = (2\pi)^2\,\delta(\mathbf{k}_\perp - \mathbf{k}'_\perp)W(\mathbf{k}_\perp)\,. \tag{2.28}$$

Using the above mentioned properties, and noting that in backscatter direction ($\phi_s = \phi_i + \pi$, $\theta_s = \theta_i$) $S_{hv}^{(1)} = S_{vh}^{(1)} = 0$, the cross-polarized backscattering coefficients can be obtained and are given by

$$\begin{aligned}\sigma^0_{hvhv} = \sigma^0_{vhvh} = {} & \frac{\left|k_0 k_z^i(\epsilon-1)^2\right|^2}{16\pi^3}\left|\left(1-R_v^i\right)\left(1+R_h^i\right)C_0^h(\mathbf{k}^i,d)C_0^v(\mathbf{k}^i,d)\right|^2 \\ & \cdot\int_{-\infty}^{\infty} W(\mathbf{k}_\perp-\mathbf{k}_\perp^i)W(\mathbf{k}_\perp+\mathbf{k}_\perp^i)\sin^2(\phi-\phi_i)\cos^2(\phi-\phi_i) \\ & \cdot\left|\frac{k_0^2}{k_z+k_{1z}}C_0^h(\mathbf{k},d) - \frac{k_z k_{1z}}{k_{1z}+\epsilon k_z}C_0^v(\mathbf{k},d)\right|^2 d\mathbf{k}_\perp\ ,\end{aligned} \tag{2.29}$$

which satisfies the reciprocity condition. To examine the validity of (2.29), a homogeneous profile is considered having $R_h = r_h$ and $R_v = r_v$. In this case

$$\begin{aligned}\sigma^0_{hvhv} = \sigma^0_{vhvh} = {} & \frac{2}{\pi^3}\left|\frac{k_0(k_z^i)^2k_{1z}^i\left(k_1^2-k_0^2\right)^2}{\left(k_0^2k_{1z}^i+k_1^2k_z^i\right)\left(k_z^i+k_{1z}^i\right)}\right|^2 \\ & \cdot\int\left|\frac{\left(k_x^ik_y-k_y^ik_x\right)\left(k_x^ik_x+k_y^ik_y\right)}{(k_\rho^i)^2\left(k_0^2k_{1z}+k_1^2k_z\right)}\right|^2 W(\mathbf{k}_\perp-\mathbf{k}_\perp^i)W(\mathbf{k}_\perp+\mathbf{k}_\perp^i)\,d\mathbf{k}_\perp\ ,\end{aligned} \tag{2.30}$$

which is in agreement with result reported in [62].

2.2.2 Phase Statistics

Traditionally, scattering models for rough surfaces provide formulations for co- and cross-polarized scattering coefficients. With the advances in the development of polarimetric radar, the statistics of the phase difference of scattering matrix elements can be measured and used in inversion algorithms to retrieve the target parameters. In a polarimetric backscatter measurement, apart from the backscattering coefficients, the co- and cross-polarized phase differences, defined by $\phi_c = \phi_{hh} - \phi_{vv}$ and $\phi_x = \phi_{hv} - \phi_{vv}$, are two additional independent parameters which can be used in an inversion process. In a recent paper [45], it was shown that the statistics of the phase difference can be derived from the elements of the target covariance matrix ($\langle S_{ij} S_{pq}^* \rangle$) and that the pdf of each phase-difference can be fully determined in terms of two parameters : (1) coherent phase difference (ζ) and (2) degree of correlation (α). The coherent phase difference is the phase difference at which the pdf assumes its maximum. The degree of correlation is a real number that can vary from 0 to 1 and is proportional to the spread of the pdf around ζ, where $\alpha = 0$ corresponds to a uniform distribution and $\alpha = 1$ corresponds to a delta function. In terms of covariance matrix elements, ζ and α are given by

$$\zeta = \tan^{-1} \frac{Im\left[\langle S_{ij} S_{vv}^* \rangle\right]}{Re\left[\langle S_{ij} S_{vv}^* \rangle\right]} , \qquad \alpha = \sqrt{\frac{|\langle S_{ij} S_{vv}^* \rangle|^2}{\langle |S_{ij}|^2 \rangle \langle |S_{vv}|^2 \rangle}} , \tag{2.31}$$

where subscript $ij = hh$ for co-polarized and $ij = vh$ or hv for cross-polarized phase difference respectively. Referring to (2.17)–(2.20) it can easily be shown that $\alpha_c = 1$ and $\alpha_x = 0$ for the first-order scattering solution. Hence α_c and α_x do not contain any information about the surface power spectral density or the surface dielectric constant. Noting that to the first-order solutions, elements of the covariance matrix are linearly proportional to the power spectral density, ζ_c is only a function of the

surface dielectric profile.

To characterize the dependency of α_c and α_x on the surface power spectral density, we have to resort to the second-order scattering solution. Combining the first-order solution given by (2.17)−(2.20) and the second-order and third-order solutions, closed form expressions for the parameters of phase-difference statistics can be obtained. It is found that α_x vanishes when the surface power spectral density is azimuthally symmetric, that is, if $W(k_x, k_y) = W(\sqrt{k_x^2 + k_y^2})$. This is usually the case for most practical situations, which implies the co- and cross-polarized backscattered fields are mutually uncorrelated.

2.3 Data Simulation and Experimental Results

In the previous section, an analytical model for predicting polarimetric scattering behavior of inhomogeneous rough surfaces based on a perturbation expression of induced polarization current was obtained. Here, data simulation based on the complete second-order analytical model is carried out to investigate the sensitivity of the radar backscatter measurements to physical parameters of the surface, such as the surface dielectric profile and surface power spectral density. Also, polarimetric backscatter measurements were conducted to examine the significance of the second-order solution on the overall backscatter response as a function of surface parameters and radar attributes.

Figures 2.2a and 2.2b demonstrate the significance of the second-order solution, where the ratio of the first-order to the complete co-polarized second-order solutions $(\sigma^{0(1)})/\sigma^{0(2)})$ are plotted versus incidence angle. An exponential correlation function given by

$$\rho(x, y) = s^2 \, e^{-\frac{\sqrt{x^2+y^2}}{l}} \quad , \tag{2.32}$$

where s is the rms height and l is the surface correlation length, is used in these simulations. In Figs. 2.2a and 2.2b, ks and kl are varied as free parameters, and the soil surface is assumed to be a homogeneous medium with $\epsilon = 8.0 + i\,2.51$. This dielectric constant corresponds to a moist soil surface with volumetric moisture content $m_v = 0.2$ and is computed using the empirical formula given in [14] at 1.25 GHz with $S = 0.1$ and $C = 0.3$. It is shown that the second-order scattering term is more sensitive to variations in rms height(s) than it is to the surface correlation length (l). The sensitivity to s is higher at lower angles of incidence for σ^0_{vvvv} unlike σ^0_{hhhh}. Figures 2.3a and 2.3b show the ratio of the first-order to the complete co-polarized second-order solutions of the homogeneous rough surface as a function of soil moisture at $\theta = 45^o$. Here it is shown that as the soil moisture increases from 0.01 ($\epsilon = 2.21 + i\,0.002$) to 0.4 ($\epsilon = 14.68 + i\,7.5$), the contribution from the second-order scattering term to the overall backscattering increases slightly. This effect is more pronounced for σ^0_{hhhh}. Figures 2.2 and 2.3 demonstrate that the inclusion of the second-order solution is more important for calculation of σ^0_{hhhh} than for σ^0_{vvvv}. Figures 2.4 and 2.5 show the co-polarized coherent phase difference ζ_c calculated from the first-order and complete second-order solutions for the homogeneous surface as a function of incidence angle and soil moisture. To the first order, ζ_c is independent of surface roughness parameters, however, the second-order solution shows a weak dependency on ks and kl. It is interesting to note that the sensitivity to roughness parameters disappears for incidence angles larger than 50^o. As shown in Fig. 2.5, ζ_c is relatively insensitive to moisture content for a homogeneous surface.

As mentioned before, the second-order solution is the dominant component for the cross-polarized backscattering coefficient. σ^0_{hvhv} is directly proportional to the square of the rms height, thus the dependency to s is not examined. Figure 2.6

shows σ^0_{hvhv} of the homogeneous surface as a function of incidence angle for different values of kl and m_v while $ks = 0.2$ is kept constant. Note that σ^0_{hvhv} increases with increasing dielectric constant and decreases with increasing surface correlation length. The co-polarized degree of correlation is another potential parameter that can be used in retrieval of surface physical parameters. The first-order scattering solution predict $\alpha_c = 1$ independent of the surface physical parameters. Figures 2.7 and 2.8 show α_c for the homogeneous rough surface as a function of incidence angle and dielectric constant for different values of ks and kl. Note that α_c, in general, has a decreasing trend with increasing incidence angle, rms height, and soil moisture. It is also noted that α_c increases when kl is decreased. The total dynamic range of α_c as a function of the surface parameters is rather limited.

Next we examine the sensitivity of the polarimetric backscatter data to the surface dielectric inhomogeneity. Three dielectric profiles are considered here: (1) exponentially increasing moisture with depth, (2) exponentially decreasing moisture with depth, and (3) a two-layer step profile, as shown in Fig. 2.9. The exponential profiles are chosen according to [28] and are given by:

$$m_v(z) = \begin{cases} m_{vs} + \triangle m_v \, \frac{e^{\beta z}-1}{e^{-\beta d}-1} & -d \le z \le 0 \ , \\ m_v(z) = m_v(-d) & z \le -d \ , \end{cases}$$

where m_{vs} is the surface moisture content and $\triangle m_v$ is the increment of moisture at a depth d below the surface. The moisture content below depth d is considered to be uniform. In all cases the backscatter parameters are compared with a homogeneous profile having a dielectric constant equal to that of the inhomogeneous profile at the interface. Figures 2.10 and 2.11 show the backscattering coefficients for a surface with the increasing and decreasing exponential dielectric profiles and having $ks = 0.2$, $kl = 2$. Note that the backscattering coefficients are insensitive to

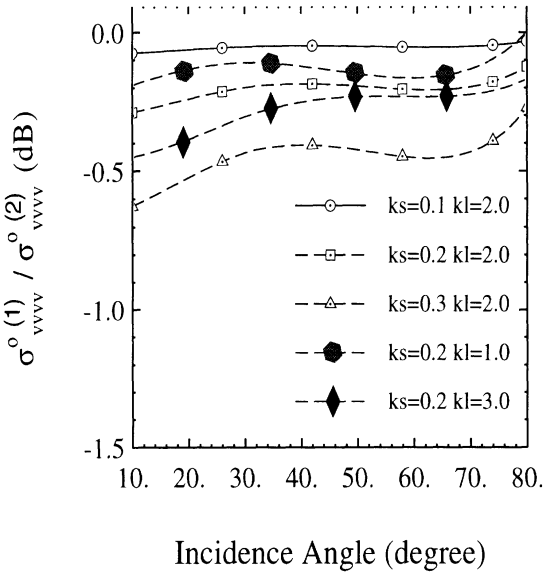

(a)

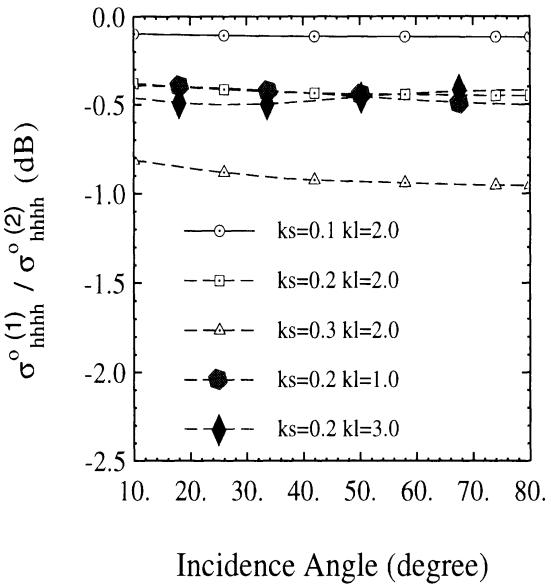

(b)

Figure 2.2: Ratio of the first-order to the complete second-order solution of a homogeneous rough surface with $m_v = 0.2$ ($\epsilon = 8.0 + i\,2.51$ at 1.25 GHz) as a function of incidence angle for different values of ks and kl.

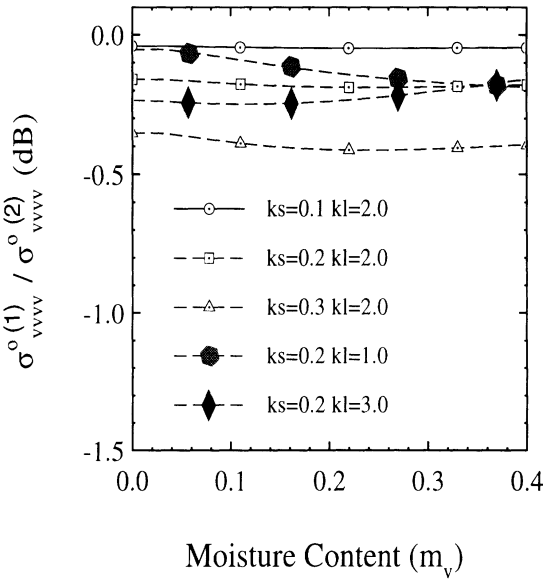

(a)

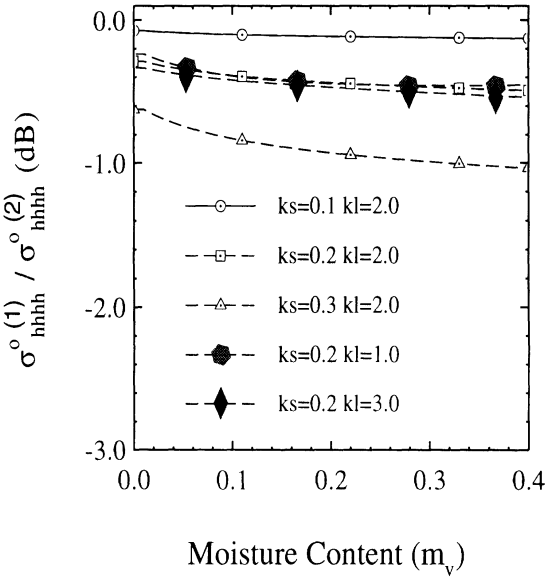

(b)

Figure 2.3: Ratio of the first-order to the complete second-order solution of a homogeneous rough surface as a function of moisture content for different values of ks and kl at $\theta = 45^o$.

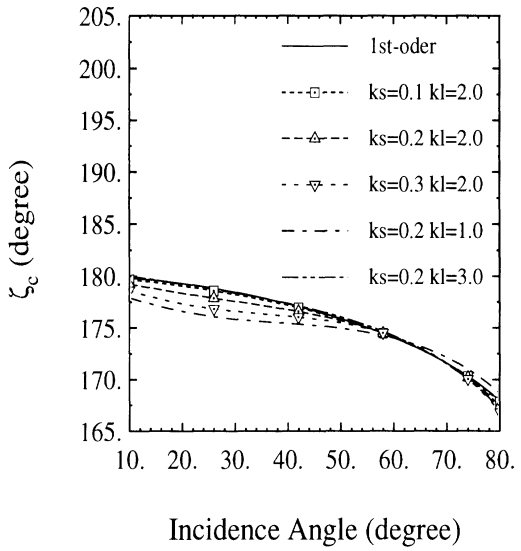

Figure 2.4: Co-polarized coherent phase difference of homogeneous rough surface with $m_v = 0.2$ ($\epsilon = 8.0 + i\,2.51$ at 1.25 GHz) as a function of incidence angle for different values of ks and kl.

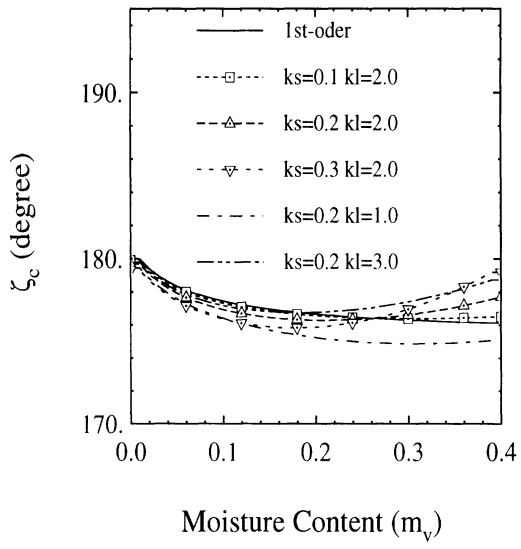

Figure 2.5: Co-polarized coherent phase difference of homogeneous rough surface as a function of moisture content for different values of ks and kl at $\theta = 45^o$.

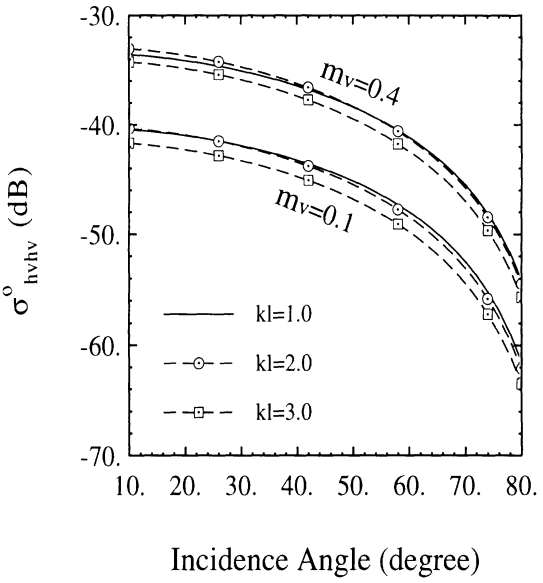

Figure 2.6: Variations of cross-polarized backscattering coefficient as a function of incidence angle, moisture content ($\epsilon = 4.89 + i\,0.92$ for $m_v = 0.1$ and $\epsilon = 14.68 + i\,7.5$ for $m_v = 0.4$ at 1.25 GHz) and correlation length for a surface with $ks = 0.2$.

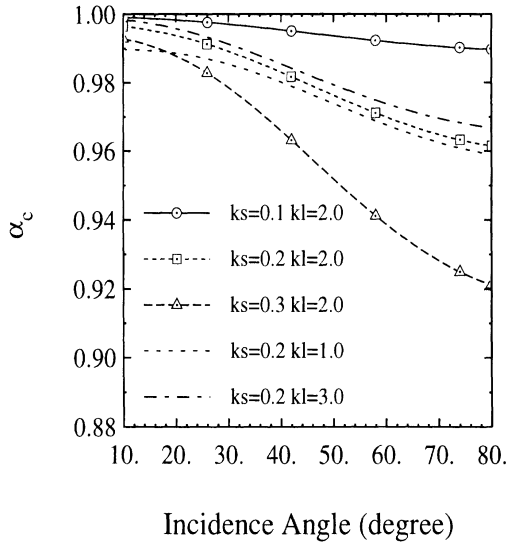

Figure 2.7: Sensitivity of co-polarized degree of correlation to incidence angle for different values of ks and kl and moisture content $m_v = 0.2$ ($\epsilon = 8.0 + i\,2.51$ at 1.25 GHz).

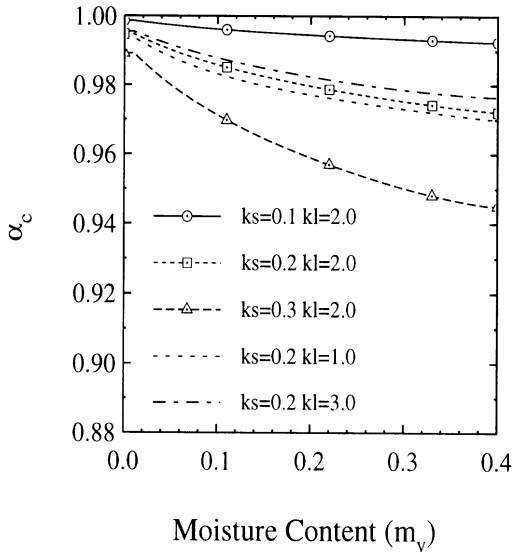

Figure 2.8: Sensitivity of co-polarized degree of correlation to soil moisture content for different values of ks and kl at $\theta = 45^o$. α_c does not show much sensitivity to kl.

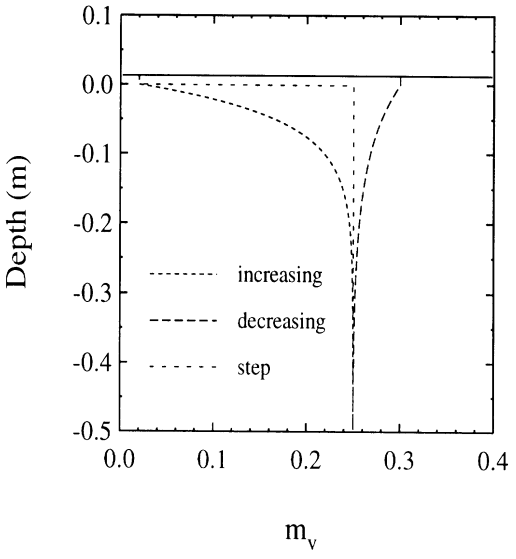

Figure 2.9: Three different moisture profiles used in the backscattering simulations: increasing exponential with $\beta = 20$, decreasing exponential with $\beta = 10$, and step.

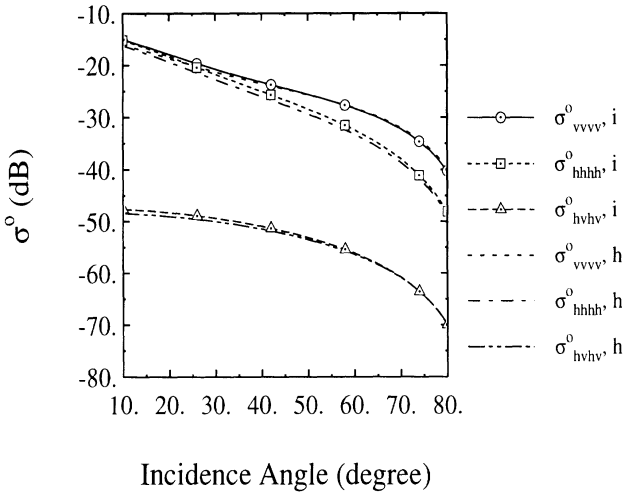

Figure 2.10: Comparison of backscattering coefficients calculated for the homogeneous and increasing exponential moisture profiles for a rough surface with $ks = 0.2$ and $kl = 2$.

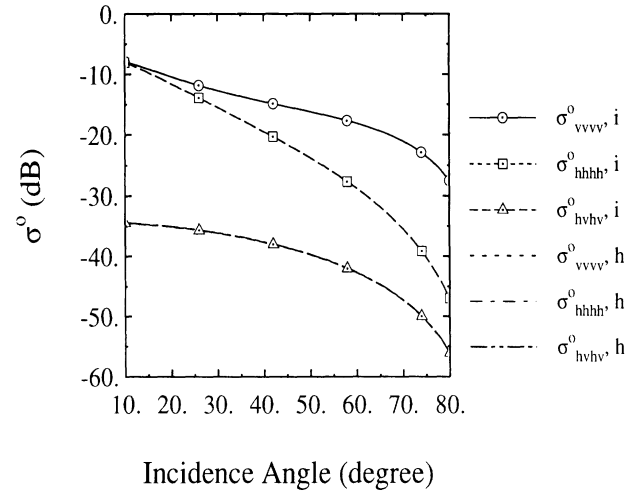

Figure 2.11: Comparison of backscattering coefficients calculated for the homogeneous and decreasing exponential moisture profiles for a rough surface with $ks = 0.2$ and $kl = 2$.

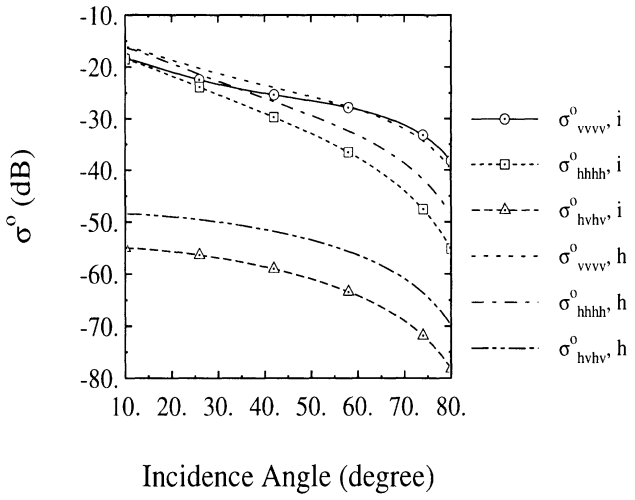

Figure 2.12: Comparison of backscattering coefficients calculated for the homogeneous and step moisture profiles for a rough surface with $ks = 0.2$ and $kl = 2$.

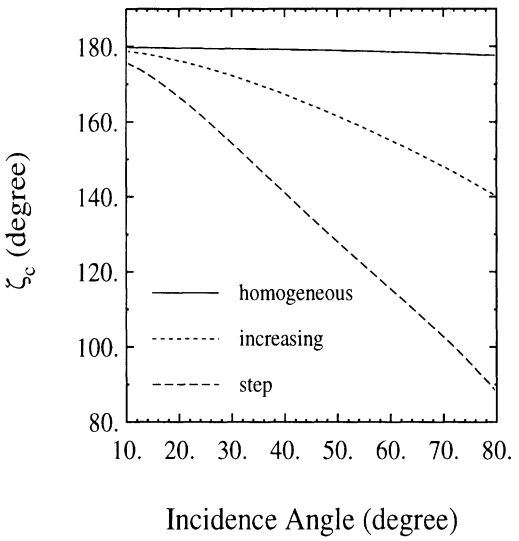

Figure 2.13: Co-polarized coherent phase difference calculated for the homogeneous, increasing exponential, and step moisture profiles for a rough surface with $ks = 0.2$ and $kl = 2$.

moisture profiles, and the backscattering coefficients are basically indistinguishable from those of the homogeneous profile having the same dielectric constant as that of the inhomogeneous profile at the interface. This is due to the tapered impedance matching nature of the profile. However, this is not the case for the step profile as shown in Fig. 2.12. The difference in σ^o, depending on the incidence angle, can be as high as 10 dB. The only sensitive parameter to moisture variations in depth for continuous profiles is the co-polarized coherent phase difference as is shown in Fig. 2.13, where ζ_c for the homogeneous, increasing, and step moisture profiles are shown. ζ_c does not shown any sensitivity for decreasing profiles. It should be pointed out that the calculation of the complete second-order solution involves numerical evaluation of two-fold integrals. To provide a feeling for the required computation time, the calculation of backscattering coefficients and phase difference statistics for one incidence angle would take about one minute on a Sun workstation Ultra 2.

The validity of the analytical results are also examined by conducting backscatter measurements. The backscatter measurements were performed polarimetrically using the indoor bistatic facilities of the Radiation Laboratory at the University of Michigan [9]. The backscatter data were collected from a rough layer of sand above a perfectly conducting ground plane at center frequency 9.25 GHz with a bandwidth of 1.5 GHz. A $6' \times 6'$ sand-box on top of a computer controlled turntable was used to contain the sand layer. The antenna footprint covered an area of about $0.27 \sec\theta \ m^2$ on the sand-box and collection of independent backscatter data was facilitated by rotating the sand-box at steps of 5^o. The wide bandwidth of the radar system was used to range-gate the possible unwanted radar backscatter from the sand-box walls and edges. A simplified block diagram of the measurement system is shown in Fig. 2.14.

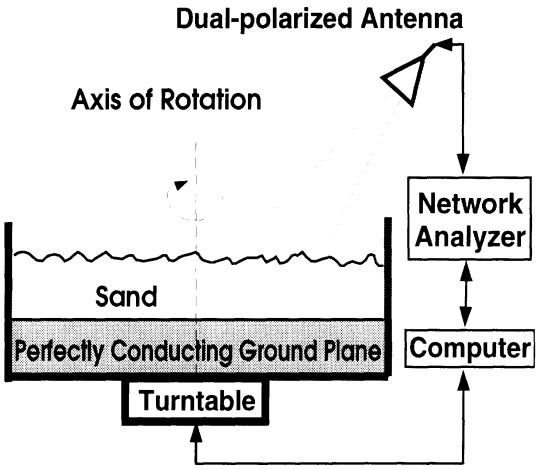

Figure 2.14: Simplified block diagram of the experimental setup.

An uniform sand with maximum particle dimension of 0.15 mm was chosen to minimize the effect of volume scattering from the sand layer. The effective dielectric constant of the sand medium was measured to be $\epsilon_r = 2.7 + i\,0.05$. The radar was calibrated polarimetrically using STCT [38]. To generate a desired roughness over the sand surface repeatedly, a template was made. The imprint of the template on the surface generated a rough surface with almost an exponential auto-correlation function with $ks = 0.122$ and $kl = 2.69$. The surface roughness statistics were measured using a laser ranging system with a range resolution of 0.1 mm. The backscatter measurements conducted for two layers having thicknesses $d = 2.52$ cm and $d = 3.53$ cm over the angular range $20^o \sim 50^o$.

Figures 2.15a and 2.15b show the measured and simulated σ^0 versus incidence angle. All the measured results are shown to be in a very good agreement with the complete second order solution except for the cross-polarized responses at $\theta = 50^o$. For these cases we were limited by the system noise floor. Figures 2.16a and 2.16b show the response of the co-polarized coherent phase difference as a function of incidence angle. Both the first-order and second-order solutions are shown and it is obvious that the second-order contribution is insignificant at angles below 40^o.

Figures 2.17a and 2.17b compare the measured and theoretical ratio of $\sigma^0_{hhhh}/\sigma^0_{vvvv}$, versus incidence angle. Here it is shown that at high incidence angles first-order results are incapable of accurate prediction of backscattering coefficients whereas the second-order solution provide satisfactory results. Figures 2.18a and 2.18b show the the measured and calculated co-polarized degree of correlation versus incidence angle, where a relatively good agreement has been obtained considering the difficulties in the accurate measurement of α [46].

2.4 Conclusions

In this chapter, a bistatic polarimetric scattering model for random dielectric surfaces with inhomogeneous permittivity profiles and small surface roughness is developed using a perturbation expansion of volumetric polarization current. A complete second-order solution for the backscattering coefficients and the statistics of the phase difference between the elements of scattering matrix is obtained. The validity of the model is verified in a limiting case, where it is shown that the formulation for surface with inhomogeneous permittivity profile reduces to the known formulation for homogeneous rough surfaces. Also, polarimetric backscatter measurements from rough surfaces with known dielectric profiles and roughness statistics were collected and compared with the theoretical calculations. Comparisons with the measured data show excellent agreement. The sensitivity analysis in terms of the surface physical parameters is also performed. It is shown that, in general, the backscatter parameters, such as backscattering coefficients and phase-difference statistics, are more sensitive to ks than kl. The contribution of the second-order solution for calculation of σ^o_{hhhh} is more significant than that for the calculation of σ^o_{vvvv}. The contribution of the second-order solution to overall σ^o_{hhhh} can be as high as 2 dB for $ks \leq 0.3$. It is

shown that for continuous inhomogeneous profiles, the backscattering coefficients are insensitive to the variations of moisture content as a function of depth. In the other words, the backscattering coefficients of a surface with a continuous soil moisture profile are equal to those of a homogeneous surface having a moisture content equivalent to that of the inhomogeneous profile at the interface. The only backscatter parameter sensitive to moisture profile is the co-polarized coherent phase difference (ζ_c). However, both the backscattering coefficients and phase-difference statistics are very sensitive to step discontinuities in moisture profile.

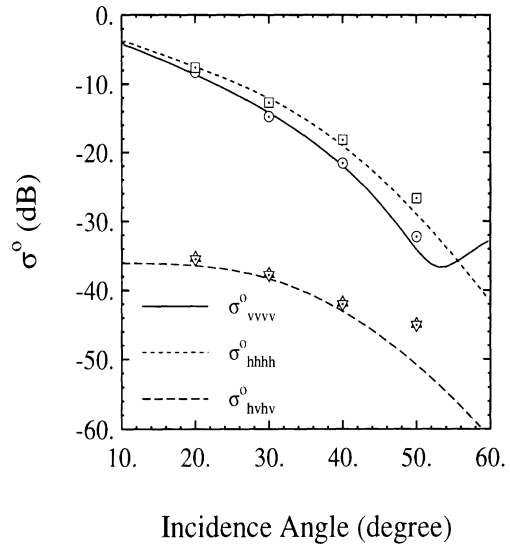

(a)

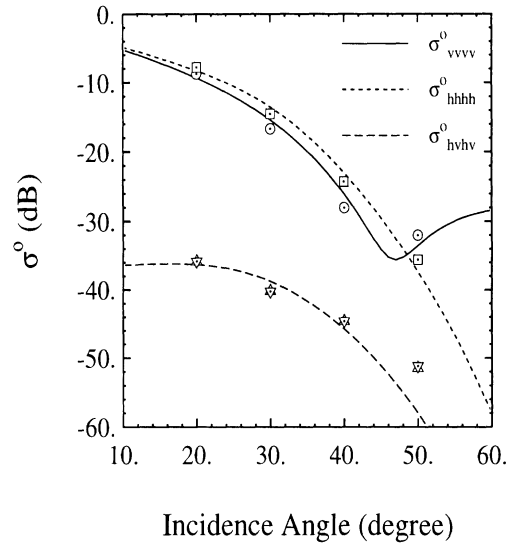

(b)

Figure 2.15: Comparison of the measured and the complete second-order simulated backscatter for a sand layer of thickness 2,52 cm (a) and 3.53 cm (b) above a perfectly conducting ground plane at 9.25 GHz. Symbols represent the measured quantities and the lines are the theoretical calculations.

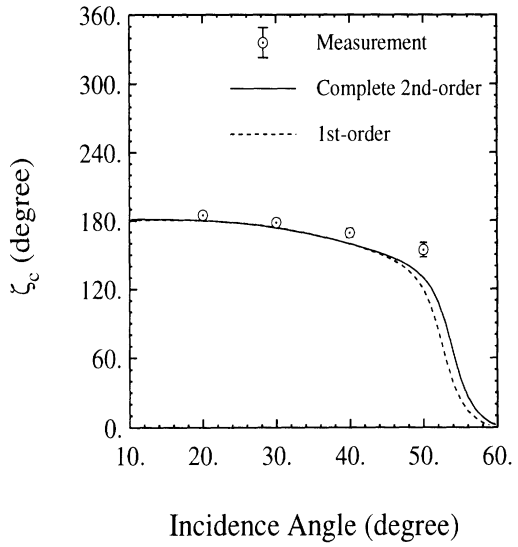

(a)

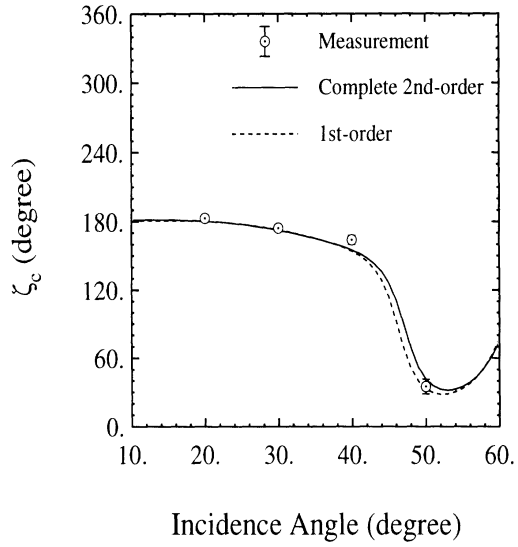

(b)

Figure 2.16: Comparison of the measured and the calculated co-polarized coherent phase difference for a sand layer of thickness 2,52 cm (a) and 3.53 cm (b) above a perfectly conducting ground plane at 9.25 GHz.

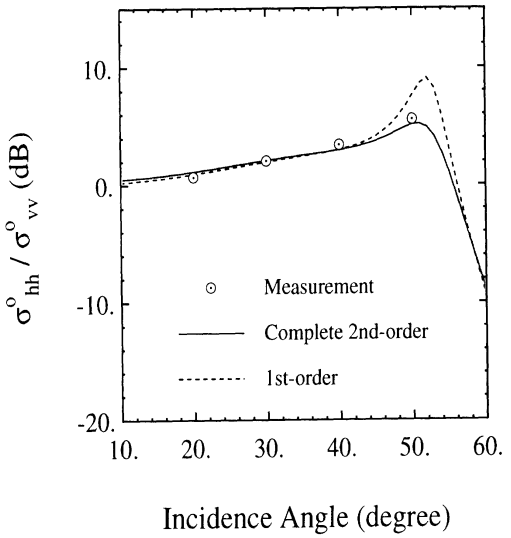

(a)

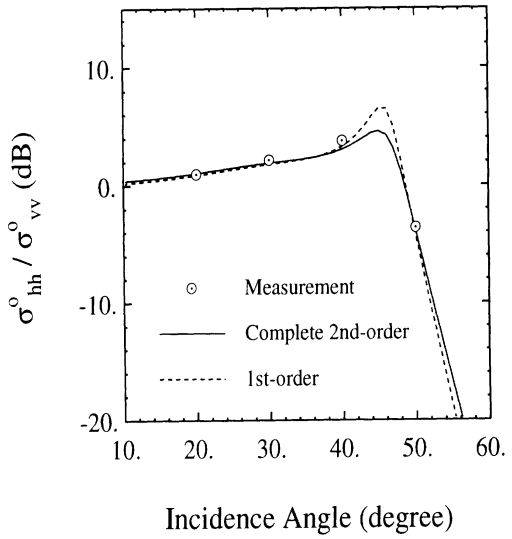

(b)

Figure 2.17: Comparison of the measured and the calculated $\sigma^o_{hhhh}/\sigma^o_{vvvv}$ for a sand layer of thickness 2,52 cm (a) and 3.53 cm (b) above a perfectly conducting ground plane at 9.25 GHz.

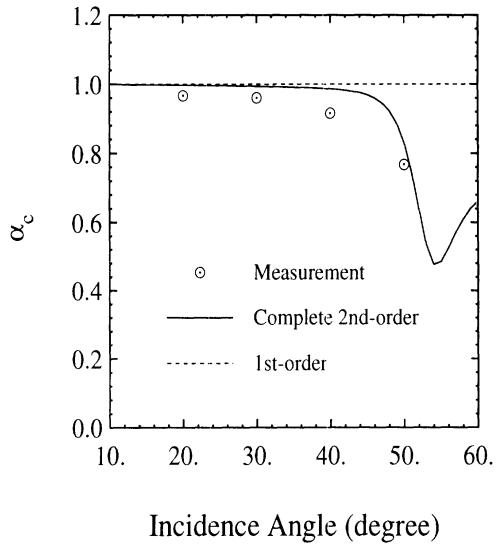

(a)

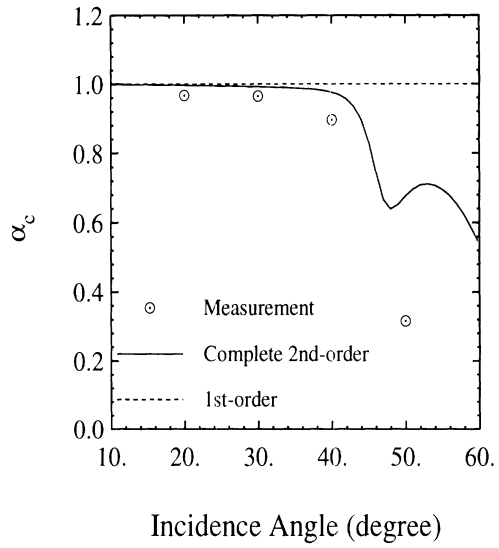

(b)

Figure 2.18: Comparison of the measured and the calculated co-polarized degree of correlation for a sand layer of thickness 2,52 cm (a) and 3.53 cm (b) above a perfectly conducting ground plane at 9.25 GHz.

CHAPTER III

ELECTROMAGNETIC SCATTERING INTERACTION BETWEEN A DIELECTRIC CYLINDER AND A SLIGHTLY ROUGH SURFACE

3.1 Introduction

Characterization of scattering behavior of targets above rough surfaces has a number of important practical applications. Assessing the performance of a radar system in detecting a point target in a clutter background like a low-flying aircraft or a military ground-vehicle can be mentioned as one such application. In radar remote sensing of vegetation, accurate scattering models that can describe the interaction of electromagnetic waves and vegetation-covered terrain is of great importance. The common approach is to regard the vegetation-covered surfaces as a random collection of dielectric particles with canonical geometries, such as cylinders representing stems and branches and thin dielectric disks representing leaves, above a half-space dielectric medium with rough interface representing the ground. Most scattering models developed for this problem are based on single scattering properties of the scatterers [69]. In these models, the scattering interaction among the vegetation particles, and the vegetation particles and the rough surface are ignored. In more

advanced models, such as radiative transfer [62] (numerical or second-order iterative solutions), the scattering interaction among scatterers are accounted for assuming that the particles are in the far-field of each other. This is not an accurate model because most vegetation structures contain large particles, such as tree trunk, long branches, and the main stems for grasses. The length of these particles are comparable to the vegetation layer thickness and are usually much larger than the wavelength. In these cases the near-field interaction, as opposed to the far-field interaction, must be taken into account [16, 47, 48]. Experimental results indicate that although the first-order scattering models are capable of predicting the co-polarized backscatter adequately, they are not able to predict the cross-polarized backscatter within a desirable accuracy [24].

The underlying ground plane, its dielectric constant and surface roughness play an important role in determining the scattering behavior of a vegetation-covered terrain. Existing scattering models for vegetation account for the interaction between the ground and the other vegetation scatterers by modeling the ground plane as a flat half-space dielectric and using the image theory. The effect of the surface roughness is accounted for by simply modifying the Fresnel reflection coefficient [8]. Therefore the backscatter from an individual scatterer above the ground plane simplifies to four major scattering mechanisms including: 1) the direct backscatter from the target, 2) bistatic scattering from the target reflected from the ground plane, 3) bistatic scattering from the target illuminated by the reflected incident wave, and 4) backscatter from the target illuminated by the reflected wave. Obviously, this solution ignores the near-field interaction between the target and surface roughness which is the subject of the investigation in this chaper.

The purpose of this study is to develop an analytical and computationally

tractable solution in order to investigate the significance of the interaction between a cylinder and a rough surface. Our approach is based on a recently developed technique which provides the dominant scattering interaction between two arbitrary objects [48]. This approach is very efficient since only the current distribution and scattered fields of isolated scatterers are needed to evaluate the interaction in the far-field region. This method is briefly discussed in section 3.2.1. In section 3.2.2, expressions for the scattered fields in the near field region of a tilted dielectric cylinder is provided. In section 3.2.3, expressions for the polarization currents induced in the top layer of a slightly rough surface with an inhomogeneous dielectric profile are presented. To simplify the calculation a theorem is developed which indicates that in the backscattering direction the near-field interaction of the cylinder with the rough surface is equal to the interaction of the rough surface with the cylinder. This theorem is discussed in the Appendix B. A sensitivity study is carried out and the pertinent results and discussion are provided. Also polarimetric backscatter measurements are performed at the bistatic scattering facility of the University of Michigan in support of the theoretical model.

3.2 Theoretical Analysis

Analytical scattering solution that accounts for the near-field interaction between a cylinder and a rough surface is developed in this section. The solution is composed of three basic formulations: 1) the fundamental formulation based on the reciprocity theorem which provides the scattered field, up to the first-order interaction, 2) analytical expansions for the induced current and the scattered field from a dielectric cylinder, and 3) the induced polarization current and the scattered field from a half-space with rough interface. In what follows, the aforementioned formulations are

described briefly and then, in section 3.2.4, are combined to arrive at the desired polarimetric backscattered expressions for the cylinder-rough surface target.

3.2.1 Electromagnetic Scattering from Two Adjacent Objects

A general method was developed for characterizing scattering interaction between two adjacent target using the scattering properties of the isolated scatterers [48]. In this section we briefly summarize the method and focus on its application to the problem at hand.

Consider two adjacent dielectric objects illuminated by a plane wave. The incident wave would induce a polarization current $\mathbf{J}_1$ in object ♯1 in the absence of object ♯2. Considering the volumetric current $\mathbf{J}_1$ as the primary source, this current would induce a volumetric current $\mathbf{J}_{12}$ in the dielectric object ♯2. The total fields produced in this case, denoted as $\mathbf{E}_1$ and $\mathbf{H}_1$, are the primary scattered fields from object ♯1 and the secondary scattered field from object ♯2. In order to compute these fields in the far-field region, consider an an elementary current source $\mathbf{J}_e$ placed at the observation point illuminating object ♯2, while the current source $\mathbf{J}_1$ is removed. The elementary current $\mathbf{J}_e = \hat{p}\delta(r - r_c)$ in the presence of object ♯2 produces an electromagnetic field which will be denoted by $\mathbf{E}_{e2}$ and $\mathbf{H}_{e2}$. The induced current in object ♯2 with relative permittivity ϵ_2 can be expressed in terms of the total electric field and ϵ_2. The induced polarization in each of the aforementioned cases are given by:

$$\mathbf{J}_{12}(\mathbf{r}) = -ik_0Y_0(\epsilon_2 - 1)\mathbf{E}_1(\mathbf{r}) \ , \qquad \mathbf{r} \in V_2, \tag{3.1}$$

$$\mathbf{J}_{e2}(\mathbf{r}) = -ik_0Y_0(\epsilon_2 - 1)\mathbf{E}_{e2}(\mathbf{r}) \ , \qquad \mathbf{r} \in V_2, \tag{3.2}$$

where k_0 and Y_0 are the wave number and characteristic admittance of free space respectively, and V_2 is the region occupied by object ♯2. Applying the reaction

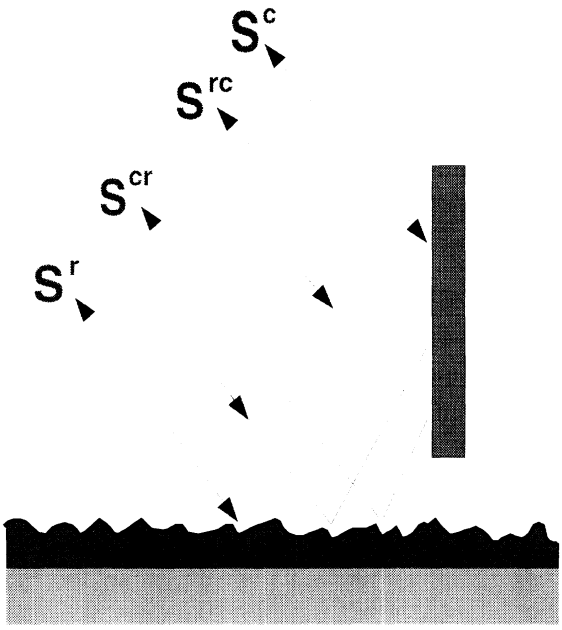

Figure 3.1: Configuration of the scattering problem.

theorem [15] over the entire space results in

$$\int_{S_\infty} (\mathbf{E}_1 \times \mathbf{H}_{e2} - \mathbf{E}_{e2} \times \mathbf{H}_1) \cdot \hat{n}\, ds = -\int_{V_1} \mathbf{J}_1 \cdot \mathbf{E}_{e2}\, dv - \int_{V_2} \mathbf{J}_{12} \cdot \mathbf{E}_{e2}\, dv + \int_{V_2} \mathbf{J}_{2e} \cdot \mathbf{E}_1\, dv + \hat{p} \cdot \mathbf{E}_1 \ . \tag{3.3}$$

Using the radiation condition, it can easily be shown that the integral on the left-hand side vanishes. Also by substituting (3.1) and (3.2) into the second and the third integrals on the right-hand side, it can be shown that the last two integrals cancel each other. Therefore, the sum of the primary scattered field from object ♯1 and the secondary scattered field from object ♯2 is given by

$$\hat{p} \cdot \mathbf{E}_1 = \int_{V_1} \mathbf{J}_1 \cdot \mathbf{E}_{e2}\, dv \ . \tag{3.4}$$

Applying this technique, the scattering formulation for a dielectric cylinder above a slightly rough surface which includes the near-field interaction between the cylinder and the rough surface can be obtained. The geometry of the scattering problem is shown in Fig. 3.1. By inspection, the backscatter from this composite target can

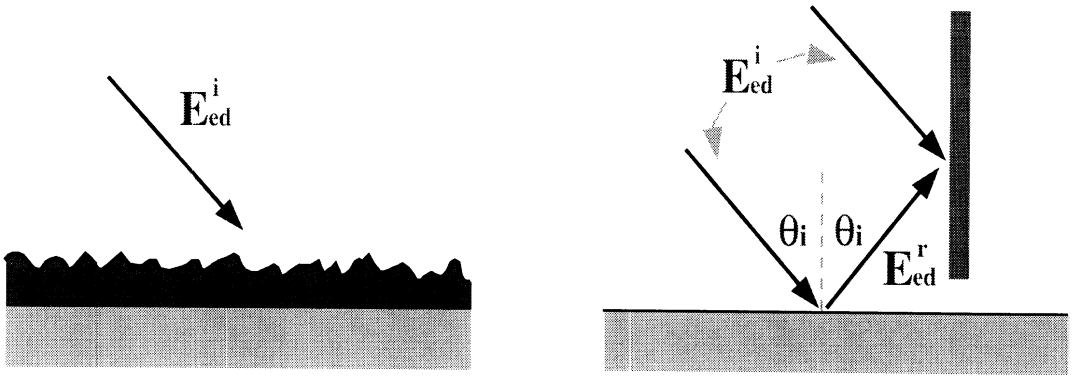

(a) (b)

Figure 3.2: The target is decomposed into two isolated targets above a half-space dielectric: (a) a rough layer of dielectric and (b) a dielectric cylinder.

be decomposed into four scattering terms: 1) direct backscatter from the cylinder ($\mathbf{S}^c$), 2) direct backscatter from the rough surface ($\mathbf{S}^r$), 3) cylinder-surface scattering ($\mathbf{S}^{cr}$), and 4) surface-cylinder scattering ($\mathbf{S}^{rc}$). $\mathbf{S}^c$ can be calculated using a semi-exact solution which is based on the eigen-function expansion and physical optics approximation [48]. To calculate $\mathbf{S}^r$, a complete second-order perturbation is applied. Using this method, the scattered fields and induced polarization current of a rough surface with inhomogeneous profile can be calculated as shown in [52]. The challenge here is the calculation of $\mathbf{S}^{cr}$ and $\mathbf{S}^{rc}$. In what follows, analytical expressions for $\mathbf{S}^{rc}$ will be formulated using (3.4). However, in this approach there are some subtleties involved as one of the two objects is a distributed scatterer. Figures 3.2(a) and 3.2(b), respectively, show the geometry of the two isolated scatterers, namely, a rough dielectric slab and a cylinder over a dielectric ground layer. Using the plane wave expansion of the scattered fields and applying reciprocity theorem, it is shown that $S^{cr} = S^{rc}$. Thus employing (3.4) for calculation of S^{rc}, an expression for the scattered field from the cylinder illuminated by an elementary current (E_{e2}) and the induced polarization current in the top rough layer of the surface illuminated by a

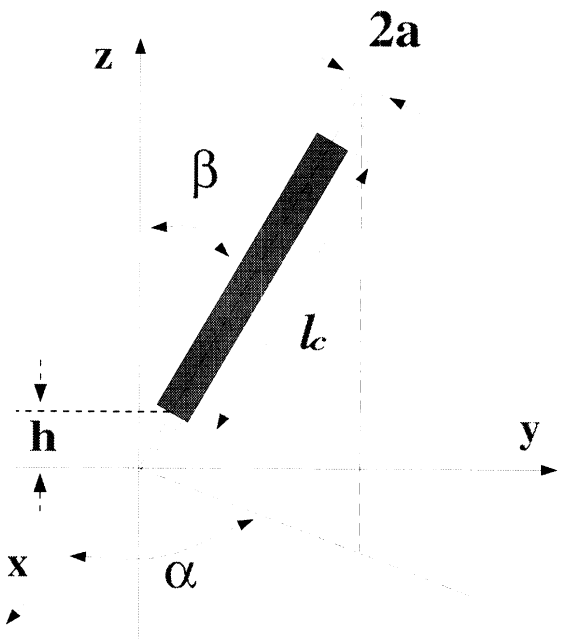

Figure 3.3: The parameters indicating the dimensions and orientation angles for a cylinder.

plane wave (J_1) are needed.

3.2.2 Scattered Field from a Tilted Dielectric Cylinder Above a Flat Surface

In this section an expression for the scattered field from a tilted dielectric cylinder above a half-space dielectric layer illuminated by an elementary current (E_{e2}) is obtained. Since the elementary current is in the far-field region of the cylinder, it is assumed that the cylinder is illuminated by a plane wave. The orientation of the cylinder is specified by a unit vector parallel to the cylinder axis given by

$$\hat{\mathbf{c}} = \hat{x}\sin\beta\cos\alpha + \hat{y}\sin\beta\sin\alpha + \hat{z}\cos\beta \ , \tag{3.5}$$

where β and α are the elevation and azimuth angles of the cylinder respectively, as shown in Fig. 3.3. Also the center of the cylinder is specified by a position vector $\bar{r}_c = (x_c, y_c, z_c)$.

The radiated field of the elementary current with polarization $\hat{p}$ ($\mathbf{J_e} = \hat{p}\delta(r - r_o)$)

in the vicinity of the cylinder, as shown in Fig. 3.2(b), is approximately given by

$$\mathbf{E}_{ed}(r) = \mathbf{E}^i_{ed}(r) + \mathbf{E}^r_{ed}(r) \ . \tag{3.6}$$

Here $\mathbf{E}^i_{ed}(r)$ is given by [48]

$$\mathbf{E}^i_{ed}(r) = \frac{-ik_o Z_o}{4\pi r_o} e^{ik_o r_o} e^{-ik_o \hat{k}_s \cdot \mathbf{r}} \hat{k}_s \times \hat{k}_s \times \hat{p} \ , \tag{3.7}$$

where $-\hat{k}_s$ is the unit vector representing the direction of propagation of $\mathbf{E}^i_{ed}(r)$ and is given by $\hat{k}_s = \hat{x}\sin\theta_s\cos\phi_s + \hat{y}\sin\theta_s\sin\phi_s + \hat{z}\cos\theta_s$. $\mathbf{E}^r_{ed}(r)$ is the field reflected by the surface given by

$$\mathbf{E}^r_{ed}(r) = \frac{ik_o Z_o}{4\pi r_o} e^{ik_o r_o} e^{ik_o \hat{k}^r_s \cdot \mathbf{r}} \left\{ r_v(\theta_s)(\hat{p}\cdot\hat{v}_s)\hat{v}^r_s - r_h(\theta_s)(\hat{p}\cdot\hat{h}_s)\hat{h}^r_s \right\} \ , \tag{3.8}$$

where $\hat{k}^r_s = -\hat{k}_s + 2(\hat{k}_s\cdot\hat{z})\hat{z}$, $\hat{h}^r_s = (\hat{k}^r_s \times \hat{z})/|\hat{k}^r_s \times \hat{z}|$, $\hat{v}^r_s = \hat{h}^r_s \times \hat{k}^r_s$, and r_v and r_h are the Fresnel reflection coefficients of the ground plane.

Both fields are approximated locally by plane waves. To express the near-zone scattered fields from the cylinder, it is convenient to express the illuminating field in a local coordinate system (x', y', z') in which z'-axis coincides with the cylinder axis. The coordinate transformation between these two systems is simply given by

$$\begin{bmatrix} x \\ y \\ z \end{bmatrix} = \begin{pmatrix} \cos\beta\cos\alpha & -\sin\alpha & \sin\beta\cos\alpha \\ \cos\beta\sin\alpha & \cos\alpha & \sin\beta\sin\alpha \\ -\sin\beta & 0 & \cos\beta \end{pmatrix} \begin{bmatrix} x' \\ y' \\ z' \end{bmatrix} \ . \tag{3.9}$$

If we confine our interest in the backscatter direction, that is $\hat{k}^s = -\hat{k}^i$, the propagation direction of incident wave in the new system are given by

$$\hat{k}_i = \hat{x}'\sin\theta'_i\cos\phi'_i + \hat{y}'\sin\theta'_i\sin\phi'_i - \hat{z}'\cos\theta'_i \ , \tag{3.10}$$

where

$$\cos\theta_i' = \frac{-\hat{k}_i \cdot \hat{\mathbf{c}}}{|\hat{k}_i| \cdot |\hat{\mathbf{c}}|} = -\sin\theta_i \sin\beta \cos(\phi_i - \alpha) + \cos\theta_i \cos\beta \ , \tag{3.11}$$

$$\sin\theta_i' = \sqrt{1 - \cos^2\theta_i'} \ , \tag{3.12}$$

$$\cos\phi_i' = [\sin\theta_i \cos\beta \cos(\phi_i - \alpha) + \sin\beta \cos\theta_i] \,/\, \sin\theta_i' \ , \tag{3.13}$$

$$\sin\phi_i' = \sin\theta_i \sin(\phi_i - \alpha) / \sin\theta_i' \ . \tag{3.14}$$

Expanding the tangential electric and magnetic fields in terms of eigen-functions of the cylindrical coordinate system and applying the stationary phase approximation only along the direction perpendicular to the cylinder axis [47], the scattered field from the cylinder when illuminated by the $\mathbf{E}^i_{ed}(r)$ in the absence of the top rough layer of the ground plane is given by

$$\mathbf{E}^i_{ec} = \frac{-ik_o Z_o e^{ik_o r_o}}{4\pi r_o} e^{ik_o \hat{k}_i \cdot \bar{\rho}_c} \mathbf{F}^i(\phi' - \phi_i', z') H_0^{(1)}(k_o \sin\theta_i' \rho') \ . \tag{3.15}$$

Here $\bar{\rho}_c = \hat{x}(x_c - z_c \tan\beta\cos\alpha) + \hat{y}(y_c - z_c \tan\beta \sin\alpha)$, $H_0^{(1)}(\cdot)$ is the zeroth-order Hankel function of the first kind, and

$$\begin{aligned}
\mathbf{F}^i(\phi' - \phi_i', z') = \frac{-1}{\sin^2\theta_i'} \sum_{m=-\infty}^{\infty} e^{im(\phi' - \phi_i')} \Bigg\{ & \left[A_m(\hat{k}_c' \times \hat{k}_c' \times \hat{z}') + B_m(\hat{k}_c' \times \hat{z}') \right] e^{ik_{cz}' z'} \\
& + \Bigg[r_v(\theta'') \left(\left[A_m(\hat{k}_c' \times \hat{k}_c' \times \hat{z}') + B_m(\hat{k}_c' \times \hat{z}') \right] \cdot \left(\hat{k}_c' \times \hat{k}_c' \times \hat{n} \right) \right) \frac{\hat{k}_c'' \times \hat{k}_c'' \times \hat{n}}{|\hat{k}_c' \times \hat{k}_c' \times \hat{n}|^2} \\
& + r_h(\theta'') \left(\left[A_m(\hat{k}_c' \times \hat{k}_c' \times \hat{z}') + B_m(\hat{k}_c' \times \hat{z}') \right] \cdot \left(\hat{k}_c' \times \hat{n} \right) \right) \frac{\hat{k}_c'' \times \hat{n}}{|\hat{k}_c' \times \hat{n}|^2} \Bigg] e^{ik_{cz}'' z'} \Bigg\} \ .
\end{aligned} \tag{3.16}$$

For (3.15) to be valid, two requirements have to be met. First, since the internal polarization currents are assumed to be the same as those of a infinite long cylinder with the same cross-section, the length of the finite cylinder should be electrically long and its dielectric should be somewhat lossy. Second, because of the application of the stationary phase approximation along the cylinder axis, the observation point

must satisfy the far-field criterion in regard with the cylinder diameter, that is

$$\rho > \frac{2d^2}{\lambda} , \tag{3.17}$$

where ρ is the distance between the observation point and the cylinder axis, and d is the cylinder diameter. Accuracy of (3.15) has been verified by performing polarimetric radar measurements [47] and examining it against the method of moment solution [31,48].

Equation (3.16) includes the two components shown in Fig. 3.4(a). The first component is the bistatic scattered field from the cylinder, which propagates along the direction given by

$$\hat{k}_c' = \hat{x}' \sin\theta_i' \cos\phi' + \hat{y}' \sin\theta_i' \sin\phi' - \hat{z}' \cos\theta_i' \ , \tag{3.18}$$

And the second term is the reflected scattered field generated by the ground plane, and its direction of propagation is denoted by

$$\hat{k}_c'' = \hat{k}_c' - 2(\hat{n} \cdot \hat{k}_c')\hat{n} \ . \tag{3.19}$$

The unit vector $\hat{n}$ is the surface normal and is given by

$$\hat{n} = \hat{z} = -\hat{x}' \sin\beta + \hat{z}' \cos\beta \ , \tag{3.20}$$

and (3.16) $r_v(\theta'')$ and $r_h(\theta'')$ are the Fresnel reflection coefficients of the ground plane at $\theta'' = \cos^{-1}(-\hat{n} \cdot \hat{k}_c')$. The coefficients A_m and B_m are given by

$$\begin{aligned} A_m &= C_m^{TM}(\theta_i')\ \hat{k}_s \times (\hat{k}_s \times \hat{p}) \cdot \hat{z}' + i\bar{C}_m(\theta_i')\ (\hat{k}_s \times \hat{p}) \cdot \hat{z}' \ , \\ B_m &= C_m^{TE}(\theta_i')\ (\hat{k}_s \times \hat{p}) \cdot \hat{z}' - i\bar{C}_m(\theta_i')\ \hat{k}_s \times (\hat{k}_s \times \hat{p}) \cdot \hat{z}' \ , \end{aligned} \tag{3.21}$$

in which C_m^{TM}, C_m^{TE} and $\bar{C}_m$ are expressed in terms of the cylinder radius, orientation angles, relative permittivity, the frequency, and the incidence angle (see [68] or 4.26).

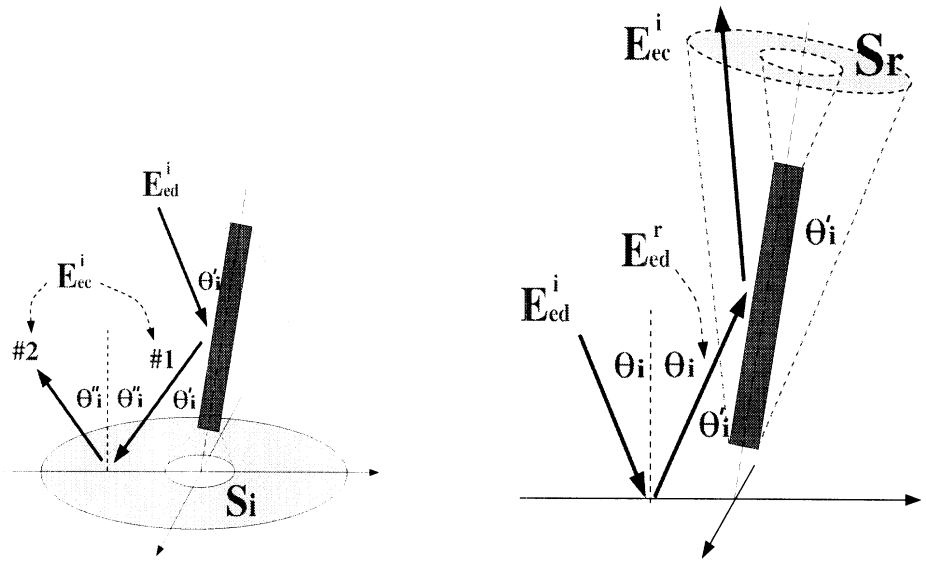

(a) (b)

Figure 3.4: The conical regions of the significant scattered field from a cylinder for the direct incident fields $\mathbf{E}^i_{ed}$ (a) and the reflected incident field $\mathbf{E}^r_{ed}$ (b).

It should be noted that $\mathbf{F}^i(\phi' - \phi'_i, z')$ is non-vanishing at observation points for which the stationary point is located on the surface of the finite cylinder, that is, the region of the significant scattered field is confined to the forward scattering cone as shown in Fig. 3.4(a). The illuminated region (S_i) may be a finite or infinite area, depending on the incidence angle and the orientation angle of the cylinder. If $\theta'_i + \beta \geq 90^o$, then S_i has infinite area. when $\theta'_i + \beta < 90^o$, S_i is an elliptical region (for tilted cylinders) or a circular region (for vertical cylinders).

Similarly, the scattered field from the cylinder when illuminated by the $\mathbf{E}^r_{ed}(r)$ in the absence of the top rough layer of the ground plane is shown in Fig. 3.4(b). The region of the significant scattered field is confined to the forward scattering cone as well. Noting that the observation points of interest are within the top rough layer, significant scattering exist only when $\theta'_r + \beta > 90^o$. Also the illuminated region S_r, if exist, is always infinite. In this chapter, we confine our interest to vertical or

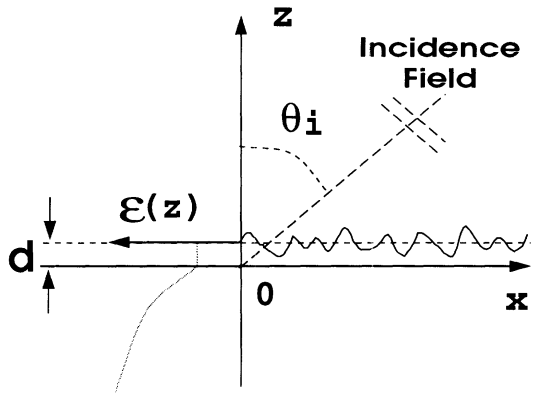

Figure 3.5: An inhomogeneous half-space medium with a rough interface. Left side of this figure shows the dielectric profile.

nearly vertical cylinders for which $S_r = 0$. Therefore, this mechanism will not be considered.

3.2.3 Induced Polarization Current in a Slightly Rough Surface

The expression for the polarization current induced by a plane wave in the top rough layer of a stratified half-space medium is obtained in a recently developed scattering model for slightly rough surface with inhomogeneous dielectric profile introduced in Chapter II. Unlike the traditional small perturbation model (SPM) [33], this new model was developed based on a volume integral in conjunction with the half-space dyadic Green's function which take into account the effect of dielectric inhomogeneity under the rough surface. This section will only present the formulation required in this chapter.

Consider an inhomogeneous half-space medium with a rough interface as shown in Fig. 3.5. It is assumed that the medium is stratified, that is, the relative permittivity is only a function of z, and the permittivity of the top layer down to a depth of d is uniform where $-d < min\{\text{surface profile}\}$. The surface profile is denoted as $\triangle f(x,y)$ where $f(x,y)$ is a zero-mean stationary random process with a known autocorrelation function, and $\triangle$ is a small constant known as the perturbation pa-

rameter. The top rough layer is replaced with an equivalent polarization current, and using a volumetric integral equation in conjunction with the dyadic Green's function of the remaining stratified half-space medium, the scattering problem is formulated. Analytical expressions for the induced polarization currents up to any desired order can be derived, nevertheless, in this treatment, only the induced polarization current up to the second-order are needed. That is, the total polarization current is approximated by:

$$\mathbf{J}(\mathbf{r}) = \mathbf{J}_0(\mathbf{r}) + \triangle \mathbf{J}_1(\mathbf{r}) + \triangle^2 \mathbf{J}_2(\mathbf{r}) \ . \tag{3.22}$$

These currents are expressed in term of their two-dimensional Fourier transforms defined by

$$\mathbf{J}_n(\mathbf{r}) = \frac{1}{(2\pi)^2} \int \tilde{\mathbf{J}}_n(\mathbf{k}_\perp, z) e^{i\mathbf{k}_\perp \bar{\rho}} \, d\mathbf{k}_\perp \ , \tag{3.23}$$

in a recursive manner. The expression for $\tilde{\mathbf{J}}_0(\mathbf{k}_\perp, z)$ is given by

$$\begin{aligned} \tilde{\mathbf{J}}_0(\mathbf{k}_\perp, z) =& (2\pi)^2 \delta(\mathbf{k}_\perp - \mathbf{k}_\perp^i) \mathbf{J}_0(z) \\ =& (2\pi)^2 \delta(\mathbf{k}_\perp - \mathbf{k}_\perp^i) \left[J_{oh}(z) \hat{h}(k_z^i) + J_{ot}(z) \hat{t}(k_z^i) + J_{oz}(z) \hat{z} \right] \ , \end{aligned} \tag{3.24}$$

where $\hat{h}(k_z^i) = (\hat{k}_i \times \hat{z})/|\hat{k}_i \times \hat{z}|$, $\hat{t}(k_z^i) = \hat{z} \times \hat{h}(k_z^i)$, and

$$\begin{aligned} J_{0h}(z) =& -i \frac{2k_0 k_z^i}{k_z^i + k_{1z}^i} Y_0 \, (\epsilon - 1) \ C_0^h(\mathbf{k}^i, z) \ \left[\mathbf{E}_o \cdot \hat{h}(k_z^i) \right] \ e^{-ik_z^i d} \ , \\ J_{0t}(z) =& -i \frac{2k_0 k_z^i k_{1z}^i}{k_\rho^i \, (\epsilon k_z^i + k_{1z}^i)} Y_0 (\epsilon - 1) \, C_0^v(\mathbf{k}^i, z) \ [\mathbf{E}_o \cdot \hat{z}] \ e^{-ik_z^i d} \ , \\ J_{0z}(z) =& -i \frac{2k_0 k_z^i}{\epsilon k_z^i + k_{1z}^i} Y_0 (\epsilon - 1) \, C_1^v(\mathbf{k}^i, z) \ [\mathbf{E}_o \cdot \hat{z}] \ e^{-ik_z^i d} \ , \end{aligned}$$

The parameters in these expressions for the zeroth-order current are given by

$$k_{1z}^i = k_0\sqrt{\epsilon - \sin^2\theta_i}\,, \qquad k_\rho^i = k_0 \sin\theta_i\,, \qquad R_h^i = \frac{k_z^i - k_{1z}^i}{k_z^i + k_{1z}^i}\,, \qquad R_v^i = \frac{\epsilon k_z^i - k_{1z}^i}{\epsilon k_z^i + k_{1z}^i}\,,$$

$$C_n^h(\mathbf{k},z) = \frac{(-1)^n\,(R_h - r_h)\,e^{ik_{1z}z} + (R_h r_h - 1)\,e^{-ik_{1z}z}}{R_h\,(R_h - r_h)\,e^{ik_{1z}d} + (R_h r_h - 1)\,e^{-ik_{1z}d}}\,,$$

$$C_n^v(\mathbf{k},z) = \frac{(-1)^n\,(r_v - R_v)\,e^{ik_{1z}z} + (R_v r_v - 1)\,e^{-ik_{1z}z}}{R_v\,(R_v - r_v)\,e^{ik_{1z}d} + (R_v r_v - 1)\,e^{-ik_{1z}d}}$$

As before r_h and r_v denotes the Fresnel reflection coefficients of the half-space medium. The expressions for higher order currents are similar to that of the zeroth order, and are given by

$$\widetilde{J}_{Nh}(\mathbf{k}_\perp,z) = \frac{ik_0^2\,(\epsilon-1)}{k_z + k_{1z}}\,C_0^h(\mathbf{k},z)\,\left[\tilde{\mathbf{V}}_N \cdot \hat{h}(k_z)\right]\,,$$

$$\widetilde{J}_{Nt}(\mathbf{k}_\perp,z) = \frac{ik_0k_{1z}\,(\epsilon-1)}{\epsilon k_z + k_{1z}}\,C_0^v(\mathbf{k},z)\,\left[\tilde{\mathbf{V}}_N \cdot \hat{v}(-k_z)\right]\,,$$

$$\widetilde{J}_{Nz}(\mathbf{k}_\perp,z) = \frac{ik_0k_\rho\,(\epsilon-1)}{\epsilon k_z + k_{1z}}\,C_1^v(\mathbf{k},z)\,\left[\tilde{\mathbf{V}}_N \cdot \hat{v}(-k_z)\right]\,,$$

where

$$\tilde{\mathbf{V}}_N = \sum_{n=0}^{N-1}\sum_{m=0}^{N-n-1}\frac{\binom{N-n-1}{m}\,(ik_z)^m}{(N-n)!}\cdot\left[\frac{\partial^{N-n-m-1}}{\partial\,(z')^{N-n-m-1}}\widetilde{\mathbf{J}}_n(\mathbf{k}_\perp,d)\right] * \bigotimes^{N-n} F(\mathbf{k}_\perp)\,.$$

Here $\bigotimes^n$ denotes the n-fold self-convolution operator ($\bigotimes^n F = \overbrace{F * F * \cdots * F}^{n}$).

3.2.4 Evaluation of the Secondary Scattered Field

Substituting (3.15) and (3.22) into (3.4), the secondary scattered field from the cylinder is given by

$$\hat{p}\cdot\mathbf{E}_s^{rc} = \iint_{S_i'} dxdy \int_0^{d+\Delta f(x,y)} \mathbf{J}(\mathbf{r})\cdot\mathbf{E}_{ec}^i(\bar{\rho},z)\,dz\,. \tag{3.25}$$

It is noted that $\mathbf{E}_{ed}^i$ and $\mathbf{E}_{ed}^r$ are not included in (3.25), since these fields would produce the direct backscatter from the rough surface. For surface with small rms

height $\triangle f(x,y)$ is a small quantity, and therefore (3.25) can be approximately by

$$\hat{p}\cdot\mathbf{E}_s^{rc} = \iint\limits_{S_i^i} dxdy \int\limits_0^d \mathbf{J}(\mathbf{r})\cdot\mathbf{E}_{ec}^i(\bar{\rho},z)\,dz + \sum_{n=0}^{\infty}\iint\limits_{S_i^i}\frac{[\triangle f(x,y)]^{n+1}}{(n+1)!}\frac{\partial^n}{\partial z^n}\left\{\mathbf{J}(\mathbf{r_d})\cdot\mathbf{E}_{ec}^i(\bar{\rho},d)\right\}dxdy\ , \tag{3.26}$$

where $\mathbf{r_d} = \hat{x}x + \hat{y}y + \hat{z}d$. Substituting (3.23) into (3.26), the first-order secondary scattered field can be expressed as:

$$\hat{p}\cdot\mathbf{E}_s^{rc(1)} = \frac{\triangle}{(2\pi)^2}\int\limits_0^d dz\int\limits_{-\infty}^{\infty}\tilde{\mathbf{J}}_1(\mathbf{k}_\perp,z)\iint\limits_{S_i}\mathbf{E}_{ec}^i(\bar{\rho},z)e^{i\mathbf{k}_\perp\bar{\rho}}\,ds\,d\mathbf{k}_\perp + \frac{\triangle}{(2\pi)^2}\mathbf{J}_0(d)\int\limits_{-\infty}^{\infty}F(\mathbf{k}_\perp-\mathbf{k}_\perp^i)\iint\limits_{S_i}\mathbf{E}_{ec}^i(\bar{\rho},d)e^{i\mathbf{k}_\perp\bar{\rho}}\,ds\,d\mathbf{k}_\perp\ . \tag{3.27}$$

Similarly, the second-order secondary scattered field is given by:

$$\begin{aligned}\hat{p}\cdot\mathbf{E}_s^{rc(2)} = {}& \left(\frac{\triangle}{2\pi}\right)^2\int\limits_0^d dz\int\limits_{-\infty}^{\infty}\tilde{\mathbf{J}}_2(\mathbf{k}_\perp,z)\iint\limits_{S_i}\mathbf{E}_{ec}^i(\bar{\rho},z)e^{i\mathbf{k}_\perp\bar{\rho}}\,ds\,d\mathbf{k}_\perp \\ &+\left(\frac{\triangle}{2\pi}\right)^2\int\limits_{-\infty}^{\infty}F(\mathbf{k}_\perp)\star\tilde{\mathbf{J}}_1(\mathbf{k}_\perp,d)\iint\limits_{S_i}\mathbf{E}_{ec}^i(\bar{\rho},d)e^{i\mathbf{k}_\perp\bar{\rho}}\,ds\,d\mathbf{k}_\perp \\ &+\left(\frac{1}{2\pi}\right)^2\frac{\triangle^2}{2}\mathbf{J}_0(d)\int\limits_{-\infty}^{\infty}F(\mathbf{k}_\perp)\star F(\mathbf{k}_\perp-\mathbf{k}_\perp^i)\iint\limits_{S_i}\frac{\partial}{\partial z}\mathbf{E}_{ec}^i(\bar{\rho},d)e^{i\mathbf{k}_\perp\bar{\rho}}\,ds\,d\mathbf{k}_\perp \\ &+\left(\frac{1}{2\pi}\right)^2\frac{\triangle^2}{2}\frac{d}{dz}\mathbf{J}_0(d)\int\limits_{-\infty}^{\infty}F(\mathbf{k}_\perp)\star F(\mathbf{k}_\perp-\mathbf{k}_\perp^i)\iint\limits_{S_i}\mathbf{E}_{ec}^i(\bar{\rho},d)e^{i\mathbf{k}_\perp\bar{\rho}}\,ds\,d\mathbf{k}_\perp\ .\end{aligned} \tag{3.28}$$

Note that for evaluating the zeroth-order secondary scattered field, one can simply use the formulation derived for a cylinder above a smooth ground plane.

The polarimetric response of a target can be expressed in terms of its complex scattering matrix defined as

$$\mathbf{E}^s = \frac{e^{ikr}}{r}\bar{\bar{\mathbf{S}}}\,\mathbf{E}^i\ .$$

For random targets, the expected radar cross section for a particular transmit and receive polarization configuration can be calculated from

$$\sigma_{pqpq} = 4\pi\langle|S_{pq}|^2\rangle \ , \qquad p,\, q \in \{h,\, v\}\,, \tag{3.29}$$

where $\langle\cdot\rangle$ denotes ensemble averaging. Depending on the order of the scattered field, $\mathbf{S}^{rc}$ can also be expanded in terms of a perturbation series, i.e., $\mathbf{S}^{rc} \approx \mathbf{S}^{rc(0)} + \triangle\mathbf{S}^{rc(1)} + \triangle^2\mathbf{S}^{rc(2)}$. As mentioned earlier, $\mathbf{S}^{rc(0)}$ can easily be obtained from

$$S_{pq}^{rc(0)} = r_p(\theta_i)\, S_{pq}^{cyl}(\hat{k}_r, \hat{k}_s) e^{ik_o(\hat{k}_r - \hat{k}_s)\cdot\bar{r}_c} \ . \tag{3.30}$$

Here $r_p(\theta_i)$ is the reflection coefficient of the ground plane and the top rough layer with a flat interface ($\triangle = 0$), $\hat{k}_r = \hat{k}_i - 2(\hat{k}_i\cdot\hat{n})\hat{n}$, and S_{pq}^{cyl} denotes a bistatic scattering matrix element of the cylinder located at the origin in free space which can be evaluated by using the infinite-cylinder approximation [54], which will be introduced in Section 4.3. Expressions for $\mathbf{S}^{rc(1)}$ and $\mathbf{S}^{rc(2)}$ can be obtained from (3.27) and (3.28), respectively. The calculation of $\mathbf{S}^{cr}$ directly is even more complicated than $\mathbf{S}^{rc}$. It can be shown that $\mathbf{S}^{cr}$ can be evaluated from $\mathbf{S}^{rc}$ using $\bar{\bar{\mathbf{S}}}^{cr} = [\bar{\bar{\mathbf{S}}}^{rc}]^{(-t)}$, that is

$$\begin{pmatrix} S_{vv}^{cr} & S_{vh}^{cr} \\ S_{hv}^{cr} & S_{hh}^{cr} \end{pmatrix} = \begin{pmatrix} S_{vv}^{rc} & -S_{hv}^{rc} \\ -S_{vh}^{rc} & S_{hh}^{rc} \end{pmatrix} \ . \tag{3.31}$$

Here the superscript $(-t)$ denotes the matrix transposing and multiplying the off-diagonal elements by -1. The proof of this identity is presented in Appendix B.

Finally an analytical expression for the average RCS of the cylinder-rough surface composite target illuminated by a collimated beam, illuminating an area A of the

rough surface, is given by

$$\frac{\sigma_{pqpq}}{4\pi} = |S^c_{pq} + S^{rc(0)}_{pq} + S^{cr(0)}_{pq}|^2 + \langle |S^{rc(1)}_{pq} + S^{cr(1)}_{pq}|^2 \rangle \triangle^2$$
$$+2\,Re\left\{\langle S^{r(1)}_{pq}(S^{rc(1)}_{pq} + S^{cr(1)}_{pq})^*\rangle + (S^c_{pq} + S^{rc(0)}_{pq} + S^{cr(0)}_{pq})\langle (S^{rc(2)}_{pq} + S^{cr(2)}_{pq})\rangle^*\right\}\triangle^2$$
$$+\sigma^{r0}_{pqpq}\frac{A}{4\pi}\,. \qquad p,\, q \in \{h,\, v\}\,. \tag{3.32}$$

The first term in (3.32) represents the zero-order solution, and the second term accounts for the first-order secondary scattered field. The third term in (3.32) represents the coherent interaction of the cylinder and rough surface scattered fields. The complete second-order backscattering coefficient from the rough surface along is represented by the fourth term of (3.32) and is given by

$$\sigma^{r0}_{pqpq} = \lim_{A\to\infty}\frac{4\pi}{A}\left\{\left\langle |S^{r(1)}_{pq}|^2\right\rangle \triangle^2 + \left[\left\langle |S^{r(2)}_{pq}|^2\right\rangle + 2Re\left\langle S^{r(1)}_{pq}S^{r(3)*}_{pq}\right\rangle\right]\triangle^4\,,\right\} \tag{3.33}$$

where $S^{r(1)}_{pq}$, $S^{r(2)}_{pq}$, and $S^{r(3)}_{pq}$ are the first-, second-, and third-order backscatter of the the rough surface. The expressions for $S^{r(1)}_{pq}$ are given by

$$S^{r(1)}_{hh} = \frac{k_0^2 k^i_z k^s_z\,(\epsilon-1)\,e^{-i(k^i_z+k^s_z)d}}{\pi\,(k^i_z+k^i_{1z})\,(k^s_z+k^s_{1z})}\,C^h_0(\mathbf{k}^s,d)\,C^h_0(\mathbf{k}^i,d)\,\cos(\phi_s-\phi_i)\,F(\mathbf{k}^s_\perp-\mathbf{k}^i_\perp)\,, \tag{3.34}$$

$$S^{r(1)}_{hv} = \frac{k_0 k^i_z k^s_z k^i_{1z}\,(\epsilon-1)\,e^{-i(k^i_z+k^s_z)d}}{\pi\,(\epsilon k^i_z+k^i_{1z})\,(k^s_z+k^s_{1z})}\,C^h_0(\mathbf{k}^s,d)\,C^v_0(\mathbf{k}^i,d)\,\sin(\phi_s-\phi_i)\,F(\mathbf{k}^s_\perp-\mathbf{k}^i_\perp)\,, \tag{3.35}$$

$$S^{r(1)}_{vh} = \frac{k_0 k^i_z k^s_z k^s_{1z}\,(\epsilon-1)\,e^{-i(k^i_z+k^s_z)d}}{\pi\,(\epsilon k^s_z+k^s_{1z})\,(k^i_z+k^i_{1z})}\,C^h_0(\mathbf{k}^i,d)\,C^v_0(\mathbf{k}^s,d)\,\sin(\phi_s-\phi_i)\,F(\mathbf{k}^s_\perp-\mathbf{k}^i_\perp)\,, \tag{3.36}$$

$$S^{r(1)}_{vv} = \frac{k^i_z k^i_{1z}\,(\epsilon-1)\,e^{-i(k^i_z+k^s_z)d}}{\pi\,(\epsilon k^i_z+k^i_{1z})\,(\epsilon k^s_z+k^s_{1z})}\Big[-k^s_z k^s_{1z}C^v_0(\mathbf{k}^s,d)C^v_0(\mathbf{k}^i,d)\cos(\phi_s-\phi_i) + \frac{\epsilon k^s_z k^s_\rho k^i_\rho}{k^i_{1z}}$$
$$\cdot\, C^v_1(\mathbf{k}^s,d)C^v_1(\mathbf{k}^i,d)\Big]\,F(\mathbf{k}^s_\perp-\mathbf{k}^i_\perp)\,, \tag{3.37}$$

where $F(\cdot)$ is the Fourier transform of the surface roughness ($f(\cdot)$), and the rather lengthy expressions for $S^{r(2)}_{pq}$ and $S^{r(3)}_{pq}$ can be found in Appendix A. For a distributed

target composed of uniformly distributed cylinders with a number density N above a rough surface, the scattering coefficients can be computed from:

$$\frac{\sigma^0_{pqpq}}{4\pi} = N\Bigg\{ |S^c_{pq} + S^{rc(0)}_{pq} + S^{cr(0)}_{pq}|^2 + \langle |S^{rc(1)}_{pq} + S^{cr(1)}_{pq}|^2 \rangle \triangle^2 + 2\,Re\Big\{ \langle S^{r(1)}_{pq} (S^{rc(1)}_{pq} + S^{cr(1)}_{pq})^* \rangle + (S^c_{pq} + S^{rc(0)}_{pq} + S^{cr(0)}_{pq}) \langle (S^{rc(2)}_{pq} + S^{cr(2)}_{pq}) \rangle^* \Big\} \triangle^2 \Bigg\} + \frac{\sigma^{r0}_{pqpq}}{4\pi} \ , \quad p,\, q \in \{h,\, v\} \, , \tag{3.38}$$

where the mutual interaction between cylinders is ignored.

To evaluate the ensemble average in (3.32) some properties of Gaussian processes can be applied. For example if $F(\mathbf{k}_\perp)$ appears as a multiplicative factor, such as those in (3.34), (3.35), (3.36), and (3.37), then the following definition can be used:

$$\lim_{A\to\infty} \frac{1}{A} \left\langle \left| \triangle F(\mathbf{k}^s_\perp - \mathbf{k}^i_\perp) \right|^2 \right\rangle = W(\mathbf{k}^s_\perp - \mathbf{k}^i_\perp) \ , \tag{3.39}$$

where $W(\mathbf{k}_\perp)$ is the power spectral density of the surface. For some expressions $F(\mathbf{k}_\perp)$ appears inside an integration and therefore the evaluation of $\langle F(\mathbf{k}_\perp) F^*(\mathbf{k}'_\perp) \rangle$ is required. In such cases the following identity can be used [62]:

$$\triangle^2 \langle F(\mathbf{k}_\perp) F^*(\mathbf{k}'_\perp) \rangle = (2\pi)^2 \, \delta(\mathbf{k}_\perp - \mathbf{k}'_\perp) W(\mathbf{k}_\perp) \ , \tag{3.40}$$

which simplifies the evaluation of a two-fold integration. Other useful properties needed for the evaluation of the ensemble averages can be found in Section 2.2.1.

A particular case of interest is when the cylinder axis is vertical to the mean surface. In this case the cross-polarized backscatter is mainly generated from the interaction between the cylinder and the rough surface and the rough surface itself. In this case $S^{r(1)}_{vh}$, $S^{rc(0)}_{vh}$, $S^{cr(0)}_{vh}$,and S^c_{vh} are zero, and the expression for the cross-polarized RCS is simplified to

$$\sigma_{vhvh} = 4\pi \langle |S^{rc(1)}_{vh} + S^{cr(1)}_{vh}|^2 \rangle \triangle^2 + \sigma^{or}{}_{vhvh} A \ , \tag{3.41}$$

where the expressions for $S_{vh}^{rc(1)}$ and $S_{vh}^{cr(1)}$ are given in Appendix C, and the expression for the cross-polarized backscattering coefficient is given by

$$\sigma^{or}_{hvhv} = \sigma^{or}_{vhvh} = \frac{|k_0 k_z^i(\epsilon-1)^2|^2}{16\pi^3} \left|\left(1-R_v^i\right)\left(1+R_h^i\right) C_0^h(\mathbf{k}^i,d) C_0^v(\mathbf{k}^i,d)\right|^2 \cdot \int_{-\infty}^{\infty} W(\mathbf{k}_\perp - \mathbf{k}_\perp^i) W(\mathbf{k}_\perp + \mathbf{k}_\perp^i) \sin^2(\phi-\phi_i)\cos^2(\phi-\phi_i) \cdot \left|\frac{k_0^2}{k_z+k_{1z}} C_0^h(\mathbf{k},d) - \frac{k_z k_{1z}}{k_{1z}+\epsilon k_z} C_0^v(\mathbf{k},d)\right|^2 d\mathbf{k}_\perp \ , \quad (3.42)$$

At low frequencies or for electrically thin cylinders, the Rayleigh solution or only the zeroth-order component in (3.16) corresponding to $m = 0$ is sufficient to calculate $\mathbf{E}_{ec}$. In this case, S_{vh}^{rc} and S_{hv}^{rc} are respectively given by

$$S_{vh}^{rc} = \frac{\triangle Z_o k_o}{(2\pi)^2} e^{ik_o(\hat{\mathbf{k}}_i - \hat{\mathbf{k}}_s)\cdot\bar{\rho}_c} C_0^{TM} J_{0h}(d) \Bigg\{ \cos\theta_s \int \Bigg[\frac{\left(e^{-ik_z^s d} - 1 + r_v^s(e^{ik_z^s d} - 1)\right)}{k_z^s} \frac{k_z k_{1z}(\epsilon-1)}{k_{1z}+\epsilon k_z} + \left(e^{-ik_z^s d} - r_v^s e^{ik_z^s d}\right)\Bigg] F(\mathbf{k}_\perp - \mathbf{k}_\perp^i) \sin\phi_k B_1(\mathbf{k}_\perp)\, d\mathbf{k}_\perp - i\sin\theta_s \int \frac{\left(e^{-ik_z^s d} - 1 - r_v^s(e^{ik_z^s d} - 1)\right)}{k_z^s} \frac{k_z k_{1z}(\epsilon-1)}{k_{1z}+\epsilon k_z} F(\mathbf{k}_\perp - \mathbf{k}_\perp^i) \sin\phi_k B_2(\mathbf{k}_\perp)\, d\mathbf{k}_\perp \ , \Bigg\} \quad (3.43)$$

$$S_{hv}^{rc} = \frac{\triangle Z_o k_o k_z^s}{(2\pi)^2} e^{ik_o(\hat{\mathbf{k}}_i - \hat{\mathbf{k}}_s)\cdot\bar{\rho}_c} C_0^{TE} J_{0t}(d) \cdot \int \Bigg[\frac{\left(e^{-ik_z^s d} - 1 - r_h^s(e^{ik_z^s d} - 1)\right)}{k_z^s} \frac{k_o^2(\epsilon-1)}{k_{1z}+\epsilon k_z} + \left(e^{-ik_z^s d} + r_h^s e^{ik_z^s d}\right)\Bigg] F(\mathbf{k}_\perp - \mathbf{k}_\perp^i) \sin\phi_k B_1(\mathbf{k}_\perp)\, d\mathbf{k}_\perp \ , \quad (3.44)$$

where

$$B_1(\mathbf{k}_\perp) = \int_{a+h\tan\theta_i}^{a+(l_c+h)\tan\theta_i} H_0^{(1)}(k_o \sin\theta^s \rho') J_0'(|\mathbf{k}_\perp|\rho')\rho' d\rho' \ ,$$

$$B_2(\mathbf{k}_\perp) = \int_{a+h\tan\theta_i}^{a+(l_c+h)\tan\theta_i} H_0^{(1)}(k_o \sin\theta^s \rho') J_0(|\mathbf{k}_\perp|\rho')\rho' d\rho' \ .$$

3.3 Simulation and Experimental Data Analysis

In this section a sensitivity analysis is presented to demonstrate the significance of the scattering interaction between cylinders and rough surfaces to the overall backscatter. Also polarimetric backscatter measurement that demonstrates the validity of the scattering formulation are presented.

We begin the sensitivity analysis with a realistic scenario. Consider a soybean plant above a ground plane with a slightly rough interface. The scattering interaction between the main stem of the plant and the rough surface is of interest. Typical values of $0.71m$ and $0.385cm$ are chosen for the length and radius of the main stem respectively, and the simulation is performed at 1.25 GHz. The length of the main stem is 2.96λ, and the ratio of the length to the radius is 184.4. For these dimensions the far-field criterion given by (3.17) requires that $\rho > 0.048$ cm. Hence for most practical situation (3.15) is valid. The dielectric constant of a stem with moisture constant $m_v = 0.58$ is found to be $43.4 + i13.2$ at 1.25 GHz [7]. The cylinder, which is used to model the main stem of the soybean, is placed right above the rough surface with $ks = 0.1$ and $kl = 2.0$ having an exponential correlation function. The volumetric soil moisture content is set to be 0.1, and the dielectric constant is calculated by applying an empirical model [14] choosing a soil texture with 10% sand and 30% clay. Figures 3.6 shows the RCS ratio of the zeroth-order (the first term in (3.32)) to the complete first-order backscattering solution excluding the direct backscatter from the rough surface (the first three terms in (3.32)) is plotted versus incidence angle. The RCSs are calculated and averaged over many azimuthal angles (α) for six different cylinder tilt angles (β): 2^o, 4^o, 6^o, 8^o, 10^o, and 12^o. In this simulation azimuthal symmetry (uniform distribution over α) is assumed. Figure 3.6(a) and Fig.

3.6(b) show that, for the co-polarized backscatter, the average of the zeroth-order solution is sufficient except when the incidence angle is close to normal incidence. On the other hand, Fig. 3.6(c) shows that the cylinder-rough surface interaction is significant for the cross-polarized scattering, especially for nearly vertical cylinders. The simulation for the vertical cylinder corresponding to $\beta = 0^o$ is not plotted here, because the zeroth-order solution predicts no cross-polarized backscatter. As the tilt angle increases, the cross-polarized backscatter predicted by the zeroth-order solution increases, and therefore the cylinder-rough surface interaction becomes less important.

It should be noted here that the numerical evaluations of the integrals which account for the interaction between the cylinder and rough surface is much more time-consuming for a tilted cylinder than for a vertical cylinder. The reason for this is that the lit area, shown in Fig. 3.4(a), has a circular contour when the cylinder is vertical and the integration along ϕ can be carried out analytically. For tilted cylinder the contour is elliptical and four-fold numerical integrations must be carried out. Besides, for tilted cylinders an averaging over the azimuthal angle α is required. On a Sun workstation Ultra 2, while it takes only less that 10 second to evaluate the scattering interaction for a vertical cylinder, it takes about 15 to 130 minutes for a tilted cylinder, depending on the incidence angle. As mentioned earlier the interaction between cylinders and rough surfaces become less important as the cylinders' tilt angle increases. Therefore, the focus in the rest of simulations will be on the cross-polarized backscatter for nearly vertical cylinders, which is often a case of interest in problems such as scattering from vegetation canopies. The complete first-order cross-polarized RCS (the first three terms in (3.32)) of the example shown in Fig. 3.6 is presented in Fig. 3.7. It is shown that the scattering interaction

increases with the increase in the incidence angle and the cylinder's tilt angle. It is also shown that for $\beta \leq 6^o$ the cross-polarized RCS can be approximated well by that of the vertical cylinder.

The effect of surface roughness parameters (ks and kl) on the cross-polarized RCS of the vertical cylinder and rough surface is also examined. The direct backscatter from rough surface is still excluded in this investigation to focus on the interaction between these two targets, so the RCS will only include the first term in (3.41). In Fig. 3.8 the correlation length is kept constant ($kl = 3.0$) while the surface rms height is varied. It is found that the cross-polarized RCS is rather sensitive to the variation of ks. In Fig. 3.9, the rms height is kept constant ($ks = 0.1$) and the correlation length is varied. It is shown that the sensitivity to kl diminishes when when $kl > 1.5$.

Figure 3.10 shows the cross-polarized RCS (only the first term in (3.41)) of the vertical cylinder and rough surface as a function of the cylinder radius. In this simulation the cylinder length and dielectric constant are, respectively, $0.71m$ and $\epsilon = 43.4 + i13.2$, and the surface parameters are $ks = 0.1$ and $kl = 3.0$. When the cylinder is electrically thin ($ka\sqrt{|\epsilon|} << 1$) the cross-polarized RCS can be calculated using (3.43) and (3.44), which indicates that the cross-polarized RCS varies as $(ka)^4$. As ka increase further, the cross-polarized RCS begins to oscillate, and exhibits a much gentler rate of increase with increasing ka. Figure 3.11 shows the dependency of the cross-polarized RCS (only the first term in (3.41)) on the vertical cylinder length. In this simulation the cylinder radius is fixed at $a = 0.385cm$. It is shown that for relatively short cylinders ($kl_c < 20$) the cross-polarized RCS increases rapidly as its length increases, and the increasing rate becomes gentler for cylinders with $kl_c > 30$.

In the previous simulations, the lower end of the cylinders were placed right above

the surface. In the following simulation the effect of the cylinder height location on the scattering interaction between the cylinder and rough surface is considered. Figure 3.12 shows the cross-polarized RCS (without the direct backscatter from the rough surface) as a function of the height of the vertical cylinder's lower end. It is shown that as the height increases, the RCS increases first, and then become almost a constant function. Note that the rough surface is a distributed target. As the height increases, the area of the illuminated region also increases, thus the RCS does not decrease as the distance between these two target increases.

The sensitivity to the dielectric constants of the cylinder is also examined and the results are shown in Fig. 3.13. Instead of varying the complex dielectric constant, its corresponding volumetric moisture content is varied. The empirical model [67] is used to calculate the dielectric constants for the chosen moisture content. In Fig. 3.13, the cross-polarized RCS (only the first term in (3.41)) is plotted versus the cylinder's volumetric moisture content, while the volumetric moisture content of the surface is kept at 10%. The temperature is assumed to be 23^oC in the calculation of the cylinder's dielectric constant. It is found that the interaction increases as the moisture content (or dielectric constant) increases.

For vertical cylinders, ignoring the cylinder-rough-surface interaction, the main source of the cross-polarized backscatter is the rough surface alone (second-order and higher-order perturbation terms). Fig. 3.14 compares the cross-polarized backscatter of the rough surface and the rough-surface-cylinder for different values of cylinder number density. These cylinders are uniformly randomly distributed on the rough surface, and the mutual coupling between them is ignored. While the cross-polarized backscatter from the rough surface ($ks = 0.1$ and $kl = 3.0$) alone decreases rapidly as the incidence angle increases, the backscatter of the composite target increases.

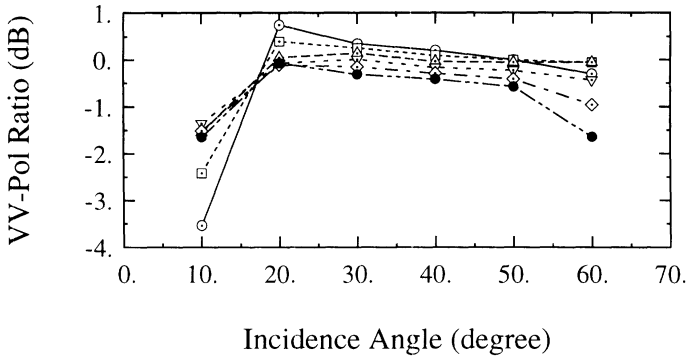

(a)

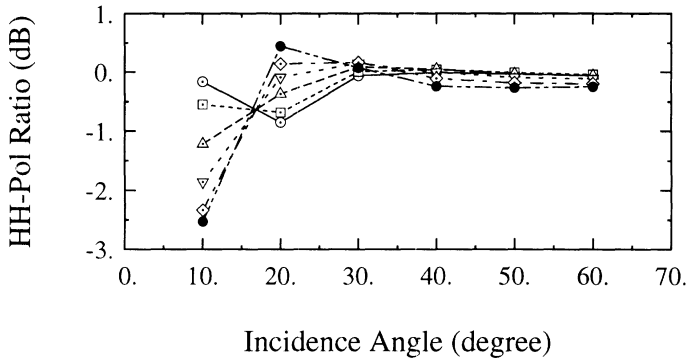

(b)

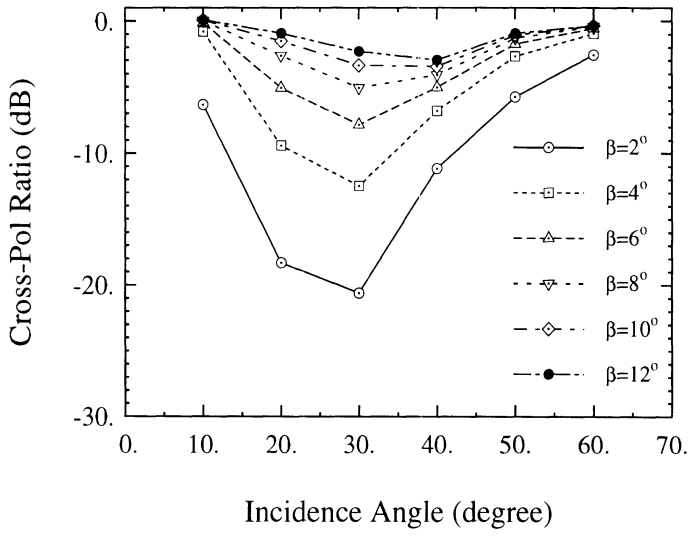

(c)

Figure 3.6: The RCS ratios of the zeroth-order to the complete first-order for (a) vv-polarized, (b) hh-polarized, and (c) cross-polarized backscatter and for different cylinder tilt angles. The simulation is carried out for a surface with $ks = 0.1$ and $kl = 3.0$.

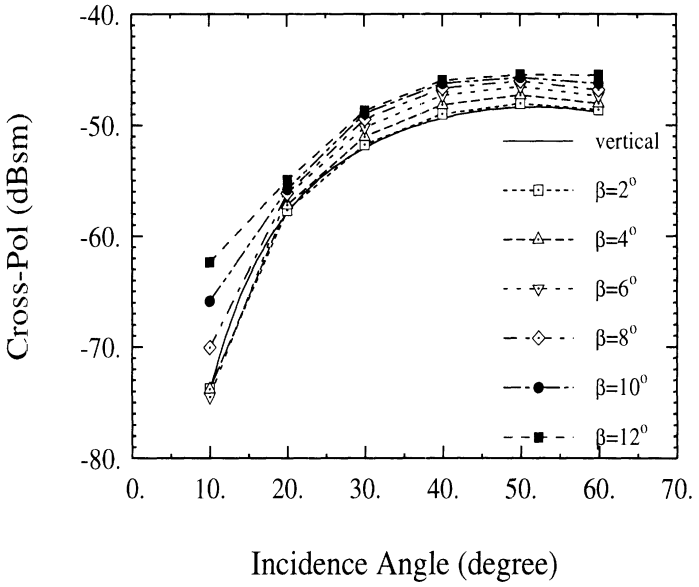

Figure 3.7: The cross-polarized RCS caused by the interaction between a cylinder ($a = 0.385cm$, $l_c = 0.71m$, and $\epsilon_c = 43.4 + i13.2$) and a rough surface ($ks = 0.1$, $kl = 3.0$, and $\epsilon_g = 4.9 + i0.9$).

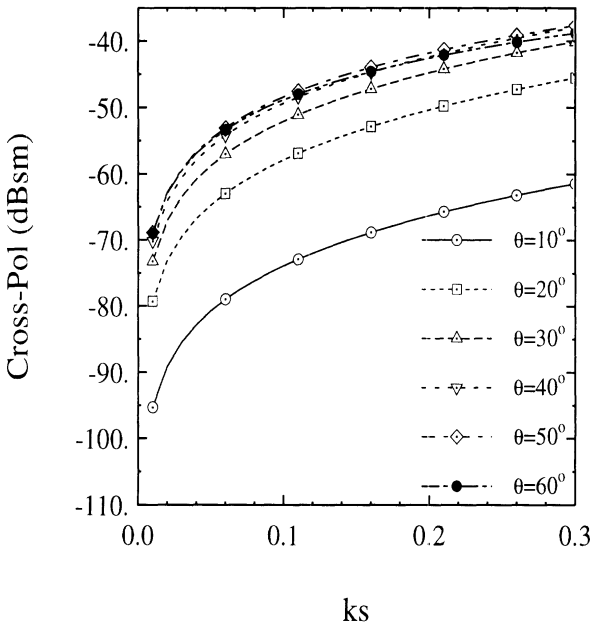

Figure 3.8: The cross-polarized RCS of the cylinder-rough surface composite target versus ks of the rough surface ($a = 0.385cm$, $l_c = 0.71m$, $\epsilon_c = 43.4+i13.2$, $kl = 3.0$, and $\epsilon_g = 4.9 + i0.9$).

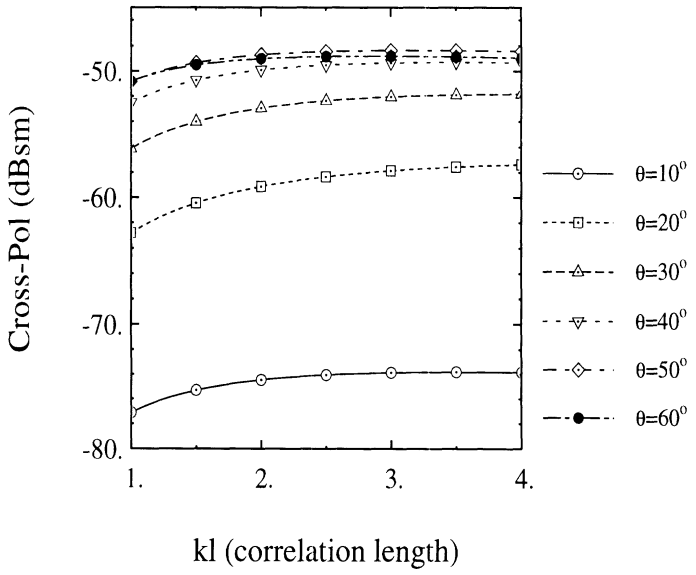

Figure 3.9: The cross-polarized RCS of the cylinder-rough surface composite target versus kl of the rough surface ($a = 0.385cm$, $l_c = 0.71m$, $\epsilon_c = 43.4+i13.2$, $ks = 1.0$, and $\epsilon_g = 4.9 + i0.9$).

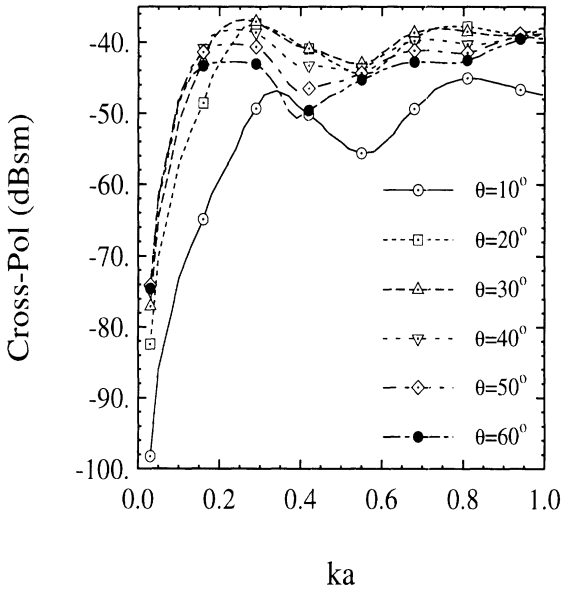

Figure 3.10: The cross-polarized RCS of the cylinder-rough surface composite target versus the radius of the vertical cylinder ($l_c = 0.71m$, $\epsilon_c = 43.4 + i13.2$, $ks = 0.1$, $kl = 3.0$, and $\epsilon_g = 4.9 + i0.9$).

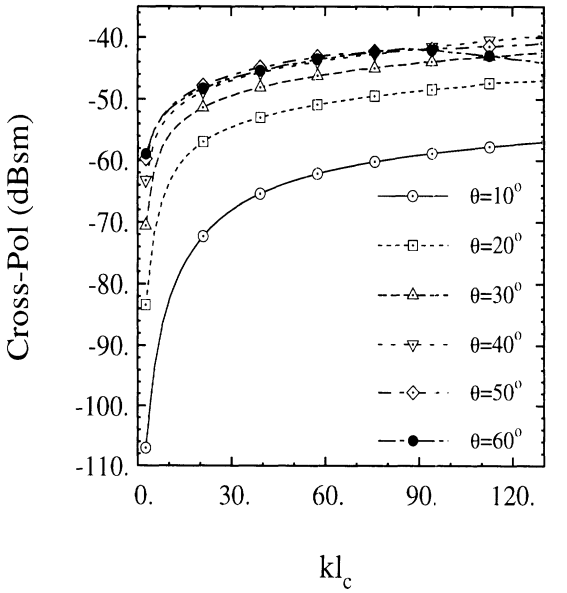

Figure 3.11: The cross-polarized RCS of the cylinder-rough surface composite target versus the length of the vertical cylinder ($a = 0.385cm$, $\epsilon_c = 43.4 + i13.2$, $ks = 0.1$, $kl = 3.0$, and $\epsilon_g = 4.9 + i0.9$).

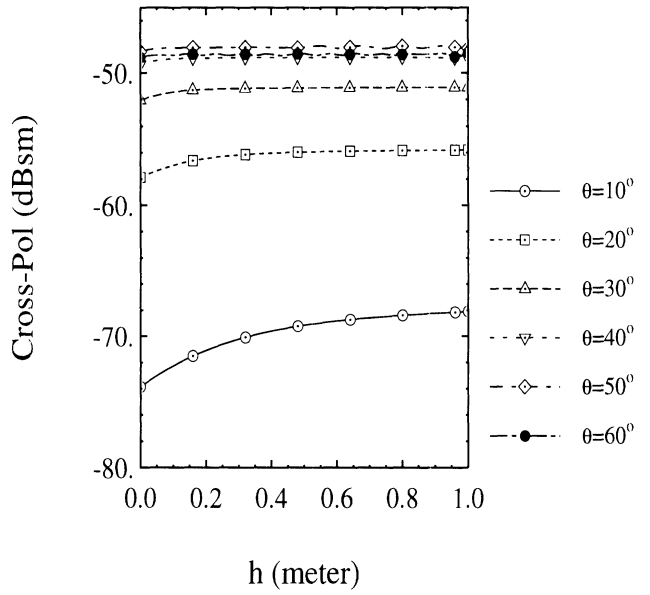

Figure 3.12: The cross-polarized RCS of the cylinder-rough surface composite target versus the height of the cylinder lower end above the ground ($a = 0.385cm$, $l_c = 0.71m$, $\epsilon_c = 43.4 + i13.2$, $ks = 0.1$, $kl = 3.0$, and $\epsilon_g = 4.9 + i0.9$).

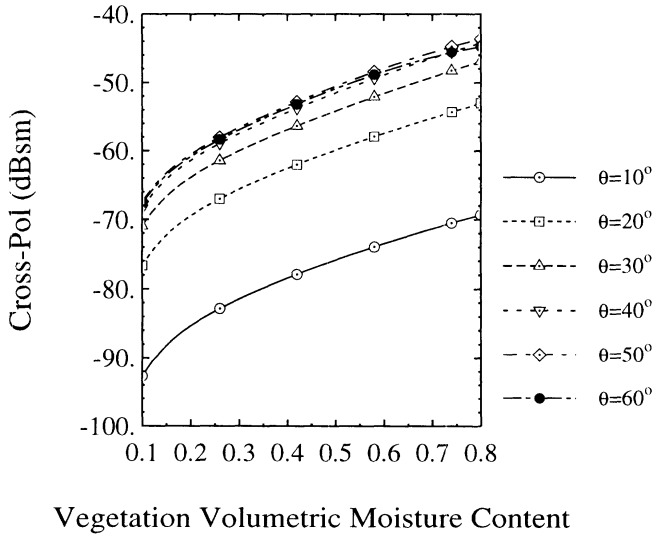

Figure 3.13: The cross-polarized RCS of the cylinder-rough surface composite target versus the volumetric moisture content of the vertical cylinder ($a = 0.385cm$, $l_c = 0.71m$, $ks = 0.1$, $kl = 3.0$, and $\epsilon_g = 4.9 + i0.9$).

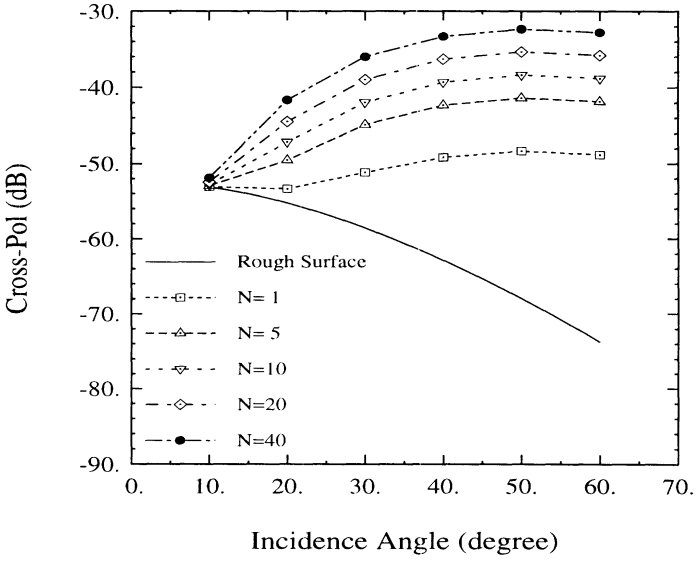

Figure 3.14: A comparison of the cross-polarized backscatter of the vertical cylinder-rough surface composite target to that of the rough surface along. The RCS is plotted as a function of incidence angle and number density. The direct backscattering from rough surface alone (σ_{pq}^0) is also plotted for comparison ($a = 0.385cm$, $l_c = 0.71m$, $\epsilon_c = 43.4 + i13.2$, $ks = 0.1$, $kl = 3.0$, and $\epsilon_g = 4.9 + i0.9$).

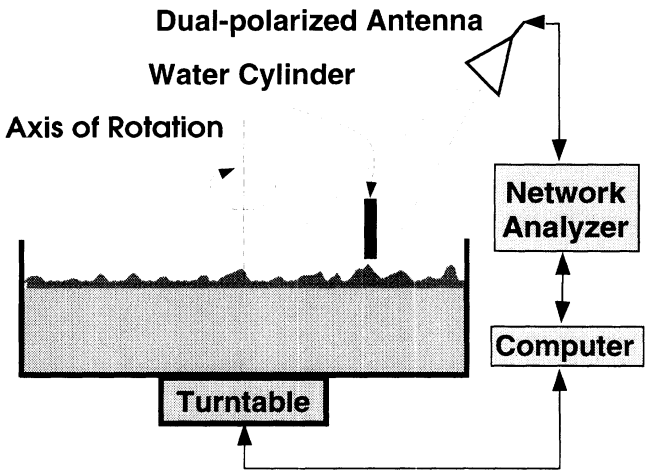

Figure 3.15: The experimental setup for the backscatter measurement of a vertical cylinder above a rough ground plane.

To examine the validity of the scattering formulations, backscatter measurements were performed polarimetrically using the indoor bistatic facilities of the Radiation Laboratory at the University of Michigan. The radar was calibrated polarimetrically using STCT [38]. In these experiments, an X-band stepped frequency radar with the center frequency 9.25 GHz and the bandwidth 1.5 GHz was used. The experimental setup is shown in Fig. 3.15. A lossy circular cylinder was made by filling a cylindrical cavity in a Styrofoam block with water. The radius and length of the water cylinder were 0.83 cm and 11 cm, respectively. A computer-generated Gaussian random rough surface with $ks = 0.2$ and $kl = 0.9$ was made by milling the surfaces of floral foam blocks, and then they were soaked in water. Because of the gravity, the water content at the top of the layer was found to be around 30%. The water content is assumed to increase linearly to nearly 100% at 0.5 cm below the top rough layer. The dielectric constant of water calculated from the Debye formula was found to be 53.4 + i 39.3.

Figure 3.16 shows the measured and the theoretical backscattering coefficients of the rough surface without the cylinder. The excellent agreement indicates that the physical parameters and the complete second-order perturbation solution the

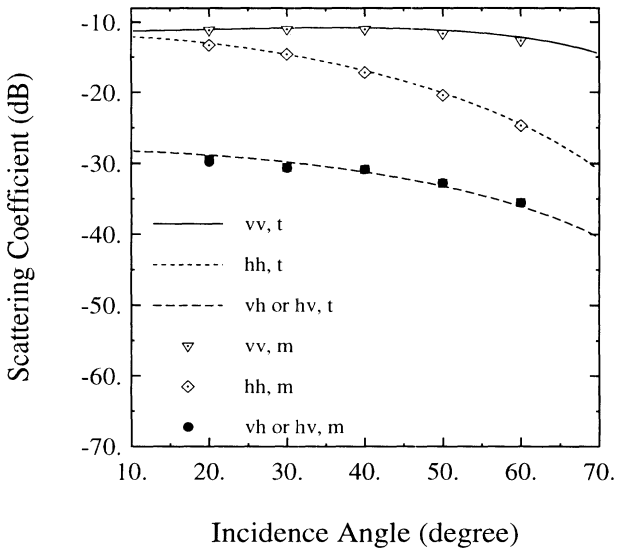

Figure 3.16: The backscattering coefficients of the rough surface with $ks = 0.2$ and $kl = 1.0$ at 9.25 GHz.

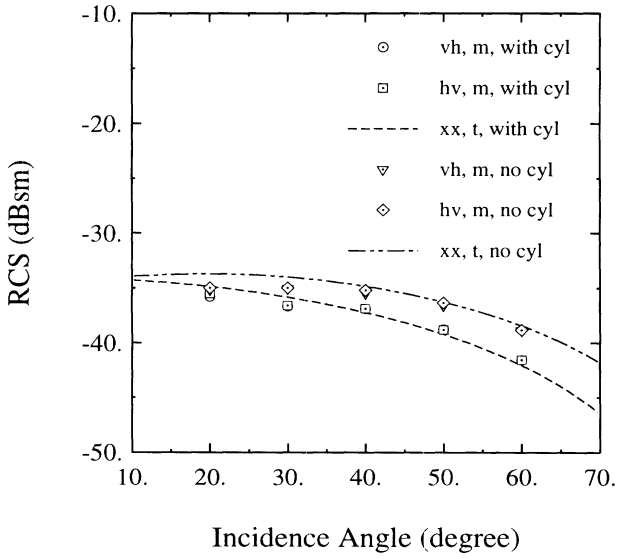

Figure 3.17: The cross-polarized RCS of a water cylinder with $a = 0.83cm$ and $l_c = 11.0cm$ above the rough surface at 9.25 GHz. The RCS of the rough surface alone ($\sigma^0_{pq}A$) is also shown for comparison.

rough surface are very accurate. Figure 3.17 shows the measured and theoretical cross-polarized RCS of the rough surface with and without the water cylinder. The inclusion of the cylinder does increase the cross-polarized backscattered field significantly. Note that the interaction of a vertical cylinder with flat surface does not produce any cross-polarized backscatter.

3.4 Conclusions

In this chapter, an electromagnetic scattering solution for the evaluation of the scattering interaction between a dielectric cylinder and a slightly rough surface is presented. Taking the advantage of a newly-developed technique which utilize the reciprocity theorem, the difficulty in formulating the secondary scattered fields from the composite target reduces to the evaluation of integrals involving the scattered fields from the cylinder and polarization currents of the rough surface induced by a plane wave. The scattered field from the cylinder is evaluated in the near-field region using a stationary phase approximation along the cylinder axis. Also the expressions of the polarization current induced within the top rough layer of the rough surface are employed which are derived from the iterative solution of an integral equation. The expression for the scattering matrix of the composite target, which is of interest for modeling of vegetation, are formulated. A sensitivity analysis is performed which shows that the cross-polarized backscatter from the vertical or nearly vertical cylinders is dominated by the scattering interaction between the cylinder and the rough surface. Although the evaluation of the scattering interaction for tilted cylinder is computationally inefficient, it was found that the scattering interaction for cylinders with tilt angle $\beta < 6^o$ is approximately the same as that for the cylinder with $\beta = 0^o$. The results of the sensitivity analysis indicate that the cross-polarized backscatter

generated by the scattering interaction between the cylinder and the rough surface increases with increases in the incidence angle, rms height and correlation length of the rough surface, cylinder radius and length, and dielectric constants of the cylinder and the rough surface. The accuracy of the theoretical formulation is also verified by conducting polarimetric backscatter measurements from a lossy dielectric cylinder above a slightly rough surface. Excellent agreement between the theoretical prediction and experimental results is obtained.

CHAPTER IV

ELECTROMAGNETIC SCATTERING FROM VEGETATION PARTICLES

Simple geometries, for which analytical scattering solutions are available, are often chosen to model vegetation particles. For example, leaves are modeled using circular disks, while stems, branches, and pods are modeled using circular cylinders. In this chapter, analytical scattering solutions for these geometries will be introduced.

First, the coordinate system and direction vectors which will be used in this chapter are defined. Consider a global coordinate system with the x-y plane parallel to a horizontal ground plane and z-axis along the vertical direction, as shown in Fig. 4.1. Suppose a plane wave given by

$$\mathbf{E^i}(\mathbf{r}) = \mathbf{E_0^i} e^{ik_0 \hat{k}_i \cdot \mathbf{r}} \ . \tag{4.1}$$

is illuminating the ground plane from the upper half-space, where $\hat{k}_i$ is the unit vector along the propagation direction given by

$$\hat{k}_i = \hat{x} \sin\theta_i \cos\phi_i + \hat{y} \sin\theta_i \sin\phi_i - \hat{z} \cos\theta_i \ . \tag{4.2}$$

The vector $\mathbf{E_0^i}$ in (4.1) is expressed in terms of a local coordinate system ($\hat{v}_i$,$\hat{h}_i$,$\hat{k}_i$) where $\hat{h}_i = (\hat{k}_i \times \hat{z})/|\hat{k}_i \times \hat{z}|$ and $\hat{v}_i = \hat{h}_i \times \hat{k}_i$ denote the horizontal and vertical unit vectors, respectively. Representing the direction of the observation point by $\hat{k}_s$, the

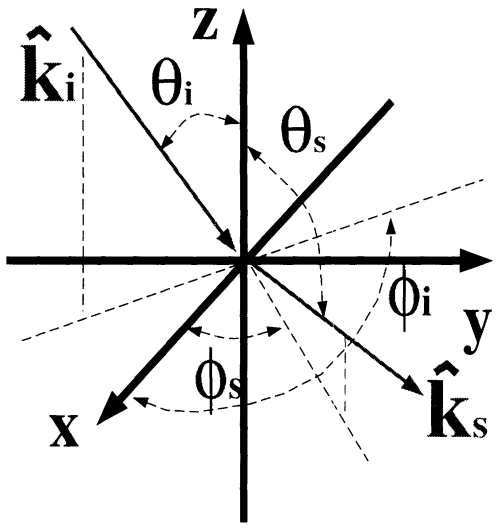

Figure 4.1: Vectors of the incident and scattering directions.

polarization of the scattered field can also be expressed in terms of a local coordinate system $(\hat{v}_s,\hat{h}_s,\hat{k}_s)$ where

$$\hat{k}_s = \hat{x}\sin\theta_s\cos\phi_s + \hat{y}\sin\theta_s\sin\phi_s + \hat{z}\cos\theta_s \ , \tag{4.3}$$

and $\hat{v}_s$ and $\hat{h}_s$ can be obtained using similar expressions as those given for $\hat{v}_i$ and $\hat{h}_i$, respectively.

4.1 Electromagnetic Scattering from an Elliptical Disk

The scattering solution for an elliptical disk will be given in this section. First, the notation of the dimension and orientation parameters of the elliptical disk is given in Fig. 4.2. After applying a coordinate transformation with the matrix

$$\bar{\bar{\mathbf{U}}}_{\mathbf{d}}' = \begin{bmatrix} \cos\beta_d\cos\alpha_d & -\sin\alpha_d & \sin\beta_d\cos\alpha_d \\ \cos\beta_d\sin\alpha_d & \cos\alpha_d & \sin\beta_d\sin\alpha_d \\ -\sin\beta_d & 0 & \cos\beta_d \end{bmatrix} \ , \tag{4.4}$$

the disk will be parallel to the new x-y plane. However, the long axis and the short axis will not necessarily to be parallel to either the x-axis or the y-axis. To make

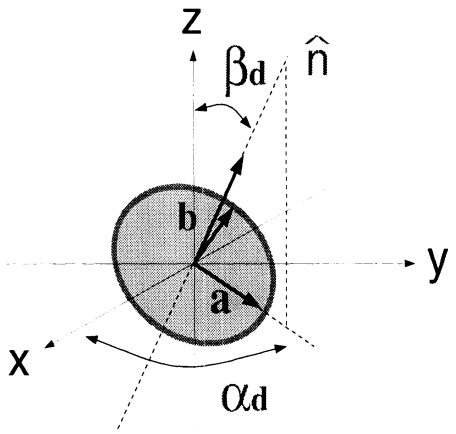

Figure 4.2: Denotation of the dimensional and orientational parameters for a elliptical disk.

later formulation simpler, one more coordinate transformation is performed with the matrix given by

$$\bar{\bar{\mathbf{U}}}_{\mathbf{d}}'' = \begin{bmatrix} \cos\alpha_d' & -\sin\alpha_d' & 0 \\ \sin\alpha_d' & \cos\alpha_d' & 0 \\ 0 & 0 & 1 \end{bmatrix} . \tag{4.5}$$

The total transformation matrix

$$\begin{aligned} \bar{\bar{\mathbf{U}}}_{\mathbf{d}} &= \bar{\bar{\mathbf{U}}}_{\mathbf{d}}''\bar{\bar{\mathbf{U}}}_{\mathbf{d}}' \\ &= \begin{bmatrix} \cos\beta_d\cos(\alpha_d+\alpha_d') & -\sin(\alpha_d+\alpha_d') & \sin\beta_d\cos(\alpha_d+\alpha_d') \\ \cos\beta_d\sin(\alpha_d+\alpha_d') & \cos(\alpha_d+\alpha_d') & \sin\beta_d\sin(\alpha_d+\alpha_d') \\ -\sin\beta_d & 0 & \cos\beta_d \end{bmatrix} \end{aligned} \tag{4.6}$$

transforms the normal, the long axis, and the short axis of the disk to the z-axis, the x-axis, and the y-axis of the coordinate system, respectively.

The thickness of the soybean leaves is usually small compared to the wavelength in microwave range. Also the ratio of the thickness to the larger diameter of the leaf is much less than one. Therefore, the Rayleigh-Gans approach [53] will be applied to derive the scattering solution for the leaves. Assume that an arbitrarily oriented

elliptical disk is illuminated by the incident wave

$$\mathbf{E^i}(\mathbf{r}) = \mathbf{E_0^i} e^{ik_0 \hat{k}_i \cdot \mathbf{r}} \ . \tag{4.7}$$

The induced polarization current inside the disk is given by

$$\mathbf{J_{ed}}(\mathbf{r}') = -ik_o Y_o \bar{\bar{\mathbf{P}}}_\mathbf{d} \cdot \mathbf{E^i}(\mathbf{r}') \ . \tag{4.8}$$

Here $\bar{\bar{\mathbf{P}}}_\mathbf{d}$ is the polarizability tensor of the disk and is defined as $\bar{\bar{\mathbf{P}}}_\mathbf{d} = \bar{\bar{\mathbf{U}}}_\mathbf{d}^{-1} \bar{\bar{\mathbf{P}}}_\mathbf{d}^{0} \bar{\bar{\mathbf{U}}}_\mathbf{d}$, where $\bar{\bar{\mathbf{P}}}_\mathbf{d}^{0}$ is given by

$$\bar{\bar{\mathbf{P}}}_\mathbf{d}^{0} = \begin{bmatrix} t(\epsilon_r - 1) & 0 & 0 \\ 0 & t(\epsilon_r - 1) & 0 \\ 0 & 0 & t(\epsilon_r - 1)/\epsilon_r \end{bmatrix} \ . \tag{4.9}$$

The scattered field can be evaluated using

$$\mathbf{E_d^s} = -\frac{ik_0 Z_0}{4\pi} \frac{e^{ik_0 r}}{r} \hat{k}_s \times \hat{k}_s \times \int_{S_d} \mathbf{J_{ed}}(\mathbf{r}') e^{-ik_0 \hat{k}_s \cdot \mathbf{r}'} ds' \tag{4.10}$$

Note that, since $\bar{\bar{\mathbf{P}}}_\mathbf{d} \cdot \mathbf{E_o^i}$ is constant over the disk, (4.10) can be written as

$$\begin{aligned} \mathbf{E_d^s} &= -\frac{k_0^2}{4\pi} \frac{e^{ik_0 r}}{r} \hat{k}_s \times \hat{k}_s \times (\bar{\bar{\mathbf{P}}}_\mathbf{d} \cdot \mathbf{E_0^i}) \int_{S_d} e^{k_0 (\hat{k}_i - \hat{k}_s) \cdot \mathbf{r}'} ds' \\ &= -\frac{e^{ik_0 r}}{r} \frac{k_0^2}{4\pi} \hat{k}_s \times \hat{k}_s \times (\bar{\bar{\mathbf{P}}}_\mathbf{d} \cdot \mathbf{E_0^i}) \frac{2A_d J_1(\sqrt{(aA)^2 + (bB)^2})}{\sqrt{(aA)^2 + (bB)^2}} \ , \end{aligned} \tag{4.11}$$

where A_d is the area of the disk, J_1 is the first-order Bessel function of the first kind, and A and b are given by

$$\begin{aligned} A &= k_0 \left[\bar{\bar{\mathbf{U}}}_\mathbf{d}^{-1} \cdot (\hat{k}_i - \hat{k}_s) \right] \cdot \hat{x} \\ B &= k_0 \left[\bar{\bar{\mathbf{U}}}_\mathbf{d}^{-1} \cdot (\hat{k}_i - \hat{k}_s) \right] \cdot \hat{y} \ . \end{aligned} \tag{4.12}$$

In (4.11), it is seen that

$$\hat{k}_s \times \hat{k}_s \times (\bar{\bar{\mathbf{P}}}_\mathbf{d} \cdot \mathbf{E_0^i}) = \left[\hat{k}_s \cdot (\bar{\bar{\mathbf{P}}}_\mathbf{d} \cdot \mathbf{E_0^i}) \right] \hat{k}_s - (\bar{\bar{\mathbf{P}}}_\mathbf{d} \cdot \mathbf{E_0^i}) \ . \tag{4.13}$$

Noting that $\hat{v}_s \cdot \hat{k}_s = \hat{h}_s \cdot \hat{k}_s = 0$, the elements of the scattering matrix can be expressed as:

$$
\begin{aligned}
S_{vv} &= \frac{k_0^2}{4\pi} \hat{v}_s \cdot (\bar{\bar{\mathbf{P}}}_{\mathbf{d}} \cdot \hat{v}_i) \frac{2A_d J_1(\sqrt{(aA)^2 + (bB)^2})}{\sqrt{(aA)^2 + (bB)^2}} , \\
S_{hv} &= \frac{k_0^2}{4\pi} \hat{h}_s \cdot (\bar{\bar{\mathbf{P}}}_{\mathbf{d}} \cdot \hat{v}_i) \frac{2A_d J_1(\sqrt{(aA)^2 + (bB)^2})}{\sqrt{(aA)^2 + (bB)^2}} , \\
S_{vh} &= \frac{k_0^2}{4\pi} \hat{v}_s \cdot (\bar{\bar{\mathbf{P}}}_{\mathbf{d}} \cdot \hat{h}_i) \frac{2A_d J_1(\sqrt{(aA)^2 + (bB)^2})}{\sqrt{(aA)^2 + (bB)^2}} , \\
S_{hh} &= \frac{k_0^2}{4\pi} \hat{h}_s \cdot (\bar{\bar{\mathbf{P}}}_{\mathbf{d}} \cdot \hat{h}_i) \frac{2A_d J_1(\sqrt{(aA)^2 + (bB)^2})}{\sqrt{(aA)^2 + (bB)^2}} .
\end{aligned} \tag{4.14}
$$

4.2 Electromagnetic Scattering from a Slim Circular Cylinder

If the radius of the cylinder is very small compared to the wavelength, and the ratio of the cylinder length to radius is large, the Rayleigh-Gans approach can again be applied to obtain the scattering solution. The notation of the dimension and orientation parameters is given in Fig. 4.3. The polarization current induced by the incident field is given by

$$
\mathbf{J}_{\mathbf{ec}}(\mathbf{r}') = -ik_o Y_o \bar{\bar{\mathbf{P}}}_{\mathbf{c}} \cdot \mathbf{E}^{\mathbf{i}}(\mathbf{r}') . \tag{4.15}
$$

Here $\bar{\bar{\mathbf{P}}}_{\mathbf{c}}$ is the polarizability tensor of the cylinder and is defined as $\bar{\bar{\mathbf{P}}}_{\mathbf{c}} = \bar{\bar{\mathbf{U}}}_{\mathbf{c}}^{-1} \bar{\bar{\mathbf{P}}}_{\mathbf{c}}^{\mathbf{0}} \bar{\bar{\mathbf{U}}}_{\mathbf{c}}$, where $\bar{\bar{\mathbf{P}}}_{\mathbf{c}}^{\mathbf{0}}$ is given by

$$
\bar{\bar{\mathbf{P}}}_{\mathbf{c}}^{\mathbf{0}} = \begin{bmatrix} 2a^2\pi\frac{\epsilon_r - 1}{\epsilon_r + 1} & 0 & 0 \\ 0 & 2a^2\pi\frac{\epsilon_r - 1}{\epsilon_r + 1} & 0 \\ 0 & 0 & a^2\pi(\epsilon_r - 1) \end{bmatrix} , \tag{4.16}
$$

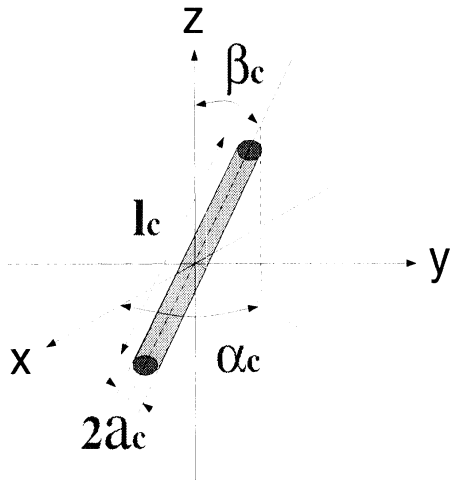

Figure 4.3: Dimensional and orientational parameters for a cylinder.

and $\bar{\bar{\mathbf{U}}}_c$, which transforms the z-axis to the axis of the cylinder, is given by

$$\bar{\bar{\mathbf{U}}}_c = \begin{bmatrix} \cos\beta_c \cos\alpha_c & -\sin\alpha_c & \sin\beta_d \cos\alpha_c \\ \cos\beta_c \sin\alpha_c & \cos\alpha_c & \sin\beta_d \sin\alpha_c \\ -\sin\beta_c & 0 & \cos\beta_c \end{bmatrix} . \tag{4.17}$$

The scattered field is given by

$$\begin{aligned} \mathbf{E}_c^s &= -\frac{ik_0 Z_0}{4\pi}\frac{e^{ik_0 r}}{r}\hat{k}_s \times \hat{k}_s \times \int_{l_c} \mathbf{J}_{ec}(\mathbf{r}') e^{-ik_0 \hat{k}_s \cdot \mathbf{r}'} dl' \\ &= -\frac{e^{ik_0 r}}{r}\frac{k_0^2}{4\pi}\hat{k}_s \times \hat{k}_s \times (\bar{\bar{\mathbf{P}}}_c \cdot \mathbf{E}_0^i) \int_{l_c} e^{-ik_0 \hat{k}_s \cdot \mathbf{r}'} dl' \\ &= -\frac{e^{ik_0 r}}{r}\frac{k_0^2}{4\pi}\hat{k}_s \times \hat{k}_s \times (\bar{\bar{\mathbf{P}}}_c \cdot \mathbf{E}_0^i)\ l\ \mathrm{sinc}(U) . \end{aligned} \tag{4.18}$$

Here U is given by $k_0(\hat{k}_i - \hat{k}_s) \cdot \hat{n}_c$ where $\hat{n}_c$ is the unit vector in the direction of the cylinder axis. Using an equality similar to (4.13), the scattering matrix elements can be obtained:

$$\begin{aligned} S_{vv} &= \frac{k_0^2}{4\pi}\hat{v}_s \cdot (\bar{\bar{\mathbf{P}}}_c \cdot \hat{v}_i)\ l\ \mathrm{sinc}(U) , \\ S_{hv} &= \frac{k_0^2}{4\pi}\hat{h}_s \cdot (\bar{\bar{\mathbf{P}}}_c \cdot \hat{v}_i)\ l\ \mathrm{sinc}(U) , \\ S_{vh} &= \frac{k_0^2}{4\pi}\hat{v}_s \cdot (\bar{\bar{\mathbf{P}}}_c \cdot \hat{h}_i)\ l\ \mathrm{sinc}(U) , \\ S_{hh} &= \frac{k_0^2}{4\pi}\hat{h}_s \cdot (\bar{\bar{\mathbf{P}}}_c \cdot \hat{h}_i)\ l\ \mathrm{sinc}(U) . \end{aligned} \tag{4.19}$$

4.3 Electromagnetic Scattering from a Circular Cylinder – a Semi-exact Solution

In the previous section, the Rayleigh-Gans solution was presented for slim cylinders. If the radius of the cylinder is large, such as for the main stem of the soybean, that solution is no longer valid. In vegetation scattering modeling, a semi-exact solution has been used for cylinders with larger radius. As we know, the exact solution exists only when the length is infinite. For a cylinder of finite length, the semi-exact solution assumes that the fields induced inside the cylinder are the same as those inside an infinite cylinder having the same dielectric constant. These internal fields are then used to calculate the fields scattered from the cylinder. The formulation summarized below was presented by Sarabandi [51].

Suppose that a non-magnetic infinite circular cylinder of radius is illuminated by the incident field given in (4.7). The axis of the cylinder is in the $\hat{n}_c$ direction which is given by

$$\hat{n}_c = \hat{x}\sin\beta_c\cos\alpha_c + \hat{y}\sin\beta_c\sin\alpha_c + \hat{z}\cos\beta_c \ . \tag{4.20}$$

Assume that the axis of the cylinder is coincident with the z'-axis of a local Cartesian coordinate system (x',y',z'). Further assume that the incident vector $\hat{k}_i$ lies in the x'-z' plane with

$$\begin{aligned} \hat{k}_i \cdot \hat{x}' &= -\sin\beta \ , \\ \hat{k}_i \cdot \hat{z}' &= \cos\beta \ , \end{aligned} \tag{4.21}$$

and

$$\begin{aligned} \mathbf{E}^{\mathbf{i}} \cdot \hat{z}' &= e_z e^{ik_0(-x'\sin\beta + z'\cos\beta)} \ , \\ \mathbf{H}^{\mathbf{i}} \cdot \hat{z}' &= Y_0 h_z e^{ik_0(-x'\sin\beta + z'\cos\beta)} \ , \end{aligned} \tag{4.22}$$

where $e_z = \mathbf{E}_0^{\mathbf{i}} \cdot \hat{z}'$ and $h_z = \mathbf{H}_0^{\mathbf{i}} \cdot \hat{z}'$.

By invoking the field equivalence principle, the scattered field outside the cylinder region can be attributed to fictitious electric ($\mathbf{J_e}$) and magnetic ($\mathbf{J_m}$) surface currents given by

$$\mathbf{J_e} = \hat{n}' \times \mathbf{H} \ ,$$

$$\mathbf{J_m} = -\hat{n}' \times \mathbf{E} \ , \tag{4.23}$$

where $\hat{n}'$ is the outward unit vector normal to the surface, and $\mathbf{E}$ and $\mathbf{H}$ are the total electric and magnetic fields on the surface. The tangential components of $\mathbf{E}$ and $\mathbf{H}$ are given by

$$\begin{aligned}
E_{z'} &= \sum_{m=-\infty}^{\infty} (-i)^m \left\{ e_z J_m(x_0) + A_m H_0^{(1)}(x_0) \right\} e^{im\phi' + ik_0 z' \cos\beta)} \ , \\
H_{z'} &= Y_0 \sum_{m=-\infty}^{\infty} (-i)^m \left\{ h_z J_m(x_0) + B_m H_0^{(1)}(x_0) \right\} e^{im\phi' + ik_0 z' \cos\beta} \ , \\
E_{\phi'} &= \frac{1}{ik_0 \sin^2\beta} \sum_{m=-\infty}^{\infty} (-i)^m \Bigg\{ k_0 \sin\beta \left[h_z J_m'(x_0) + B_m H_0^{(1)\,\prime}(x_0) \right] \\
&\qquad - \frac{im\cos\beta}{a} \left[e_z J_m(x_0) + A_m H_0^{(1)}(x_0) \right] \Bigg\} e^{im\phi' + ik_0 z' \cos\beta} \ , \\
H_{\phi'} &= \frac{Y_0}{ik_0 \sin^2\beta} \sum_{m=-\infty}^{\infty} (-i)^m \Bigg\{ -k_0 \sin\beta \left[e_z J_m'(x_0) + A_m H_0^{(1)\,\prime}(x_0) \right] \\
&\qquad - \frac{im\cos\beta}{a} \left[h_z J_m(x_0) + B_m H_0^{(1)}(x_0) \right] \Bigg\} e^{im\phi' + ik_0 z' \cos\beta} \ ,
\end{aligned} \tag{4.24}$$

where J_m is the mth order Bessel function of the first kind, $H_0^{(1)}$ is the zeroth order Hankel function of the first kind, and $x_0 = k_0 a \sin\beta$. Applying the boundary conditions at $\rho' = a$, A_m and B_m can be evaluated using [37]

$$A_m = C_m^{TM} e_z + i\bar{C}_m h_z \ ,$$

$$B_m = C_m^{TE} h_z - i\bar{C}_m e_z \ , \tag{4.25}$$

where

$$C_m^{TM} = -\frac{V_m P_m - q_m^2 J_m(x_0) H_m^{(1)}(x_0) J_m(x_1)}{P_m N_m - \left[q_m H_m^{(1)}(x_0) J_m(x_1)\right]^2} ,$$

$$C_m^{TE} = -\frac{M_m N_m - q_m^2 J_m(x_0) H_m^{(1)}(x_0) J_m(x_1)}{P_m N_m - \left[q_m H_m^{(1)}(x_0) J_m(x_1)\right]^2} ,$$

$$\bar{C}_m = \frac{2i}{\pi x_0 \sin\beta} \frac{q_m J_m^2(x_1)}{P_m N_m - \left[q_m H_m^{(1)}(x_0) J_m(x_1)\right]^2} \tag{4.26}$$

with

$$x_1 = k_0 a \sqrt{\epsilon - \cos^2\beta} ,$$

$$q_m = m k_0 a \cos\beta \left(\frac{1}{x_1^2} - \frac{1}{x_0^2}\right) ,$$

$$V_m = k_0 a \left\{\frac{\epsilon}{x_1} J_m(z_0) J_m'(x_1) - \frac{1}{x_0} J_m'(z_0) J_m(x_1)\right\} ,$$

$$P_m = k_0 a \left\{\frac{1}{x_1} H_m^{(1)}(z_0) J_m'(x_1) - \frac{1}{x_0} H_m^{(1)\prime}(z_0) J_m(x_1)\right\} ,$$

$$N_m = k_0 a \left\{\frac{\epsilon}{x_1} H_m^{(1)}(z_0) J_m'(x_1) - \frac{1}{x_0} H_m^{(1)\prime}(z_0) J_m(x_1)\right\} ,$$

$$M_m = k_0 a \left\{\frac{1}{x_1} J_m(z_0) J_m'(x_1) - \frac{1}{x_0} J_m'(z_0) J_m(x_1)\right\} , \tag{4.27}$$

From (4.23), the surface currents are given by

$$\mathbf{J_e} = Y_0(\hat{x}'\sin\phi' - \hat{y}'\cos\phi') e^{ik_0 z'\cos\beta} \sum_{m=-\infty}^{\infty} (-i)^m \left\{h_z J_m(x_0) + B_m H_m^{(1)}(x_0)\right\} e^{im\phi'}$$

$$- \hat{z}' \frac{Y_0}{ik_0 \sin^2\beta} e^{ik_0 z'\cos\beta} \sum_{m=-\infty}^{\infty} (-i)^m \left\{k_0 \sin\beta \left[e_z J_m'(x_0) + A_m H_m^{(1)\prime}(x_0)\right]\right.$$

$$\left. + \frac{im\cos\beta}{a} \left[h_z J_m'(x_0) + B_m H_m^{(1)\prime}(x_0)\right]\right\} e^{im\phi'} ,$$

$$\mathbf{J_m} = -(\hat{x}'\sin\phi' - \hat{y}'\cos\phi') e^{ik_0 z'\cos\beta} \sum_{m=-\infty}^{\infty} (-i)^m \left\{e_z J_m(x_0) + A_m H_m^{(1)}(x_0)\right\} e^{im\phi'}$$

$$- \hat{z}' \frac{1}{ik_0 \sin^2\beta} e^{ik_0 z'\cos\beta} \sum_{m=-\infty}^{\infty} (-i)^m \left\{k_0 \sin\beta \left[h_z J_m'(x_0) + B_m H_m^{(1)\prime}(x_0)\right]\right.$$

$$\left. + \frac{im\cos\beta}{a} \left[e_z J_m'(x_0) + A_m H_m^{(1)\prime}(x_0)\right]\right\} e^{im\phi'} . \tag{4.28}$$

In order to find the scattered field of a cylinder with finite length l, it is assumed that the currents on the curved side are the same as those on the infinite cylinder. Thus ignoring the effect of the end caps, the Hertz vectors describing the scattered field are given by

$$\Pi_{\mathbf{e}}(\mathbf{r}) = \frac{e^{ik_0 r}}{r}\frac{iZ_0}{4\pi k_0}\int_{-\frac{l}{2}}^{\frac{l}{2}} dz' e^{ik_0\hat{k}_s\cdot\hat{z}'z'}\int_0^{2\pi}\mathbf{J}_{\mathbf{e}}e^{-ik_0 aB\cos(\phi'-\tilde{\phi})}ad\phi' ,$$
$$\Pi_{\mathbf{m}}(\mathbf{r}) = \frac{e^{ik_0 r}}{r}\frac{iY_0}{4\pi k_0}\int_{-\frac{l}{2}}^{\frac{l}{2}} dz' e^{ik_0\hat{k}_s\cdot\hat{z}'z'}\int_0^{2\pi}\mathbf{J}_{\mathbf{m}}e^{-ik_0 aB\cos(\phi'-\tilde{\phi})}ad\phi' , \tag{4.29}$$

where

$$B = \left[(\hat{k}_s\cdot\hat{x}')^2 + (\hat{k}_s\cdot\hat{y}')^2\right]^{\frac{1}{2}} ,$$
$$\cos\tilde{\phi}' = \frac{\hat{k}_s\cdot\hat{x}'}{B} ,$$
$$\sin\tilde{\phi}' = \frac{\hat{k}_s\cdot\hat{y}'}{B} . \tag{4.30}$$

In (4.29), the integrations can be carried out analytically. The z' integration results in $l\,\mathrm{sinc}(V)$ with $V = \frac{1}{2}k_0 l(\hat{k}^i - \hat{k}_s)\cdot\hat{z}'$, and

$$\int_0^{2\pi} e^{-ik_0 aB\cos(\phi'-\tilde{\phi})}e^{im\phi'}d\phi' = 2\pi(-i)^m J_m(y_0)e^{im\phi'} ,$$
$$\int_0^{2\pi}\cos\phi' e^{-ik_0 aB\cos(\phi'-\tilde{\phi})}e^{im\phi'}d\phi' = 2\pi(-i)^m\left[i\cos\tilde{\phi}J_m'(y_0) + \frac{m}{y_0}\sin\tilde{\phi}J_m(y_0)\right]e^{im\phi'} ,$$
$$\int_0^{2\pi}\sin\phi' e^{-ik_0 aB\cos(\phi'-\tilde{\phi})}e^{im\phi'}d\phi' = 2\pi(-i)^m\left[i\sin\tilde{\phi}J_m'(y_0) - \frac{m}{y_0}\cos\tilde{\phi}J_m(y_0)\right]e^{im\phi'} , \tag{4.31}$$

where $y_0 = k_0 aB$. Therefore, the scattered field is given by

$$\mathbf{E}^{\mathbf{s}} = \frac{e^{ik_0 r}}{r}\frac{k_0 al}{2\sin\beta}\Big\{\left(D^e e_z + i\bar{D}^e hz\right)\hat{k}_s\times(\hat{k}_s\times\hat{z}')$$
$$+\left(D^h h_z - i\bar{D}^h ez\right)\hat{k}_s\times\hat{z}'\Big\}\mathrm{sinc}(V) , \tag{4.32}$$

where

$$D^e = \sum_{m=-\infty}^{\infty} (-1)^m \Bigg\{ J_m'(x_0)J_m(y_0) - \frac{\sin\beta}{B} J_m(x_0)J_m'(y_0) + C_m^{TM}\left[H_m^{(1)\,\prime}(x_0)J_m(y_0) - \frac{\sin\beta}{B} H_m^{(1)}(x_0)J_m'(y_0)\right] + \frac{m\cos\beta}{x_0}\left(1 - \frac{\hat{k}_s\cdot\hat{z}'}{\cos\beta}\frac{x_0\sin\beta}{y_0 B}\right)\bar{C}_m H_m^{(1)}(x_0)J_m(y_0)\Bigg\} e^{im\tilde{\phi}} , \tag{4.33}$$

$$D^h = \sum_{m=-\infty}^{\infty} (-1)^m \Bigg\{ J_m'(x_0)J_m(y_0) - \frac{\sin\beta}{B} J_m(x_0)J_m'(y_0) + C_m^{TE}\left[H_m^{(1)\,\prime}(x_0)J_m(y_0) - \frac{\sin\beta}{B} H_m^{(1)}(x_0)J_m'(y_0)\right] + \frac{m\cos\beta}{x_0}\left(1 - \frac{\hat{k}_s\cdot\hat{z}'}{\cos\beta}\frac{x_0\sin\beta}{y_0 B}\right)\bar{C}_m H_m^{(1)}(x_0)J_m(y_0)\Bigg\} e^{im\tilde{\phi}} , \tag{4.34}$$

$$\bar{D}^e = \sum_{m=-\infty}^{\infty} (-1)^m \Bigg\{ \bar{C}_m\left[H_m^{(1)\,\prime}(x_0)J_m(y_0) - \frac{\sin\beta}{B} H_m^{(1)}(x_0)J_m'(y_0)\right] + \frac{m\cos\beta}{x_0}\left(1 - \frac{\hat{k}_s\cdot\hat{z}'}{\cos\beta}\frac{x_0\sin\beta}{y_0 B}\right)\left[J_m(x_0) + C_m^{TE}H_m^{(1)}(x_0)\right] J_m(y_0)\Bigg\} e^{im\tilde{\phi}} , \tag{4.35}$$

$$\bar{D}^h = \sum_{m=-\infty}^{\infty} (-1)^m \Bigg\{ \bar{C}_m\left[H_m^{(1)\,\prime}(x_0)J_m(y_0) - \frac{\sin\beta}{B} H_m^{(1)}(x_0)J_m'(y_0)\right] + \frac{m\cos\beta}{x_0}\left(1 - \frac{\hat{k}_s\cdot\hat{z}'}{\cos\beta}\frac{x_0\sin\beta}{y_0 B}\right)\left[J_m(x_0) + C_m^{TM}H_m^{(1)}(x_0)\right] J_m(y_0)\Bigg\} e^{im\tilde{\phi}} , \tag{4.36}$$

and the elements of the scattering matrix are

$$S_{vv} = -\Bigg\{ \left[D^e(\hat{v}_i\cdot\hat{z}') + i\bar{D}^e(\hat{h}_i\cdot\hat{z}')\right](\hat{v}_s\cdot\hat{z}') + \left[D^h(\hat{h}_i\cdot\hat{z}') - i\bar{D}^h(\hat{v}_i\cdot\hat{z}')\right]\left(\hat{h}_s\cdot\hat{z}'\right)\Bigg\}\frac{k_0 a_c l_c}{2\sin\beta}\frac{\sin V}{V} , \tag{4.37}$$

$$S_{vh} = -\left\{\left[D^e(\hat{h}_i\cdot\hat{z}') - i\bar{D}^e(\hat{v}_i\cdot\hat{z}')\right](\hat{v}_s\cdot\hat{z}') - \left[D^h(\hat{v}_i\cdot\hat{z}') + i\bar{D}^h(\hat{h}_i\cdot\hat{z}')\right]\left(\hat{h}_s\cdot\hat{z}'\right)\right\}\frac{k_0 a_c l_c}{2\sin\beta}\frac{\sin V}{V}\,, \tag{4.38}$$

$$S_{hv} = -\left\{\left[D^e(\hat{v}_i\cdot\hat{z}') + i\bar{D}^e(\hat{h}_i\cdot\hat{z}')\right]\left(\hat{h}_s\cdot\hat{z}'\right) - \left[D^h(\hat{h}_i\cdot\hat{z}') - i\bar{D}^h(\hat{v}_i\cdot\hat{z}')\right](\hat{v}_s\cdot\hat{z}')\right\}\frac{k_0 a_c l_c}{2\sin\beta}\frac{\sin V}{V}\,, \tag{4.39}$$

$$S_{hh} = -\left\{\left[D^e(\hat{h}_i\cdot\hat{z}') - i\bar{D}^e(\hat{v}_i\cdot\hat{z}')\right]\left(\hat{h}_s\cdot\hat{z}'\right) - \left[D^h(\hat{v}_i\cdot\hat{z}') + i\bar{D}^h(\hat{h}_i\cdot\hat{z}')\right](\hat{v}_s\cdot\hat{z}')\right\}\frac{k_0 a_c l_c}{2\sin\beta}\frac{\sin V}{V}\,. \tag{4.40}$$

Generally, in order for this solution to be valid, the ratio of the length to the diameter should be large, so that the fringing effects at both ends of the cylinder can be ignored. The accuracy of the scattering matrix elements deteriorates with increasing $\hat{k}_i\cdot\hat{z}'$ or $\hat{k}_s\cdot\hat{z}'$, but for aspect angles that are not too oblique the transverse resonances of the cylinder should be accurately simulated.

4.4 Electromagnetic Scattering Interaction between Leaves and Thin Branches

Recently the effect of multiple scattering between vegetation particles has been found to be important for accurately predicting the scattering behavior. Although the volume fraction of vegetation particles is very low, smaller vegetation particles generally tend to accumulate around bigger ones. Therefore a single vegetation structure could often be considered a locally dense medium where multiple scattering could be significant. Characterization of the exact solution including all higher-order

multiple scattering for a vegetation medium is nearly impossible. Approximate analytical solutions capable of accounting for near-field interactions are computationally efficient and are extremely useful for developing accurate scattering models of vegetation.

In this section, simple formulations which include scattering interaction up to the second order are developed for thin dielectric disks and thin dielectric cylinders representing leaves and stems. In this iterative approach, the Rayleigh-Gans approximation is used to calculate the internal electric field, or equivalently the induced polarization current, of the particles. The Rayleigh-Gans approximation has been shown to be valid for scatterers having at least one dimension which is much smaller than a wavelength and having a lossy permittivity.

First the polarization current induced by the incident wave at each point within a particle is expressed in terms of the incident wave and the polarizability tensor of a thin dielectric disk or cylinder having the same thickness or diameter as the particle. To calculate the second-order scattered field, the exact near-fields scattered from all nearby particles are evaluated numerically and used as the excitation. As before, the second-order polarization current at any given point within the scatterer is determined using the appropriate polarizability tensor. Since the polarizability tensors are assumed uniform for both particles, the numerical integration involved in the calculation of the near field is rather simple. To calculate the second-order scattered field, two-fold and four-fold numerical integrations must be carried out for cylinders and disks, respectively. The second-order scattered field can also be obtained using a recently developed technique based on the reciprocity theorem; the results are the same. Numerical simulations have also been performed to demonstrate the effect of the near-field interaction at different frequencies and particle orientations.

4.4.1 Scattering from an Object in Free Space

Assume a dielectric object is illuminated by the incident wave in free space. The incident field induces a polarization current **J** within the object which is the source of the scattered field. The electric Hertz vector potential Π_e due to this current density is given by

$$\Pi_e(\mathbf{r}) = \frac{\mu}{4\pi}\int_V \mathbf{J}(\mathbf{r}')\frac{e^{ik_0R}}{R}\,dv' \ , \tag{4.41}$$

where the primed coordinate represents the source, the unprimed coordinate represents the observation point, and $R = |\mathbf{r} - \mathbf{r}'|$. The corresponding electric field can be written as

$$\mathbf{E}(\mathbf{r}) = \nabla \times \nabla \times \Pi_e(\mathbf{r}) = \frac{iZ_0}{4\pi k_0}\int_V \mathbf{J}(\mathbf{r}')\cdot\bar{\bar{\mathbf{G}}}(k_0,R)e^{ikR}\,dv' \ . \tag{4.42}$$

Here

$$\bar{\bar{\mathbf{G}}}(k_0,R) = \left(\frac{-1+ik_0R+k_0^2R^2}{R^3}\right)\bar{\bar{\mathbf{I}}} + \left(\frac{3-3ik_0R-k_0^2R^2}{R^3}\right)\hat{R}\hat{R} \ , \tag{4.43}$$

where $\hat{R}\hat{R}$ is a dyadic, and $\hat{R}$ is a unit vector given by $(\mathbf{r}-\mathbf{r}')/|\mathbf{r}-\mathbf{r}'|$.

Applying the volume equivalence principle [15], the polarization current can be expressed in terms of the dielectric constant and the total internal field. For objects that are small compared to the wavelength in at least one direction, such as needles or flat plates, the internal field can be calculated using the Rayleigh approximation, i.e. that the field is static along the direction with small dimension. Using this approach, the polarization currents can be expressed in terms of the incident field and the polarizability tensor [41]:

$$\mathbf{J}(\mathbf{r}') = -ik_oY_o\bar{\bar{\mathbf{P}}}\cdot\mathbf{E}_\mathbf{0}^\mathbf{i}e^{ik_0\hat{k}_i\cdot\mathbf{r}'} \ , \tag{4.44}$$

where $\bar{\bar{\mathbf{P}}}$ is the polarizability tensor of the target. Substituting (4.44) into (4.42) and noting that $\bar{\bar{\mathbf{P}}} \cdot \mathbf{E}_0^{\mathbf{i}}$ is constant inside the target, the near-field scattered field can be written as

$$\mathbf{E}(\mathbf{r}) = \frac{1}{4\pi} \left(\bar{\bar{\mathbf{P}}} \cdot \mathbf{E}_0^{\mathbf{i}} \right) \cdot \int_V \bar{\bar{\mathbf{G}}}(k_0, R) e^{ik_0(\hat{k}_i \cdot \mathbf{r}' + R)} \, dv' \ . \tag{4.45}$$

Note that the integration in (4.45) is one-fold and two-fold integrals for a cylinder and a disk, respectively.

If the observation point is in the far-field region, i.e. $R >> \lambda$, the following approximations can be applied to (4.45):

$$\bar{\bar{\mathbf{G}}}(k_0, R) \approx \frac{k_0^2}{R} \left(\bar{\bar{\mathbf{I}}} - \hat{k}_s \hat{k}_s \right) \ , \qquad e^{ik_0 R} \approx e^{ik_0 r} e^{-ik_0 \hat{k}_s \cdot \mathbf{r}'} \ . \tag{4.46}$$

Equation (4.45) could then be written as

$$\mathbf{E}(\mathbf{r}) \approx -\frac{k_0^2}{4\pi} \frac{e^{ik_0 r}}{r} \left\{ \hat{k}_s \times \hat{k}_s \times \left(\bar{\bar{\mathbf{P}}} \cdot \mathbf{E}_0^{\mathbf{i}} \right) \right\} \int_V e^{ik_0(\hat{k}_i - \hat{k}_s) \cdot \mathbf{r}'} \, dv' \ . \tag{4.47}$$

And the scattering matrix can be obtained as

$$\bar{\bar{S}}(\hat{k}_s, \hat{k}_i) = -\frac{k_0^2}{4\pi} \left\{ \hat{k}_s \times \hat{k}_s \times \left(\bar{\bar{\mathbf{P}}} \cdot \mathbf{E}_0^{\mathbf{i}} \right) \right\} \int_V e^{ik_0(\hat{k}_i - \hat{k}_s) \cdot \mathbf{r}'} \, dv' \ . \tag{4.48}$$

4.4.2 Secondary Scattered Fields — A Direct Approach

Consider two objects: object #1 and object #2. The second-order scattered field $\mathbf{E_{21}}$ (from #1 to #2) can be formulated in a direct manner which will be described in this section. In the absence of object #2, the scattered field from object #1 illuminated by the incident field is given by

$$\mathbf{E_1}(\mathbf{r}) = \frac{1}{4\pi} \left\{ \int_{V_1} \bar{\bar{\mathbf{G}}}(k_0, R) e^{ik_0(\hat{k}_i \cdot \mathbf{r}' + R)} \, dv' \right\} \cdot \left(\bar{\bar{\mathbf{P}}}_{\mathbf{1}} \cdot \mathbf{E}_0^{\mathbf{i}} \right) \ . \tag{4.49}$$

In (4.49), the polarization-current term has been moved to the end because $\bar{\bar{\mathbf{G}}}$ is a symmetric dyadic. For object #2, the polarization current induced only by $\mathbf{E_1}$ can

be written as

$$\mathbf{J_2}(\mathbf{r}'') = -ik_o Y_o \bar{\bar{\mathbf{P}}}_\mathbf{2} \cdot \mathbf{E_1} = -\frac{ik_o Y_o}{4\pi} \bar{\bar{\mathbf{P}}}_\mathbf{2} \cdot \left\{ \int_{V_1} \bar{\bar{\mathbf{G}}}(k_0, R) e^{ik_0(\hat{k}_i \cdot \mathbf{r}' + R)} \, dv' \right\} \cdot \left(\bar{\bar{\mathbf{P}}}_\mathbf{1} \cdot \mathbf{E}_\mathbf{0}^\mathbf{i} \right) \ . \tag{4.50}$$

The second-order scattered field can be written as

$$\mathbf{E}_\mathbf{21}^\mathbf{s} = -\frac{ik_0 Z_0}{4\pi} \frac{e^{ik_0 r}}{r} \hat{k}_s \times \hat{k}_s \times \int_{V_2} \mathbf{J_2}(\mathbf{r}'') e^{-ik_0 \hat{k}_s \cdot \mathbf{r}''} dv'' \ . \tag{4.51}$$

Since $\hat{p} \cdot \hat{k}_s = 0$ if $\hat{p} \in \{\hat{v}_s, \hat{h}_s\}$, and $\bar{\bar{\mathbf{P}}}_\mathbf{2}$ is symmetric, it is found that

$$\begin{aligned} \hat{p} \cdot \mathbf{E}_\mathbf{21}^\mathbf{s} = & \left(\frac{k_0}{4\pi} \right)^2 \frac{e^{ik_0 r}}{r} \left(\bar{\bar{\mathbf{P}}}_\mathbf{2} \cdot \hat{p} \right) \\ & \cdot \left\{ \int_{V_1} \int_{V_2} \bar{\bar{\mathbf{G}}}(k_0, R) e^{ik_0(\hat{k}_i \cdot \mathbf{r}' - \hat{k}_s \cdot \mathbf{r}'' + R)} \, dv' dv'' \right\} \cdot \left(\bar{\bar{\mathbf{P}}}_\mathbf{1} \cdot \mathbf{E}_\mathbf{0}^\mathbf{i} \right) \ , \end{aligned} \tag{4.52}$$

The elements of the scattering matrix can be written as

$$S_{21}^{pq} = \left(\frac{k_0}{4\pi} \right)^2 \left(\bar{\bar{\mathbf{P}}}_\mathbf{2} \cdot \hat{p} \right) \cdot \left\{ \int_{V_1} \int_{V_2} \bar{\bar{\mathbf{G}}}(k, R) e^{ik_0(\hat{k}_i \cdot \mathbf{r}' - \hat{k}_s \cdot \mathbf{r}'' + R)} \, dv' dv'' \right\} \cdot \left(\bar{\bar{\mathbf{P}}}_\mathbf{1} \cdot \hat{q} \right) \ , \tag{4.53}$$

where $\hat{q} \in \{\hat{v}_i, \hat{h}_i\}$, $\hat{p} \in \{\hat{v}_s, \hat{h}_s\}$, and $p, q \in \{v, h\}$. Note that the integration in (4.53) will be carried out numerically. Since the currents have been moved outside the integral, the computation becomes rather simple.

4.4.3 Secondary Scattered Field — A Reciprocal Approach

The second-order scattered field $\mathbf{E_{21}}$ can be also be formulated by applying the equation given by [48]

$$\hat{p} \cdot \mathbf{E_{21}} = \int_{V_1} \mathbf{E}_{e2} \cdot \mathbf{J}_1 \, dv \ , \tag{4.54}$$

where $\mathbf{E}_{e2}$ is the scattered field from object #2 illuminated by $\mathbf{E_{ed}}$ in the absence of object #1, and $\mathbf{J}_1$ is the induced polarization current of object #1 illuminated by the incident field in the absence of object #2. It should be noted that $\mathbf{E_{ed}}$ is

radiated by the elementary current $\mathbf{J_e} = \hat{p}\delta(\mathbf{r} - \mathbf{r_0})$ located in the far-field region of the particles and given by

$$\mathbf{E_{ed}}(\mathbf{r}) = \frac{ik_0 Z_0}{4\pi} \frac{e^{ik_0 r_0}}{r_0} \epsilon^{-ik_0 \hat{k}_s \mathbf{r}} \hat{p} \ , \tag{4.55}$$

where $\hat{p}$ is either $\hat{v}_s$ or $\hat{h}_s$. Substituting (4.55) into (4.45), the scattered field can be written as

$$\mathbf{E_{e2}}(\mathbf{r}) = \frac{ik_0 Z_0}{(4\pi)^2} \frac{e^{ik_0 r_0}}{r_0} \left(\bar{\bar{\mathbf{P}}}_\mathbf{2} \cdot \hat{p} \right) \cdot \int_{V_2} \bar{\bar{\mathbf{G}}}(k_0, R) e^{ik_0(-\hat{k}_s \cdot \mathbf{r}' + R)} \, dv' \ , \tag{4.56}$$

where $\bar{\bar{\mathbf{P}}}_\mathbf{2}$ is the polarizability tensor of object #2. From (4.44), $\mathbf{J}_1$ is given by

$$\mathbf{J_1}(\mathbf{r}') = -ik_o Y_o \bar{\bar{\mathbf{P}}}_\mathbf{1} \cdot \mathbf{E_0^i} e^{ik_0 \hat{k}_i \cdot \mathbf{r}'} \ , \tag{4.57}$$

where $\bar{\bar{\mathbf{P}}}_\mathbf{1}$ is the polarizability tensor of object #1. Substituting (4.56) and (4.57) into (4.54), the secondary scattered field $\mathbf{E_{21}}$ can be written as

$$\begin{aligned} \hat{p} \cdot \mathbf{E_{21}}(\mathbf{r}) = & \left(\frac{k_0}{4\pi} \right)^2 \frac{e^{ik_0 r_0}}{r_0} \left(\bar{\bar{\mathbf{P}}}_\mathbf{2} \cdot \hat{p} \right) \\ & \cdot \left\{ \int_{V_1} \int_{V_2} \bar{\bar{\mathbf{G}}}(k_0, R) e^{ik_0(\hat{k}_i \cdot \mathbf{r}' - \hat{k}_s \cdot \mathbf{r}'' + R)} \, dv' dv'' \right\} \cdot \left(\bar{\bar{\mathbf{P}}}_\mathbf{1} \cdot \mathbf{E_0^i} \right) \ , \end{aligned} \tag{4.58}$$

which is the same as (4.52).

4.4.4 Secondary Scattered Fields — Far-field Interaction

If the distance between the two objects is large, the integrand in (4.52) reduces to

$$\bar{\bar{\mathbf{G}}}(k_0, R) e^{ik_0(\hat{k}_i \cdot \mathbf{r}' - \hat{k}_s \cdot \mathbf{r}'' + R)} \approx \frac{k_0^2}{R_0} \left(\bar{\bar{I}} - \hat{R}_0 \hat{R}_0 \right) e^{ik_0(\hat{k}_i - \hat{R}_0) \cdot \mathbf{r}'} e^{ik_0(\hat{R}_0 - \hat{k}_s) \cdot \mathbf{r}''} \ . \tag{4.59}$$

In (4.59) $R_0 = |\mathbf{r_{c2}} - \mathbf{r_{c1}}|$ where $\mathbf{r_{c1}}$ and $\mathbf{r_{c2}}$ are the centers of object #1 and #2, respectively, and $\hat{R}_0 = \frac{\mathbf{r_{c2}} - \mathbf{r_{c1}}}{R_0}$. Substituting (4.59) into (4.52), the secondary scattered field can be written as

$$\hat{p} \cdot \mathbf{E_{21}^s} = \frac{1}{R_0} \frac{e^{ik_0 r}}{r} \hat{p} \cdot \left\{ \bar{S}_2(\hat{k}_s, \hat{R}_0) \bar{S}_1(\hat{R}_0, \hat{k}_i) \mathbf{E_0^i} \right\} \ . \tag{4.60}$$

So, when the distance between two objects is large, the scattering matrix of the secondary scatter can be written as

$$\bar{S}_{21}(\hat{k}_s, \hat{k}_i) = \frac{1}{R_0} \bar{S}_2(\hat{k}_s, \hat{R}_0) \bar{S}_1(\hat{R}_0, \hat{k}_i) \tag{4.61}$$

4.4.5 Reciprocal Property of the Secondary Scattering Matrix

Similar to (4.53), S_{12}^{pq} can is written as

$$S_{12}^{pq} = \left(\frac{k_0}{4\pi}\right)^2 \left(\bar{\bar{\mathbf{P}}}_1 \cdot \hat{p}\right) \cdot \left\{ \int_{V_1} \int_{V_2} \bar{\bar{\mathbf{G}}}'(k_0, R') e^{ik_0(\hat{k}_i' \cdot \mathbf{r}'' - \hat{k}_s' \cdot \mathbf{r}' + R')} \, dv' dv'' \right\} \cdot \left(\bar{\bar{\mathbf{P}}}_2 \cdot \hat{q}\right) , \tag{4.62}$$

where $\hat{R}'$ is $(\mathbf{r}'' - \mathbf{r}')/|\mathbf{r}'' - \mathbf{r}'|$. Let $\hat{k}_i' = -\hat{k}_s$ and $\hat{k}_s' = -\hat{k}_i$. The local coordinate systems become $(\hat{v}_s, -\hat{h}_s, -\hat{k}_s)$ for the incident field and $(\hat{v}_i, -\hat{h}_i, -\hat{k}_i)$ for the scattered field. Also note that $\bar{\bar{\mathbf{G}}}'(k, R')$ is symmetric, and $\hat{R}'\hat{R}' = \hat{R}\hat{R}$. (4.62) can be rearranged as

$$S_{12}^{pq} = \left(\frac{k_0}{4\pi}\right)^2 \left(\bar{\bar{\mathbf{P}}}_2 \cdot \hat{q}\right) \cdot \left\{ \int_{V_1} \int_{V_2} \bar{\bar{\mathbf{G}}}(k, R) e^{ik_0(-\hat{k}_s \cdot \mathbf{r}'' + \hat{k}_i \cdot \mathbf{r}' + R)} \, dv' dv'' \right\} \cdot \left(\bar{\bar{\mathbf{P}}}_1 \cdot \hat{p}\right) , \tag{4.63}$$

where $\hat{q} \in \{\hat{v}_s, -\hat{h}_s\}$, $\hat{p} \in \{\hat{v}_i, -\hat{h}_i\}$, and $p, q \in \{v, h\}$. Comparing (4.63) to (4.53), it is seen that

$$\bar{\bar{\mathbf{S}}}_{12}(\hat{k}_s, \hat{k}_i) = \begin{pmatrix} S_{vv}^{12}(\hat{k}_s, \hat{k}_i) & S_{vh}^{12}(\hat{k}_s, \hat{k}_i) \\ S_{hv}^{12}(\hat{k}_s, \hat{k}_i) & S_{hh}^{12}(\hat{k}_s, \hat{k}_i) \end{pmatrix} = \begin{pmatrix} S_{vv}^{21}(-\hat{k}_i, -\hat{k}_s) & -S_{hv}^{21}(-\hat{k}_i, -\hat{k}_s) \\ -S_{vh}^{21}(-\hat{k}_i, -\hat{k}_s) & S_{hh}^{21}(-\hat{k}_i, -\hat{k}_s) \end{pmatrix} . \tag{4.64}$$

4.4.6 Data Simulations

In this section, the formulation presented in the previous section will be used to investigate the effect of the near-field interaction between Rayleigh-Gans particles. Demonstration of the the effect of the near-field interaction in vegetation will require realistic description of the vegetation structure. This is beyond the scope of this

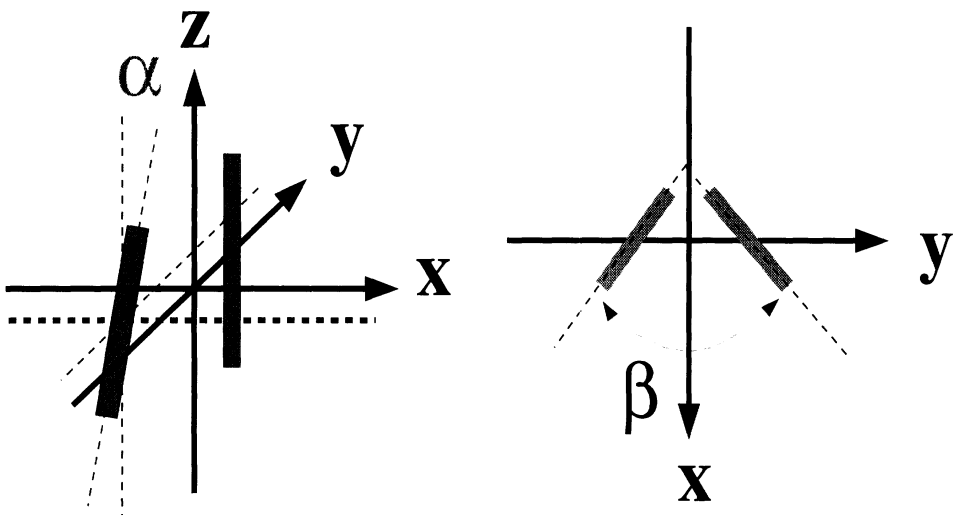

(a) (b)

Figure 4.4: Positions of (a) two dielectric cylinders and (b) two disks. The angle between the two cylinder axes is denoted as α. The angle between the two disk planes is denoted as β.

section. Therefore, simulation will be performed on a pair of particles varying orientation and frequency. Circular cylinders and disks are of interest here. The length, radius, and relative dielectric constant of the cylinder are 20cm, 2mm, and 30+i10. The radius, thickness, and relative dielectric constant for the disk are 5cm, 0.2mm, and 30+i10. The incident and scattering directions are $+x$ and $-x$, respectively. These values will be used for the rest of this section. The polarizability tensors for both geometries can be found in [41,53].

The first simulation is to demonstrate the near-field interaction at different frequencies. The positions of both cylinders are shown in Fig. 4.4(a) with $\alpha = 0^o$. One cylinder is placed at (0,5mm,0), and the other is placed at (0,-5mm,0). The cylinders are parallel to the z-axis. Since both cylinders are aligned in the $\hat{v}$ direction, the interaction is not significant for hh-polarizations. Figure 4.5 shows the radar cross section (RCS) and co-polarized phase difference ($\phi_{hh} - \phi_{vv}$) of the two

cylinders versus frequency. The first-order and complete second-order solutions are plotted together for the purpose of comparison. For vv-polarization, the interaction becomes stronger as frequency increases. The interaction was expected to become weaker as the frequency and electrical length of the separation increase. However, as frequency increases, the size of the cylinders relative to the wavelength also increase, so overall, the interaction becomes stronger. Figure 4.6 shows the radar cross section (RCS) and co-polarized phase difference of two disks versus frequency. Two disks are placed at (0,5.5cm,0) and (0,-5.5cm,0) with $\beta = 90^0$, as shown in Fig. 4.4(b). The near-field interaction does become significant at higher frequencies. However, The interaction is negligible at frequencies lower than 2 GHz. In both of the simulations, the orientations of the particles are chosen to favor of the second-order scattering. While the two cylinders are parallel to each other, the two disks are expected to function as a dihedral. Nevertheless, the second-order interaction seems to be insignificant. This implies that in vegetation scattering problems, the near-field interaction between leaves (or pine needles) could be ignored at L-band.

The second simulation investigates the near-field interaction at different particle orientation. Figure 4.7 shows the RCS and co-polarized phase difference of the two cylinders versus α at 5.0 GHz. As shown in Fig. 4.4(a), one cylinder is placed at (0,5mm,0), parallel to the z-axis, and the other is placed at (-5mm,-5mm,0) and rotated in the y-z plane starting at $\alpha = 0^o$. It is interesting to find that the interaction can be ignored when $\alpha > 60^0$ even at so short a distance. Since one of the cylinders is always parallel to the $\hat{v}$ direction, the near-field interaction does not have significant effect on hh-polarized and cross-polarized RCSs. Figure 4.8 shows the RCS and co-polarized phase difference of two disks versus β at 5.0 GHZ. Two disks are placed at (0,5.5cm,0) and (0,-5.5cm,0) as shown in Fig. 4.4(b). While the interaction is very

dominant when β is around 90^0, it can be ignored when $\beta > 135^0$.

Both simulations show that the significant the near-field interaction at high frequencies also depends on the orientation of particles. For example, for some plants, leaves on the same branch tend to lie in the same plane. In this case the near-field interaction between leaves on the same branch could be ignored.

4.4.7 Conclusions

A scattering solution for the second-order interaction between two particles is developed based on the Rayleigh-Gans approach. This formulation can be easily implemented into computer codes, and the numerical integration involved in the calculation of the near-field is not intensive. Therefore, in a field where models often involve heavy computation, this solution provides a convenient tool to handle the near-field interaction between leaves and thin branches. The effect of the near-field interaction is also demonstrated by many examples. When the frequency is low, for example at L-band, the second-order interaction for leaves and slim branches can be ignored. The effect is also investigated for different particle orientations. When developing vegetation scattering models, such simulations can help decide whether the near-field interaction should be included.

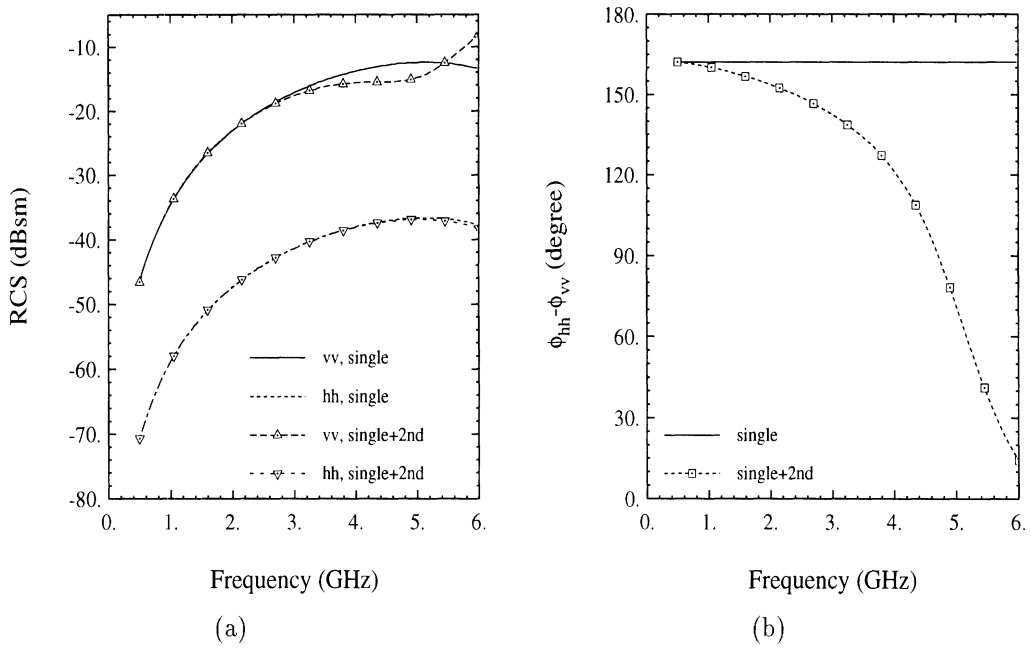

Figure 4.5: The first-order and complete second-order (a) RSC and (b) co-polarized phase difference of two cylinders versus frequency. The positions of both cylinders are shown in Fig. 4.4(a) with $\alpha = 0^0$.

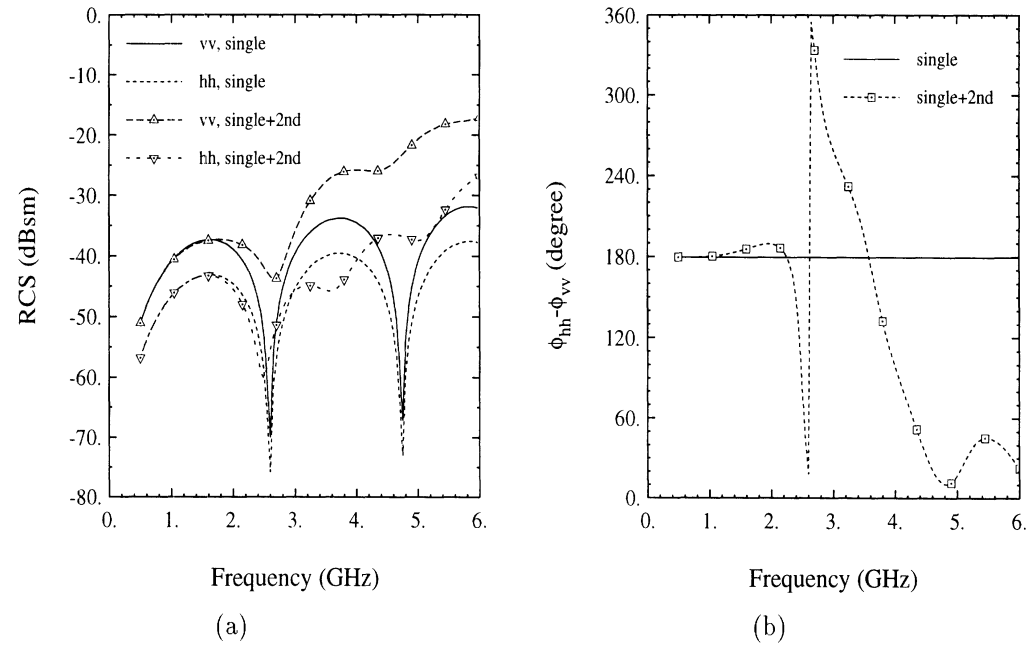

Figure 4.6: The first-order and complete second-order (a) RSC and (b) co-polarized phase difference of two disks versus frequency. The positions of both disks are shown in Fig. 4.4(b) with $\beta = 90^0$.

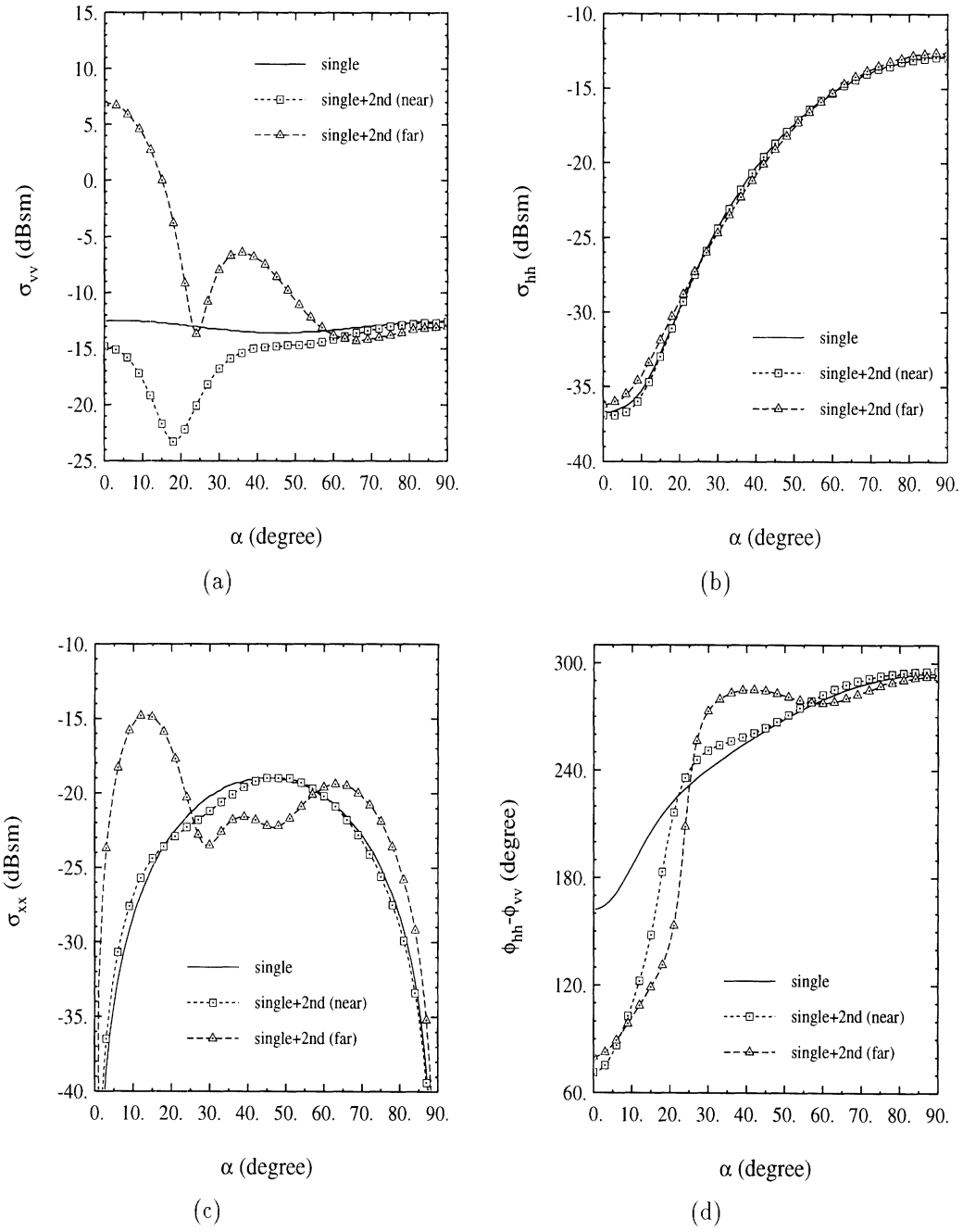

Figure 4.7: (a) Vv-polarized RCS, (b) hh-polarized RCS, (c) cross-polarized RCS, and (d) co-polarized phase difference of two cylinders versus α at 5 GHz. The positions of both cylinders are shown in Fig. 4.4(a).

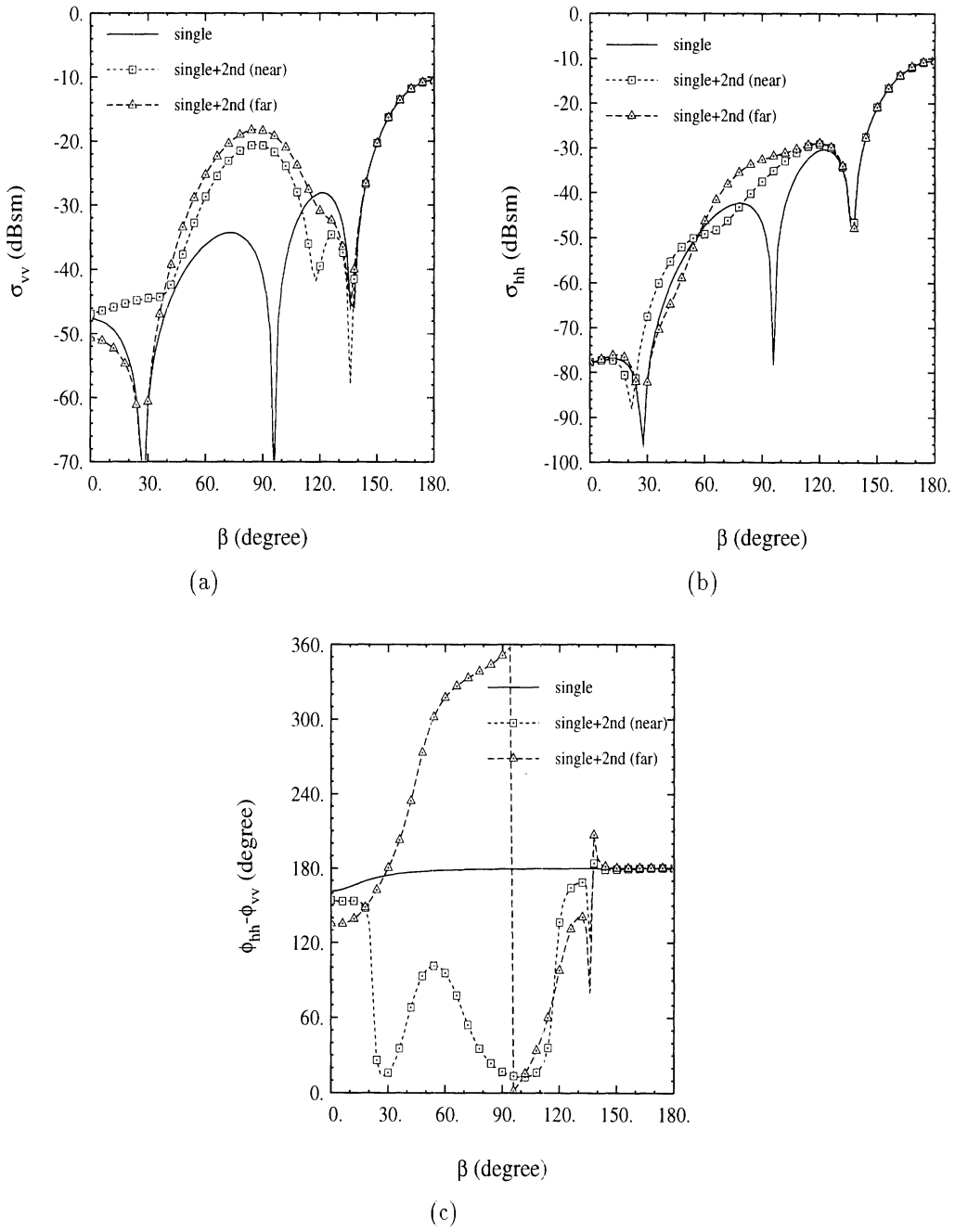

Figure 4.8: (a) Vv-polarized RCS, (b) hh-polarized RCS, and (c) co-polarized phase difference of two disks versus β in y-direction at 5 GHz. The positions of both disk are shown in Fig. 4.4(b).

CHAPTER V

ELECTROMAGNETIC SCATTERING FROM SHORT BRANCHING VEGETATION

5.1 Introduction

In the early vegetation scattering models, the vegetation medium was simplified in terms of a homogeneous random medium and the single scattering theory was applied to account for the scattering and propagation in the random medium [18,21,69]. For example, in [69] a forest stand is represented in terms of a two-layer random medium including a crown layer composed of randomly oriented cylinders and disks representing branches and leaves and a trunk layer containing nearly vertical cylinders representing tree trunks below the crown layer. Although these models are capable of predicting the scattering behavior of vegetation qualitatively, they are incapable of predicting the scattering behavior quantitatively due to their simplifying assumptions. An important feature of a high fidelity scattering model is to preserve the structure of vegetation as different species of vegetation have their own unique structures, which are expected to exhibit their own scattering behaviors. An important effect of the vegetation structure is the coherence effect caused by the relative position of the vegetation particles which produce certain interference pattern. It is shown that the coherence effects caused by the vegetation structure become more

significant at lower frequencies [65]. In the remote sensing of vegetation-covered terrain where the underlying soil surface is the target of interest , low microwave frequencies are recommended and therefore the coherence effects must be carefully accounted for. The model developed by Yueh et al. [74] may be among the first to address the coherence effects caused by the vegetation structure. In their scattering model for soybeans, a two-scale branching vegetation structure was constructed, and the scattered fields from particles were added coherently. Lin et al. [23] also proposed a coherent scattering model for forest canopies in which rather realistic tree-like structures are constructed using the fractal theory. In both models, the scattering solutions are formulated using the single scattering theory.

Another important issue in modeling the scattering from vegetation is the effect of the multiple scattering among vegetation particles. Vegetation particles are usually arranged in clusters within a single plant, such as leaves around end branches and branches around main stems and trunks. Therefore, a vegetation medium may be appropriately considered as locally dense. In such cases, the near-field multiple scattering is strong and may significantly affect the overall response. To accurately evaluate the near-field interaction, the realistic description of the relative positions and orientations of the vegetation particles and accurate and efficient scattering formulations are required. In recent years, some advanced scattering solutions that account for the near-field interaction between scatterers have been presented [48,64]. However, vegetation scattering models which can handle the near-field interaction with realistic vegetation structures have not been developed yet. The evaluation of the near-field interaction is usually numerically intensive, considering the huge number of particles in the medium.

In this chapter, a scattering model for soybeans is presented which incorporates

realistic computer-generated vegetation structures and accounts for the second-order near-field scattering interaction. Soybeans are erect branching plants composed of components which can be often found in many vegetation: stems, branches, leaves and fruits (pods) arranged in a very well-defined manner. Hence it is very appropriate for studying the effect of the vegetation structure on the radar backscatter. Also because of its moderate number of particles, the computation of the second-order near-field interaction is not formidable. Also from the experimental point of view, the dimensions of soybean plants are small enough to allow for conducting controlled experiments using truck-mounted scatterometers. Due to the uniformity of the plants and underlying soil surface, gathering the ground truth data is rather simple. The chapter is organized as follows: Section 5.2 gives the theoretical description of the model, including the vegetation structure modeling and the scattering solution. In Section 5.3 the experimental procedures using the University of Michigan truck-mounted scatterometer and AIRSAR are discussed. Finally in Section 5.4 model validation using the measured data and a sensitivity analysis are presented.

5.2 Theoretical Analysis

Consider a global coordinate system with x-y plane parallel to a horizontal ground plane and z-axis along the vertical direction, as shown in Fig. 5.1. Suppose a plane wave given by

$$\mathbf{E^i}(\mathbf{r}) = \mathbf{E_0^i} e^{ik_0 \hat{k}_i \cdot \mathbf{r}} \ . \tag{5.1}$$

is illuminating the ground plane from the upper half-space, where $\hat{k}_i$ is the unit vector along the propagation direction given by

$$\hat{k}_i = \hat{x} \sin\theta_i \cos\phi_i + \hat{y} \sin\theta_i \sin\phi_i - \hat{z} \cos\theta_i \ . \tag{5.2}$$

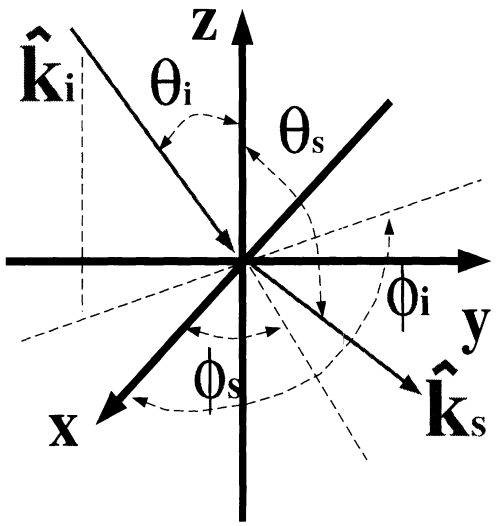

Figure 5.1: Definition of the incident and scattering angles.

The vector $\mathbf{E}_0^i$ in (5.1) is expressed in terms of a local coordinate system $(\hat{v}_i,\hat{h}_i,\hat{k}_i)$ where $\hat{h}_i = \hat{k}_i \times \hat{z}/|\hat{k}_i \times \hat{z}|$ and $\hat{v}_i = \hat{h}_i \times \hat{k}_i$ denote the horizontal and vertical unit vectors, respectively. Representing the direction of the observation point by $\hat{k}_s$, the polarization of the scattered field can also be expressed in terms of a local coordinated system $(\hat{v}_s,\hat{h}_s,\hat{k}_s)$ where

$$\hat{k}_s = \hat{x}\sin\theta_s\cos\phi_s + \hat{y}\sin\theta_s\sin\phi_s + \hat{z}\cos\theta_s \ , \tag{5.3}$$

and $\hat{v}_s$ and $\hat{h}_s$ can be obtained using similar expressions as those given for $\hat{v}_i$ and $\hat{h}_i$, respectively.

5.2.1 Vegetation Structure Modeling

To make the proposed scattering solution tractable, simple geometries are chosen to represent vegetation particles. Leaves are represented by elliptical thin dielectric disks. The other particles, which include stems, branches, and pods, are modeled using circular cylinders. Analytical scattering solutions are available for both geometries and will be introduced in the next section.

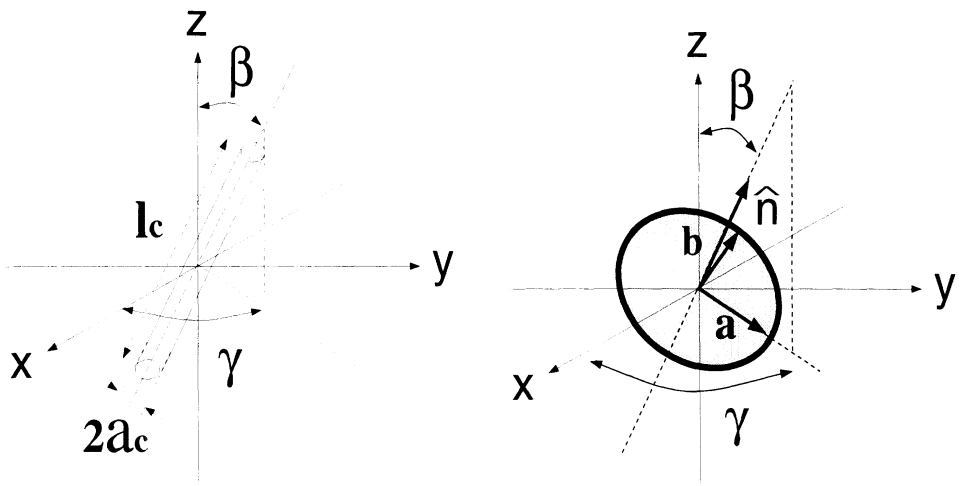

(a) (b)

Figure 5.2: Denotation of the dimensional and orientational parameters for (a) a cylinder and (b) a disk.

The orientation and dimension of each particle are described by four parameters, as shown in Fig. 5.2. The values of these parameters are determined by random number generators during the simulation with predescribed probability distribution functions (pdf). The orientation parameters of the particles are described by two angles: β(elevation angle) and γ(azimuth angle). Azimuthal symmetry is assumed for γ, and its pdf is given by

$$p(\gamma) = \frac{1}{2\pi}, \qquad \gamma \in [0, 2\pi) \ . \tag{5.4}$$

However, for β, a bell-shaped pdf is chosen:

$$p(\beta) = \frac{e^{-((\beta-\beta_m)/\beta_s)^2}}{\int_0^\pi e^{-((\beta'-\beta_m)/\beta_s)^2}\, d\beta'}, \qquad \beta \in [0, \pi] \ . \tag{5.5}$$

For leaves, the axis ratio (b/a) assumed constant and the thickness and major axis (a) are given Gaussian pdfs. Three types of cylinders are considered for main stems, branches, and pods. For these cylinders, Gaussian pdfs are chosen to describe the statistics of their radii and lengths.

The branching structure of soybeans is rather simple and can be developed using the following algorithm:

1. All parameters of main stem are determined using random number generators.

   The main stem is then divided into subsections, whose lengths are again decided by Gaussian random number generator.

2. At each node (connecting point of two subsections of the stem), a branch is placed whose orientation is obtained from (5.4) and (5.5). Depending on the growth stage, pods may be added at each node.

3. To each branch end a leaf is attached. In this model, the number of leaflets at each branch end is three (this may be different for other soybean species). Azimuthal orientation angle of leaves is determined from the orientation angle of the branches they are connected to.

Figure 5.9 shows a typical computer-generated soybean structures according to the aforementioned algorithm.

5.2.2 Scattering Mechanism and Scattering Formulations for the Vegetation Particles and Rough Surfaces

Several scattering mechanisms are considered for the scattering model. Figure 5.3 depicts 6 different mechanisms including: (1) direct backscatter from the underlying rough surface, (2) direct backscatter from vegetation particles, (3) single ground bounce, (4) double ground bounce, (5) second-order scattering interaction among vegetation particles, and (6) scattering interaction between main stem and the rough surface. The first four mechanisms are included in almost all existing vegetation scattering models. Mechanism #5 is a second-order solution which accounts for the

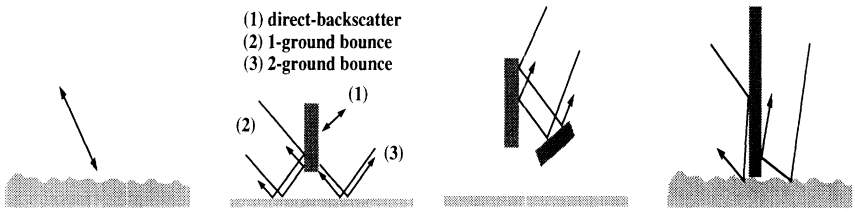

(a) (b) (c) (d)

Figure 5.3: Scattering mechanisms. (a) direct backscatter from rough surface, (b) direct backscatter from vegetation, single ground-bounce, and double ground-bounce, (c) second-order near-field interaction, and (d) incoherent main stem-rough surface interaction.

near-field interaction within a single plant. Mechanism #6 is only considered for predicting the cross-polarized scattering at L-band according to a study reported in the previous chapter. where it is shown that the co-polarized scattering of mechanism #6 at L-band is weak compared to that of Mechanism #2.

Mechanism #6 is also ignored at C-band, because of attenuation experienced by the wave propagating through the vegetation layer. In what follows, the scattering solutions for each mechanism is briefly described.

1. **Mechanism #1:**

   There exist many rough-surface scattering models available in the literature. In this model, a second-order small perturbation model(SPM) [52], which has been presented in Chapter II, and a physical optic (PO) model [66] are incorporated to handle the backscatter from the rough surface.

2. **Mechanisms #2~#4:**

   These mechanisms are often referred to as the single scattering solutions in which only the scattering solutions for the isolated vegetation particles are considered. The effect of the ground surface in mechanisms #3 and #4 are

considered by introducing the ground reflection coefficients. If the SPM is used in mechanism #1, the Fresnel reflection coefficients are used directly. If the PO is needed according to the surface roughness condition, the reflection coefficients are modified by $e^{-2(ks\cos\theta_i)^2}$ to account for the reduction in the surface reflectivity [17]. The single scattering solutions for dielectric disks and cylinders are obtained from the following formulations:

(a) **Elliptical disk:**

The thickness of the soybean leaves ($\approx 0.2 - 0.3mm$) is usually small compared to the wavelength in microwave region and the ratio of the thickness to the diameter of the leaves is much less than unity. Also by noting that the dielectric constant of vegetation is lossy, the Rayleigh-Gans formulation [53] can be applied to derive the scattering solution for the elliptical disks representing the vegetation leaves. For an elliptical disk, the scattering matrix elements are found to be

$$S_{pq}^{d} = \hat{p} \cdot (\bar{\bar{\mathbf{P}}}_{\mathbf{d}} \cdot \hat{q}) \frac{A_d k_0^2}{2\pi} \frac{J_1(\sqrt{(aA)^2 + (bB)^2})}{\sqrt{(aA)^2 + (bB)^2}} , \tag{5.6}$$

where A_d, a and b are the area, major axis, and minor axis of the disk respectively. In (5.6), $\bar{\bar{\mathbf{P}}}_{\mathbf{d}} = \bar{\bar{\mathbf{U}}}_{\mathbf{d}}^{-1} \bar{\bar{\mathbf{P}}}_{\mathbf{d}}^{\mathbf{0}} \bar{\bar{\mathbf{U}}}_{\mathbf{d}}$, where $\bar{\bar{\mathbf{P}}}_{\mathbf{d}}^{\mathbf{0}}$ is the disk's polarizability tensor which can be found in [41, 53], and $\bar{\bar{\mathbf{U}}}_{\mathbf{d}}$ is the matrix of coordinate transformation which transfers the global coordinate system to a local coordinate system defined by the major axis, minor axis, and the normal of the disk respectively. The explicit expression for $\bar{\bar{\mathbf{U}}}_{\mathbf{d}}$ can be

obtained from [62]. Also A and B are given by

$$A = k_0 \left[\bar{\bar{\mathbf{U}}}_{\mathbf{d}}^{-1} \cdot (\hat{k}_i - \hat{k}_s) \right] \cdot \hat{x}$$
$$B = k_0 \left[\bar{\bar{\mathbf{U}}}_{\mathbf{d}}^{-1} \cdot (\hat{k}_i - \hat{k}_s) \right] \cdot \hat{y} \ . \tag{5.7}$$

The detailed derivation of (5.6) has been given in Section 4.1.

(b) **Circular cylinder:**

Exact scattering solution does not exist for cylinders of finite length, but an approximated solution, which assumes the internal field induced within the finite cylinder is the same as that of the infinite cylinder with the same cross section and dielectric constant, can be used [54]. The detailed expressions of this solution have been given in Section 4.3. Generally, this solution is valid when the ratio of the length to the diameter is large.

3. **Mechanism #5:**

The second-order scattered field between two particles is formulated using an efficient algorithm based on the reciprocity theorem [48] which has been briefly introduced in Section 3.2.1. For two adjacent particles we have

$$\hat{p} \cdot \mathbf{E_{21}} = \int_{V_1} \mathbf{E}_{e2} \cdot \mathbf{J}_1 \, dv \ . \tag{5.8}$$

where $\mathbf{E}_{e2}$ is the scattered field from particle #2 illuminated by an infinitesimal current source at the observation point in the absence of particle #1, and $\mathbf{J}_1$ is the induced polarization current of particle #1 illuminated by the incidence field in the absence of particle #2. $\mathbf{E_{12}}$ can be obtained using the reciprocity theorem. Hence the second-order scattered field are conveniently obtained from the plane wave solution of the induced polarization current and near field of individual particles. These quantities for disks and cylinders are given by:

(a) **Disk:** The induced polarization current is obtained from Rayleigh-Gans approximation and is given by

$$\mathbf{J_1}(\mathbf{r}) = -ik_o Y_o \bar{\bar{\mathbf{P}}}_{\mathbf{d}} \cdot \mathbf{E}_{\mathbf{0}}^{\mathbf{i}} e^{ik_0 \hat{k}_i \cdot \mathbf{r}} , \tag{5.9}$$

where $\bar{\bar{\mathbf{P}}}_{\mathbf{d}}$ is the polarizability tensor. The exact near-field scattered field must be numerically evaluated from

$$\mathbf{E_{e2}}(\mathbf{r}) = \frac{ik_0 Z_0}{(4\pi)^2} \frac{e^{ik_0 r_0}}{r_0} \left(\bar{\bar{\mathbf{P}}}_{\mathbf{d}} \cdot \hat{p} \right) \cdot \int_{S_2} \bar{\bar{\mathbf{G}}}(k, R) e^{ik_0(-\hat{k}_s \cdot \mathbf{r}' + R)} \, ds' , \tag{5.10}$$

where

$$\bar{\bar{\mathbf{G}}}(k_0, R) = \left(\frac{-1 + ik_0 R + k_0^2 R^2}{R^3} \right) \bar{\bar{\mathbf{I}}} + \left(\frac{3 - 3ik_0 R - k_0^2 R^2}{R^3} \right) \hat{R}\hat{R} , \tag{5.11}$$

and $\hat{R}$ is a unit vector defined by $\hat{R} = (\mathbf{r} - \mathbf{r}')/|\mathbf{r} - \mathbf{r}'|$.

If both particles are disks, the formulation for the interaction between them has been given in Section 4.4.

(b) **Cylinder:** The formulation for finite finite cylinders is used again to calculate the induced polarization current and the near-field scattered field. The formulation of the scattered field in the vicinity of the cylinder is given by [48]

$$\mathbf{E_{e2}}(\mathbf{r}) = -\frac{ik_o Z_o e^{ik_o r_o}}{4\pi r_o} \mathbf{F}(\phi - \phi_s) H_o^{(1)}(k_o \sin\theta_s \rho) e^{k_o \cos\theta_s z} . \tag{5.12}$$

Equation (5.12) is derived using the stationary phase approximation along the axial direction of the cylinder axis. This solution has been verified by the method of moments [31,48], and the region of validity is given by

$$\rho > 2d_c^2/\lambda , \tag{5.13}$$

where d_c is the diameter of the cylinder, and ρ is the radial distance between the observation point and the cylinder axis. For the main stem of soybeans, the radius is usually less than 5mm. Applying (5.13) it is found that $\rho > 3.5mm$ at C-band (5.3 GHz). Therefore, (5.12) is appropriate for calculating the near-field interaction.

4. **Mechanism #6:**

The incoherent interaction between the main stems and rough surface is formulated using the reciprocity technique introduced in [48]. The details and lengthy formulation for the cylinder-rough surface scattering interaction can be found in Chapter III. This model is only applied to calculate the scattering interaction between the main stem and underlying rough surface. The reason for this is that for a titled cylinder with large elevation angle (β) such as branches, the cross-polarized scattering from mechanisms #2 and #3 is dominant. However, main stems often grow nearly vertically and its interaction with the ground becomes a important source of the cross-polarized scattering, noting that the mechanisms #2 and #3 of nearly vertical cylinders do not produce significant cross-polarized scattering field. As will be shown later, the cross-polarized scattering at L-band is mainly dominated by two scattering mechanisms #2 and #6.

5.2.3 Propagation in a Lossy Layered Media

5.2.3.1 Foldy's Approximation

The scattering solutions provided in the previous section are for targets in free space. However, for vegetation canopies the targets are within a lossy random medium. Thus, a particle is illuminated by not only the incident plane wave, but also

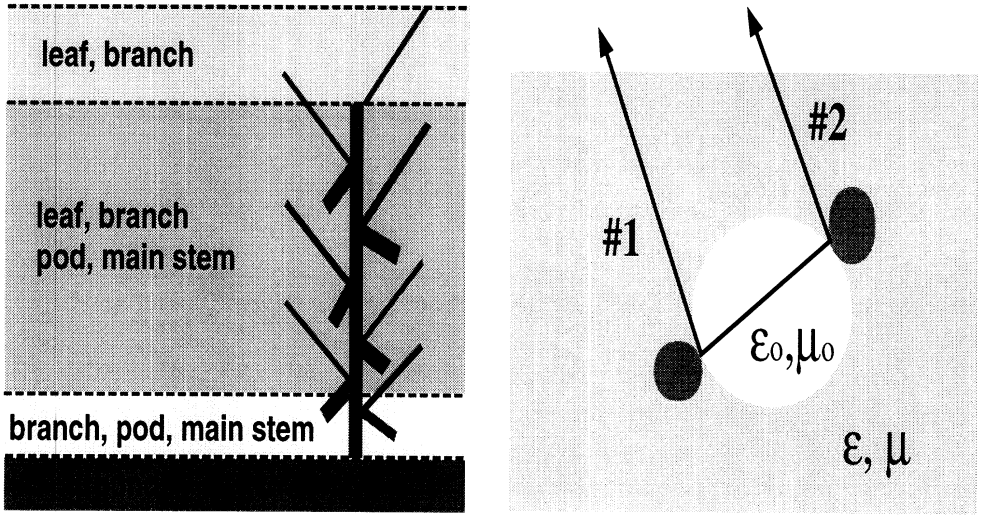

(a) (b)

Figure 5.4: Vegetation particles embedded in the lossy medium. (a) Stratified structure for the calculation of the equivalent propagation constant. (b) Free space is assumed in the calculation of the second-order near-field interaction.

by the scattered fields from other particles. To calculate the total scattered field from a particle, it is usually assumed that the particle is embedded in homogeneous lossy medium, as shown in Fig. 5.4(a). The vegetation layer can be divided into many sub-layers which contain different types and number density of vegetation particles, and thus each layer exhibits different equivalent propagation constants.

Foldy's approximation [62] has been widely used in many vegetation scattering models to account for the attenuation experienced by the wave traveling through the vegetation medium. According to the Foldy's approximation the vertical and horizontal components of the mean electric field in a sparse random medium satisfy

$$\begin{aligned} \frac{dE_h}{ds} &= i\left(k_0 + M_{hh}\right) E_h + iM_{hv}E_v \\ \frac{dE_v}{ds} &= iM_{vh}E_h + i\left(k_0 + M_{vv}\right) E_v \ , \end{aligned} \tag{5.14}$$

where s is the length along the propagation path within the medium and

$$M_{pq} = \frac{2\pi n_0}{k_0}\langle S_{pq}(\hat{k},\hat{k})\rangle \ , \qquad p,q \in \{h,v\} \ . \tag{5.15}$$

Here n_0 is the number density of the scatterers within the medium, and $\langle S_{pq}(\hat{k},\hat{k})\rangle$ is the averaged forward scattering matrix element of the scatterers. Since the vegetation structure exhibits statistical azimuthal symmetry, there is no coupling between horizontal and vertical components of the coherent field and therefore $M_{hv} = M_{vh} = 0$. From (5.14), the effective propagation constants for both polarizations are given by

$$\begin{aligned} k_h^e &= k_0 + M_{hh} \\ k_v^e &= k_0 + M_{vv} \ . \end{aligned} \tag{5.16}$$

As mentioned previously, the second-order near-field interaction is incorporated in this model, and it will only be calculated for the scatterers within a single plant. It is reasonable to assume that no extinction should be considered for the calculation of the near-field interaction. However, since both particle are still embedded in the vegetation layer, extinction is considered for the incident wave and secondary scattered fields. As shown in Fig. 5.4(b), the space between two scatterers is considered as free space, and Foldy's approximation is still used on paths #1 and #2.

5.2.3.2 Propagation Paths

In this section, the phase difference and extinction caused by the wave propagating in the vegetation layer will be formulated using the method presented in [58]. To build a coherent scattering model, the phase of each scattering mechanism has to be calculated with respect to a phase reference point. Figure 5.5(a) shows the propagation geometry for the direct path. The reference phase point is taken to be the origin of the coordinate system. Using ray optics, the propagation from the

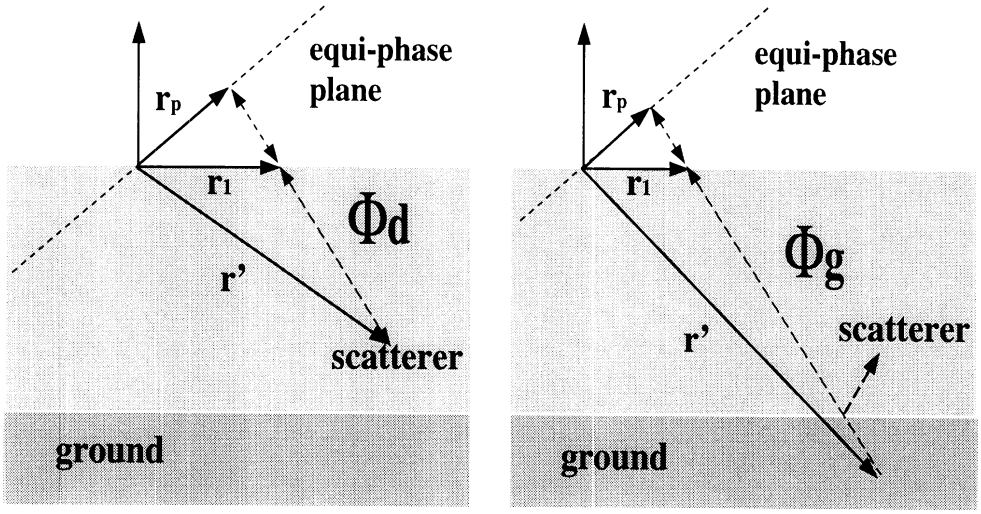

(a) (b)

Figure 5.5: Propagation paths in the vegetation layer. (a) direct and (b) ground bounce.

equi-phase plane (shown in Fig. 5.5(a)) directly to the scatterer is given by

$$\Phi'_d(\hat{k}_0, \mathbf{r}', p) = k_0 \mathbf{r_1} \cdot \hat{k}_0 + k_p^e(\mathbf{r}' - \mathbf{r_1}) \cdot \hat{k}_e \ , \tag{5.17}$$

where $\mathbf{r_1}$ denotes the location where the ray intersects the interface between the vegetation layer and free-space. Here the effect of refraction is ignored assuming a diffuse boundary between the vegetation layer and free-space ($\hat{k}_e = \hat{k}_0$) and p denotes the polarization of the wave. Substituting (5.16) into (5.17), it is found that

$$\Phi'_d(\hat{k}_0, \mathbf{r}', p) = k_0 \mathbf{r}' \cdot \hat{k}_0 + M_{pp}(\mathbf{r}' - \mathbf{r_1}) \cdot \hat{k}_0 \ . \tag{5.18}$$

The first term on the right-hand side of (5.18) is the free-space propagation term and will be included in the scattering matrix elements of the scatterer. The second-term on the right-hand side is the extra phase difference and extinction caused by the propagation in the lossy vegetation media, and will be denoted as $\Phi_d(\hat{k}_0, \mathbf{r}', p)$. The free space-vegetation interface is set to be the x-y plane, so it is found that

$$(\mathbf{r}' - \mathbf{r_1}) \cdot \hat{k}_0 = \frac{z'}{\hat{k}_o \cdot \hat{z}} \ . \tag{5.19}$$

Therefore, $\Phi_d(\mathbf{r}', p)$ can be written as

$$\Phi_d(\hat{k}_0, \mathbf{r}', p) = M_{pp} \frac{z'}{\hat{k}_o \cdot \hat{z}} \ . \tag{5.20}$$

The ground-bounce path, as shown in Fig. 5.5(b), includes a reflection from the ground plane. In Fig. 5.5(b), the image position is given by

$$\mathbf{r}'_{image} = x'\hat{x} + y'\hat{y} - (z' + 2d)\hat{z} \ , \tag{5.21}$$

where d is the thickness of the layer. Using (5.20), it is found that $\Phi_g(\hat{k}_0, \mathbf{r}', p)$, which only accounts for the extra phase difference and extinction caused by the propagation in the lossy vegetation media, can be written as

$$\Phi_g(\hat{k}_0, \mathbf{r}', p) = -M_{pp} \frac{z' + 2d}{\hat{k}_o \cdot \hat{z}} \ . \tag{5.22}$$

5.2.4 Scattering from Soybean Fields and Monte-Carlo Simulation

Consider an area of soybean field with N_p soybean plants per unit area. For a given computer-generated soybean plant (the k-th plant with N_s particles), the total scattering amplitude can be written as

$$S_{pq,k} = \left\{ \sum_{i=1}^{N_s} \left[S^d_{pq,ki} + S^{gg}_{pq,ki} + S^{g1}_{pq,ki} + S^{g2}_{pq,i} \right] + \sum_{i=1}^{N_s} \sum_{\substack{j=1 \\ j \neq i}}^{N_s} S^{2nd}_{pq,kij} \right\} e^{ik_0(\hat{k}_i - \hat{k}_s)\cdot \mathbf{r_k}} \ , \tag{5.23}$$

where $\mathbf{r_k}$ is the location of the plant. In (5.23) each term includes the attenuation and phase shift due to the propagation:

$$\begin{aligned}
\text{direct:} \qquad & S^d_{pq,ki} = S_{pq,ki}(\hat{k}_s, \hat{k}_i) e^{i\Phi_d(-\hat{k}_s, \mathbf{r}_{ki}, p)} e^{i\Phi_d(\hat{k}_i, \mathbf{r}_{ki}, q)} \\
\text{ground-plant:} \qquad & S^{g1}_{pq,ki} = S_{pq,ki}(\hat{k}_s, \hat{k}'_i) R_p e^{i\Phi_g(-\hat{k}_s, \mathbf{r}_{ki}, p)} e^{i\Phi_d(\hat{k}_i, \mathbf{r}_{ki}, q)} \\
\text{plant-ground:} \qquad & S^{g1}_{pq,ki} = S_{pq,ki}(\hat{k}'_s, \hat{k}_i) R_q e^{i\Phi_d(-\hat{k}_s, \mathbf{r}_{ki}, p)} e^{i\Phi_g(\hat{k}_i, \mathbf{r}_{ki}, q)} \\
\text{ground-ground:} \qquad & S^{gg}_{pq,ki} = S_{pq,ki}(\hat{k}'_s, \hat{k}'_i) R_q R_q e^{i\Phi_g(-\hat{k}_s, \mathbf{r}_{ki}, p)} e^{i\Phi_g(\hat{k}_i, \mathbf{r}_{ki}, q)} \\
\text{near-field 2nd-order:} \qquad & S^{2nd}_{pq,kij} = S^{2nd}_{pq,kij}(\hat{k}_s, \hat{k}_i) e^{i\Phi_d(-\hat{k}_s, \mathbf{r}_{ki}, p)} e^{i\Phi_d(\hat{k}_i, \mathbf{r}_{kj}, q)} \ ,
\end{aligned} \tag{5.24}$$

where $\hat{k}_i' = \hat{k}_i - 2(\hat{k}_i \cdot \hat{z})\hat{z}$ and $\hat{k}_s' = \hat{k}_s - 2(\hat{k}_s \cdot \hat{z})\hat{z}$. Note that all scattering mechanisms are added coherently to capture the coherence effect caused by the vegetation structure.

The scattering coefficient of the soybean field is then computed by incoherent addition of the scattered powers from vegetation, rough surface, and main stem-rough surface interaction. Hence

$$\sigma^0_{pqpq} = \sigma^0_{pqpq}(\text{vegetation}) + \sigma^0_{pqpq}(\text{rough surace}) + \sigma^0_{pqpq}(\text{stem-rough surface}) \ , \tag{5.25}$$

where

$$\sigma^0_{pqpq}(\text{vegetation}) = 4\pi \left\langle \left| \sum_{k=1}^{N_p} S_{pq,k} \right|^2 \right\rangle \tag{5.26}$$

$$\sigma^0_{pqpq}(\text{rough surface}) = \sigma^0_{pqpq,r} \left| e^{i\Phi_d(-\hat{k}_s,-d\hat{z},p)} e^{i\Phi_d(\hat{k}_i,-d\hat{z},q)} \right|^2 \tag{5.27}$$

$$\begin{aligned} \sigma^0_{pqpq}(\text{stem-rough surface}) = 4\pi N_p \Big\langle \Big| & S^{rc}_{pq} e^{i\Phi_d(-\hat{k}_s,-d\hat{z},p)} e^{i\Phi_d(\hat{k}_i,(-d+0.5l_c)\hat{z},q)} \\ & + S^{cr}_{pq} e^{i\Phi_d(\hat{k}_i,-d\hat{z},p)} e^{i\Phi_d(-\hat{k}_s,(-d+0.5l_c)\hat{z},q)} \Big|^2 \Big\rangle \ . \end{aligned} \tag{5.28}$$

In calculation of the contribution from the direct rough surface and the stem-rough surface, the propagation attenuation through vegetation layer is also included. S^{rc}_{pq} and S^{cr}_{pq} are, respectively, the rough surface-cylinder and cylinder-rough surface scattering amplitudes. The ensemble averaging in (5.28) is carried out analytically using the SPM formulation, and the details are reported in the previous chapter. As mentioned earlier, the contribution from this term is only significant at L-band for the cross-polarized term.

The ensemble averaging in (5.26) is carried out using a Monte-Carlo simulation. For each realization in the Monte-Carlo simulation, a group of computer-generated soybean plants are generated and distributed on a square area of 1 m^2, and then the

scattered fields are computed. This procedure will be repeated until a convergence is reached. To examine the coherence effect, the scattered power from the vegetation is also calculated incoherently from

$$\sigma^0_{pqpq}(\text{vegetation}) = 4\pi\left\langle \sum_{k=1}^{N_p}\left\{ \sum_{i=1}^{N_s}\left[\left|S^d_{pq,ki}\right|^2 + \left|S^{gg}_{pq,ki}\right|^2 + \left|S^{g1}_{pq,ki}\right|^2 + \left|S^{g2}_{pq,i}\right|^2 \right] + \sum_{i=1}^{N_s}\sum_{\substack{j=1 \\ j\neq i}}^{N_s} \left|S^{2nd}_{pq,kij}\right|^2 \right\} \right\rangle . \tag{5.29}$$

5.3 Experimental Results

In this section, the experimental procedure and the multi-frequency multi-polarization backscatter measurements using polarimetric scatterometer systems and JPL AIRSAR are presented.

5.3.1 Measurement Using the University of Michigan's POLARSCAT

In August of 1995, a series of polarimetric measurements were conducted on a soybean field near Ann Arbor, MI. These measurement were conducted using the University of Michigan polarimetric scatterometer systems (POLARSCAT) [60]. The polarimetric backscatter data were collected at two different frequencies (L-band and C-band) over a wide range of incidence angles (from 20^o to 70^0 at 10^o increment). The overall goal of these experiments was to investigate the feasibility of soil-moisture retrieval of vegetation-covered terrain from radar backscatter data. Experiments were designed to observe the radar-backscatter variations due to the change in soil moisture while the vegetation parameters were almost the same. Two sets of data were collected. In one measurement the angular polarimetric data were collected on August 14 when the underlying soil surface was dry, and in another a similar data was collected right after a heavy rain on August 18. At the time of experiments the soy-

	Aug. 14	Aug. 18
soil (m_v)	0.06	0.17
rms height(s)	$0.0115m$	
correlation length(l)	$0.0879m$	
vegetation (m_g)	0.769	0.767
number density of plant	34 ± 13 plants/m^2	
biomass	1.97 kg/m^2	

Table 5.1: Measured ground truth for the POLARSCAT data set.

bean plants were fully grown with significant number of pods. In fact the vegetation biomass was at its maximum. Since the separation between the time of experiments were only about 4 days, no significant change in the vegetation parameters were observed.

The vegetation structural parameters and moisture in addition to the soil surface roughness and moisture were carefully characterized. The dielectric constant of the soil surface was measured by using a C-band field-portable dielectric probe [6]. The measured relative dielectric constant (ϵ_r) was used to estimate the moisture contents (m_v) by inverting a semi-empirical model [14] which give ϵ_r in terms of m_v. The mean m_v, which is shown in Table 5.1, is then used to estimate ϵ_r at L-band.

Two dielectric measurement techniques [40,49] were used to measure the dielectric constant of leaves and stems. These measurement were performed at C-band using WR-187 waveguide sample holder, and the results are shown in Fig. 5.6. The corresponding dielectric constants at L-band was then calculated using the empirical model provided in [67]. The gravimetric moisture content (m_g) of the vegetation was also measured on the day of radar measurement to monitor the variation of the biomass. As shown in Table 5.1, the vegetation moisture remained almost the same on both dates of the experiments.

The dimensions and orientations of vegetation particles were also recorded. Table

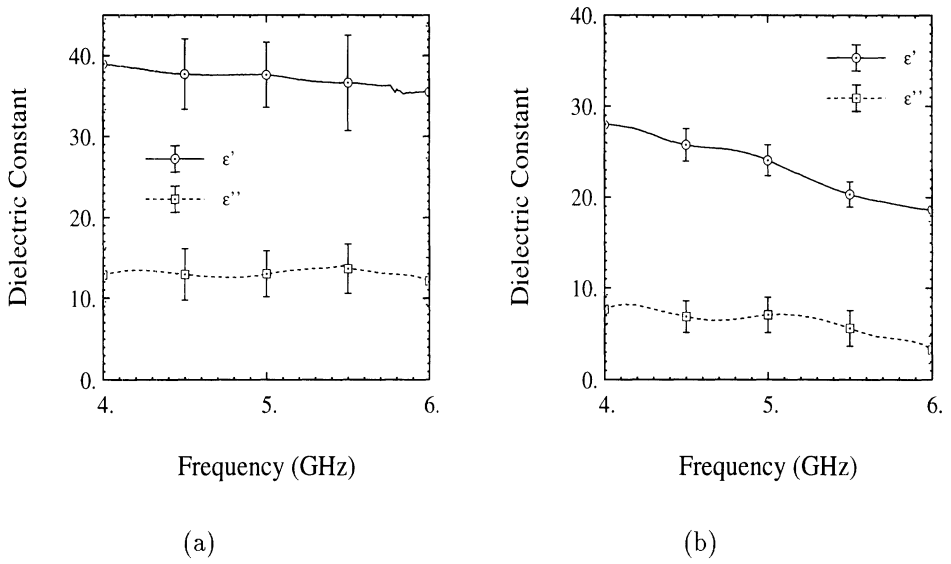

Figure 5.6: Measured dielectric constants for (a) branches and main stems, and (b) leaves at C-band using the procedure outlined in [40,49].

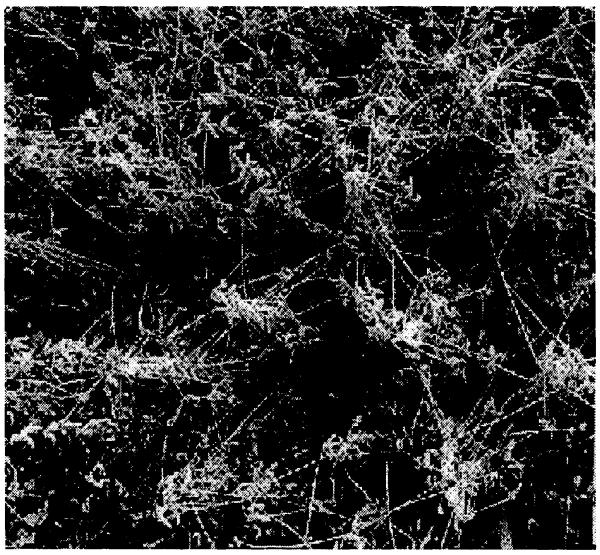

Figure 5.7: Picture of the soybean plant distribution for POLARSCAT data set. It was taken from the top of the field when plants were dry. Unlike the row structure which is often seen in many cultivated field, the distribution pattern is rather random.

	β_m, β_s (degree)	radius (cm)	length or thickness (cm)
stem	5, 5	0.3 ± 0.09	73.0 ± 3.4
node	5, 5	0.3 ± 0.09	5.4 ± 1.4
branch	45.8, 25.6	0.12 ± 0.031	20.7 ± 6.5
pod	135.5, 30.8	0.35 ± 0.03	3.7 ± 0.48
leaf	45.6, 30.1	$3.8 \pm 0.07(0.576)$	0.022 ± 0.002

Table 5.2: Measured vegetation parameters of soybeans for the POLARSCAT data set.

5.2 shows the means and standard deviations of vegetation parameters. Unlike most cultivated fields where the plants are planted in row structures, the soybean plants of this field were distributed in a rather random pattern, as shown in Fig. 5.7. This picture shows the top-view at the end of the season where all the leaves were fallen. The surface roughness parameters were also measured and reported in Table 5.1.

5.3.2 Measurement Using AIRSAR

JPL Airborne Synthetic Aperture Radar (AIRSAR) [75] was deployed to conduct backscatter measurements on a number of cultivated fields. Although AIRSAR is capable of measuring polarimetric backscatter at three microwave frequencies (P-,L-, and C-band), only L-band and C-band data were collected. The backscatter data were collected by AIRSAR during its flight over the Kellogg Biological Station near Kalamazoo, Michigan, on July 12, 1995. Also these data sets were collected at three different incidence angles: 30, 40, 45 degree. Unfortunately the soybean fields were not within the research site of the station and the ground truth data was rather limited. The only available informations are that the soybean were about a month old and the volumetric soil moisture content was less than 0.1. Figure 5.8 shows the composite L-band and C-band SAR image at 45^o incidence angle.

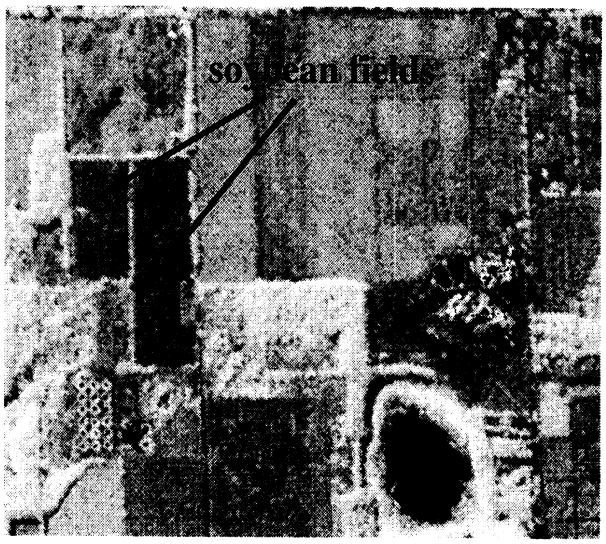

Figure 5.8: AIRSAR image of the Kellogg Biological Station in July of 1995. This image combined the L-band and C-band backscatter data at 45 degree of incidence angle. Two soybean field is on the left side of the image with dark color.

5.4 Data Simulation and Analysis

The vegetation scattering model is first validated using the data collected by POLARSCAT. Guided by the ground truth data, many soybean plant structures were generated in order to carry on the data simulation (see Fig. 5.9(a)). The computer-generated plants were uniformly distributed using a random number generator. The Monte-Carlo simulations are performed at incidence angles ranging from 20^o to 70^o at 5^o increment. Figures 5.10(a) and 5.11(a) show the simulated and measured backscattering coefficients versus incidence angle at L-band and C-band, respectively. Good agreement is achieved by allowing the dielectric constants of vegetation particles vary within the confidence region shown in Fig. 5.6. In figures 5.10(b), (c), and (d), the contributions from individual scattering mechanisms are plotted as functions of incidence angle at L-band. The cross products of among different mechanisms, which account for the coherence effect, are not presented in these figures. It is quite obvious that the contribution from the second-order near-field interac-

(a) (b)

Figure 5.9: Computer-generated soybean plants for (a) POLARSCAT data set and (b) AIRSAR data set.

tion at L-band is negligible for both co- and cross-polarized terms. It is also shown that for co-polarized backscattering coefficient the direct backscatter from soybean, direct backscatter from rough surface, and single ground-bounce are sufficient to characterize the scattering behavior. For cross-polarization, however, the two most significant mechanisms are the direct backscatter from vegetation and the incoherent rough surface-stem interaction. The later mechanism contains information regarding the underlying soil surface including the soil moisture. Figures 5.11(b), (c), and (d) show scattering contributions from different mechanisms versus incidence angle at C-band. The direct backscatter form vegetation and the second-order near-field interaction are the dominant scattering mechanisms at C-band. Because of larger near-field region, the near-field interaction is stronger at C-band than at L-band. Also the second-order near-field interaction has more profound effect on the vv- and cross-polarization, because the orientation of the main stems is nearly vertical. The

other mechanisms, which include the soil moisture information, are not significant for two reasons: (1) high extinction through the vegetation layer, and (2) surface roughness which decreases the reflectivity of the ground surface.

From these analysis it is found that the backscatter at C-band or higher frequencies are mainly sensitive to vegetation parameters for sufficiently high vegetation biomass (in this case, biomass = 1.97 kg/m^2). At L-band or lower frequencies, it is possible to sense the soil moisture for surfaces covered with short vegetation and relatively high biomass. Figures 5.12(a), (b), and (c) demonstrate the sensitivity of the backscatter to soil moisture as a function of incidence angle for the soybean field. The simulations are performed under four different soil-moisture conditions: $m_v = 0.1, 0.2, 0.3$ and 0.4 at L-band. The backscatter data collected on August 14 and August 18 are also plotted in these figures for comparison. These results suggest that the appropriate range of incidence angle for the the purpose of soil-moisture retrieval is $\theta_i < 50^o$ where there is about 6-dB of dynamic range. At incidence angles larger than 50^o, the sensitivity to soil moisture decreases due to the high extinction caused by the vegetation. To retrieve the soil moisture accurately, vegetation parameters must be estimated as accurately as possible. It seems a combination of high and low frequency backscatter data is needed to estimate the vegetation and soil moistures accurately.

Due to the limited ground-truth data, the AIRSAR data set is used for estimating the vegetation and surface roughness parameters. Although the retrieval algorithm presented here is based on trial and error, it indicates the feasibility of estimating vegetation parameters and soil moisture from image radars. The procedure for estimating these parameters is described below:

1. Based on a series of trial simulations, it is found that the second-order near-field

interaction can be ignored at L- and C-band for the one-month old soybeans. In this case the soybean plants are still young with shorter branches and stems and much fewer number of vegetation particles. Also there are no pods on the plants whose interaction with the main stem is the major source of the near-field interaction.

2. Judging from the measured values of the co-polarized scattering coefficients reported in Fig. 5.13(a), it is inferred that the vegetation biomass is rather low. In this case, depending on the surface roughness, the surface scattering mechanism can be dominant at low incidence angles. If the surface scattering is dominant entirely, it is expected that σ^o_{vv} be larger than σ^o_{hh}. However, this is not observed from the measured data at 30°. Hence, there is at least a comparable backscattering contribution from the vegetation. Under this condition, a significant contribution to the backscatter at C-band comes from the vegetation.

3. At relatively low biomass, it is found that cross-polarized scattering coefficient is dominated by the direct backscatter from the soybean at both frequency bands. The size of the main stems for one-month-old soybean is small, so the rough surface-stem interaction is not significant. Also at C-band the direct backscatter from the rough surface is weak due to the small rms height and extinction through the vegetation layer. Therefore, the dimension, the number density, and the dielectric constant of the soybean can be estimated by matching the cross-polarized backscatter at C-band. This is done by confining the range of the vegetation dielectric constants to those reported in Fig. 5.6. The elevation angles of all vegetation particles can be estimated by matching the

soil (m_v)	0.05
rms height(s)	0.0038 m
correlation length(l)	0.038 m
number density of plant	19 plants/m^2
biomass	0.22 kg/m^2

Table 5.3: Estimated ground truth for the AIRSAR data set.

	β_m, β_s (degree)	radius (cm)	length or thickness (cm)
stem	7.5, 5	0.18 ± 0.05	30.2 ± 3.4
node	7.5, 5	0.18 ± 0.05	5.0 ± 1.0
branch	60.8, 25.6	0.12 ± 0.031	14.7 ± 4.5
leaf	47.0, 30.0	$3.7 \pm 0.08(0.6)$	0.02 ± 0.001

Table 5.4: Estimated vegetation parameters of soybeans for the AIRSAR data set.

co-polarized scattering coefficient ratio $\sigma^0_{vv}/\sigma^0_{hh}$ and cross-polarized scattering coefficient. The vegetation parameters as a first iteration is decided by matching the data at C-band. Then, by matching the data at L-band with the same vegetation structure, the parameters of the rough surface is estimated. The simulation is then iterated between L-band and C-band until the simulated and measured data match at both frequency bands.

After matching the backscatter data at both L- and C-band, the final estimated target parameters are shown in Tables 5.3 and 5.4. A typical corresponding computer-generated soybean plant is shown in Fig. 5.9(b). Figures 5.13(a) and 5.14(a) show the simulated and measured scattering coefficients versus incidence angle at L- and C-band, respectively. Monte-Carlo simulation are performed at 5 degree increments. Figures 5.13(b), (c), and (d) show scattering contributions from different mechanisms versus incidence angle at L-band. As predicted, the scattering between stems and rough surface is not significant due to the shorter and slimmer main stems and smaller surface roughness. Figures 5.13(b), (c), and (d) show scattering contri-

butions from different mechanisms versus incidence angle at C-band. As predicted, the second-order scattering can be neglected.

Finally, Figs. 5.15 and 5.16 show the coherence effect of the vegetation structure. The scattering coefficients do not include the contribution from the main stems-rough surface scattering and the direct backscatter from the rough surface. In these figures the coefficients denoted as "coherent" are calculated using (5.26), while those which are denoted as "incoherent" are calculated using (5.29). It is shown that for a fully grown soybean, the coherence effect is significant at L-band for co-polarized components, while the effect is not observable at C-band. However, for low biomass condition (AIRSAR data), it is found that the coherent effect is also significant at C-band. This can be explained noting that a fully-grown soybean plant has more complex structure with more particles than a one-month-old plant. Nevertheless, it should be noted that the second-order near-field interaction is

significant for POLARSCAT data at C-band, and can be evaluated only when the relative distance and orientation of particles are given. Therefore, to some extent, the coherence effect of structure embedded in this mechanism is also important at C-band. For the cross-polarized scattering, the coherence effect is less significant in both low and high biomass conditions at both frequencies.

5.5 Conclusions

In this chapter, an electromagnetic scattering model for short branching vegetation is presented. The vegetation particles are modeled as simple geometries such as cylinders and disks for which analytical scattering solutions are available. With the realistic structures which reasonably describe the relative positions of the particles, this model is is constructed so that the coherence effect due to the phase difference

between the scattered fields from different particles and the second-order near-field interaction among particles are accounted for. Also the interaction between the main stems and underlying rough surface is incorporated into this model which is shown to be important only at low frequencies (L-band) and for cross-polarized backscattering coefficient.

The model accuracy is verified using polarimetric radar backscatter measurements of a soybean field obtained from truck-mounted scatterometers. Through an extensive ground-truth data collection, target parameters such as the soil and vegetation moisture contents, geometry of the soybean plants, and surface roughness were characterized. Monte-Carlo simulations were carried out simulating the statistical properties of the backscatter at different incidence angles. Good agreement is obtained between the model prediction and measured backscattering coefficients. From a sensitivity analysis, it is found that: (1) the second-order near-field interaction is more significant at C-band than at L-band, (2) the interaction between the main stems and rough surfaces could be significant for cross-polarized scattering at L-band, (3) the double ground-bounce mechanism is generally not important, and (4) high-frequency data (C-band or higher) can be used to probe the vegetation, and low-frequency data (L-band or lower) is needed to probe the soil moisture through vegetation.

The model was also used to estimate the parameters of a soybean field using the AIRSAR data, and reasonable results which agree with the limited ground-truth data was obtained. The coherence effect was also examined using the model simulation.

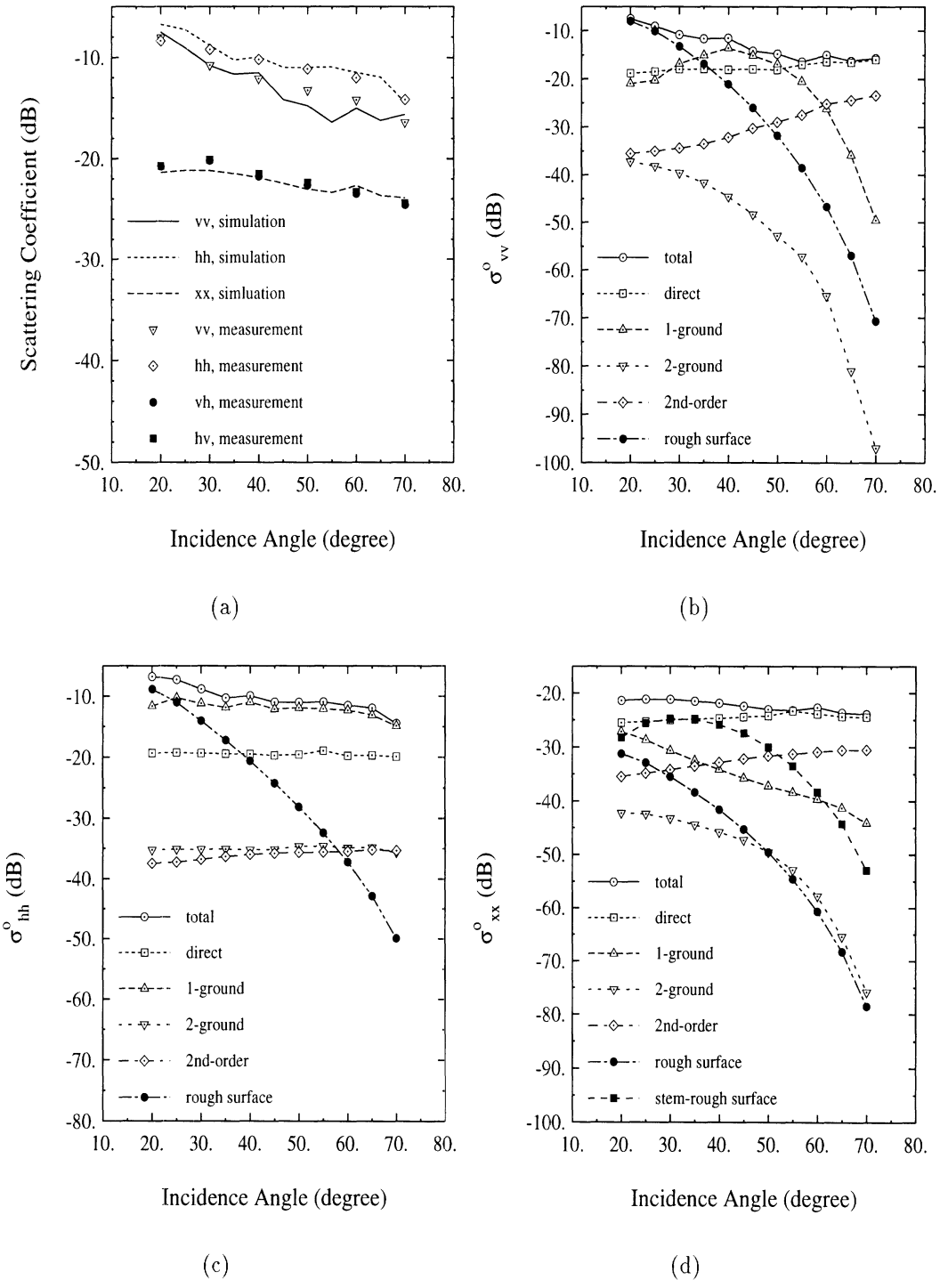

Figure 5.10: Scattering coefficients versus incidence angle at L-band for August 14 POLARSCAT data set: (a) model validation, and (b)(c)(d) scattering mechanism analysis for vv-, hh-, and cross-polarizations, respectively.

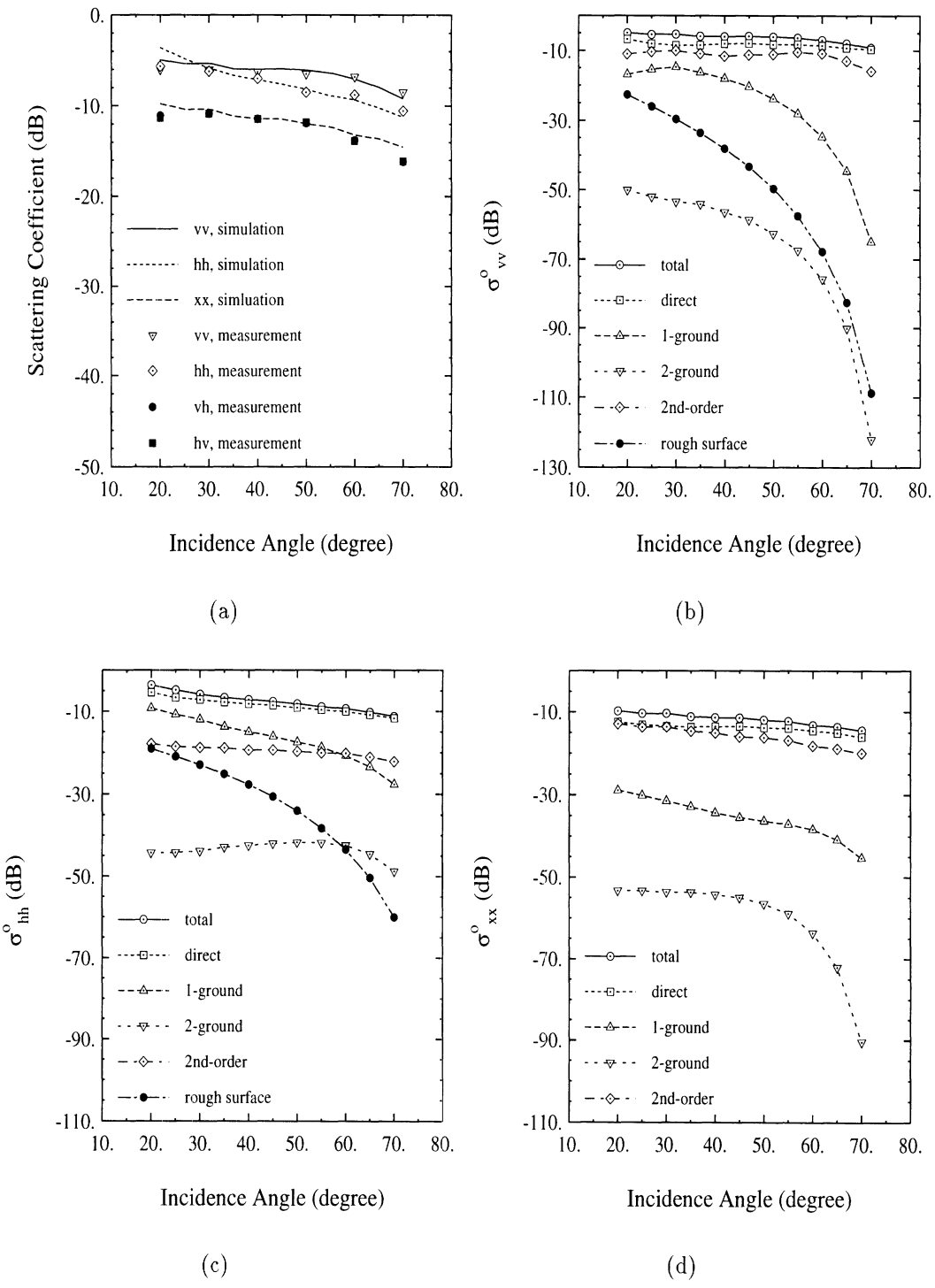

Figure 5.11: Scattering coefficients versus incidence angle at C-band for August 14 POLARSCAT data set: (a) model validation, and (b)(c)(d) scattering mechanism analysis for vv-, hh-, and cross-polarizations, respectively.

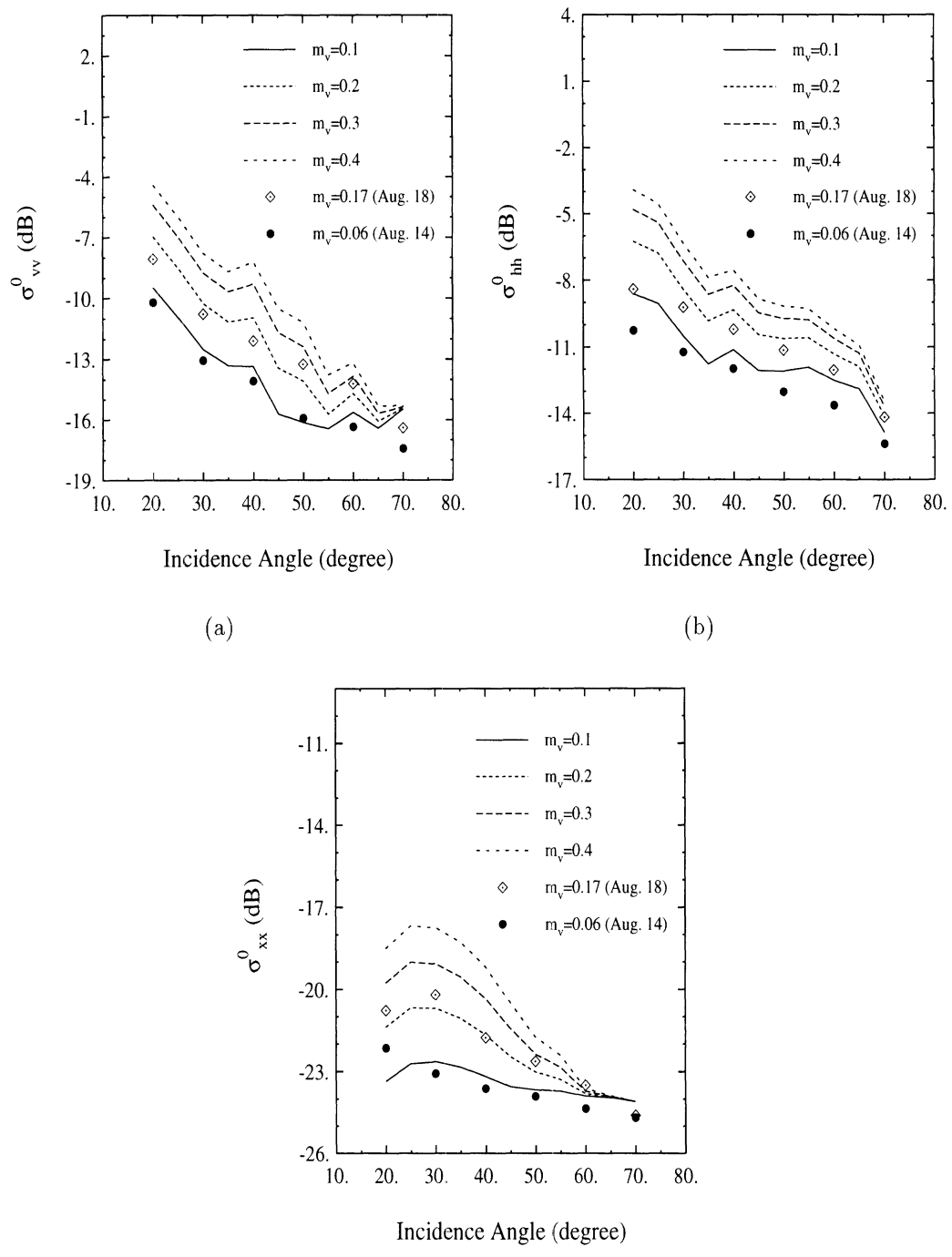

Figure 5.12: Analysis of sensitivity to the variation of the soil moisture for the POLARSCAT data set at L-band.(a) vv-polarization, (b) hh-polarization, and (c) cross-polarization.

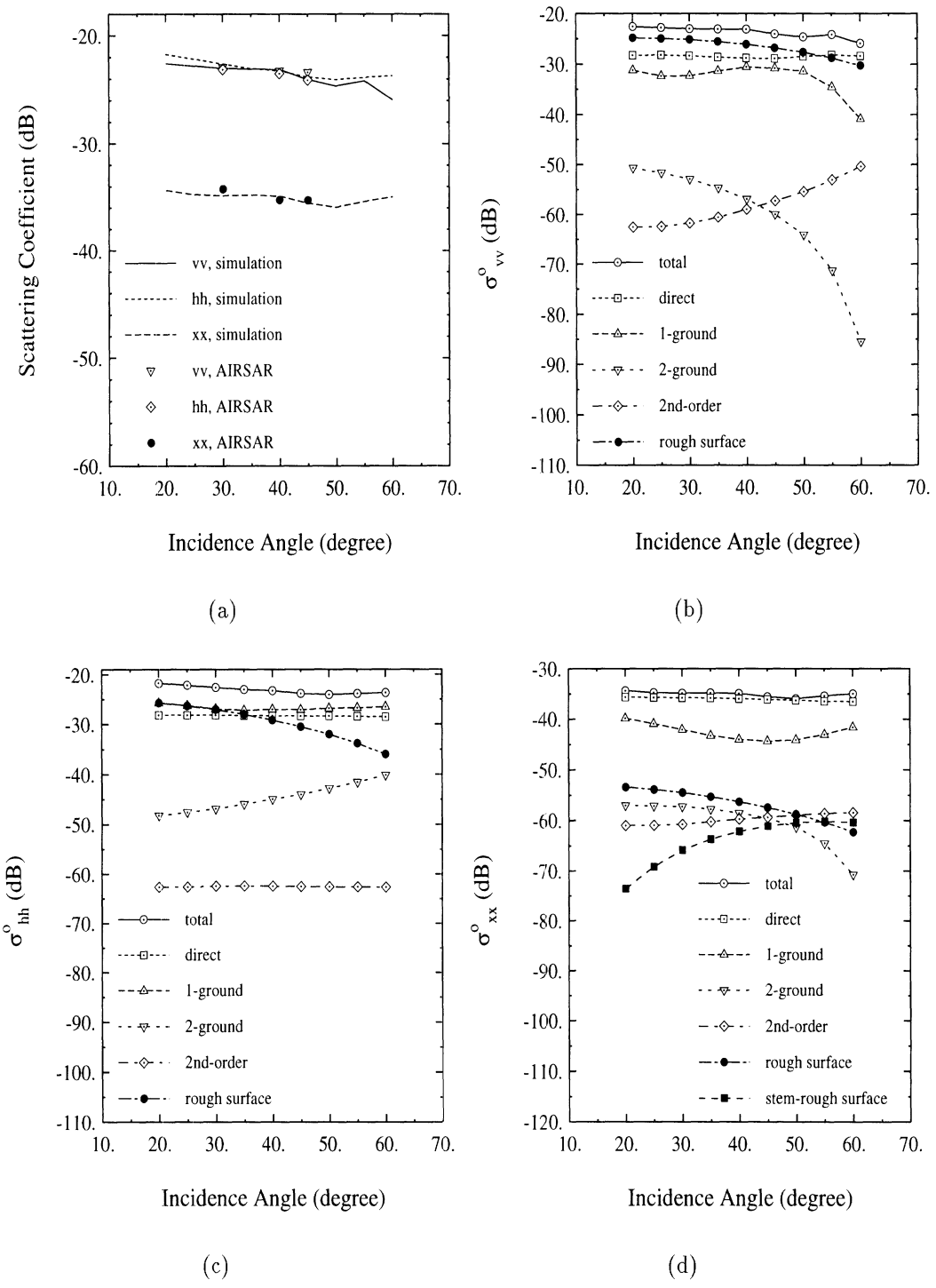

Figure 5.13: Scattering coefficients versus incidence angle at L-band for AIRSAR data set: (a) model validation, and (b)(c)(d) scattering mechanism analysis for vv-, hh-, and cross-polarizations, respectively.

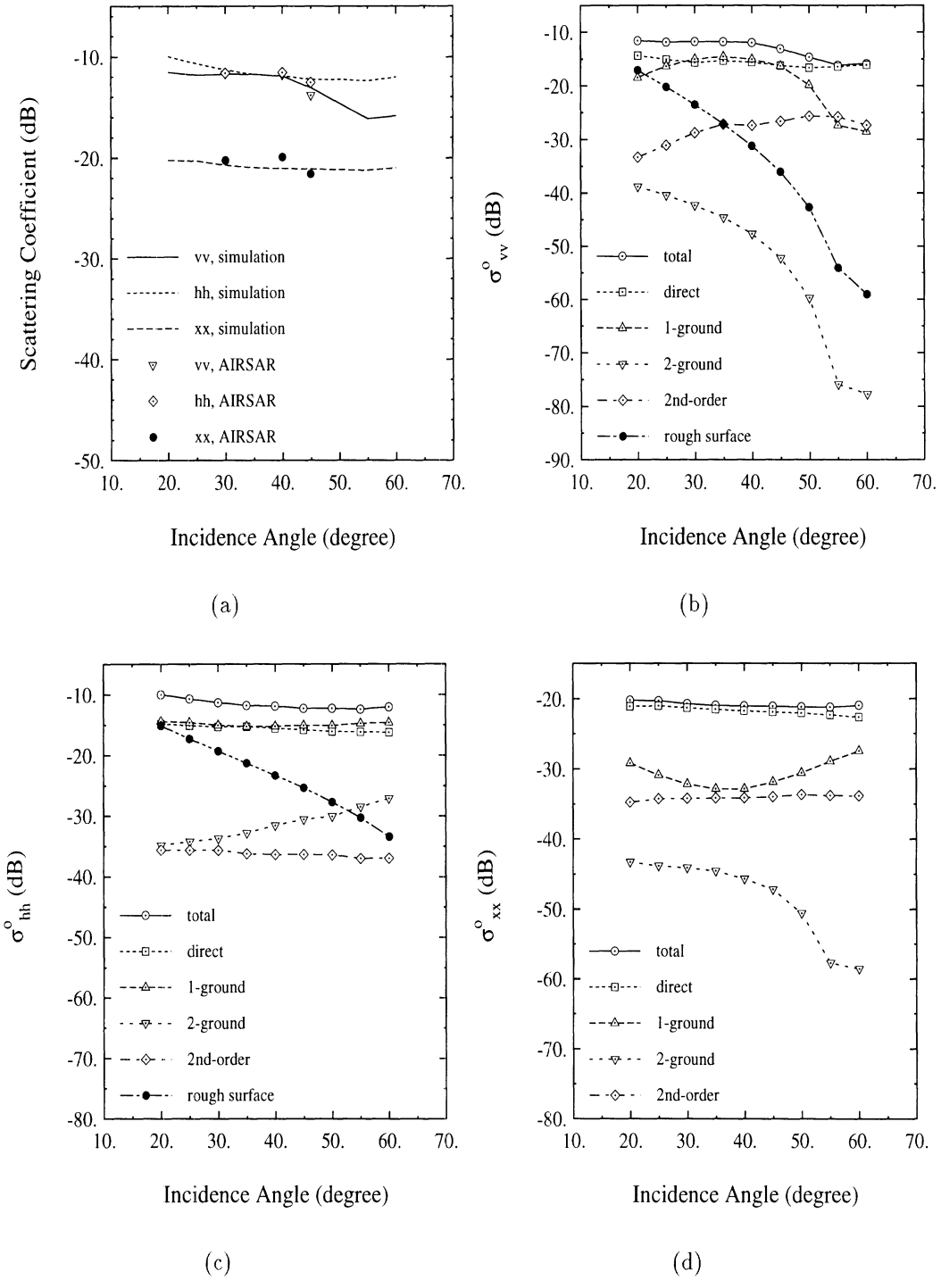

Figure 5.14: Scattering coefficients versus incidence angle at C-band for AIRSAR data set: (a) model validation, and (b)(c)(d) scattering mechanism analysis for vv-, hh-, and cross-polarizations, respectively.

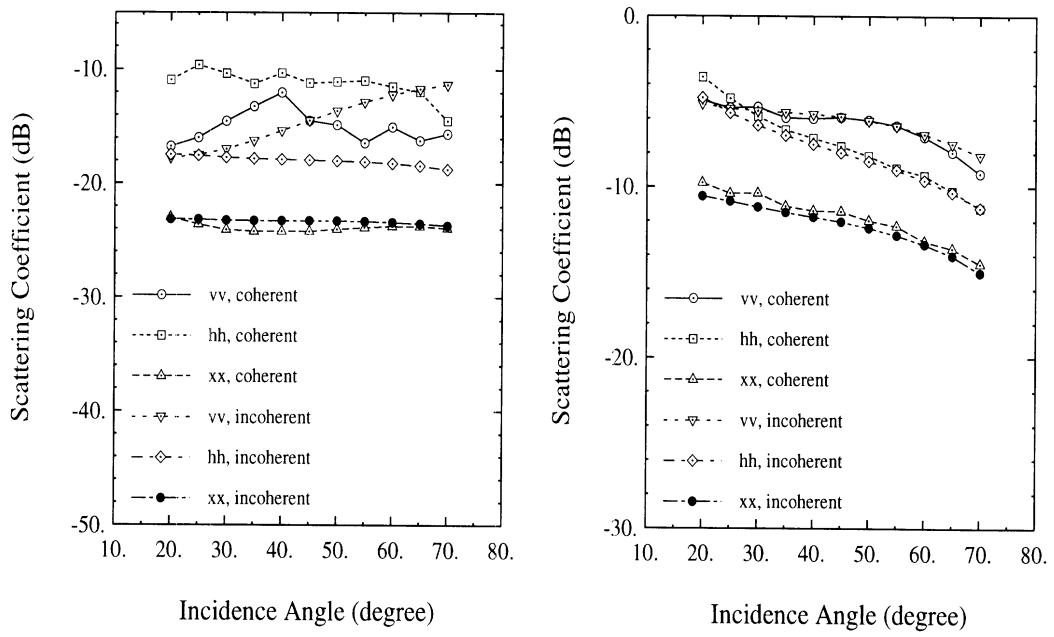

Figure 5.15: Demonstration of the coherence effect caused by the soybean plant structure for a fully grown soybean field at (a) L-band and (b) C-band.

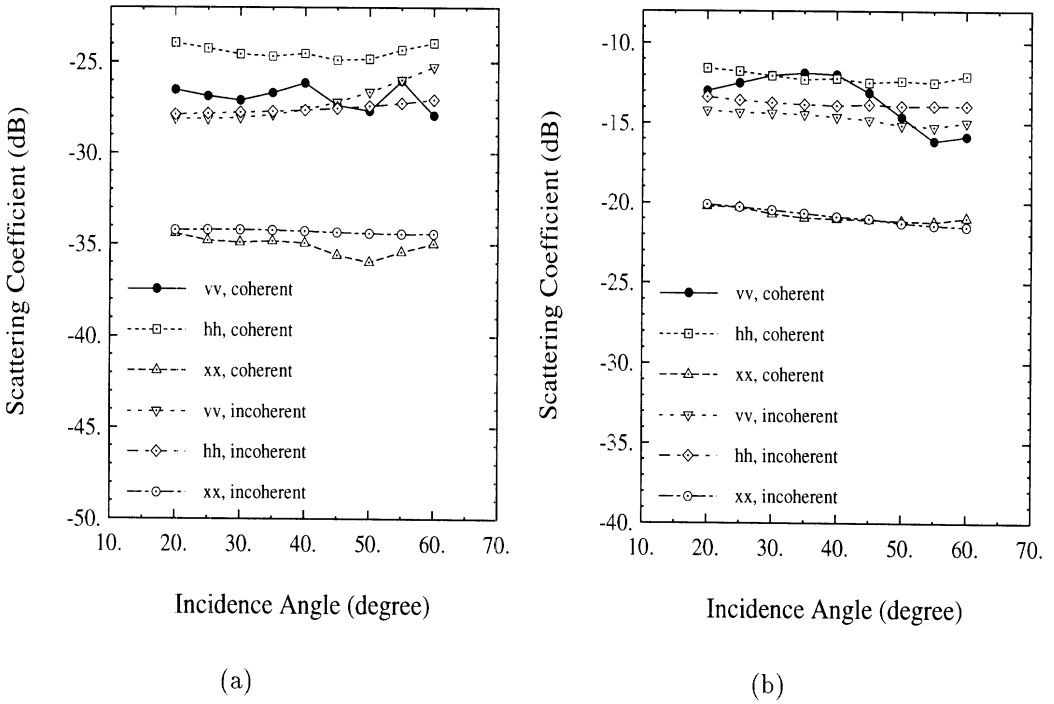

Figure 5.16: Demonstration of the coherence effect caused by the soybean plant structure for a young soybean field at (a) L-band and (b) C-band.

CHAPTER VI

OPTIMUM CORNER REFLECTORS FOR CALIBRATION OF IMAGING RADARS

6.1 Introduction

Quantitative interpretation of images acquired by synthetic aperture radars requires an external calibration procedure. Generally, in calibration procedures the radar return from individual pixels in the image is compared with that of a pixel including the calibration target with known scattering matrix [44,71]. The success of an external calibration procedure is directly influenced by five counteracting characteristics of the calibration target. These include: (1) large radar cross section (RCS), (2) wide RCS pattern, (3) small physical size, (4) stable RCS, and (5) insensitive RCS to the surrounding environment. Noting that the calibration targets are deployed over a surface with a non-zero radar backscatter, it is required that the RCS of the target be much larger than the direct backscatter of the terrain and also that the coherent interaction of the target and the terrain be as small as possible. The wide RCS pattern or insensitivity of target alignment to the radar coordinate and the small physical size requirements are needed to assure the ease of target deployment under the field conditions.

From the observation of the measurement results, it has been found that, es-

pecially at low frequencies, the radar backscatter is sensitive to the soil-moisture variation of the ground covered with short vegetation. While this indicates a direction to achieve the soil-moisture retrieval of such ground surfaces, a potential problem arises in the radar calibration. Trihedral corner reflectors have long been used as radar reflectors and calibration targets [57]. With the advances in the imaging radar technology and the need for quantitative data, trihedral corner reflectors, having most of the above mentioned characteristics, are being widely used as a calibration target for imaging radars [56,71]. However, at low frequencies such as P- and L-band the physical size of the panels for the required RCS becomes prohibitively large. In these cases the trihedral structure is susceptible to geometrical deformation which would cause a departure from the theoretical RCS of the target. In a recent cross-calibration study using the JPL AIRSAR and the University of Michigan polarimetric scatterometers it was shown that the coherent and incoherent interaction of the ground surface with a trihedral corner reflector can distort the expected scattering matrix of the target significantly [50]. The uncertainties in the RCS and the scattering matrix of the trihedrals exceed the maximum tolerable errors required for most remote sensing science applications.

Traditionally, the choice of panel geometry for corner reflectors has been a triangular shape due, perhaps, to the simplicity in the structural design and manufacturing. In this chapter, an optimum panel geometry for a corner reflector is sought so that the RCS of the reflector is least affected by the coherent ground interaction and its RCS is maximized for a given panel area while minimizing the edge length. As will be shown later, the first two conditions are met if the panels of the corner reflector are completely illuminated after two reflections of the incoming wave from the other panels. A general procedure for characterizing the panel geometry of a

self-illuminating corner reflector is outlined and it is shown that the surface area of such corner reflector is 2/3 of the surface area of a trihedral corner reflector having identical RCS at boresight illumination. Then the geometry of an optimum reflector which has the shortest edge length among the self-illuminating polygonal corner reflectors is obtained. Two simple self-illuminating reflectors, namely, the square and pentagonal corner reflectors are considered in this chapter. Analytical solutions for backscatter cross section of these corner reflectors are derived and compared with the backscatter measurements.

The chapter is organized as follows: first, the theoretical analyses for the radar cross section based on the geometrical optics (GO) and a near-field physical optics (PO) approximation are given; then, experimental results for a pentagonal corner reflector and a square corner reflector at X-band are presented and compared with those obtained from their triangular corner reflector counterpart. Also, the measured backscatter from the pentagonal and triangular corner reflectors in the presence of a smooth perfectly conducting and lossy dielectric ground planes are presented. It is also shown that the scattering matrix and the RCS of self-illuminating corner reflectors are less affected by the ground plane.

6.2 Theoretical Analysis

6.2.1 RCS Calculation

In this section a brief discussion of the evaluation of RCS for a corner reflector with arbitrary panel geometry based on the GO and a near-field PO approximations is given. Here the region of interest for calculation of the RCS is confined to the first quadrant containing the corner reflector's boresight. The literature concerning calculation of RCS pattern of corner reflectors is limited to the GO solution for triangular

and square corner reflectors over a limited region around their boresight [57]- [34]. In addition, the GO solution for the RCS pattern of square corner reflectors is reported incorrectly [37]. Analytical expressions for the RCS pattern of triangular, square, and pentagonal corner reflectors based on the GO approximation are derived in this section. These results are valid over a wide range of incidence angles. More accurate approximate solutions such as geometrical theory of diffraction (GTD), uniform theory of diffraction (UTD), or physical theory of diffraction (PTD) have been applied to dihedral corner reflectors [13, 20]. Although the application of UTD or PTD to simple geometries is rather simple, for concave scatterers such as trihedral corner reflectors the analysis becomes very complex. The difficulty is in the computation of the diffracted wave contributions that enter the corner reflector cavity. In addition, for the problem at hand where the RCS is required only around the boresight and the dimensions of the panels are much larger than the wavelength, the contribution from the edge diffraction can be ignored. It should also be noted that exact numerical solutions, such as the finite element method and the method of moments, for most practical corner reflectors (typical dimension $> 10\lambda$) are not tractable.

Considering a right-angle corner reflector it can easily be shown that for any incident ray entering the corner reflector cavity, after triple reflection, there exists a specular point in the backscatter direction and therefore the GO solution can be used for the RCS calculations. To outline a procedure for the RCS calculation using the GO method, consider a corner reflector with arbitrary panel geometry whose internal edges form the axes of a Cartesian coordinate system (x, y, z) as shown in Fig. 6.1(a). Let us denote the panels in the $x-y$, $y-z$, and $z-x$ planes, respectively, by panels #1, #2, and #3. In order to compute the backscatter contribution from each panel, the illuminated area on each panel must be calculated. Panel #1 is illuminated

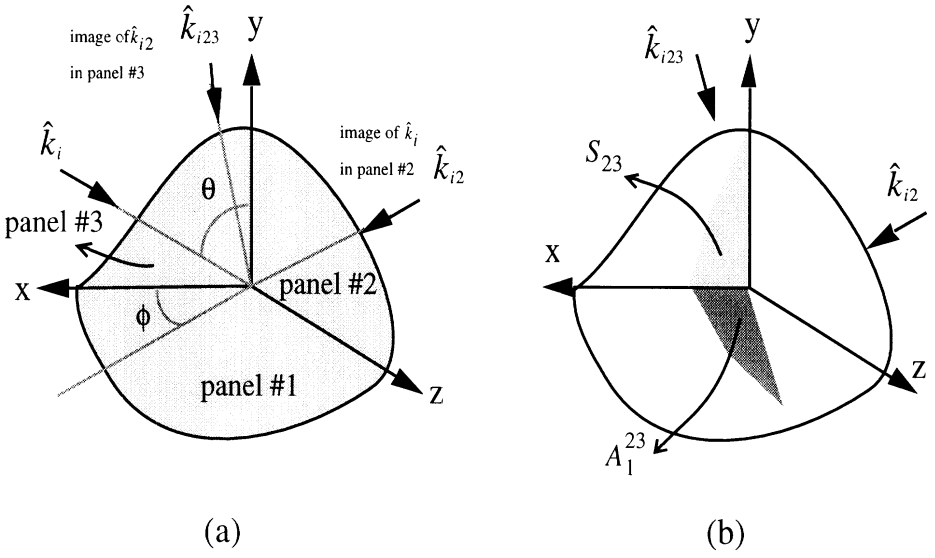

Figure 6.1: A corner reflector with arbitrary panel geometry illuminated by a plane wave (a). The lit area on panel #1 after two reflections of the incident wave from panel #2 and then panel #1 (b).

by two plane waves resulting from double reflections of the incident wave from (1) panel #2 then panel #3, and (2) panel #3 then panel #2. The propagation unit vector of the image of the incident wave in panel #2 and its image in panel #3 are, respectively, given by

$$\begin{aligned} \hat{k}_{i2} &= \hat{k}_i - 2(\hat{x} \cdot \hat{k}_i)\hat{x} \ , \\ \hat{k}_{i23} &= -\hat{k}_i + 2(\hat{z} \cdot \hat{k}_i)\hat{z} \ , \end{aligned}$$

where

$$\hat{k}_i = -\sin\theta\cos\phi\hat{x} - \sin\theta\sin\phi\hat{y} - \cos\theta\hat{z} \ .$$

If panels #2 and #3 were infinite in extent, panel #1 would be entirely illuminated. However, both panel #2 and panel #3 are finite and therefore only a portion of panel #1 is illuminated. In this case, panel #2 can be viewed as a window for the image wave $\hat{k}_{i2}$ which illuminates panel #3 partially as shown in Fig. 6.1(b) (indicated by

S_{23}). Similarly, the area S_{23} on panel #3 can be regarded as a window for the image wave $\hat{k}_{i23}$ that partially illuminates panel #1. The area of this region is denoted by A_1^{23}. In a similar manner, the area on panel #1 illuminated by the second image wave ($\hat{k}_{i32}$) can be obtained and is denoted by A_1^{32}. It should be noted that these illuminated areas on the $x-y$ plane may exceed the geometrical extent of panel #1. In such cases A_1^{23} and A_1^{32} are the areas of the intersection of the illuminated regions and panel #1. The two image waves that illuminate panel #1 are parallel ($\hat{k}_{i23} = \hat{k}_{i32}$), in-phase, and co-polarized. The expression representing the image wave is found to be

$$\boldsymbol{E}_{im} = [-\boldsymbol{E}_0 + 2(\hat{z} \cdot \boldsymbol{E}_0)\hat{z}]e^{ik_0 \hat{k}_{i23} \cdot \boldsymbol{r}} ,$$

which can be used to find the backscatter from panel #1. The following expression for the scattered field from panel #1 can be obtained [55] as follows:

$$\boldsymbol{E}_{s1} = \frac{iA_1}{\lambda_0} \cos\theta \boldsymbol{E}_0, \tag{6.1}$$

where $A_1 = A_1^{23} + A_1^{32}$. This process must be repeated to find the backscatter contribution of panel #2 ($\boldsymbol{E}_{s2}$) and panel #3 ($\boldsymbol{E}_{s3}$) from which the overall RCS can be computed from

$$\sigma = 4\pi |\sum_{j=1}^{3} \boldsymbol{E}_{sj}|^2. \tag{6.2}$$

The GO solution for estimation of the RCS is simple and widely used, but its accuracy degrades when a typical dimension of the scatterer becomes comparable with the wavelength. A more accurate estimation of RCS can be obtained using the PO solution. However, the PO solution for flat plates cannot be used directly for corner reflectors. The difficulty is in the calculation of the PO currents generated by the reflected fields. The panels are in the near-field region of each other and the

reflected fields can no longer be assumed to be plane waves. In this case, the PO current on panel #2 induced by the primary PO current on panel #1 ($\boldsymbol{J}_1$) must be computed from

$$\boldsymbol{J}_{12} = 2\hat{x} \times \boldsymbol{H}^s_{12} \, ,$$

where

$$\boldsymbol{H}^s_{12} = \int \boldsymbol{J}_1(\boldsymbol{r}') \nabla \times \overline{\overline{\boldsymbol{G}}}(\boldsymbol{r}, \boldsymbol{r}') d\boldsymbol{r}'. \tag{6.3}$$

From [59] we note that

$$\nabla \times \overline{\overline{\boldsymbol{G}}}(\boldsymbol{r}, r') = (ik_0 - \frac{1}{|\boldsymbol{r} - \boldsymbol{r}'|}) \frac{e^{ik_0|\boldsymbol{r}-\boldsymbol{r}'|}}{4\pi|\boldsymbol{r} - \boldsymbol{r}'|^2} (\boldsymbol{r} - \boldsymbol{r}') \times \overline{\overline{\boldsymbol{I}}} \, .$$

Therefore, (6.3) can be reduced to

$$\boldsymbol{H}^s_{12} = \int (\boldsymbol{r} - \boldsymbol{r}') \times \boldsymbol{J}_1(r') (ik_0 - \frac{1}{|\boldsymbol{r} - \boldsymbol{r}'|}) \frac{e^{ik_0|\boldsymbol{r}-\boldsymbol{r}'|}}{4\pi|\boldsymbol{r} - \boldsymbol{r}'|^2} d\boldsymbol{r}'. \tag{6.4}$$

Finally in order to find the induced current on panel #3 ($\boldsymbol{J}_{123}$), $\boldsymbol{J}_{12}$ must be used in an integral similar to (6.4). Unfortunately a closed form expression for (6.4) cannot be obtained and costly numerical integrations must be performed. In order to find the scattered field a six-folded integration is required which makes the RCS evaluation numerically very inefficient. To make the RCS evaluation more efficient, without compromising the accuracy too much, a hybrid GO-PO solution is considered [13]. In this approach, for the first reflection the GO solution is used and for the two following reflections the PO solution is used. This method will be referred to as the GO-PO-PO solution. The GO-PO-PO solution requires a four-fold numerical integration, and its validity can be justified by noting that the majority of the reflection points on the third panel are far enough from the reflection points on the first panel for the GO solution to be used for the first reflection. It should be mentioned here that the

RCS calculation for corner reflectors based on a GO-GO-PO method is not, in any significant way, different from the GO solution and therefore it is not pursued in this chapter.

6.2.2 Triangular Corner Reflector

The radar cross section of triangular corner reflectors has been characterized and studied thoroughly [30,35,37]. Backscatter RCS measurements indicate that the GO solution can accurately predict the RCS of triangular corner reflectors near boresight. An approximate expression for the backscatter RCS of triangular corner reflectors based on the GO solution is given by [37]

$$\begin{aligned}\sigma(\theta,\phi) \approx & \frac{4\pi}{\lambda^2}\cdot l^4\cdot[\cos\theta+\sin\theta(\sin\phi+\cos\phi)\\ & -2\cdot[\cos\theta+\sin\theta(\sin\phi+\cos\phi)]^{-1}]^2,\end{aligned} \tag{6.5}$$

where l is the trihedral height as shown in Fig. 6.2. This approximation is valid when $l >> \lambda$ and θ and ϕ are near boresight. A more accurate GO solution which is valid over a wide range of θ and ϕ is given in Appendix D.1. To examine whether the GO-PO-PO method produces a more accurate RCS estimation or not, the RCS pattern of a triangular corner reflector with $l = 10\lambda$ at 9.5 GHz was measured and compared with the GO and GO-PO-PO solutions. Figures 6.2(a) and 6.2(b) show the horizontal and elevation RCS patterns of the trihedral as measured by a polarimetric radar and predicted by the GO and GO-PO-PO methods. It should be noted that the elevation pattern is defined as the $\phi = 45°$ plane and the elevation angle is $54.73 - \theta$. In practice the elevation pattern can be measured easily. However, this is not the case for the azimuth pattern where $\theta = 54.73$ must be kept constant (conical surface). Instead the pattern in the horizontal plane is measured. The horizontal plane is defined as the plane which contains the trihedral boresight and is parallel to

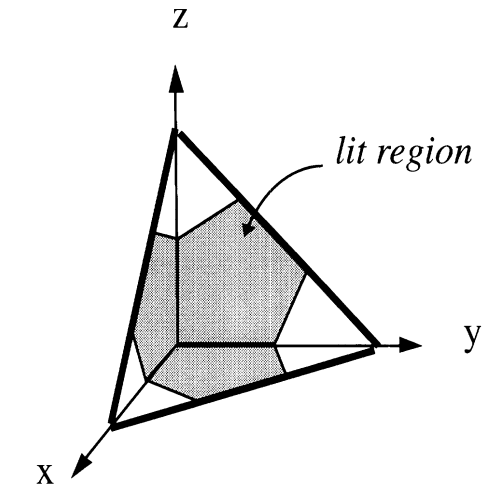

(a)

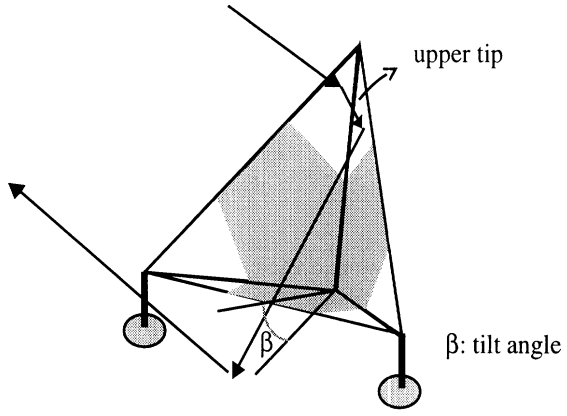

(b)

Figure 6.2: The geometry of lit region on a triangular corner reflector (a), and the interaction of a triangular corner reflector with the ground plane (b).

the lower panel edge. If the incident direction in the horizontal plane as measured from the boresight direction is denoted by α, then

$$\begin{aligned} \phi &= \tan^{-1}\left[\frac{\sqrt{2}\cos\alpha + \sqrt{3}\sin\alpha}{\sqrt{2}\cos\alpha - \sqrt{3}\sin\alpha}\right], \\ \theta &= \cos^{-1}\left[\frac{\cos\alpha}{\sqrt{3}}\right]. \end{aligned}$$

Figures 6.3(a) and 6.3(b) show that the GO and GO-PO-PO solutions agree very well with the measured data and hence the GO solution is accurate enough in this

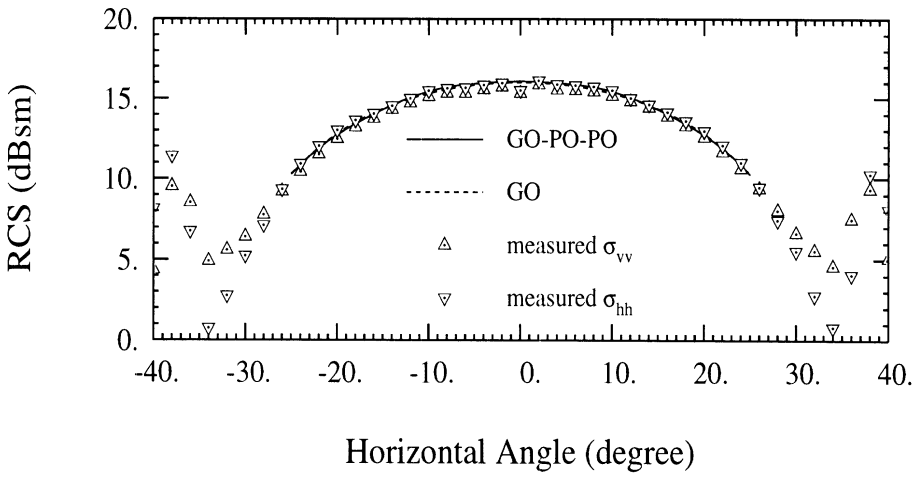

(a)

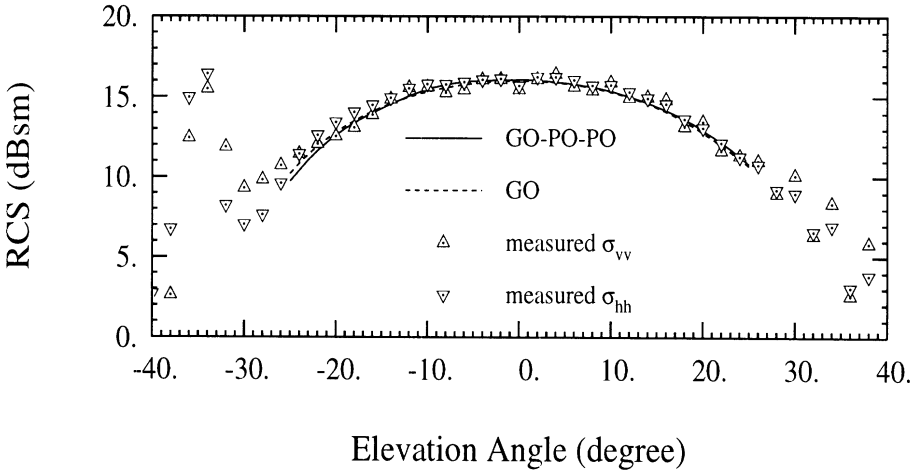

(b)

Figure 6.3: RCS patterns of a triangular corner reflector as a function of horizontal (a) and elevation angles (b). $l = 10\lambda$ at 9.5 GHz.

case. The small ripple in the measured data is caused by the direct backscatter contribution of single and double bounce reflections which are not included in our GO and GO-PO-PO solutions.

6.2.3 Pentagonal and Square Corner Reflectors

For a triangular corner reflector, at boresight incidence, only a portion of each panel is illuminated, as shown in Fig. 6.2(a). Appendix D.1 gives the expressions for the area of the lit regions as a function of incidence angle for a triangular corner reflector. In characterization of the lit regions for a triangular corner reflector it is noticed that at boresight incidence ($\phi = 45°, \quad \theta = 54.7°$) where the RCS is maximized, only two-thirds of the area on each panel is lit and gives rise to the maximum RCS ($\sigma = 4\pi l^4/3\lambda^2$). The geometry of the lit area on each panel is a pentagon, as shown in Fig. 6.2. This fact has been known for a long time [20, 35], but no formal analysis or discussion of the performance of a corner reflector with pentagonal panel geometry can be found. One obvious advantage of a corner reflector with pentagonal panels, which will be referred to as a pentagonal corner reflector, is the reduction in the surface area (weight) by 1/3 without reducing the maximum RCS. An important feature of a corner reflector, when considered as a calibration target for imaging radars, is its interaction with the ground plane. Since the reflected rays from the tips of the trihedral corner reflectors are not captured by the other panels, they may interact with the scatterers on the ground plane and give rise to some unknown backscatter contribution (see Fig. 6.2(b)). For high angles of incidence where the lower panel is almost parallel with the ground plane, the specular reflection from the ground plane illuminates the upper tip of the corner reflector which again can increase its RCS. For the pentagonal corner reflector, on the other

hand, all the rays that enter the reflector's cavity experience the triple reflection and return to the radar. Therefore, its interaction with the ground plane is expected to be minimal. It can be shown that a corner reflector with square panel geometry has the same property (self-illuminating).

The RCS pattern for these reflectors can be obtained using the GO method in a straightforward manner. Analytical expressions for the RCS of the square and pentagonal corner reflectors are given in Appendices D.2 and D.3 respectively. Although square corner reflectors have long been used, their maximum RCS and their RCS patterns have been reported incorrectly. For example, the expression for the RCS pattern reported by Ruck et. al. [37] is incorrect. In this section the GO-PO-PO method is also used in the RCS calculation. It will be shown that the GO method cannot accurately predict the RCS of a self-illuminating corner reflector at boresight unless the dimensions of the corner reflector are extremely large compared to the wavelength. Figures 6.4 and 6.5 show, respectively, the RCS patterns of square and pentagonal corner reflectors, each having a panel area of $100\lambda^2/3$ at 9.5 GHz. In these figures, both the GO and GO-PO-PO predictions are shown. It is also shown that the GO solution is overestimating the RCS at boresight and the derivative of the RCS pattern is discontinuous there. The discontinuity of the slope of the RCS pattern (non-physical) stems from the fact that the illuminated area abruptly changes away from the boresight illumination. The numerical GO-PO-PO solution which includes the near-field effects predicts the accurate results as will be shown in section 3. To make the simple GO solution for self-illuminating corner reflectors useful, the difference between the RCS calculations as predicted by the GO and GO-PO-PO methods is plotted in Fig. 6.6 as a function of normalized dimension $\sqrt{A}/\lambda$. Figure 6.6 shows that the discrepancy between the GO and GO-PO-PO prediction decreases

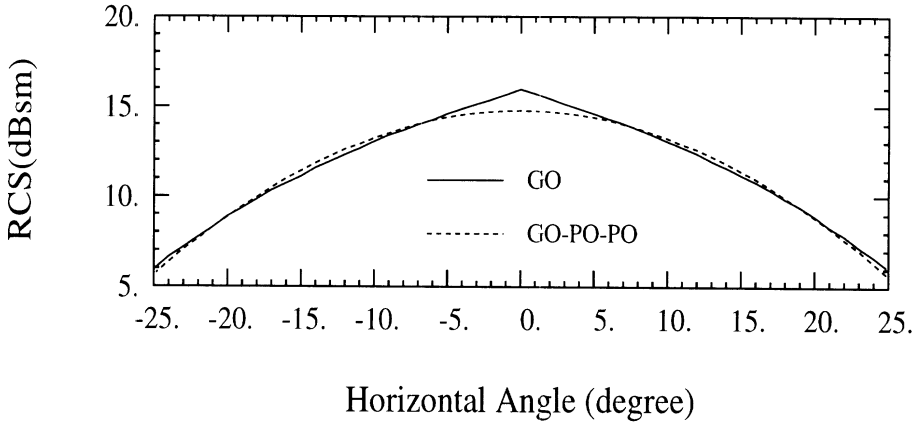

(a)

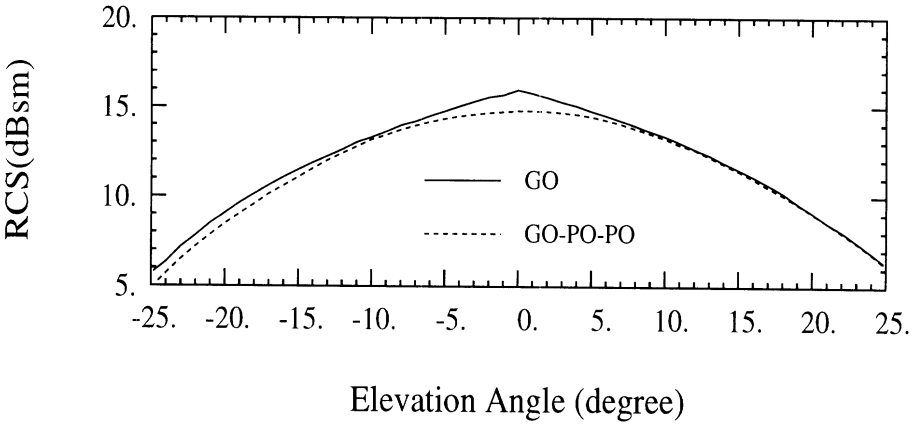

(b)

Figure 6.4: RCS patterns of a square corner reflector as a function of horizontal (a) and elevation angles (b). Panel area is $100\lambda^2/3$ at 9.5 GHz.

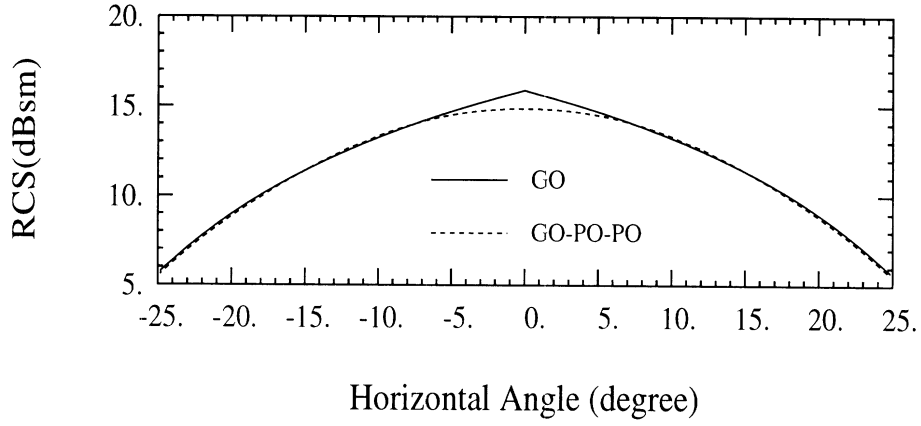

(a)

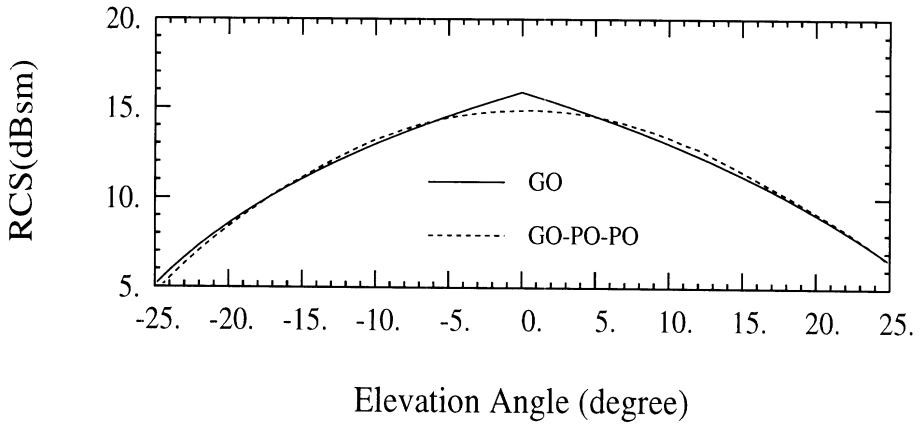

(b)

Figure 6.5: RCS patterns of a pentagonal corner reflector as a function of horizontal (a) and elevation angles (b). Panel area is $100\lambda^2/3$ at 9.5 GHz.

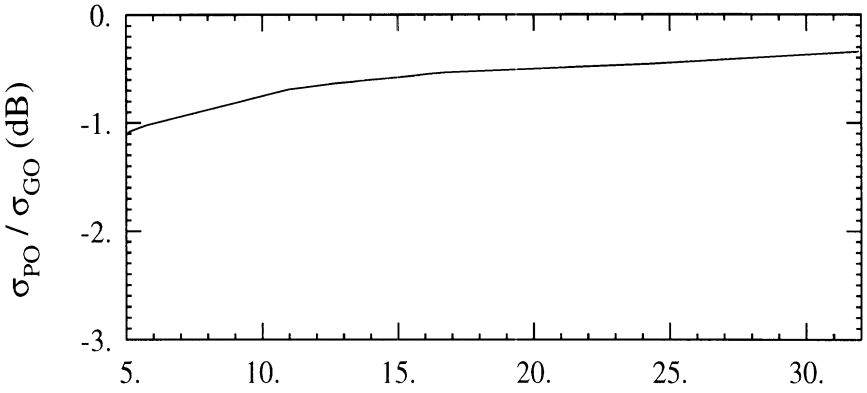

Figure 6.6: The ratio of RCS predictions using the GO-PO-PO and GO methods for self-illuminating corner reflectors (square and pentagonal) at boresight illumination.

as $\sqrt{A}/\lambda$ increases.

6.2.4 The Self-illuminating Corner Reflectors

In the previous section, it was shown that every point on the surface of a pentagonal corner reflector contributes to the RCS at boresight. Using the area of the lit region ($A_p = l^2/3$) in (5), the maximum RCS of a pentagonal corner reflector can be obtained from

$$\sigma^p_{MAX} = 12\pi \cdot \left(\frac{A_p}{\lambda}\right)^2.$$

However, the maximum RCS for a triangular corner reflector in terms of its panel area, A_t, is

$$\sigma^t_{MAX} = \frac{16\pi}{3} \cdot \left(\frac{A_t}{\lambda}\right)^2$$

which is smaller than that of a pentagonal corner reflector having the same panel area by a factor of 4/9 (-3.5 dB). It was also shown that the lit region (at boresight) after two reflections has exactly the same geometry as that of the panel (self-illuminated)

and therefore reflected rays from the ground plane are not captured by the corner reflector cavity. In this section we seek a class of geometries for the panels of corner reflectors that are self-illuminating at boresight incidence. For these reflectors, every point on the panels will contribute to the backscatter and a maximum RCS of $\sigma_{MAX} = 12\pi \cdot (A_p/\lambda)^2$ is achievable independent of panel geometry.

It is required that each panel be illuminated completely at boresight. The self-illuminating requirement imposes a symmetry condition on the acceptable geometries for the panels. That is, the three panels of the corner reflector have to be identical so that the corner reflector becomes self-illuminating at boresight. Suppose the internal edges of a self-illuminating corner reflector coincide with the axes of a Cartesian coordinate system (x, y, z). Let us also denote the tip of each edge along the $z-$, $x-$ and $y-$axis by A, B and C respectively as shown in Fig. 6.7. The incident wave at boresight propagates along

$$\hat{k}_i = -\frac{1}{\sqrt{3}} \cdot \hat{x} - \frac{1}{\sqrt{3}} \cdot \hat{y} - \frac{1}{\sqrt{3}} \cdot \hat{z}.$$

After two reflections, it can be shown that points A, B and C are imaged on the $x-y$, $y-z$ and $x-z$ planes which are denoted by A', B' and C' respectively. Representing the internal edge length of the corner reflector by l, the coordinates of A', B' and C' are given by $(l, l, 0)$, $(0, l, l)$ and $(l, 0, l)$ respectively. It can also be shown that the region $z \geq y$ in the $y-z$ plane is imaged (after the first reflection) on the first quadrant of the $x-z$ plane which in turn is imaged (after the second reflection) on the region $x \geq y$ in the $x-y$ plane. Suppose that the boundary of the self-illuminating corner reflector between points A and B' is specified by a curve denoted by $\mathcal{C}$. Considering the symmetry properties of the panel geometry, a similar curve specifies the boundary between points C and B' (mirror image with respect

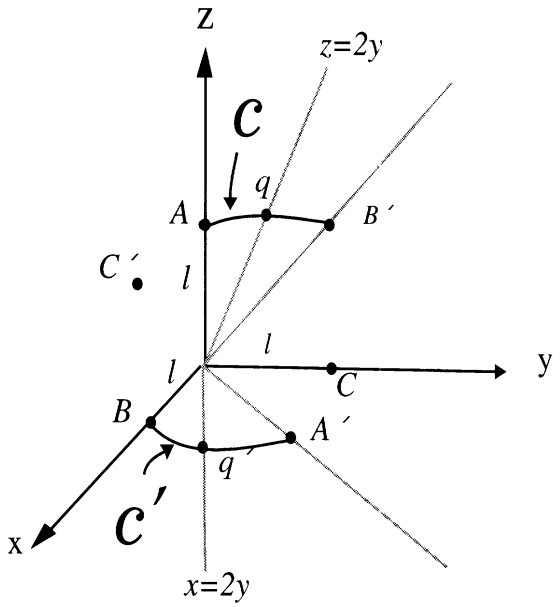

(a)

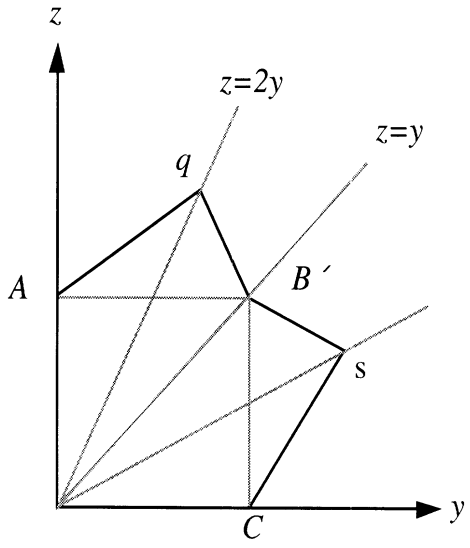

(b)

Figure 6.7: Mapping of a general curve $\mathcal{C}$ from $y-z$ plane to $x-y$ plane after two reflections (a), and the panel geometry of a general self-illuminating hexagonal corner reflector (b).

to $z = y$ plane). Therefore, characterization of curve $\mathcal{C}$ would completely specify the geometry of the self-illuminating corner reflector. Assume curve $\mathcal{C}$ is represented by a parametric equation

$$\mathcal{C}(\tau) = (0, f(\tau), g(\tau)), \quad \tau \in [0, t],$$

where the following constraints $f(0) = 0$, $f(t) = l$, $g(0) = l$ and $g(t) = l$ are imposed to ensure that $\mathcal{C}$ would pass through A and B'.

After two reflections, a point p on $\mathcal{C}$ is mapped to p' on the $x - y$ plane whose coordinates in terms of p are given by

$$\begin{aligned} x_{p'} &= z_p , \\ y_{p'} &= z_p - y_p. \end{aligned} \tag{6.6}$$

The mapping is a linear transformation which is one-to-one and onto. This transformation maps $\mathcal{C}(\tau)$ to a plane curve $\mathcal{C}'(\tau)$ on $x - y$ plane given by

$$\mathcal{C}'(\tau) = (g(\tau), g(\tau) - f(\tau), 0), \quad \tau \in [0, t].$$

As τ goes from 0 to t, $\mathcal{C}$ and $\mathcal{C}'$ trace from A to B' and A' to B respectively. Noting that the mapped curve in the $x - y$ plane must be identical to the curve in the $y - z$ plane, there is a parameter $t = t_o$ corresponding to points q and q', so that

$$\begin{aligned} x_{q'} &= z_q , \\ y_{q'} &= y_q. \end{aligned} \tag{6.7}$$

Using (6.7) in (6.6), it can be shown that

$$z_q = 2y_q , \quad x_{q'} = 2y_{q'} .$$

That is, the similar points q and q' on lines $z = 2y$ (in $y - z$ plane) and $x = 2y$ (in $x - y$ plane) are reached at the same time. This fact suggests the following procedure

for the construction of $\mathcal{C}(\tau)$. Consider an arbitrary point q on the line $z = 2y$ and an arbitrary curve $\mathcal{C}_1(\tau) = (0, f_1(\tau), g_1(\tau))$ between points A and q. This curve is mapped in the $x - y$ plane to

$$\mathcal{C}_1'(\tau) = (g_1(\tau), g_1(\tau) - f_1(\tau), 0)\,, \quad \tau \in [0, t],$$

which spans A' to q'. Since the curve between B' and q ($\mathcal{C}_2$) must be identical to the curve between A' and q' ($\mathcal{C}_1'$), then

$$\mathcal{C}_2(\tau) = (0, g_1(\tau), g_1(\tau) - f_1(\tau))\,, \quad \tau \in [0, t].$$

The combination of $\mathcal{C}_1$ and $\mathcal{C}_2$ uniquely specifies the continuous curve $\mathcal{C}$. It can easily be shown that $\mathcal{C}_2$ is mapped to

$$\mathcal{C}_2'(\tau) = (g_1(\tau), f_1(\tau), 0)\,, \quad \tau \in [0, t].$$

which is identical to $\mathcal{C}_1$ as expected.

Referring to equations (6.1) and (6.2), it can easily be shown that the RCS of all self-illuminating corner reflectors at boresight can be obtained from

$$\sigma_{MAX} = 12\pi \cdot \left(\frac{A}{\lambda}\right)^2, \tag{6.8}$$

where A is the surface area of a panel. An expression for the surface area in terms of the parametric equation of $\mathcal{C}_1$ can be obtained easily and is given by

$$A = 2 \cdot \int_0^t (f_1' g_1 - g_1' f_1)\, d\tau. \tag{6.9}$$

The geometrical optics expression for RCS given by (6.8) is valid when all dimensions of the panel are very large compared to the wavelength. As the wavelength increases, contributions from higher order scattering mechanisms, such as edge diffraction, become comparable to the GO contribution and therefore the accuracy of (6.8) decreases. The contribution from edge diffraction is proportional to the edge length

and therefore it is desirable to minimize the length of the corner reflector edges. Moreover, the edge length minimization would minimize the largest dimension of the reflector. The edge length of a self-illuminating corner reflector can be obtained from

$$L = 2 \cdot \int_0^T \left\{ \sqrt{f'^2_1 + g'^2_1} + \sqrt{(f'_1 - g'_1)^2 + g'^2_1} \right\} d\tau. \tag{6.10}$$

The optimum corner reflector is a self-illuminating corner reflector whose edge length is minimized. That is, for a given RCS, the optimum corner reflector has the smallest surface area and the shortest edge length. Mathematically speaking, $f_1(\tau)$ and $g_1(\tau)$ must be chosen so that they would minimize functional (6.10) subject to constraint (6.9). This problem resembles the isoperimetric problem in the variational calculus except for a boundary condition which is not imposed on $f_1(\tau)$ and $g_1(\tau)$. Therefore, the conditions for the fundamental lemma of the calculus of variations [25] are not met and the solution to the isoperimetric problem cannot be used here. Since no analytical procedure can be formulated for the problem at hand, an iterative solution is considered. First we confine our search to linear functions and obtain an optimum polygonal geometry and use that as an initial guess for the next higher order functions and so on.

The simplest curve that can be chosen for $\mathcal{C}_1$ is a straight line. Under linear transformation, a line segment is mapped into another line segment and therefore the geometry of the panel becomes a general hexagon. This hexagon can easily be generated by choosing an arbitrary point q on $z = 2y$ line, finding its mirror image point with respect to $z = y$ plane (s), and finally connecting points A, q, B', s and C as shown in Fig. 6.5(b). The square and pentagonal corner reflectors are two special cases of the hexagonal self-illuminating corner reflectors. Points $q_s = (0, l/2, l)$ and $q_p = (0, 2l/3, 4l/3)$ generate a square and a pentagonal corner reflector respectively.

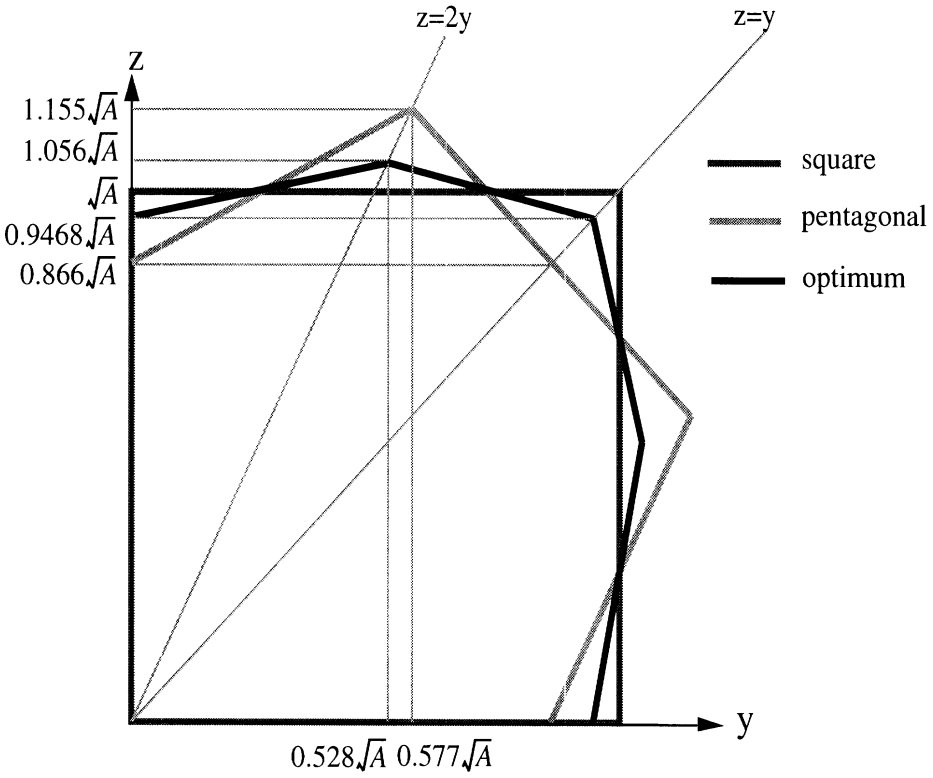

Figure 6.8: The geometry of a square, pentagonal, and optimum hexagonal corner reflector having the same panel area.

Using (6.9) and (6.10) for a linear function and after a tedious algebraic manipulation, the equation of the optimum line describing $\mathcal{C}_1$ is found to be

$$z = 0.2066y + 0.9468\sqrt{A}, \tag{6.11}$$

where as before A is the surface area of the panel. The edge length of the optimum hexagonal corner reflector is found to be $1.944\sqrt{A}$ whereas the edge length of the square and pentagonal corner reflectors are $2\sqrt{A}$ and $2.1\sqrt{A}$ respectively. Figure 6.8 shows the panel geometry of a square, pentagonal, and the optimum hexagonal corner reflectors having the same surface areas. Higher order curves can be obtained by perturbing (6.11) which would result in a very complex minimization problem and is not pursued here. The RCS patterns of the square and pentagonal corner reflectors, as shown in Figures 6.4 and 6.5, are very similar and therefore it is expected that the RCS pattern of the optimum corner reflector will be similar to those as well.

6.2.5 Sensitivity to Corner Angle

One last issue of practical importance is the sensitivity of the corner reflector RCS to deviations of corner angles from 90°. It is quite obvious that any manufacturing error in the corner angle will reduce the nominal RCS value of a corner reflector. In fact, from the GO point of view, the scattered rays after the third reflection are not parallel to the incident ray and therefore the RCS predicted by GO for non-perpendicular panels is zero. In reality, the scattered wave from each panel has a finite beamwidth and the PO can be used to predict the RCS. It is reported that the RCS of square corner reflectors are twice as sensitive to errors in the corner angles than that of triangular corner reflectors [57]. In this section, using our GO-PO-PO model, the sensitivity of RCS of triangular and optimal corner reflectors to errors in corner angles is examined.

There is more than one way of distorting the corner angles. In this study we modify the corner angles in a symmetrical fashion, that is, increase or decrease all three corner angles simultaneously by the same amount. We also keep the interior edge length of the corner reflector constant (the same as those of the undistorted ones). Using the GO-PO-PO method, the RCS of a triangular, a pentagonal, and a square corner reflector at boresight are computed as a function of the corner angle. Figure 6.9 shows the RCS of distorted corner reflectors normalized to that of undistorted ones ($A_t = 50\lambda^2$ or $A_p = A_s = 100\lambda^2/3$ at 9.5 GHz) as a function of the corner angle. It is shown that the sensitivity in corner angle errors for all these corner reflectors is almost on the same order. RCS calculation of metallic plates based on PO approximation is accurate in the mainlobe around the specular direction. Therefore, the accuracy of the GO-PO-PO solution in predicting the RCS of corner reflectors as a function of corner angle deviations is limited to small angles (a few degrees from

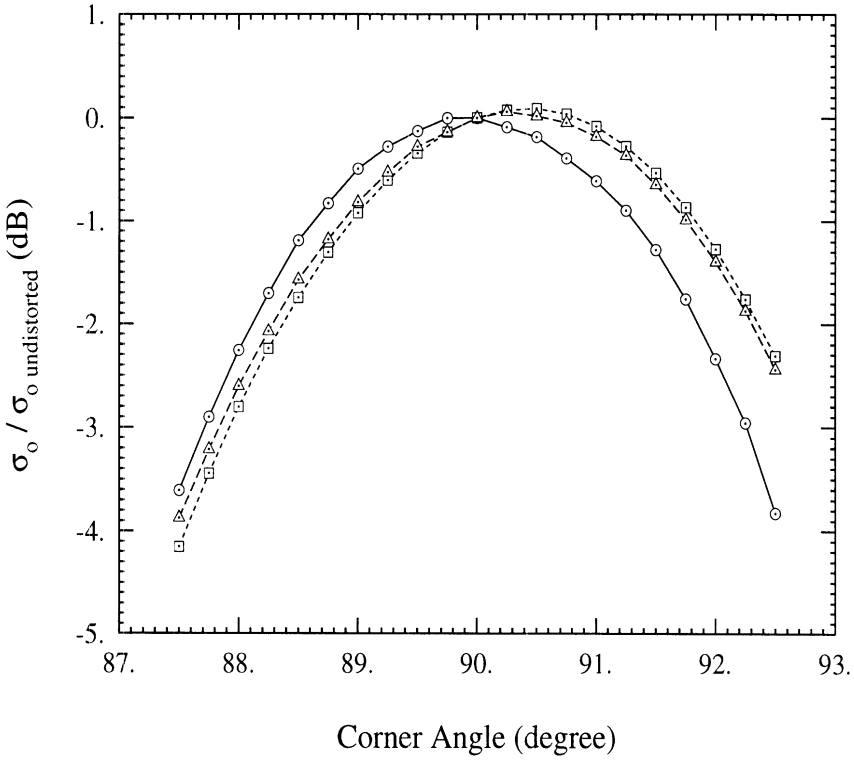

Figure 6.9: RCS of distorted corner reflectors normalized to that of the undistorted ones as a function of corner angle. The backscatters are calculated at 9.5 GHz for reflectors with $A_s = A_p = 100\lambda^2/3$ and $A_t = 50\lambda^2$.

90^0).

6.3 Experimental Results

In this section the measured RCS patterns of a triangular, a pentagonal, and a square corner reflector over a wide range of incidence angles at 9.5 GHz are presented and compared with the GO and GO-PO-PO predications. The corner reflectors are designed to have the same geometrical optics RCS of 15.9 dBsm ($A = 332.4cm^2$). The GO-PO-PO method predicts an RCS of 15.9, 14.8, and 14.7 dBsm for the triangular, square and pentagonal corner reflectors , respectively. Also the effect of a perfectly conducting ground plane on the RCS is demonstrated experimentally.

The backscatter measurements were performed polarimetrically using an HP-8753 network-analyzer-based scatterometer operating in a linear chirped mode. A chirp frequency of 9-10 GHz was used which allowed for a range-gating with a spatial resolution of about 15 cm. The measurements were conducted in a 15-m-long anechoic chamber where the targets were mounted on a Styrofoam pedestal attached to a stepper motor positioner. The effect of the distortion parameters of the radar system, such as the channel imbalances and the antenna cross-talk factors, on the measured scattering matrices were removed using the single target calibration technique (STCT) [42].

Figure 6.2 shows the RCS patterns of the triangular corner reflector in the azimuth and elevation planes. Comparison of the measured co-polarized backscatters (σ_{vv}, σ_{hh}) show an excellent agreement with the GO and GO-PO-PO prediction. The measured results indicate a co- to cross-polarized ratio (σ_{vv}/σ_{hh}) of better than 35 dB over the range of incidence angle $-10° < \alpha < +10°$. Similar agreement was obtained for the elevation pattern ($\phi = 45°$). In the elevation plane the cross-polarized RCS remains very low ($\sigma_{vv}/\sigma_{hh} > 35$ dB) over a much wider angular range ($-30° < \theta < +30°$). The 1-dB RCS beamwidths in the horizontal and elevation planes for a triangular corner reflector were found to be 24°. Figures 6.10 and 6.11 show the measured and estimated polarimetric RCS patterns of the square and the pentagonal corner reflectors, in the horizontal and elevation planes. Similar agreement with the GO-PO-PO method was obtained in these two cases. The measured 1-dB RCS beamwidths in the azimuth and elevation planes for the two self-illuminating corner reflector were found to be around 16°.

Next, the effect of the ground plane on the RCS of corner reflectors is examined. First, backscatter cross sections of these three corner reflectors sitting on a large, flat,

perfectly conducting ground plane, as shown in Fig. 6.4(b), were measured. This configuration corresponds to positioning a corner reflector for a SAR at incidence angle $(54.74° - \beta)$. Figure 6.12 shows the measured RCS of the triangular and pentagonal corner reflectors on the ground plane corresponding to $\beta = 0°$. The measured RCS's are compared with the theoretical RCS predictions of isolated corner reflectors (GO-PO-PO). As mentioned previously the triangular corner reflector can illuminate the ground plane (or receive the reflected ray from the ground plane), hence its RCS is increased whereas the RCS of the self-illuminating reflector is unchanged. For low SAR incidence angles, the lower panel of the reflectors are tilted upward. Figure 6.13 shows, respectively, the measured and theoretical RCS of the the triangular and pentagonal corner reflectors above the ground plane with $\beta = 10°$. At boresight, the triangular corner reflector shows more serious reduction in RCS while the RCS of the self-illuminating corner reflector is less affected. The reason for such a drastic change in the RCS is the backscatter contribution of the wave which is trapped between the lower panel and the ground plane. This fact was verified experimentally. By placing an absorber under the lower panel, the scattering contribution from the ground plane and the lower panel was suppressed. The RCS of the triangular corner reflector is affected more because of its larger panel size.

The perfectly conducting ground plane enhances the effect of the ground plane on the RCS. In practice corner reflectors are placed above a soil surface. Figure 6.14 shows the RCS of the triangular corner reflector and the pentagonal corner reflector above a smooth soil surface with $\beta = 10°$. Again it can be seen that the RCS of the triangular corner is influenced more drastically than that of the pentagonal corner reflector in the presence of the ground plane.

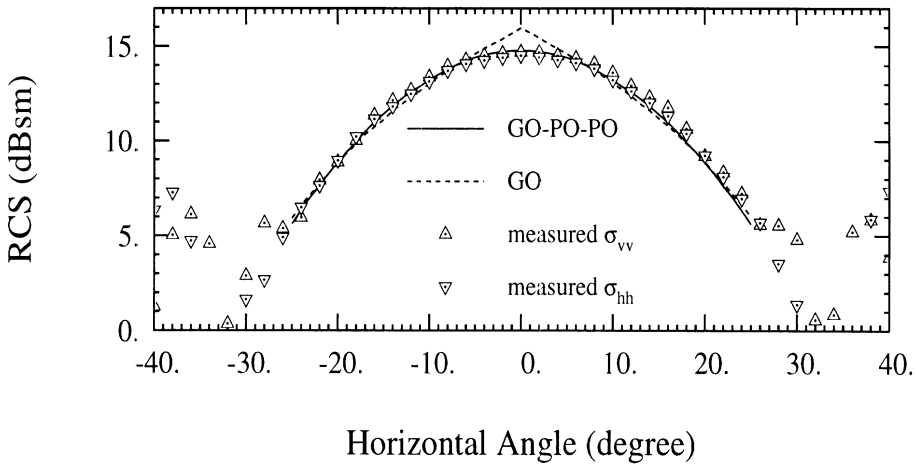

(a)

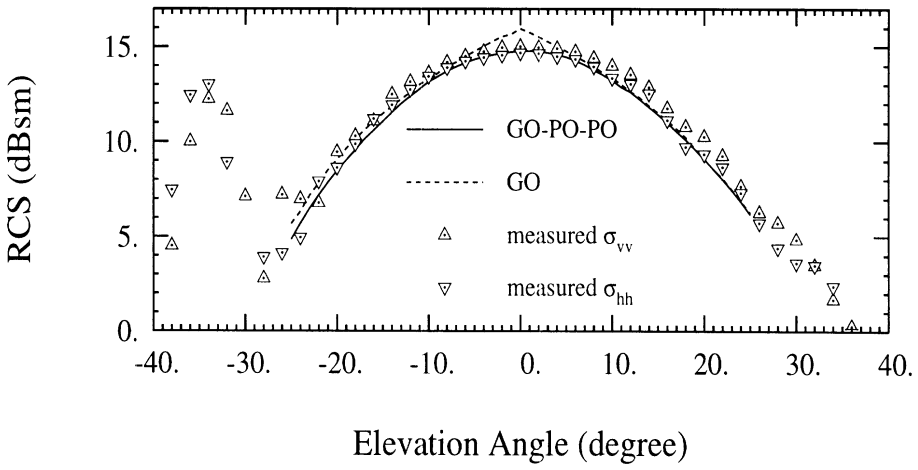

(b)

Figure 6.10: The measured RCS patterns of a square corner reflector as a function of horizontal (a) and elevation angles (b). Panel area is $100\lambda^2/3$ at 9.5 GHz.

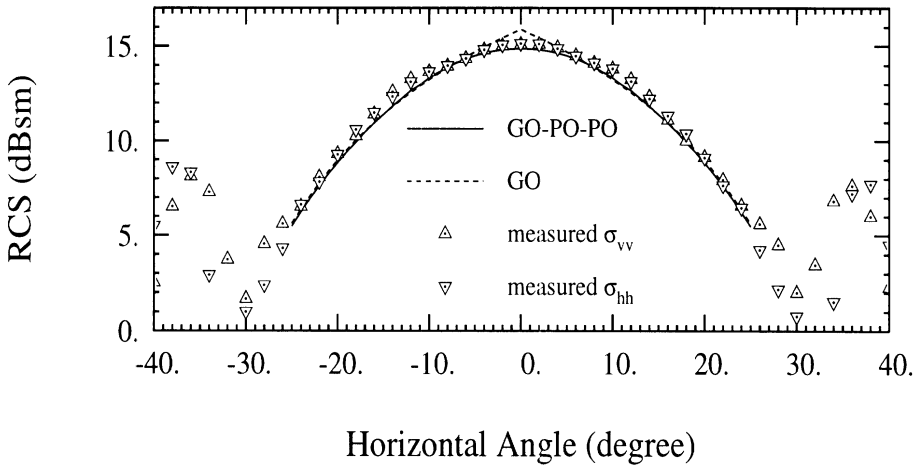

(a)

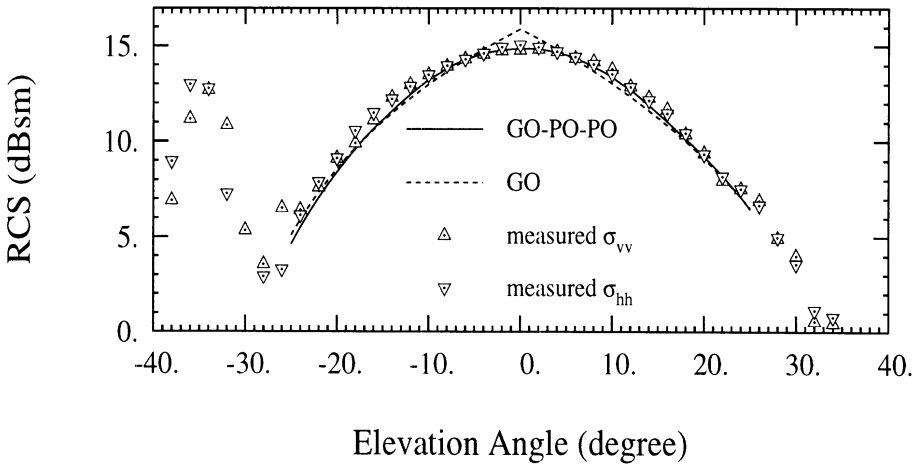

(b)

Figure 6.11: The measured RCS patterns of a pentagonal corner reflector as a function of horizontal (a) and elevation angles (b). Panel area is $100\lambda^2/3$ at 9.5 GHz.

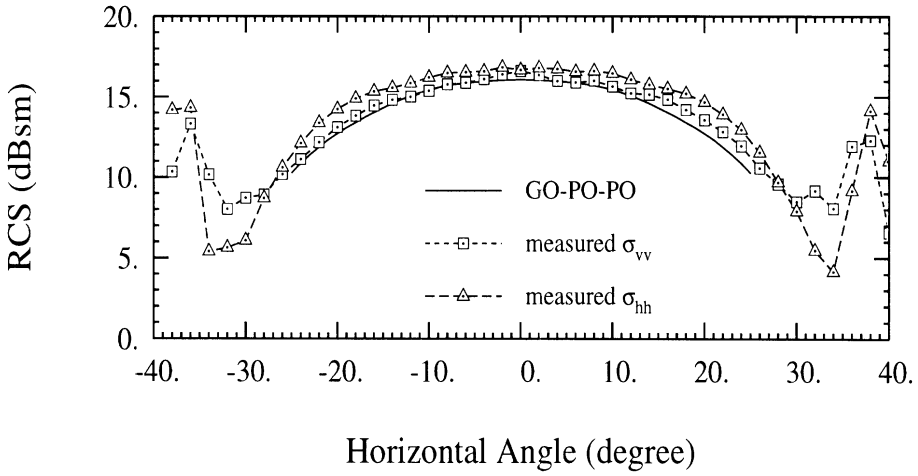

(a)

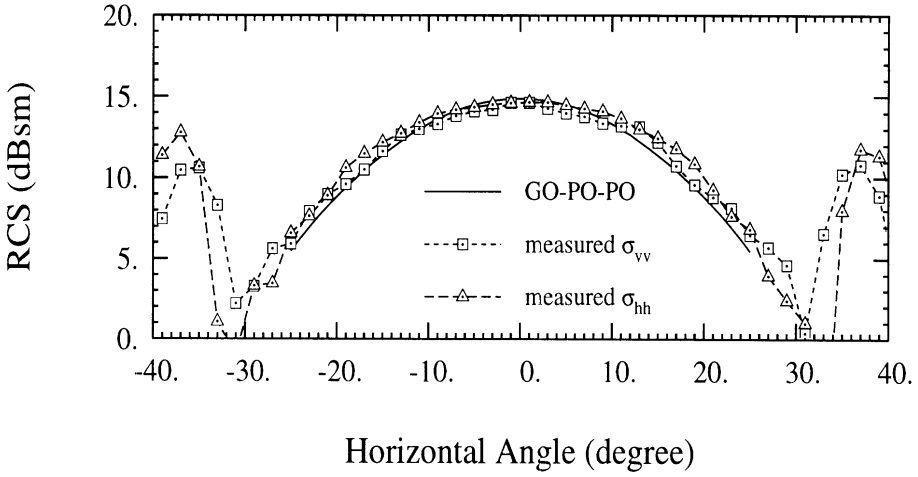

(b)

Figure 6.12: The measured RCS patterns of a triangular corner reflector with $A_t = 50\lambda^2$ (a) and a pentagonal corner reflector with $A_p = 100\lambda^2/3$ (b) at 9.5 GHz above a perfectly conducting ground plane ($\beta = 0^o$).

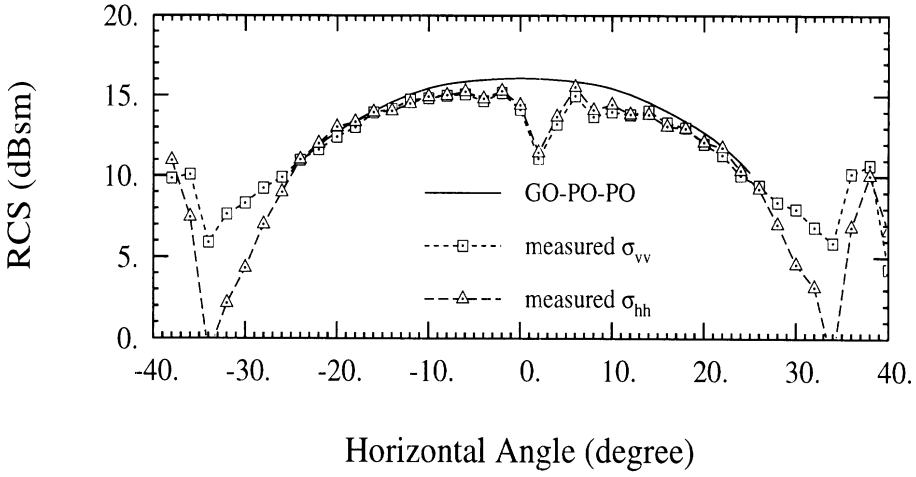

(a)

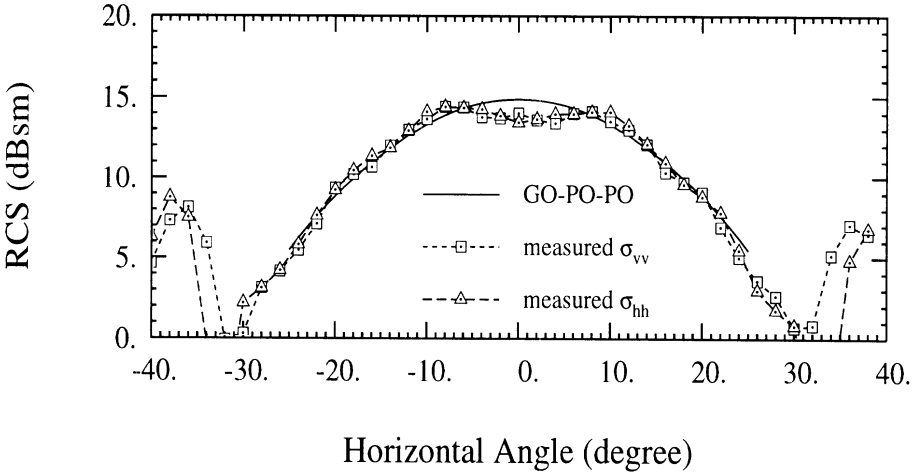

(b)

Figure 6.13: The measured RCS patterns of a triangular corner reflector with $A_t = 50\lambda^2$ (a) and a pentagonal corner reflector with $A_p = 100\lambda^2/3$ (b) at 9.5 GHz above a perfectly conducting ground plane ($\beta = 10^o$).

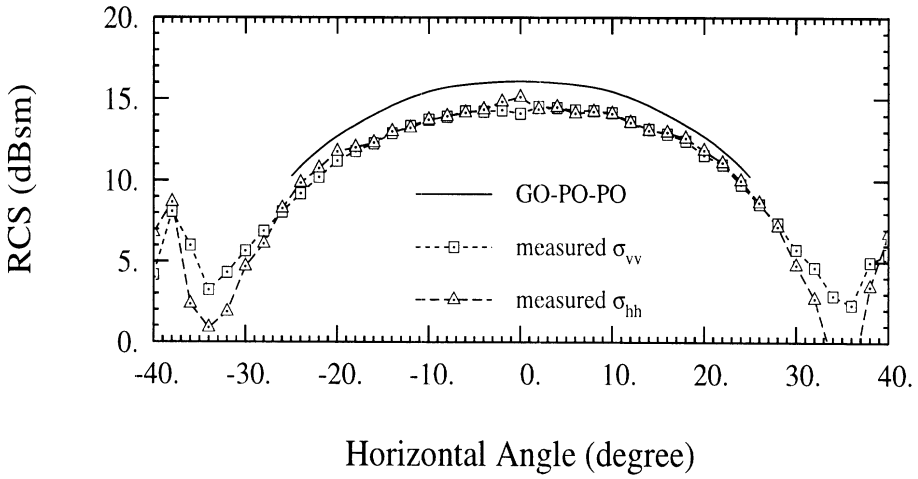

(a)

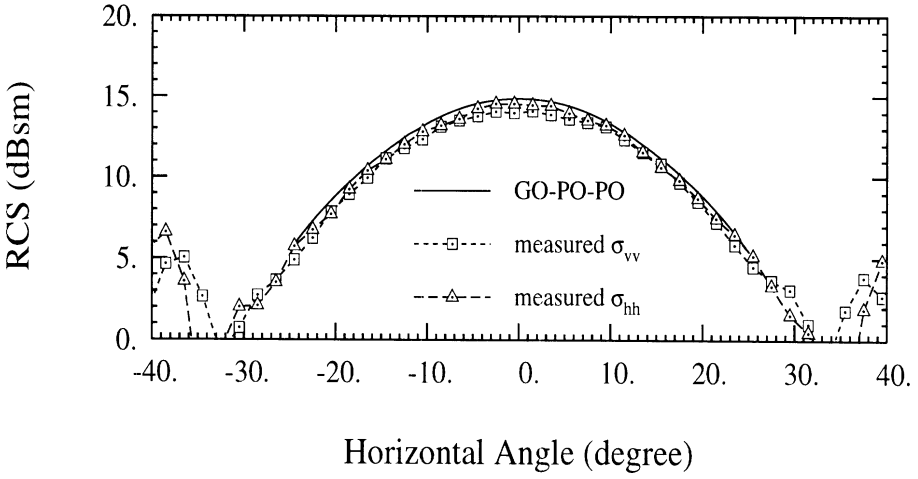

(b)

Figure 6.14: The measured RCS patterns of a triangular corner reflector with $A_t = 50\lambda^2$ (a) and a pentagonal corner reflector with $A_p = 100\lambda^2/3$ (b) at 9.5 GHz above a lossy dielectric ground plane ($\beta = 10^o$).

6.4 Conclusions

In this chapter the theoretical and experimental aspects of scattering from corner reflectors are considered. A new class of self-illuminating corner reflectors is introduced which require the minimum panel area for a given RCS value. The self-illuminating corner reflectors are proposed as calibration targets for imaging radar systems. Also the geometry of the optimum corner reflector which has the shortest edge length among polygonal self-illuminating corner reflectors is obtained. Prototype triangular, pentagonal and square corner reflectors were constructed and measured at X-band. It was shown that the self-illuminating corner reflectors offer two major improvements over the widely used triangular corner reflectors : (1) the uncertainty in the RCS of self-illuminating corner reflectors, caused by the interaction of the ground plane with the corner reflector, is significantly smaller than that of the triangular corner reflectors, and (2) for a specified RCS, the panel area is two-thirds of that of the triangular one. The 1-dB RCS beamwidths of the pentagonal and square corner reflector in azimuth and elevation planes were found to be around 16^o.

CHAPTER VII

CONCLUSIONS AND RECOMMENDATIONS

7.1 Summary

Electromagnetic scattering models for bare-soil and short-vegetation-covered ground surfaces are proposed for the purpose of information retrieval from radar backscatter. For bare-soil surfaces, a novel scattering model for random rough surfaces has been developed. In this model the scattering solutions are obtained by applying the perturbation expansion to the integral equation of the volumetric polarization current. The major contribution of this model is that it accounts for the effect of the underlying dielectric inhomogeneity. For the short-vegetation-covered ground surfaces, a coherent scattering model is proposed. In this model, soybeans are chosen as the target vegetation. A computer-generated vegetation structure is used to investigate the effect of the vegetation structure. Rough-surface scattering models are also incorporated to calculate the scattering from the ground. The significance of this model is that it accounts for the near-field interaction between vegetation particles and the ground. Both scattering models have been verified by experiment. In what follows, the summary of each chapter will be reiterated.

In Chapter 2, an analytical model for soil surfaces with a slightly rough interface and stratified permittivity profile is presented. The scattering formulation is based on

a new approach where, instead of the tangential fields, the perturbation expansion of the volumetric polarization current is used to obtain the scattered field. In this model, the top rough layer is replaced by an equivalent polarization current. The scattering problem is formulated using the volumetric integral equation in conjunction with the dyadic Green's function for the remaining stratified half-space medium. Closed form analytical expressions for the induced polarization currents to any desired order are derived and then used to evaluate the bistatic scattered fields up to and including the third order. The analytical solutions for the scattered fields are used to derive the complete second-order expressions for the backscattering coefficients as well as the statistics of the phase difference between the scattering matrix elements. The theoretical results are shown to agree well with the backscatter measurements of rough surfaces with known dielectric profiles and roughness statistics. With this model, a sensitivity analysis has been performed and it is found that the parameter most sensitive to the underlying dielectric inhomogeneity is the co-polarized phase difference.

Chapter 3 presents an electromagnetic scattering solution for the interaction between a dielectric cylinder and a slightly rough surface. Using a newly-developed technique based on the reciprocity theorem, the difficulty in formulating the secondary scattered fields from the composite target reduces to the evaluation of integrals involving the scattered fields from the cylinder and the polarization currents of the rough surface induced by a plane wave. Only the current distribution of isolated scatterers is needed to determine the interaction. The scattered field from the cylinder is evaluated in the near-field region using the stationary phase approximation along the cylinder axis. The expressions for the polarization current induced within the top rough layer of the rough surface derived from the iterative solution of an in-

tegral equation are also employed in this chapter. A sensitivity analysis is performed to investigate the dependence of the scattering interaction on target parameters such as surface rms height, dielectric constant, and the cylinder diameter and length. It is shown that for a nearly vertical cylinder, which is of interest for modeling vegetation, the cross-polarized backscatter is mainly dominated by the scattering interaction between the cylinder and the rough surface. The accuracy of the theoretical formulation is verified by conducting polarimetric backscatter measurements of a lossy dielectric cylinder above a slightly rough surface. Excellent agreement between the theoretical prediction and experimental results is obtained.

In Chapter 4, the scattering solutions for vegetation particles are described. Vegetation particles are usually modeled using simple geometries for which the analytical scattering solutions are available. Because leaves often have a thickness small compared to wavelength in the microwave range, the Rayleigh-Gans formulation is applied. Dielectric cylinders are often used to model vegetation particles such as tree trunks and branches. An exact scattering solution does not exist for cylinders of finite length, but an approximate solution, which assumes that the internal field induced within the finite cylinder is the same as that of the infinite cylinder with the same cross section and dielectric constant, can be used. Generally, in order for this solution to be valid the ratio of the length to the diameter should be large so that the fringing effects at both ends of the cylinder can be ignored. A formulation for the second-order scattering between two Rayleigh-Gans particles is also developed using the Rayleigh-Gans approach. From a sensitivity analysis, it is found that the near-field interaction becomes more significant at higher frequencies.

In Chapter 5, an electromagnetic scattering model is developed for short branching vegetation. Using structures which realistically describe the relative positions of

the particles, this model considers the coherence effect due to the phase difference between the scattered fields from different particles and handles the second-order near-field interaction between particles for which the relative positions and orientation of the particles are essential. The validation of the model by measurements is also presented; satisfactory agreement is shown. The polarimetric radar backscatter measurements of soybean plants, using a truck-mounted scatterometer, were conducted at L-band and C-band under different soil-moisture conditions. An extensive ground truth collection was also performed to record the moisture, dielectric constant, and geometry of the soybean plants and the rough surface. Thereby the uncertainty associated with inputing the values of parameters is reduced. This model also demonstrates its ability to estimate the physical parameters and moisture of a soybean field using AIRSAR image data with limited knowledge of the ground truth. Generally, it is found that the second-order near-field scattering is significant at C-band for fully-grown soybeans due to the high local density of the vegetation particles. However, it is not significant at L-band. The coherence effect is important at L-band, and could be so at C-band depending on the complexity of the vegetation structure.

Chapter 6 is concerned with the corner reflectors used for the calibration of the SAR. Trihedral corner reflectors are widely used as calibration targets for imaging radars because of their large RCS and extremely wide RCS pattern. An important source of uncertainty in the RCS of a trihedral on a ground plane is the coherent interaction of ground plane and trihedral. At UHF and low microwave frequencies the large physical size of corner reflectors becomes a limiting factor with regard to difficulties in field deployment and deviation of their RCS from the expected values. In this chapter, a general class of corner reflectors with high aperture efficiency

referred to as self-illuminating corner reflectors, is introduced. Coherent interaction with surrounding terrain is minimized and their total surface area is two-thirds of that of a triangular corner reflector having the same maximum RCS. Analytical expressions based on geometrical optics and a new numerical solution based on near-field physical optics for the RCS of two simple self-illuminating corner reflectors are presented and compared with backscatter measurements. Also the panel geometry for an optimum corner reflector which has the shortest edge length among polygonal self-illuminating corner reflectors is obtained. High aperture efficiency is achieved at the expense of azimuth and elevation beamwidth. It is shown that the 1-dB RCS beamwidths of these optimal corner reflectors are about 16° in both azimuth and elevation, which is sufficient for most practical applications. RCS measurements of corner reflectors in the presence of a ground plane show that the RCS of self-illuminating corner reflectors is less affected by the coherent ground interaction.

7.2 Future Work and Recommendations

Many scattering models are presented in this thesis. From the title of this dissertation, it is evident that the author intended to cover the issues of land scattering as comprehensively as possible. However, considering the complexity of the subject, the author could only take a short step towards what should take many outstanding researchers lifetimes to achieve.

For scattering from rough surfaces, the model presented in this dissertation can handle the underlying dielectric inhomogeneity, but is limited to surfaces with small roughness and short correlation length. This is not a big problem in this dissertation because low frequency radars are recommended in this thesis due to their ability to penetrate the vegetation and soil. At low frequencies, high surface roughness and

long correlation length do not often occur. This is also the case in the model for the interaction between the nearly vertical cylinder and the slightly rough surface. Nevertheless, This issue will not be complete unless the models which can handle rougher surfaces are developed. To develop a model for much rougher surface with the underlying dielectric inhomogeneity will be very challenging. However, to develop he model of the interaction between the nearly vertical cylinder and the much rougher surface should be possible if the PO technique were used.

For the vegetation scattering model, the key to improvement lies in having access to highly advanced computing facilities. The application of the Monte-Carlo simulation destines this model to be time-consuming. However, considerable improvement is still feasible. Not every scattering mechanism need to be simulated. For example, the double ground bounce can always be neglected, and the direct backscatter from rough surfaces is not significant at C-band if biomass is large. It is thus possible to develop an 'intelligent' model which can select the necessary mechanisms before simulation and avoid unnecessary calculation. Extensive characterization of the vegetation structure would have to be conducted in advance. Eventually, the model must be extended to simulate the scattering behavior of large vegetation structures like forest canopies. Considering the large number of particles, even one scattering mechanism would require a considerable time to calculate. The author believes that this problem could be solved by parallel computation. Different CPUs could take charge of different scattering mechanisms, and more CPUs could be assigned to time-consuming mechanisms, such as the second-order near-field interaction among vegetation particles. Once these expectations are achieved, and the author believes they will be, their applications and contributions will be unlimited.

APPENDICES

APPENDIX A

HIGHER ORDER SCATTERING MATRIX OF THE SLIGHTLY ROUGH SURFACES WITH INHOMOGENEOUS DIELECTRIC PROFILES

In this appendix closed form expressions for the second and third order elements of bistatic scattering matrix of the inhomogeneous rough surface are provided.

$$S_{hh}^{(2)} = \frac{ik_0^2(\epsilon-1)}{8\pi}\left(1+R_h^i\right)\cos(\phi_s-\phi_i)e^{-i(k_z^s+k_z^i)d}\left[k_z^s\left(R_h^i-1\right)C_1^h(\mathbf{k}^s,d)C_0^h(\mathbf{k}^i,d)\right.$$
$$\left.-k_{1z}^i\left(R_h^i+1\right)C_0^h(\mathbf{k}^s,d)C_1^h(\mathbf{k}^i,d)\right]\left(\frac{1}{2\pi}\right)^2\int_{-\infty}^{\infty}F(\mathbf{k}_\perp^s-\mathbf{k}_\perp)F(\mathbf{k}_\perp-\mathbf{k}_\perp^i)\,d\mathbf{k}_\perp$$
$$+\frac{ik_0^2(\epsilon-1)^2}{4\pi}\left(1+R_h^s\right)\left(1+R_h^i\right)C_0^h(\mathbf{k}^s,d)C_0^h(\mathbf{k}^i,d)e^{-i(k_z^s+k_z^i)d}$$
$$\cdot\left(\frac{1}{2\pi}\right)^2\int_{-\infty}^{\infty}F(\mathbf{k}_\perp^s-\mathbf{k}_\perp)F(\mathbf{k}_\perp-\mathbf{k}_\perp^i)\cdot\left[\frac{k_0^2}{k_z+k_{1z}}C_0^h(\mathbf{k},d)\cos(\phi_s-\phi)\right.$$
$$\left.\cdot\cos(\phi-\phi_i)-\frac{k_zk_{1z}}{\epsilon k_z+k_{1z}}C_0^v(\mathbf{k},d)\sin(\phi_s-\phi)\sin(\phi-\phi_i)\right]d\mathbf{k}_\perp \qquad \text{(A.1)}$$

$$S_{vv}^{(2)} = \frac{ik_z^i(\epsilon-1)}{8\pi}\left(1-R_v^i\right)e^{-i(k_z^s+k_z^i)d}\left\{\left[(k_z^s)^2\cos(\phi_s-\phi_i)-k_\rho^ik_\rho^s\right]\left(1+R_v^s\right)C_1^v(\mathbf{k}^s,d)\right.$$
$$\left.\cdot C_0^v(\mathbf{k}^i,d)-\left[k_{1z}^ik_z^s\cos(\phi_s-\phi_i)-k_\rho^ik_\rho^s\frac{k_z^s}{k_{1z}^i}\right]\left(R_v^s-1\right)C_0^v(\mathbf{k}^s,d)C_1^v(\mathbf{k}^i,d)\right\}$$
$$\cdot\left(\frac{1}{2\pi}\right)^2\int_{-\infty}^{\infty}F(\mathbf{k}_\perp^s-\mathbf{k}_\perp)F(\mathbf{k}_\perp-\mathbf{k}_\perp^i)\,d\mathbf{k}_\perp$$

$$
\begin{aligned}
&- \frac{ik_z^s k_z^i (\epsilon-1)^2}{4\pi}\left(1-R_v^s\right)\left(1-R_v^i\right) C_0^v(\mathbf{k}^s,d)e^{-i(k_z^s+k_z^i)d} \\
&\cdot \left(\frac{1}{2\pi}\right)^2 \int_{-\infty}^{\infty} F(\mathbf{k}_\perp^s-\mathbf{k}_\perp)F(\mathbf{k}_\perp-\mathbf{k}_\perp^i)\cdot\left[-\frac{k_0^2}{k_z+k_{1z}}C_0^h(\mathbf{k},d)C_0^v(\mathbf{k}^i,d)\right. \\
&\cdot \sin(\phi_s-\phi)\sin(\phi-\phi_i)+\frac{k_z k_{1z}}{\epsilon k_z+k_{1z}}C_0^v(\mathbf{k},d)C_0^v(\mathbf{k}^i,d)\cos(\phi_s-\phi) \\
&\left.\cdot \cos(\phi-\phi_i)+\frac{k_\rho^i k_\rho k_{1z}}{k_{1z}^i(\epsilon k_z+k_{1z})}C_0^v(\mathbf{k},d)C_1^v(\mathbf{k}^i,d)\cos(\phi_s-\phi)\right] d\mathbf{k}_\perp \\
&+ \frac{ik_\rho^s k_z^i (\epsilon-1)^2}{4\pi}\left(1+R_v^s\right)\left(1-R_v^i\right) C_1^v(\mathbf{k}^s,d)e^{-i(k_z^s+k_z^i)d} \\
&\cdot \left(\frac{1}{2\pi}\right)^2 \int_{-\infty}^{\infty} F(\mathbf{k}_\perp^s-\mathbf{k}_\perp)F(\mathbf{k}_\perp-\mathbf{k}_\perp^i)\frac{k_\rho}{\epsilon k_z+k_{1z}}C_1^v(\mathbf{k},d) \\
&\cdot \left[k_z C_0^v(\mathbf{k}^i,d)\cos(\phi-\phi_i)+k_\rho\frac{k_\rho^i}{k_{1z}^i}C_1^v(\mathbf{k}^i,d)\right] d\mathbf{k}_\perp
\end{aligned}
\tag{A.2}
$$

$$
\begin{aligned}
S_{vh}^{(2)} = &\frac{-ik_0 k_z^s(\epsilon-1)\left(1+R_h^i\right)}{8\pi}\sin(\phi_s-\phi_i)e^{-i(k_z^s+k_z^i)d}\left[k_{1z}^i\left(1-R_v^s\right)C_0^v(\mathbf{k}^s,d)C_1^h(\mathbf{k}^i,d)\right. \\
&\left.+k_z^s\left(1+R_v^s\right)C_1^v(\mathbf{k}^s,d)C_0^h(\mathbf{k}^i,d)\right]\left(\frac{1}{2\pi}\right)^2\int_{-\infty}^{\infty}F(\mathbf{k}_\perp^s-\mathbf{k}_\perp)F(\mathbf{k}_\perp-\mathbf{k}_\perp^i)\,d\mathbf{k}_\perp \\
&+\frac{ik_0 k_z^s(\epsilon-1)^2}{4\pi}\left(1-R_v^s\right)\left(1+R_h^i\right)C_0^v(\mathbf{k}^s,d)C_0^h(\mathbf{k}^i,d)e^{-i(k_z^s+k_z^i)d} \\
&\cdot\left(\frac{1}{2\pi}\right)^2\int_{-\infty}^{\infty}F(\mathbf{k}_\perp^s-\mathbf{k}_\perp)F(\mathbf{k}_\perp-\mathbf{k}_\perp^i)\cdot\left[\frac{k_0^2}{k_z+k_{1z}}C_0^h(\mathbf{k},d)\right. \\
&\left.\cdot\sin(\phi_s-\phi)\cos(\phi-\phi_i)+\frac{k_z k_{1z}}{\epsilon k_z+k_{1z}}C_0^v(\mathbf{k},d)\cos(\phi_s-\phi)\sin(\phi-\phi_i)\right]d\mathbf{k}_\perp \\
&-\frac{ik_0 k_\rho^s(\epsilon-1)^2}{4\pi}\left(1+R_v^s\right)\left(1+R_h^i\right)C_1^v(\mathbf{k}^s,d)C_0^h(\mathbf{k}^i,d)e^{-i(k_z^s+k_z^i)d}\left(\frac{1}{2\pi}\right)^2 \\
&\cdot\int_{-\infty}^{\infty}F(\mathbf{k}_\perp^s-\mathbf{k}_\perp)F(\mathbf{k}_\perp-\mathbf{k}_\perp^i)\cdot\frac{k_\rho k_z}{\epsilon k_z+k_{1z}}C_1^v(\mathbf{k},d)\sin(\phi-\phi_i)\,d\mathbf{k}_\perp
\end{aligned}
\tag{A.3}
$$

$$S_{hv}^{(2)} = \frac{ik_0 k_z^i (\epsilon - 1)}{8\pi} \left(R_v^i - 1\right) \sin(\phi_s - \phi_i) e^{-i(k_z^s + k_z^i)d} \left[k_{1z}^i \left(1 + R_h^s\right) C_0^h(\mathbf{k}^s, d) C_1^v(\mathbf{k}^i, d) \right.$$

$$\left. + k_z^s \left(1 - R_h^s\right) C_1^h(\mathbf{k}^s, d) C_0^v(\mathbf{k}^i, d) \right] \left(\frac{1}{2\pi}\right)^2 \int_{-\infty}^{\infty} F(\mathbf{k}_\perp^s - \mathbf{k}_\perp) F(\mathbf{k}_\perp - \mathbf{k}_\perp^i)\, d\mathbf{k}_\perp$$

$$+ \frac{ik_0 k_z^i (\epsilon - 1)^2}{4\pi} \left(1 + R_h^s\right) \left(1 - R_v^i\right) C_0^h(\mathbf{k}^s, d) e^{-i(k_z^s + k_z^i)d}$$

$$\cdot \left(\frac{\triangle}{2\pi}\right)^2 \int_{-\infty}^{\infty} F(\mathbf{k}_\perp^s - \mathbf{k}_\perp) F(\mathbf{k}_\perp - \mathbf{k}_\perp^i) \cdot \left[\frac{k_0^2}{k_z + k_{1z}} C_0^h(\mathbf{k}, d) C_0^v(\mathbf{k}^i, d) \right.$$

$$\cdot \cos(\phi_s - \phi) \sin(\phi - \phi_i) + \frac{k_z k_{1z}}{\epsilon k_z + k_{1z}} C_0^v(\mathbf{k}, d) C_0^v(\mathbf{k}^i, d) \sin(\phi_s - \phi)$$

$$\left. \cdot \cos(\phi - \phi_i) + \frac{k_\rho k_{1z}}{\epsilon k_z + k_{1z}} \frac{k_\rho^i}{k_{1z}^i} C_0^v(\mathbf{k}, d) C_1^v(\mathbf{k}^i, d) \sin(\phi_s - \phi) \right] d\mathbf{k}_\perp \qquad \text{(A.4)}$$

$$S_{hh}^{(3)} = -\frac{k_0^2 (\epsilon - 1)}{24\pi} \left(1 + R_h^i\right) e^{-i(k_z^s + k_z^i)d} \cos(\phi_s - \phi_i) \cdot \left\{ \left[(k_z^s)^2 + \left(k_{1z}^i\right)^2 \right] \left(1 + R_h^s\right) \right.$$

$$\left. \cdot C_0^h(\mathbf{k}^i, d) C_0^h(\mathbf{k}^s, d) + 2k_z^s k_{1z}^i \left(1 - R_h^s\right) C_1^h(\mathbf{k}^i, d) C_1^h(\mathbf{k}^s, d) \right\}$$

$$\cdot \frac{1}{(2\pi)^4} \iint_{-\infty}^{\infty} F(\mathbf{k}_\perp^s - \mathbf{k}_\perp) F(\mathbf{k}_\perp - \mathbf{k}_\perp') F(\mathbf{k}_\perp' - \mathbf{k}_\perp^i)\, d\mathbf{k}_\perp d\mathbf{k}_\perp'$$

$$+ \frac{k_0^2 (\epsilon - 1)^2}{8\pi} \left(1 + R_h^i\right) \left(1 + R_h^s\right) C_0^h(\mathbf{k}^i, d) C_0^h(\mathbf{k}^s, d) e^{-i(k_z^s + k_z^i)d} \frac{1}{(2\pi)^4}$$

$$\cdot \iint_{-\infty}^{\infty} F(\mathbf{k}_\perp^s - \mathbf{k}_\perp) F(\mathbf{k}_\perp - \mathbf{k}_\perp') F(\mathbf{k}_\perp' - \mathbf{k}_\perp^i) \left[\frac{k_0^2 k_{1z}'}{k_z' + k_{1z}'} C_1^h(\mathbf{k}', d) \cos(\phi' - \phi_i) \right.$$

$$\left. \cos(\phi_s - \phi') - \frac{k_z' (k_{1z}')^2}{\epsilon k_z' + k_{1z}'} C_1^v(\mathbf{k}', d) \sin(\phi' - \phi_i) \sin(\phi_s - \phi') \right] d\mathbf{k}_\perp d\mathbf{k}_\perp'$$

$$+ \frac{k_0^2 (\epsilon - 1)^2}{8\pi} \left(1 + R_h^i\right) \left(1 - R_h^s\right) C_0^h(\mathbf{k}^i, d) C_1^h(\mathbf{k}^s, d) e^{-i(k_z^s + k_z^i)d} \frac{1}{(2\pi)^4}$$

$$\cdot \iint_{-\infty}^{\infty} F(\mathbf{k}_\perp^s - \mathbf{k}_\perp) F(\mathbf{k}_\perp - \mathbf{k}_\perp') F(\mathbf{k}_\perp' - \mathbf{k}_\perp^i) \left[\frac{k_0^2 k_z^s}{k_z' + k_{1z}'} C_0^h(\mathbf{k}', d) \cos(\phi' - \phi_i) \right.$$

$$\left. \cdot \cos(\phi_s - \phi') - \frac{k_z^s k_z' k_{1z}'}{\epsilon k_z' + k_{1z}'} C_0^v(\mathbf{k}', d, 0) \sin(\phi' - \phi_i) \sin(\phi_s - \phi') \right] d\mathbf{k}_\perp d\mathbf{k}_\perp'$$

$$- \frac{k_0^2 (\epsilon - 1)^2}{8\pi} \left(1 + R_h^i\right) \left(1 + R_h^s\right) C_0^h(\mathbf{k}^s, d) e^{-i(k_z^s + k_z^i)d} \frac{1}{(2\pi)^4} \iint_{-\infty}^{\infty} d\mathbf{k}_\perp d\mathbf{k}_\perp'$$

$$F(\mathbf{k}_\perp^s - \mathbf{k}_\perp) F(\mathbf{k}_\perp - \mathbf{k}_\perp') F(\mathbf{k}_\perp' - \mathbf{k}_\perp^i) \left[k_z C_0^h(\mathbf{k}^i, d) - k_{1z}^i C_1^h(\mathbf{k}^i, d) \right] \left[\frac{k_0^2}{k_z + k_{1z}} \right.$$

$$\left. \cdot C_0^h(\mathbf{k}, d) \cos(\phi - \phi_i) \cos(\phi_s - \phi) - \frac{k_z^s k_{1z} C_0^v(\mathbf{k}, d)}{\epsilon k_z + k_{1z}} \sin(\phi - \phi_i) \sin(\phi_s - \phi) \right]$$

$$+ \frac{k_0^2 (\epsilon - 1)^3}{4\pi} \left(1 + R_h^i\right) \left(1 + R_h^s\right) C_0^h(\mathbf{k}^s, d) C_0^h(\mathbf{k}^i, d) e^{-i(k_z^s + k_z^i)d}$$

$$\cdot \frac{1}{(2\pi)^4} \iint_{-\infty}^{\infty} F(\mathbf{k}_\perp^s - \mathbf{k}_\perp) F(\mathbf{k}_\perp - \mathbf{k}_\perp') F(\mathbf{k}_\perp' - \mathbf{k}_\perp^i) \left\{ \right.$$

$$- \frac{k_0^4}{(k_z + k_{1z})(k_z' + k_{1z}')} C_0^h(\mathbf{k}', d) C_0^h(\mathbf{k}, d) \cos(\phi_s - \phi) \cos(\phi - \phi') \cos(\phi' - \phi_i)$$

$$+ \frac{k_0^2 k_z k_{1z}}{(\epsilon k_z + k_{1z})(k_z' + k_{1z}')} C_0^h(\mathbf{k}', d) C_0^v(\mathbf{k}, d) \sin(\phi_s - \phi) \sin(\phi - \phi') \cos(\phi' - \phi_i)$$

$$+ \frac{k_0^2 k_z' k_{1z}'}{(k_z + k_{1z})(\epsilon k_z' + k_{1z}')} C_0^v(\mathbf{k}', d) C_0^h(\mathbf{k}, d) \cos(\phi_s - \phi) \sin(\phi - \phi') \sin(\phi' - \phi_i)$$

$$+ \frac{k_z k_{1z} k_z' k_{1z}'}{(\epsilon k_z + k_{1z})(\epsilon k_z' + k_{1z}')} C_0^v(\mathbf{k}', d) C_0^v(\mathbf{k}, d) \sin(\phi_s - \phi) \cos(\phi - \phi') \sin(\phi' - \phi_i)$$

$$+ \frac{k_\rho' k_z' k_\rho k_{1z}}{(k_z + k_{1z})(k_z' + k_{1z}')} C_1^v(\mathbf{k}', d) C_0^v(\mathbf{k}, d) \sin(\phi_s - \phi) \sin(\phi' - \phi_i) \left. \right\} d\mathbf{k}_\perp d\mathbf{k}_\perp' \tag{A.5}$$

$$S_{vv}^{(3)} = - \frac{k_z^i (\epsilon - 1)}{24\pi} \left(1 - R_v^i\right) e^{-i(k_z^s + k_z^i)d} \left\{ k_z^s \left(\left[\left(k_{1z}^i\right)^2 + \left(k_z^s\right)^2 \right] \cos(\phi_s - \phi_i) - 2 k_\rho^i k_\rho^s \right) \right.$$

$$\cdot \left(R_v^s - 1\right) C_0^v(\mathbf{k}^s, d) C_0^v(\mathbf{k}^i, d) + \left(\left[\left(k_{1z}^i\right)^2 + \left(k_z^s\right)^2 \right] \frac{k_\rho^i k_\rho^s}{k_{1z}^i} - 2 \left(k_z^s\right)^2 k_{1z}^i \right.$$

$$\left. \left. \cdot \cos(\phi_s - \phi_i) \right) \left(R_v^s + 1\right) C_1^v(\mathbf{k}^s, d) C_1^v(\mathbf{k}^i, d) \right\}$$

$$\cdot \frac{1}{(2\pi)^4} \iint_{-\infty}^{\infty} F(\mathbf{k}_\perp^s - \mathbf{k}_\perp) F(\mathbf{k}_\perp - \mathbf{k}_\perp') F(\mathbf{k}_\perp' - \mathbf{k}_\perp^i)\, d\mathbf{k}_\perp d\mathbf{k}_\perp'$$

$$+ \frac{k_z^i (\epsilon - 1)^2}{8\pi} \left(1 - R_v^i\right) \left(R_v^s - 1\right) C_0^v(\mathbf{k}^s, d) e^{-i(k_z^s + k_z^i)d} \frac{1}{(2\pi)^4} \iint_{-\infty}^{\infty}$$

$$\cdot F(\mathbf{k}_\perp^s - \mathbf{k}_\perp) F(\mathbf{k}_\perp - \mathbf{k}_\perp') F(\mathbf{k}_\perp' - \mathbf{k}_\perp^i) \Bigg\{ -\frac{k_0^2 k_z^s k_{1z}'}{k_z' + k_{1z}'} C_0^v(\mathbf{k}^i, d) C_1^h(\mathbf{k}', d)$$

$$\cdot \sin(\phi_s - \phi') \sin(\phi' - \phi_i) + \frac{k_z^s}{\epsilon k_z' + k_{1z}'} \left[k_z' C_0^v(\mathbf{k}^i, d) \cos(\phi' - \phi_i) + \frac{k_\rho^i k_\rho'}{k_{1z}^i} \right.$$

$$\left. \cdot C_1^v(\mathbf{k}^i, d) \right] \left[\left(k_{1z}'\right)^2 \cos(\phi^s - \phi') - k_\rho^s k_\rho' \right] C_1^v(\mathbf{k}', d) \Bigg\} d\mathbf{k}_\perp d\mathbf{k}_\perp'$$

$$+ \frac{k_z^i (\epsilon - 1)^2}{8\pi} \left(1 - R_v^i\right) \left(R_v^s + 1\right) C_1^v(\mathbf{k}^s, d) e^{-i(k_z^s + k_z^i)d} \frac{1}{(2\pi)^4} \iint_{-\infty}^{\infty}$$

$$F(\mathbf{k}_\perp^s - \mathbf{k}_\perp) F(\mathbf{k}_\perp - \mathbf{k}_\perp') F(\mathbf{k}_\perp' - \mathbf{k}_\perp^i) \Bigg\{ \frac{k_0^2 \left(k_z^s\right)^2}{k_z' + k_{1z}'} C_0^v(\mathbf{k}^i, d) C_0^h(\mathbf{k}', d)$$

$$\cdot \sin\left(\phi_s - \phi'\right) \sin\left(\phi' - \phi_i\right) - \frac{k_{1z}'}{\epsilon k_z' + k_{1z}'} \left[k_z' C_0^v(\mathbf{k}^i, d) \cos(\phi' - \phi_i) + \frac{k_\rho^i k_\rho'}{k_{1z}^i} \right.$$

$$\left. \cdot C_1^v(\mathbf{k}^i, d) \right] \left[\left(k_z^s\right)^2 \cos(\phi^s - \phi') - k_\rho^s k_\rho' \right] C_0^v(\mathbf{k}', d) \Bigg\} d\mathbf{k}_\perp d\mathbf{k}_\perp'$$

$$+ \frac{k_z^i (\epsilon - 1)^2}{8\pi} \left(1 - R_v^i\right) \left(R_v^s - 1\right) e^{-i(k_z^s + k_z^i)d} \frac{1}{(2\pi)^4} \iint_{-\infty}^{\infty} F(\mathbf{k}_\perp^s - \mathbf{k}_\perp) F(\mathbf{k}_\perp - \mathbf{k}_\perp')$$

$$F(\mathbf{k}_\perp' - \mathbf{k}_\perp^i) \left\{ \frac{k_0^2 k_z^s}{k_z + k_{1z}} \left[k_z C_0^v(\mathbf{k}^i, d) - k_{1z}^i C_1^v(\mathbf{k}^i, d) \right] C_1^v(\mathbf{k}^s, d) \right.$$

$$\cdot C_0^h(\mathbf{k}, d) \sin(\phi^s - \phi) \sin(\phi - \phi^i) + \left[-\frac{k_z^s k_{1z}}{\epsilon k_z + k_{1z}} C_1^v(\mathbf{k}^s, d) C_0^v(\mathbf{k}, d) \right.$$

$$\left. \cdot \cos(\phi^s - \phi) + \frac{k_\rho}{\epsilon k_z + k_{1z}} \frac{\epsilon k_z^s k_\rho^s}{k_{1z}^s} C_0^v(\mathbf{k}^s, d) C_1^v(\mathbf{k}, d) \right] \left(\left[\left(k s_z\right)^2 \cos(\phi - \phi^i) \right. \right.$$

$$\left. \left. - k_\rho^i k_\rho \right] C_0^v(\mathbf{k}^i, d) + \left[k_\rho^i k_\rho \frac{k_z}{k_{1z}^i} - k_{1z}^i k_z \cos(\phi - \phi^i) \right] C_1^v(\mathbf{k}^i, d) \right) \Bigg\} d\mathbf{k}_\perp d\mathbf{k}_\perp'$$

$$+ \frac{k_z^i (\epsilon - 1)^3}{4\pi} \left(1 - R_v^i\right) \left(R_v^s - 1\right) C_0^v(\mathbf{k}^s, d) C_0^v(\mathbf{k}^i, d) e^{-i(k_z^s + k_z^i)d}$$

$$\cdot \frac{1}{(2\pi)^4} \iint_{-\infty}^{\infty} F(\mathbf{k}_\perp^s - \mathbf{k}_\perp) F(\mathbf{k}_\perp - \mathbf{k}_\perp') F(\mathbf{k}_\perp' - \mathbf{k}_\perp^i) \Bigg\{$$

$$\frac{k_0^4 k_z^s}{\left(k_z + k_{1z}\right)\left(k_z' + k_{1z}'\right)} C_0^h(\mathbf{k}, d) C_0^h(\mathbf{k}', d) \sin(\phi^s - \phi) \cos(\phi - \phi') \sin(\phi' - \phi^i)$$

$$
\begin{aligned}
&+\frac{k_0^2 k_z^s k_{1z}' k_z' C_0^h(\mathbf{k},d) C_0^v(\mathbf{k}',d)}{(k_z+k_{1z})(\epsilon k_z'+k_{1z}')}\sin(\phi^s-\phi)\sin(\phi-\phi')\cos(\phi'-\phi^i)\\
&+\frac{k_0^4 k_z^s k_{1z} k_z C_0^v(\mathbf{k},d) C_0^h(\mathbf{k}',d)}{(\epsilon k_z+k_{1z})(k_z'+k_{1z}')}\cos(\phi^s-\phi)\sin(\phi-\phi')\sin(\phi'-\phi^i)\\
&-\frac{k_z^s k_{1z} k_z k_{1z}' k_z' C_0^v(\mathbf{k},d) C_0^v(\mathbf{k}',d)}{(\epsilon k_z+k_{1z})(\epsilon k_z'+k_{1z}')}\cos(\phi^s-\phi)\cos(\phi-\phi')\cos(\phi'-\phi^i)\\
&-\frac{k_z^s k_z' k_{1z} k_\rho k_\rho' C_0^v(\mathbf{k},d) C_1^v(\mathbf{k}',d)}{(\epsilon k_z+k_{1z})(\epsilon k_z'+k_{1z}')}\cos(\phi^s-\phi)\cos(\phi'-\phi^i)\Bigg\}\mathbf{k}_\perp d\mathbf{k}_\perp'\\
&+\frac{k_z^i(\epsilon-1)^3}{4\pi}\left(1-R_v^i\right)\left(R_v^s-1\right)C_0^v(\mathbf{k}^s,d)C_1^v(\mathbf{k}^i,d)e^{-i(k_z^s+k_z^i)d}\\
&\cdot\frac{1}{(2\pi)^4}\iint_{-\infty}^{\infty}F(\mathbf{k}_\perp^s-\mathbf{k}_\perp)F(\mathbf{k}_\perp-\mathbf{k}_\perp')F(\mathbf{k}_\perp'-\mathbf{k}_\perp^i)\cdot\Bigg\{\\
&\frac{k_0^2 k_z^s k_\rho^i k_\rho'}{(k_z+k_{1z})(\epsilon k_z'+k_{1z}')}C_0^h(\mathbf{k},d)C_0^v(\mathbf{k}',d)\sin(\phi^s-\phi)\sin(\phi-\phi')\\
&-\frac{k_z^s k_{1z} k_z k_{1z}' k_\rho^i k_\rho'}{k_{1z}^i(\epsilon k_z+k_{1z})(\epsilon k_z'+k_{1z}')}C_0^v(\mathbf{k},d)C_0^v(\mathbf{k}',d)\cos(\phi^s-\phi)\cos(\phi-\phi')\\
&-\frac{k_z^s k_{1z} k_\rho^i k_\rho\left(k_\rho'\right)^2}{k_{1z}^i(\epsilon k_z+k_{1z})(\epsilon k_z'+k_{1z}')}C_0^v(\mathbf{k},d)C_1^v(\mathbf{k}',d)\cos(\phi^s-\phi)\Bigg\}d\mathbf{k}_\perp d\mathbf{k}_\perp'\\
&+\frac{k_z^i k_\rho^s(\epsilon-1)^3}{4\pi}\left(1-R_v^i\right)\left(1+R_v^s\right)C_1^v(\mathbf{k}^s,d)C_0^v(\mathbf{k}^i,d)e^{-i(k_z^s+k_z^i)d}\\
&\cdot\frac{1}{(2\pi)^4}\iint_{-\infty}^{\infty}F(\mathbf{k}_\perp^s-\mathbf{k}_\perp)F(\mathbf{k}_\perp-\mathbf{k}_\perp')F(\mathbf{k}_\perp'-\mathbf{k}_\perp^i)\Bigg\{\\
&\frac{k_0^2 k_z k_\rho}{(\epsilon k_z+k_{1z})(k_z'+k_{1z}')}C_1^h(\mathbf{k},d)C_0^h(\mathbf{k}',d)\sin(\phi-\phi')\sin(\phi'-\phi^i)\\
&-\frac{k_\rho k_z k_z' k_{1z}'}{(\epsilon k_z+k_{1z})(\epsilon k_z'+k_{1z}')}C_1^v(\mathbf{k},d)C_0^v(\mathbf{k}',d)\cos(\phi-\phi')\cos(\phi'-\phi^i)\\
&-\frac{k_z' k_\rho'\left(k_\rho\right)^2}{(\epsilon k_z+k_{1z})(\epsilon k_z'+k_{1z}')}C_1^v(\mathbf{k},d)C_1^v(\mathbf{k}',d)\cos(\phi'-\phi_i)\Bigg\}d\mathbf{k}_\perp d\mathbf{k}_\perp'\\
&-\frac{k_z^i k_\rho^s(\epsilon-1)^3}{4\pi}\left(1-R_v^i\right)\left(1+R_v^s\right)C_1^v(\mathbf{k}^s,d)C_1^v(\mathbf{k}^i,d)e^{-i(k_z^s+k_z^i)d}\\
&\cdot\frac{\triangle^3}{(2\pi)^4}\iint_{-\infty}^{\infty}F(\mathbf{k}_\perp^s-\mathbf{k}_\perp)F(\mathbf{k}_\perp-\mathbf{k}_\perp')F(\mathbf{k}_\perp'-\mathbf{k}_\perp^i)\Bigg\{\\
&\frac{k_z k_{1z}' k_\rho k_\rho^i k_\rho'}{k_{1z}^i(\epsilon k_z+k_{1z})(\epsilon k_z'+k_{1z}')}C_1^v(\mathbf{k},d)C_0^v(\mathbf{k}',d)\cos(\phi-\phi')\\
&+\frac{k_\rho^i\left(k_\rho\right)^2\left(k_\rho'\right)^2}{k_{1z}^i(\epsilon k_z+k_{1z})(\epsilon k_z'+k_{1z}')}C_1^v(\mathbf{k},d)C_1^v(\mathbf{k}',d)\Bigg\}d\mathbf{k}_\perp d\mathbf{k}_\perp' \qquad \text{(A.6)}
\end{aligned}
$$

APPENDIX B

RECIPROCAL PROPERTY OF THE SECONDARY SCATTERING MATRIX

The near-field scattering interaction between two adjacent targets can be evaluated approximately using an iterative approach. It is assumed that the current distribution of an isolated scatterer is the illumination source of the other scatterer and so on. In this appendix it will be shown that the secondary scattered field emanated from target ♯2 ($\mathbf{E}^s_{21}$) can be obtained from the secondary scattered field emanated from target ♯1 ($\mathbf{E}^s_{12}$). Basically, the proof of the relationship between $\bar{\bar{\mathbf{S}}}^{cr}$ and $\bar{\bar{\mathbf{S}}}^{rc}$ as given in (3.31) is presented. Without loss of generality, consider two adjacent targets in free space illuminated by a plane wave. Suppose the induced current on (or within) target ♯1 in the absence of target ♯2 is given by $\mathbf{J}_1(\mathbf{r}_1)$, then the scattered field generated by this current can be computed from

$$\begin{aligned}\mathbf{E}^s_1 &= ik_o Z_o \int_{V_1} \bar{\bar{\mathbf{G}}}(\mathbf{r},\mathbf{r}'_1)\mathbf{J}_1(\mathbf{r}'_1)\,dv'_1 \\ &= \frac{-k_o Z_o}{8\pi^2}\iint \frac{1}{k_z}\left(\bar{\bar{I}} - \hat{k}\hat{k}\right)\int_{V_1}\mathbf{J}_1(\mathbf{r}'_1)e^{ik_o\hat{k}\cdot(\mathbf{r}-\mathbf{r}')}dv'd\mathbf{k}_\perp \qquad \text{(B.1)}\end{aligned}$$

where the second equality is resulted from the application of the Fourier Transform of the dyadic Green's function $\bar{\bar{\mathbf{G}}}$. If the observation point $\mathbf{r}$ is significantly apart from V_1, most contribution of the spectral integrand for calculation of $\mathbf{E}^s_1$ come from

values of $\mathbf{k}_\perp$ for which k_z and these $\hat{k}$ are real quantities. In this case, it is recognized that

$$\mathbf{E}^s(\hat{k},\hat{k}_i) = \frac{ik_oZ_oe^{ik_or}}{4\pi r}\left(\bar{\bar{I}} - \hat{k}\hat{k}\right)\int_{V_1}\mathbf{J}_1(\mathbf{r}_1')e^{-ik_o\hat{k}\cdot\mathbf{r}'}dv' \tag{B.2}$$

is the bistatic scattering far-field of target ♯1 with the incident and scattering directions along $\hat{k}_i$ and $\hat{k}$, respectively. Also noting that this scattered field can be written as

$$\mathbf{E}^s(\hat{k},\hat{k}_i) = \frac{e^{ik_or}}{r}e^{ik_o(\hat{k}_i-\hat{k})\cdot\mathbf{r}_{c1}}\bar{\bar{\mathbf{S}}}_1(\hat{k},\hat{k}_i)\mathbf{E}^{\mathbf{i}}\ , \tag{B.3}$$

where $\bar{\bar{\mathbf{S}}}_1(\hat{k},\hat{k}_i)$ is the bistatic scattering matrix of target ♯1 and $\mathbf{r}_{c1}$ is a vector representing the location of target ♯1.

Therefore the scattered field given by (B.1) can be written as

$$\mathbf{E}_1^s = \left\{\frac{i}{2\pi}\iint\frac{1}{k_z}\bar{\bar{\mathbf{S}}}_1(\hat{k}_i,\hat{k})e^{ik_o(\hat{k}_i-\hat{k})\cdot\mathbf{r}_{c1}}e^{ik_o\hat{k}\cdot\mathbf{r}}d\mathbf{k}_\perp\right\}\mathbf{E}^{\mathbf{i}}\ . \tag{B.4}$$

In this representation the near-field scattered from target ♯1 is expanded in terms of a spectrum of plane waves. Using $\mathbf{E}_1^s$ as the illuminating field the secondary scattered field in the far-field region can be computed from

$$\begin{aligned}\mathbf{E}_{21}^s &= \frac{e^{ik_or}}{r}\left\{\frac{i}{2\pi}\iint\frac{1}{k_z}\bar{\bar{\mathbf{S}}}_2(\hat{k}_s,\hat{k})\bar{\bar{\mathbf{S}}}_1(\hat{k},\hat{k}_i)e^{ik_o(\hat{k}_i-\hat{k})\cdot\mathbf{r}_{c1}}e^{ik_o(\hat{k}-\hat{k}_s)\cdot\mathbf{r}_{c2}}d\mathbf{k}_\perp\right\}\mathbf{E}^{\mathbf{i}}\\ &= \frac{e^{ik_or}}{r}\bar{\bar{\mathbf{S}}}_{21}(\hat{k}_s,\hat{k}_i)\mathbf{E}^{\mathbf{i}}\ ,\end{aligned} \tag{B.5}$$

where $\bar{\bar{\mathbf{S}}}_2(\hat{k}_s,\hat{k})$ is the bistatic scattering matrix of target ♯2 and $\mathbf{r}_{c2}$ is the vector position of target ♯2. in a similar manner $\mathbf{E}_{12}^s$ can be obtained and is given by

$$\begin{aligned}\mathbf{E}_{12}^s &= \frac{e^{ik_or}}{r}\left\{\frac{i}{2\pi}\iint\frac{1}{k_z}\bar{\bar{\mathbf{S}}}_1(\hat{k}_s,-\hat{k})\bar{\bar{\mathbf{S}}}_2(-\hat{k},\hat{k}_i)e^{ik_o(-\hat{k}-\hat{k}_s)\cdot\mathbf{r}_{c1}}e^{ik_o(\hat{k}_i+\hat{k})\cdot\mathbf{r}_{c2}}d\mathbf{k}_\perp\right\}\mathbf{E}^{\mathbf{i}}\\ &= \frac{e^{ik_or}}{r}\bar{\bar{\mathbf{S}}}_{12}(\hat{k}_s,\hat{k}_i)\mathbf{E}^{\mathbf{i}}\ .\end{aligned} \tag{B.6}$$

Now it can easily be shown that $\bar{\bar{\mathbf{S}}}_{12}(\hat{k}_s, \hat{k}_i) = \bar{\bar{\mathbf{S}}}_{21}^{(-t)}(-\hat{k}_i, -\hat{k}_s)$, since according to reciprocity theorem (using the forward scattering alignment [68])

$$\bar{\bar{\mathbf{S}}}_1(\hat{k}_s, \hat{k}) = \bar{\bar{\mathbf{S}}}_1^{(-t)}(-\hat{k}, -\hat{k}_s) \ ,$$
$$\bar{\bar{\mathbf{S}}}_2(\hat{k}, \hat{k}_i) = \bar{\bar{\mathbf{S}}}_2^{(-t)}(-\hat{k}_i, -\hat{k}) \ .$$

In the backscattering direction,$\hat{k}_s = -\hat{k}_i$, and therefore $\bar{\bar{\mathbf{S}}}_{12}(-\hat{k}_i, \hat{k}_i) = \bar{\bar{\mathbf{S}}}_{21}^{(-t)}(-\hat{k}_i, \hat{k}_i)$ as stated in (3.31).

APPENDIX C

SCATTERING MATRIX ELEMENTS FOR THE CYLINDER-ROUGH SURFACE INTERACTION

In this appendix explicit expressions for the first-order cross-polarized interaction between a tilted cylinder and slightly rough surface are provided.

$$
\begin{aligned}
S_{vh}^{rc(1)} = & -\frac{\triangle k_o Z_o(\epsilon-1)}{16\pi^3}\frac{e^{ik_o(\hat{k}_i-\hat{k}_s)\bar{\rho}_c}}{\sin^2\theta_c\cos\beta}J_{oh}(d)\Bigg\{ \\
& k_o^2\cos\beta\int_0^\infty\frac{k_\rho dk_\rho}{k_z+k_{1z}}\int_0^{2\pi}d\phi_k\sin(\phi_k-\alpha)\cos(\phi_k-\phi_i) \\
& \qquad F(\mathbf{k}_\perp-\mathbf{k}_\perp^i)\iint_{S_i} I_4\left[F_x'C_{h0}'+F_x''C_{h0}''\right]ds \\
& -k_o^2\int_0^\infty\frac{k_\rho dk_\rho}{k_z+k_{1z}}\int_0^{2\pi}d\phi_k\cos(\phi_k-\alpha)\cos(\phi_k-\phi_i) \\
& \qquad F(\mathbf{k}_\perp-\mathbf{k}_\perp^i)\iint_{S_i} I_4\left[F_y'C_{h0}'+F_y''C_{h0}''\right]ds \\
& +k_o^2\sin\beta\int_0^\infty\frac{k_\rho dk_\rho}{k_z+k_{1z}}\int_0^{2\pi}d\phi_k\sin(\phi_k-\alpha)\cos(\phi_k-\phi_i) \\
& \qquad F(\mathbf{k}_\perp-\mathbf{k}_\perp^i)\iint_{S_i} I_4\left[F_z'C_{h0}'+F_z''C_{h0}''\right]ds
\end{aligned}
$$

$$
\begin{aligned}
&- \cos\beta \int_0^\infty \frac{k_z k_{1z} k_\rho dk_\rho}{k_z + k_{1z}} \int_0^{2\pi} d\phi_k \cos(\phi_k - \alpha) \sin(\phi_k - \phi_i) \\
&\qquad F(\mathbf{k}_\perp - \mathbf{k}_\perp^i) \iint_{S_i} I_4 \left[F_x' C_{v0}' + F_x'' C_{v0}''\right] ds \\
&- \int_0^\infty \frac{k_z k_{1z} k_\rho dk_\rho}{k_z + k_{1z}} \int_0^{2\pi} d\phi_k \sin(\phi_k - \alpha) \sin(\phi_k - \phi_i) \\
&\qquad F(\mathbf{k}_\perp - \mathbf{k}_\perp^i) \iint_{S_i} I_4 \left[F_y' C_{v0}' + F_y'' C_{v0}''\right] ds \\
&- \sin\beta \int_0^\infty \frac{k_z k_{1z} k_\rho dk_\rho}{k_z + k_{1z}} \int_0^{2\pi} d\phi_k \cos(\phi_k - \alpha) \sin(\phi_k - \phi_i) \\
&\qquad F(\mathbf{k}_\perp - \mathbf{k}_\perp^i) \iint_{S_i} I_4 \left[F_z' C_{v0}' + F_z'' C_{v0}''\right] ds \\
&+ \sin\beta \int_0^\infty \frac{k_z k_\rho^2 dk_\rho}{k_z + k_{1z}} \int_0^{2\pi} d\phi_k \sin(\phi_k - \phi_i) \\
&\qquad F(\mathbf{k}_\perp - \mathbf{k}_\perp^i) \iint_{S_i} I_4 \left[F_x' C_{v1}' + F_x'' C_{v1}''\right] ds \\
&- \cos\beta \int_0^\infty \frac{k_z k_\rho^2 dk_\rho}{k_z + k_{1z}} \int_0^{2\pi} d\phi_k \sin(\phi_k - \phi_i) \\
&\qquad F(\mathbf{k}_\perp - \mathbf{k}_\perp^i) \iint_{S_i} I_4 \left[F_z' C_{v1}' + F_z'' C_{v1}''\right] ds \Bigg\} \\
&+ \frac{\triangle k_o Z_o}{16\pi^3} e^{-ik_o d\left(\frac{\cos\theta_i'}{\cos\beta}\right)} \frac{e^{ik_o(\hat{k}_i - \hat{k}_s)\bar{\rho}_c}}{\sin^2\theta_c \cos\beta} J_{oh}(d) \int_0^\infty k_\rho dk_\rho \int_0^{2\pi} d\phi_k F(\mathbf{k}_\perp - \mathbf{k}_\perp^i) \\
&\qquad e^{ik_\rho d \tan\beta \cos(\phi_k - \alpha)} \iint_{S_i} I_4 \big[\cos\beta \sin(\phi_i - \alpha) F_x' - \cos(\phi_i - \alpha) F_y' \\
&\qquad\qquad + \sin\beta \sin(\phi_i - \alpha) F_z'\big] ds \\
&+ \frac{\triangle k_o Z_o}{16\pi^3} e^{ik_o d\left(\frac{\sin\theta_i' \cos\phi' \sin 2\beta + \cos\theta_i' \cos 2\beta}{\cos\beta}\right)} \frac{e^{ik_o(\hat{k}_i - \hat{k}_s)\bar{\rho}_c}}{\sin^2\theta_c \cos\beta} J_{oh}(d) \\
&\qquad \int_0^\infty k_\rho dk_\rho \int_0^{2\pi} d\phi_k F(\mathbf{k}_\perp - \mathbf{k}_\perp^i) e^{ik_\rho d \tan\beta \cos(\phi_k - \alpha)} \\
&\qquad \iint_{S_i} I_4 \big[\cos\beta \sin(\phi_i - \alpha) F_x'' - \cos(\phi_i - \alpha) F_y'' + \sin\beta \sin(\phi_i - \alpha) F_z''\big] ds
\end{aligned}
\tag{C.1}
$$

$$S_{hv}^{rc(1)} = -\frac{\triangle k_o Z_o(\epsilon-1)}{16\pi^3}\frac{e^{ik_o(\hat{k}_i-\hat{k}_s)\bar{\rho}_c}}{\sin^2\theta_c\cos\beta}J_{ot}(d)\Bigg\{$$

$$k_o^2\cos\beta\int_0^\infty\frac{k_\rho dk_\rho}{k_z+k_{1z}}\int_0^{2\pi}d\phi_k\sin(\phi_k-\alpha)\sin(\phi_k-\phi_i)$$
$$F(\mathbf{k}_\perp-\mathbf{k}_\perp^i)\iint\limits_{S_i}I_4\left[F_x'C_{h0}'+F_x''C_{h0}''\right]ds$$

$$-k_o^2\int_0^\infty\frac{k_\rho dk_\rho}{k_z+k_{1z}}\int_0^{2\pi}d\phi_k\cos(\phi_k-\alpha)\sin(\phi_k-\phi_i)$$
$$F(\mathbf{k}_\perp-\mathbf{k}_\perp^i)\iint\limits_{S_i}I_4\left[F_y'C_{h0}'+F_y''C_{h0}''\right]ds$$

$$+k_o^2\sin\beta\int_0^\infty\frac{k_\rho dk_\rho}{k_z+k_{1z}}\int_0^{2\pi}d\phi_k\sin(\phi_k-\alpha)\sin(\phi_k-\phi_i)$$
$$F(\mathbf{k}_\perp-\mathbf{k}_\perp^i)\iint\limits_{S_i}I_4\left[F_z'C_{h0}'+F_z''C_{h0}''\right]ds$$

$$+\cos\beta\int_0^\infty\frac{k_zk_{1z}k_\rho dk_\rho}{k_z+k_{1z}}\int_0^{2\pi}d\phi_k\cos(\phi_k-\alpha)\cos(\phi_k-\phi_i)$$
$$F(\mathbf{k}_\perp-\mathbf{k}_\perp^i)\iint\limits_{S_i}I_4\left[F_x'C_{v0}'+F_x''C_{v0}''\right]ds$$

$$+\int_0^\infty\frac{k_zk_{1z}k_\rho dk_\rho}{k_z+k_{1z}}\int_0^{2\pi}d\phi_k\sin(\phi_k-\alpha)\cos(\phi_k-\phi_i)$$
$$F(\mathbf{k}_\perp-\mathbf{k}_\perp^i)\iint\limits_{S_i}I_4\left[F_y'C_{v0}'+F_y''C_{v0}''\right]ds$$

$$+\sin\beta\int_0^\infty\frac{k_zk_{1z}k_\rho dk_\rho}{k_z+k_{1z}}\int_0^{2\pi}d\phi_k\cos(\phi_k-\alpha)\cos(\phi_k-\phi_i)$$
$$F(\mathbf{k}_\perp-\mathbf{k}_\perp^i)\iint\limits_{S_i}I_4\left[F_z'C_{v0}'+F_z''C_{v0}''\right]ds$$

$$-\sin\beta\int_0^\infty\frac{k_zk_\rho^2dk_\rho}{k_z+k_{1z}}\int_0^{2\pi}d\phi_k\cos(\phi_k-\phi_i)$$
$$F(\mathbf{k}_\perp-\mathbf{k}_\perp^i)\iint\limits_{S_i}I_4\left[F_x'C_{v1}'+F_x''C_{v1}''\right]ds$$

$$+\cos\beta\int_0^\infty\frac{k_zk_\rho^2dk_\rho}{k_z+k_{1z}}\int_0^{2\pi}d\phi_k\cos(\phi_k-\phi_i)$$
$$F(\mathbf{k}_\perp-\mathbf{k}_\perp^i)\iint\limits_{S_i}I_4\left[F_z'C_{v1}'+F_z''C_{v1}''\right]ds\Bigg\}$$

$$+\frac{\triangle k_o Z_o}{16\pi^3}e^{-ik_o d\left(\frac{\cos\theta_i'}{\cos\beta}\right)}\frac{e^{ik_o(\hat{k}_i-\hat{k}_s)\bar{\rho}_c}}{\sin^2\theta_c\cos\beta}J_{ot}(d)\int_0^\infty k_\rho dk_\rho\int_0^{2\pi}d\phi_k F(\mathbf{k}_\perp-\mathbf{k}_\perp^i)$$
$$e^{ik_\rho d\tan\beta\cos(\phi_k-\alpha)}\iint\limits_{S_i} I_4\big[\cos\beta\cos(\phi_i-\alpha)F_x'+\sin(\phi_i-\alpha)F_y'$$
$$+\sin\beta\cos(\phi_i-\alpha)F_z'\big]ds$$

$$+\frac{\triangle k_o Z_o}{16\pi^3}e^{ik_o d\left(\frac{\sin\theta_i'\cos\phi'\sin 2\beta+\cos\theta_i'\cos 2\beta}{\cos\beta}\right)}\frac{e^{ik_o(\hat{k}_i-\hat{k}_s)\bar{\rho}_c}}{\sin^2\theta_c\cos\beta}J_{ot}(d)$$
$$\int_0^\infty k_\rho dk_\rho\int_0^{2\pi}d\phi_k F(\mathbf{k}_\perp-\mathbf{k}_\perp^i)e^{ik_\rho d\tan\beta\cos(\phi_k-\alpha)}$$
$$\iint\limits_{S_i} I_4\big[\cos\beta\cos(\phi_i-\alpha)F_x''+\sin(\phi_i-\alpha)F_y''+\sin\beta\cos(\phi_i-\alpha)F_z''\big]ds$$

$$-\frac{\triangle k_o Z_o(\epsilon-1)}{16\pi^3}\frac{e^{ik_o(\hat{k}_i-\hat{k}_s)\bar{\rho}_c}}{\sin^2\theta_c\cos\beta}J_{oz}(d)\Bigg\{$$

$$\cos\beta\int_0^\infty\frac{k_\rho k_{1z}dk_\rho}{\epsilon k_z+k_{1z}}\int_0^{2\pi}d\phi_k\cos(\phi_k-\alpha)F(\mathbf{k}_\perp-\mathbf{k}_\perp^i)\iint\limits_{S_i} I_4\left[F_x'C_{h0}'+F_x''C_{h0}''\right]ds$$

$$+\int_0^\infty\frac{k_\rho k_{1z}dk_\rho}{\epsilon k_z+k_{1z}}\int_0^{2\pi}d\phi_k\sin(\phi_k-\alpha)F(\mathbf{k}_\perp-\mathbf{k}_\perp^i)\iint\limits_{S_i} I_4\left[F_y'C_{v0}'+F_y''C_{v0}''\right]ds$$

$$+\sin\beta\int_0^\infty k_{1z}\frac{k_\rho dk_\rho}{\epsilon k_z+k_{1z}}\int_0^{2\pi}d\phi_k\cos(\phi_k-\alpha)$$
$$F(\mathbf{k}_\perp-\mathbf{k}_\perp^i)\iint\limits_{S_i} I_4\left[F_z'C_{v0}'+F_z''C_{v0}''\right]ds$$

$$-\sin\beta\int_0^\infty\frac{k_\rho^3dk_\rho}{\epsilon k_z+k_{1z}}\int_0^{2\pi}d\phi_k F(\mathbf{k}_\perp-\mathbf{k}_\perp^i)\iint\limits_{S_i} I_4\left[F_x'C_{v1}'+F_x''C_{v1}''\right]ds$$

$$+\cos\beta\int_0^\infty\frac{k_\rho^3dk_\rho}{\epsilon k_z+k_{1z}}\int_0^{2\pi}d\phi_k F(\mathbf{k}_\perp-\mathbf{k}_\perp^i)\iint\limits_{S_i} I_4\left[F_z'C_{v1}'+F_z''C_{v1}''\right]ds$$

$$+\frac{\triangle k_o Z_o}{16\pi^3}e^{-ik_o d\left(\frac{\cos\theta_i'}{\cos\beta}\right)}\frac{e^{ik_o(\hat{k}_i-\hat{k}_s)\bar{\rho}_c}}{\sin^2\theta_c\cos\beta}J_{oz}(d)\int_0^\infty k_\rho dk_\rho\int_0^{2\pi}d\phi_k F(\mathbf{k}_\perp-\mathbf{k}_\perp^i)$$
$$e^{ik_\rho d\tan\beta\cos(\phi_k-\alpha)}\iint\limits_{S_i} I_4\big[\cos\beta\cos(\phi_i-\alpha)F_x'+\sin(\phi_i-\alpha)F_y'$$
$$+\sin\beta\cos(\phi_i-\alpha)F_z'\big]ds$$

$$*1cm + \frac{\triangle k_o Z_o}{16\pi^3} e^{ik_o d\left(\frac{\sin\theta_i'\cos\phi'\sin 2\beta+\cos\theta_i'\cos 2\beta}{\cos\beta}\right)} \frac{e^{ik_o(\hat{k}_i-\hat{k}_s)\bar{\rho}_c}}{\sin^2\theta_c\cos\beta} J_{oz}(d)$$
$$\int_0^\infty k_\rho dk_\rho \int_0^{2\pi} d\phi_k F(\mathbf{k}_\perp - \mathbf{k}_\perp^i) e^{ik_\rho d\tan\beta\cos(\phi_k-\alpha)}$$
$$\iint_{S_i} I_4\left[\cos\beta\cos(\phi_i-\alpha)F_x'' + \sin(\phi_i-\alpha)F_y'' + \sin\beta\cos(\phi_i-\alpha)F_z''\right] ds \tag{C.2}$$

The definitions of the symbols used in (C.1) and (C.2) are as follows:

$$F_x' = -e^{-ik_o\rho'\cos\theta_i'\cos\phi'\tan\beta} \sum_{m=-\infty}^{\infty} e^{im(\phi'-\phi_i')} \{A_m \sin\theta_i'\cos\theta_i'\cos\phi' - B_m\sin\theta_i'\sin\phi'\} \tag{C.3}$$

$$F_y' = -e^{-ik_o\rho'\cos\theta_i'\cos\phi'\tan\beta} \sum_{m=-\infty}^{\infty} e^{im(\phi'-\phi_i')} \{A_m \sin\theta_i'\cos\theta_i'\sin\phi' + B_m\sin\theta_i'\cos\phi'\} \tag{C.4}$$

$$F_z' = -e^{-ik_o\rho'\cos\theta_i'\cos\phi'\tan\beta} \sum_{m=-\infty}^{\infty} e^{im(\phi'-\phi_i')} A_m \sin^2\theta_i' \tag{C.5}$$

$$F_x'' = -e^{ik_o\rho'(\sin\theta_i'\cos\phi'\sin 2\beta+\cos\theta_i'\cos 2\beta)\cos\phi'\tan\beta} \sum_{m=-\infty}^{\infty} e^{im(\phi'-\phi_i')} \{C_{rvs} v_{nx}'' + C_{rhs} h_{nx}''\} \tag{C.6}$$

$$F_y'' = -e^{ik_o\rho'(\sin\theta_i'\cos\phi'\sin 2\beta+\cos\theta_i'\cos 2\beta)\cos\phi'\tan\beta} \sum_{m=-\infty}^{\infty} e^{im(\phi'-\phi_i')} \{C_{rvs} v_{ny}'' + C_{rhs} h_{ny}''\} \tag{C.7}$$

$$F_z'' = -e^{ik_o\rho'(\sin\theta_i'\cos\phi'\sin 2\beta+\cos\theta_i'\cos 2\beta)\cos\phi'\tan\beta} \sum_{m=-\infty}^{\infty} e^{im(\phi'-\phi_i')} \{C_{rvs} v_{nz}'' + C_{rhs} h_{nz}''\} \tag{C.8}$$

$$C_{rvs} = \frac{A_m \left[\cos\beta \sin^2\theta_i' - sin\beta \sin\theta_i' \cos\theta_i' \cos\phi'\right] + B_m \sin\beta \sin\theta_i' \sin\phi'}{\left|\sin^2\theta_i' \cos^2\beta + \cos^2\theta_i' \sin^2\beta + \sin^2\theta_i' \sin^2\beta \sin^2\phi' - 0.5 \sin 2\beta \sin 2\theta_i' \cos\phi'\right|} \tag{C.9}$$

$$C_{rhs} = \frac{B_m \left[\cos\beta \sin^2\theta_i' - sin\beta \sin\theta_i' \cos\theta_i' \cos\phi'\right] + A_m \sin\beta \sin\theta_i' \sin\phi'}{\left|\sin^2\theta_i' \cos^2\beta + \cos^2\theta_i' \sin^2\beta + \sin^2\theta_i' \sin^2\beta \sin^2\phi' - 0.5 \sin 2\beta \sin 2\theta_i' \cos\phi'\right|} \tag{C.10}$$

$$h_{nx}'' = \cos\beta \sin\theta_i' \sin\phi' \tag{C.11}$$

$$h_{ny}'' = \sin\beta \cos\theta_i' - \sin\theta_i' \cos\beta \cos\phi' \tag{C.12}$$

$$h_{ny}'' = \sin\beta \sin\theta_i' \sin\phi' \tag{C.13}$$

$$\begin{aligned} v_{nx}'' = {} & \sin\beta(\sin^2\theta_i' \sin^2\phi' + \cos^2\theta_i') - \cos\beta \sin\theta_i' \cos\theta_i' \cos\phi' \\ & + 2\sin\theta_i' \cos\phi'(\sin\beta \sin\theta_i' \cos\phi' + \cos\theta_i' \cos\beta) \\ & - 2\sin\beta(\sin\beta \sin\theta_i' \cos\phi' + \cos\theta_i' \cos\beta)^2 \end{aligned} \tag{C.14}$$

$$\begin{aligned} v_{ny}'' = {} & -\cos\beta \sin\theta_i' \cos\theta_i' \sin\phi' - \sin\beta \sin^2\theta_i' \cos\phi' \sin\phi' \\ & + 2\sin\theta_i' \sin\phi'(\sin\beta \sin\theta_i' \cos\phi' + \cos\theta_i' \cos\beta) \end{aligned} \tag{C.15}$$

$$\begin{aligned} v_{nz}'' = {} & -\cos\beta \sin^2\theta_i' + \sin\beta \sin\theta_i' \cos\theta_i' \cos\phi' \\ & - 2\cos\theta_i'(\sin\beta \sin\theta_i' \cos\phi' + \cos\theta_i' \cos\beta) \\ & + 2\cos\beta(\sin\beta \sin\theta_i' \cos\phi' + \cos\theta_i' \cos\beta)^2 \end{aligned} \tag{C.16}$$

$$I_4 = H_0^{(1)}(k_o \sin\theta_i' \rho') e^{ik_\rho \rho' \left[\frac{\cos(\phi_k - \alpha)}{\cos\beta} \cos\phi' + \sin(\phi_k - \alpha) \sin\phi'\right]} \tag{C.17}$$

$$C_{h0}' = \int_0^d C_0^h(\mathbf{k}, z) e^{i[k_\rho \tan\beta \cos(\phi_k - \alpha) - k_o \frac{\cos\theta_i'}{\cos\beta}]z} dz \tag{C.18}$$

$$C_{v0}' = \int_0^d C_0^v(\mathbf{k}, z) e^{i[k_\rho \tan\beta \cos(\phi_k - \alpha) - k_o \frac{\cos\theta_i'}{\cos\beta}]z} dz \tag{C.19}$$

$$C_{v1}' = \int_0^d C_1^v(\mathbf{k}, z) e^{i[k_\rho \tan\beta \cos(\phi_k - \alpha) - k_o \frac{\cos\theta_i'}{\cos\beta}]z} dz \tag{C.20}$$

$$C''_{h0} = \int_0^d C_0^h(\mathbf{k}, z) e^{i[k_\rho \tan\beta \cos(\phi_k - \alpha) + k_o \frac{\sin\theta'_i \sin 2\beta \cos\phi' + \cos\theta'_i \cos 2\beta}{\cos\beta}]z} dz \tag{C.21}$$

$$C''_{v0} = \int_0^d C_0^v(\mathbf{k}, z) e^{i[k_\rho \tan\beta \cos(\phi_k - \alpha) + k_o \frac{\sin\theta'_i \sin 2\beta \cos\phi' + \cos\theta'_i \cos 2\beta}{\cos\beta}]z} dz \tag{C.22}$$

$$C''_{v1} = \int_0^d C_1^v(\mathbf{k}, z) e^{i[k_\rho \tan\beta \cos(\phi_k - \alpha) + k_o \frac{\sin\theta'_i \sin 2\beta \cos\phi' + \cos\theta'_i \cos 2\beta}{\cos\beta}]z} dz \tag{C.23}$$

Using (3.21), and setting $\hat{p} = \hat{v}_s$ for (C.1) and $\hat{p} = \hat{h}_s$ for (C.2), A_m and B_m can be evaluated. Also note that the integrals in (C.18)$\sim$(C.23) can be carried out analytically. The integration over the illuminated area S_i can be carried out using the polar coordinate (ρ', ϕ'):

$$\iint_{Si} ds = \int_0^{2\pi} d\phi' \int_{D1}^{D2} \rho' d\rho' \tag{C.24}$$

where

$$D1 = \frac{h \sec\beta \tan\theta'_i + a_c}{1 + \tan\beta \tan\theta'_i \cos\phi'} \tag{C.25}$$

$$D2 = \frac{(h + l_c) \sec\beta \tan\theta'_i + a_c}{1 + \tan\beta \tan\theta'_i \cos\phi'} \tag{C.26}$$

APPENDIX D

GO-GO-GO FORMULATION FOR CORNER REFLECTORS

D.1 Triangular Corner Reflector

In this appendix analytical expressions for the area of the lit region on panel #1 of a triangular corner reflector as a function of azimuth and elevation angles (θ, ϕ) are given. Same expressions can be used to find the area of the lit regions on panels #2 and #3 using the following change of variable for θ and ϕ respectively,

$$\begin{cases} \theta' = & \cos^{-1}(\sin\theta\cos\phi) \\ \phi' = & \tan^{-1}\left(\frac{\cos\theta}{\sin\theta\cos\phi}\right) \end{cases}, \quad \begin{cases} \theta'' = & \cos^{-1}(\sin\theta\sin\phi) \\ \phi'' = & \tan^{-1}\left(\frac{\sin\theta\cos\phi}{\cos\theta}\right) \end{cases}.$$

Depending on the incidence angles, the lit area for a triangular corner reflector can obtain from equations shown below in which $T_s = \tan\theta\sin\phi$, $T_c = \tan\theta\cos\phi$, $S = \sin\theta$, and $C = \cos\theta$.

- $\boldsymbol{T_c + T_s \leq 1}$,

  $A_1 = \frac{1}{2}\, l^2 \cdot T_c T_s \cdot \frac{2+T_c+T_s}{(1+T_s)(1+T_c)}$

- $\boldsymbol{T_c + T_s > 1}$ ***and*** $\boldsymbol{-1 \leq T_c - T_s \leq 1}$,

  $A_1 = \frac{1}{2}\, l^2 \cdot \left\{ \frac{T_s-T_c+1}{T_c+T_s+1} \cdot \frac{T_c}{1+T_s} + \frac{T_s}{1+T_c} \cdot \frac{T_c-T_s+1}{T_c+T_s+1} + \frac{T_c+T_s-1}{T_c+T_s+1} \right\}$

- $\boldsymbol{T_c + T_s > 1}$ ***and*** $\boldsymbol{T_c - T_s > 1}$,

  $A_1 = \frac{1}{2}\, l^2 \cdot \frac{T_s}{1+T_c+T_s} \cdot \frac{3+3T_c-T_s}{1+T_c}$

- $\boldsymbol{T_c + T_s > 1}$ ***and*** $\boldsymbol{T_c - T_s < -1}$,

  $A_1 = \frac{1}{2}\, l^2 \cdot \frac{T_c}{1+T_c+T_s} \cdot \frac{3+3T_s-T_c}{1+T_s}$

D.2 Square Corner Reflector

In this appendix, similar to Appendix A, the area of the lit region on panel #1 of a square corner reflector is given.

- $\boldsymbol{\phi \geq 45^o, 1 \leq T_s < 2,}$ ***and*** $\boldsymbol{T_c \geq 1}$,

  $A_1 = l^2 \cdot (2 - 0.5 \cdot C/S - 0.5 \cdot S/C)$

- $\boldsymbol{\phi \geq 45^o, 1 \leq T_s < 2,}$ ***and*** $\boldsymbol{T_c < 1}$,

  $A_1 = l^2 \cdot \{2 \cdot T_c - 0.5 \cdot C/S - 0.5 \cdot T_c T_s\}$

- $\boldsymbol{45^o \leq \phi \leq \tan^{-1}(2), T_s \geq 2,}$ ***and*** $\boldsymbol{T_c \geq 1}$,

  $A_1 = l^2 \cdot \{2 - 0.5 \cdot C/S - 0.5 \cdot S/C\}$

- $\boldsymbol{\phi \geq \tan^{-1}(2), T_s \geq 2,}$ ***and*** $\boldsymbol{T_c \geq 1}$,

  $A_1 = 1.5 \cdot l^2 \cdot C/S$

- $\boldsymbol{\phi \geq 45^o, T_s \geq 2,}$ ***and*** $\boldsymbol{T_c < 1}$,

  $A_1 = 1.5 \cdot l^2 \cdot C/S$

- $\boldsymbol{T_s < 1,}$ ***and*** $\boldsymbol{T_c < 1}$,

  $A_1 = l^2 \cdot T_s T_c$

- $\phi < 45^o, 1 \leq T_c < 2, and\ T_s < 1,$

  $A_1 = l^2 \cdot \{2 \cdot T_s - 0.5 \cdot S/C - 0.5 \cdot T_s T_c\}$

- $\phi < 45^o, T_c \geq 2, and\ T_s < 1,$

  $A_1 = 1.5 \cdot l^2 \cdot S/C$

- $\phi < 45^o, 1 \leq T_c < 2, and\ T_s \geq 1,$

  $A_1 = l^2 \cdot \{2 - 0.5 \cdot C/S - 0.5 \cdot S/C\}$

- $\tan^{-1}(0.5) \leq \phi < 45^o \tan^{-1}(2), T_s \geq 2, and\ T_c \geq 1,$

  $A_1 = l^2 \cdot \{2 - 0.5 \cdot C/S - 0.5 \cdot S/C\}$

- $\phi < \tan^{-1}(0.5), T_c \geq 2, and\ T_s \geq 1,$

  $A_1 = 1.5 \cdot l^2 \cdot S/C$

D.3 Pentagonal Corner Reflector

In this appendix, similar to Appendix A, the area of the lit region on panel #1 of a pentagonal corner reflector is given. Separate expressions for A_1^{23} and A_1^{32} are derived. The expressions for A_1^{23} are given by:

- $\underline{T_s < 0.5, T_s > 2, T_c - T_s > 1, T_s - T_c > 2, or\ 5T_s - 2T_c < 1},$

  a- $A_1^{23} = 0.$

  This is an approximation which corresponds to the incidence angles far away from the boresight.

- $\underline{\phi < \tan^{-1}(0.5)},$

  a- $2T_c - T_s < 1,$

  $A_1^{23} = l^2 \cdot T_c \cdot \frac{5T_s - 1}{12(1+T_s)}$

b- $\mathbf{1 \leq 2T_c - T_s < 2}$,

$$A_1^{23} = l^2 \cdot \left\{ \frac{2T_c+T_s-2}{4(2T_c-T_s+2)} + T_c \cdot \frac{2-2T_c+T_s}{4(2T_c-T_s+2)} \right\}$$

c- $\mathbf{2T_c - T_s \geq 2}$,

$$A_1^{23} = l^2 \cdot \frac{T_s}{2(T_s+1)(2-S/C}$$

- $\underline{\mathbf{\tan^{-1}(0.5) \leq \phi < \tan^{-1}(2)}}$,

a- $\mathbf{T_c + T_s \leq 2, 2T_c - T_s < 1}$,

$$A_1^{23} = l^2 \cdot T_c \cdot \frac{5T_s-1}{12(1+T_s)}$$

b- $\mathbf{T_s + T_c \leq 2, 2T_c - T_s \geq 1}$,

$$A_1^{23} = l^2 \cdot \left\{ \frac{2T_c+T_s-2}{4(2T_c-T_s+2)} + T_c \cdot \frac{2-2T_c+T_s}{4(2T_c-T_s+2)} \right\}$$

c- $\mathbf{T_s + T_c > 2, 2T_c - T_s < 1}$,

$$A_1^{23} = l^2 \cdot \left\{ T_c \cdot \frac{T_s-T_c+1}{T_s+1} \cdot \frac{1}{2(T_c+T_s+1)} + \frac{T_c+T_s-1}{2(S/C+1)(T_c+T_s+1)} \right\}$$

d- $\mathbf{T_s + T_c > 2, 2T_c - T_s < 1 \geq 1}$,

$$A_1^{23} = l^2 \cdot \frac{5S-C}{12(C+S)}$$

- $\underline{\mathbf{\phi \geq \tan^{-1}(2)}}$,

a- $\mathbf{2T_s - T_c < 2}$,

$$A_1^{23} = l^2 \cdot T_c \cdot \frac{5T_s-1}{12(1+T_s)}$$

b- $\mathbf{2 \leq 2T_s - T_c < 2.5, T_s + T_c < 2}$,

$$A_1^{23} = l^2 \cdot T_c \cdot \left\{ \frac{2T_s-1}{12(1+T_s)} + \frac{2T_c-4T_s+5}{6(4+T_c-2T_s)} + \frac{1-2/(2S-C)}{2(4+T_c-2T_s)} \right\}$$

c- $\mathbf{2 \leq 2T_s - T_c < 2.5, T_s + T_c \geq 2}$,

$$A_1^{23} = l^2 \cdot \left\{ \frac{T_c}{2(T_s+1)(T_s+T_c+1)} + \frac{2(T_s+T_c)-1}{6(T_s+T_c+1)} + \frac{S-2C}{6(2S-C)} \right\}$$

d- $\mathbf{2T_s - T_c \geq 2.5, T_s - 2T_c > 0.5}$,

$$A_1^{23} = l^2 \cdot \left\{ T_c \cdot \frac{T_s+T_c+1}{2(T_s+1)(2T_s-T_c+2)} + \frac{|2T_s-T_c+2-1|}{(2S/C-1)(2T_s-T_c+2} \right\}$$

e- $\mathbf{2T_s - T_c \geq 2.5, T_s - 2T_c \leq 0.5}$,

$$A_1^{23} = l^2 \cdot \left\{ \frac{T_c}{2(T_s+1)(T_s+T_c+1)} + \frac{2(T_s+T_c)-1}{6(T_s+T_+1)} + \frac{S-2C}{6(2S-1C)} \right\}$$

The expressions for A_1^{32} are given by

- $\underline{\mathbf{T_c < 0.5, T_c > 2, T_s - T_c > 1, T_c - T_s > 2, or\ 5T_c - 2T_s < 1}}$,

  a- $A_1^{32} = 0$,

  This is an approximation which corresponds to the incidence angles far away from the boresight.

- $\underline{\boldsymbol{\phi < \tan^{-1}(0.5)}}$,

  a- $\mathbf{2T_c - T_s < 2}$,

  $$A_1^{32} = l^2 \cdot T_s \cdot \frac{5T_c-1}{12(1+T_c)}$$

  b- $\mathbf{2 \leq 2T_c - T_s < 2.5, T_s + T_c < 2}$,

  $$A_1^{32} = l^2 \cdot \left\{ T_s \cdot \frac{2T_c-1}{6(1+T_c)} + \frac{2T_s+3}{6(4+T_s-2T_c)} + \frac{(T_s+2)/(2C/S-1)}{2(4+T_s-2T_c)} \right\}$$

  c- $\mathbf{2 \leq 2T_c - T_s < 2.5, T_s + T_c \geq 2}$,

  $$A_1^{32} = l^2 \cdot \left\{ \frac{C-2S}{6(2C-S)} + \frac{|5T_s-T_c-1|}{6(T_s+T_c+1)} + \frac{T_s(T_c-T_s+1)}{2(T_c+1)(2T_c-T_s+1)} \right\}$$

  d- $\mathbf{2T_c - T_s \geq 2.5, T_s + T_c < 0.5}$,

  $$A_1^{32} = l^2 \cdot \left\{ \frac{S|T_c(3C-S)-(T_c+1)|}{2C(2C-S)(2T_c-T_s+2)} + \frac{T_s(T_c+T_s+1)}{2(T_c+1)(2T_c-T_s+2)} \right\}$$

  e- $\mathbf{2T_s - T_c \geq 2.5, T_s + T_c \geq 2}$,

  $$A_1^{32} = l^2 \cdot \left\{ \frac{C-2S}{6(2C-S)} + \frac{|5T_s-T_c-1|}{6(T_c+T_s+1)} + \frac{(T_s(T_c-T_s+1)}{2(T_c+1)(T_c+T_s+1)} \right\}$$

- $\underline{\boldsymbol{\tan^{-1}(0.5) \leq \phi < \tan^{-1}(2)}}$,

  a- $\mathbf{T_c + T_s \leq 2, 2T_s - T_c < 1}$,

  $$A_1^{23} = l^2 \cdot T_s \cdot \frac{5T_c-1}{12(1+T_c)}$$

b- $\boldsymbol{T_s + T_c \leq 2, 2T_s - T_c \geq 1}$,

$$A_1^{23} = l^2 \cdot \left\{ \frac{2T_s+T_c-2}{4(2T_s-T_c+2)} + T_s \cdot \frac{2-2T_s+T_c}{4(2T_s-T_c+2)} \right\}$$

c- $\boldsymbol{T_s + T_c > 2, 2T_s - T_c < 1}$,

$$A_1^{23} = l^2 \cdot \left\{ T_s \cdot \frac{T_c-T_s+1}{T_c+1} \cdot \frac{1}{2(T_c+T_s+1)} + \frac{T_c+T_s-1}{2(C/S+1)(T_c+T_s+1)} \right\}$$

d- $\boldsymbol{T_s + T_c > 2, 2T_s - T_c < 1 \geq 1}$,

$$A_1^{23} = l^2 \cdot \frac{5C-S}{12(C+S)}$$

- $\underline{\phi < \tan^{-1}(2)}$,

a- $\boldsymbol{2T_s - T_c < 1}$,

$$A_1^{23} = l^2 \cdot T_s \cdot \frac{5T_c-1}{12(1+T_c)}$$

b- $\boldsymbol{1 \leq 2T_s - T_c < 2}$,

$$A_1^{32} = l^2 \cdot T_s \cdot \left\{ \frac{2-2T_s+T_c}{2(2T_s-T_c+2)} + \frac{2T_s+T_c-2}{2(T_c+1)(2T_s-T_c+2)} \right\}$$

c- $\boldsymbol{2T_s - T_c \geq 2}$,

$$A_1^{32} = l^2 \cdot \frac{C}{4(2S-C)}$$

BIBLIOGRAPHY

BIBLIOGRAPHY

[1] Agarwal G.S., "Interaction of electromagnetic waves at rough dielectric surfaces," *Phys. Rev. B,* no. 15, pp. 2371-2383, 1977.

[2] Bahar, E., "Full-wave solutions for the depolarization of the scattered radiation fields by rough surfaces of arbitrary slope," *IEEE Trans. Antennas Propagat.*, vol. AP-29, pp. 443-454, May 1981.

[3] Bahar, E., "Examination of full-wave solutions and "exact numerical results" for one-dimensional slightly rough surfaces," *J. Geophys. Res.*, vol. 96, pp. 17123-17131, Sep. 1991.

[4] Bahar, E., "Full-wave analysis for rough surface diffuse, incoherent radar cross sections with height-slope correlations included," *IEEE Trans. Antennas Propagat.*, vol. AP-39, pp. 1293-1304, Sep. 1991.

[5] Beckmann, P. and A. Spizzichino, *The Scattering of Electromagnetic Waves from Rough Surfaces*, Pergamon, New York, NY, 1963.

[6] Brunfeldt D.R., "Theory and design of a field-portable dielectric measurement system," *IEEE Int. Geosci. Remote Sensing Symp. (IGARSS) Digest,* vol. 1, pp. 559-563, 1987.

[7] Chiu T., K. Sarabandi, and F.T. Ulaby, "Polarimetric backscattering measurement of herbaceous vegetation: a sensitivity study for soil moisture retrieval." In *Proceedings of the International Geoscience and Remote Sensing Symposium*, Lincoln, Nebraska, USA, May 1996.

[8] Durden, S.L., J.J. van Zyl, and H.A. Zebker, "Modeling and Observation of the Radar Polarization Signature of Forested Areas," *IEEE Trans. Geosci. Remote Sensing*, vol. 27, no. 3, pp. 290-301, 1989.

[9] DeRoo R., R. Hartikka, N. Peplinski, and A. Zambetti, , Bistatic Measurement Facility User's Manual, Radiation Laboratory, the University of Michigan, August, 1994.

[10] Fung, A.K. and G.W. Pan, "A scattering model for perfectly conducting random surfaces: I. model development. II. range of validity," *Int. J. Remote Sensing*, vol. 8, no. 11, pp. 1579-1605, 1987.

[11] Fung, A.K., Z. Li, and K.S. Chen, "Backscattering from a randomly rough dielectric surface," *IEEE Trans. Geosci. Remote Sensing*, vol. 30, pp. 356-359, 1992.

[12] Fung, A.K., *Microwave Scattering and Emission Models and Their Applications,* Artech House, Norwood, MA, 1994.

[13] Griesser T. and C.A. Balanis, "Backscatter analysis of dihedral corner reflectors using physical optics and the physical theory of diffraction," *IEEE Trans. Antennas Propagat.,* vol. 35, no. 10, pp. 1137-1147, Oct. 1987.

[14] Hallikainen M.T., F.T. Ulaby, M.C. Dobson, M.A. El-Rayes, and L. Wu, "Microwave dielectric behavior of wet soil — part I: empirical models and experimental observations," *IEEE Trans. Geosci. Remote Sensing,* vol. GE-23, no. 1, pp. 25-34, January 1985.

[15] Harrington, R.F., *Time-Harmonic Electromagnetic Fields,* McGraw-Hill, Inc., NY, 1961.

[16] Hsu C.C., H.C. Han, R.T. Shin, J.A. Kong, A. Beaudin, and T. LE Toan, "Radiative transfer theory theory for polarimetric remote sensing of pine forest at P band," *Int. J. Remote Sensing,* vol. 15, no. 14, pp. 2943-2954, 1994.

[17] Ishimaru A. *Wave Propagation and Scattering in Random media,* vol. 2, New York: Academic, 1978.

[18] Karam, M.A. and A.K. Fung, "Electromagnetic wave scattering from some vegetation samples," *IEEE Trans. Geosci. Remote Sensing,* vol. 26, no. 6, pp. 799-808, Nov. 1988.

[19] Karam, M.A., A.K. Fung, and Y.M.M. Antar, "Electromagnetic scattering from a layer of finite length, randomly oriented, dielectric, circular cylinders over a rough interface with application to vegetation," *Int. J. Remote Sensing,* vol. 9, no. 6, pp. 1109-1134, 1988.

[20] Knott E.F., *Radar Cross Section Measurements*, New York: Van Nostrand Reinhold, p. 188, 1993.

[21] Lang, R.H. and J.S. Sidhu,"Electromagnetic backscattering from a layer of vegetation: a discrete approach," *IEEE Trans. Geosci. Remote Sensing,* vol. 21, pp. 62-71, 1983.

[22] Lin, Y.C. and K. Sarabandi, "Electromagnetic scattering model for a tree trunk above a tilted ground plane," *IEEE Trans. Geosci. Remote Sensing,* vol. 33, no. 4, pp. 1063-1070, July 1995.

[23] Lin, Y.C. and K. Sarabandi, "A Monte Carlo Coherent Scattering Model for Forest Canopies Using Fractal Generated Trees," to be submitted to *IEEE Trans. Geosci. Remote Sensing.*

[24] Lin, Y.C., "A fractal-based coherent scattering and propagation model for forest canopies," Ph.D. disertation, the University of Michigan, Ann Arbor, 1997.

[25] Logan J.D., "Calculus of Variation." In *Applied Mathematics - A Contemporary Approach*, New York: John Wiley & Sons, chapter 3, p. 84-150, 1987.

[26] Mcdonald, K.C. and F.T. Ulaby, "Radiative transfer modeling of discontinuous tree canopies at microwave frequencies," *Int. J. Remote Sensing,* vol. 14, no. 11, pp. 2097-2128, 1993.

[27] Nieto-Vesperinas M., "Depolarization of electromagnetic waves scattered from slightly rough random surfaces: A study by means of the extinction theorem," *J. Opt. Soc.,* 72(5), pp. 539-547, 1982.

[28] Njoku E.G. and J. Kong, "Theory for passive microwave remote sensing of near-surface soil moisture," *J. Geophys. Res.,* vol. 28, pp. 1022-1033, 1990.

[29] Oh, Y., K. Sarabandi and F.T. Ulaby, "An empirical model and an inverse technique for radar scattering from bare soil surfaces," *IEEE Trans. Geosci. Remote Sensing*, vol. 30, pp. 370-382, Mar. 1992.

[30] Peters L. Jr.,"Passive bistatic radar enhancement devices," *IEE Proc.,* vol. 109, part C, no. 15, pp. 1-10, March 1962.

[31] Polatin P.F., K. Sarabandi, and F.T. Ulaby, "Monte-Carlo simulation of electromagnetic scattering from a layer of vertical cylinders," *IEEE Trans. Antennas Propagat.*, vol. 43, no. 10, pp. 1048-1057, Oct. 1995.

[32] Raven, P.H., R.F. Evert, and S.E. Eichhorn, *Biology of Plants*, Worth Publishers, INC., New York, NY, 1986.

[33] Rice S.O., "Reflection of electromagnetic wave by slightly rough surfaces," *Communication in Pure and Applied Mathematics,* vol. 4, pp. 351-378, 1951.

[34] Ridenour L.N., *Radar System Engineering.* New York: McGraw-Hill, p. 67-68, 1946.

[35] Robertson S.D., "Targets for microwave radar navigation," Bell System Technical Journal, vol. 26, pp. 852-869, 1947.

[36] Rodriguez E. and Y. Kim, "A unified perturbation expansion for surface scattering," *Radio Science,* vol. 27, no. 1, pp. 79-93, Jan-Feb, 1992.

[37] Ruck G.T., *Radar Cross Section Handbook.* New York: Plenum Press, p. 588-597, 1970.

[38] Sarabandi K. and F.T. Ulaby, "A convenient technique for polarimetric calibration of radar systems," *IEEE Trans. Geosci. Remote Sensing,* vol. GE-23, no. 1, pp. 25-34, January 1985.

[39] Sarabandi, K., T.B.A. Senior, and F.T. Ulaby, "Effect of curvature on the backscattering from a leaf," *J. Electromag. Waves and Appli.*, vol. 2, no. 7, pp. 653-670, 1988.

[40] Sarabandi K. and F.T. Ulaby, "Technique for measuring the dielectric constant of thin materials," *IEEE Trans. Instrum. Meas,* vol. 37, no. 4, pp. 631-636, Dec. 1988.

[41] Sarabandi, K. and T.B.A. Senior, "Low-frequency Scattering from Cylindrical Structures at Oblique Incidence," *IEEE Trans. Geosci. Remote Sensing*, vol. 28, no. 5, pp. 879-885, 1990.

[42] Sarabandi K., and F.T. Ulaby, "A convenient technique for polarimetric calibration of single-antenna radar systems," *IEEE Trans. Geosci. Remote sensing,* vol. 28, no. 6, pp1022-1033, Nov. 1990.

[43] Sarabandi, K., "Scattering from dielectric structures above impedance surface and resistive sheets," *IEEE Trans. Antennas Propagat.*, vol. 40, no. 1, pp. 67-78, Jan. 1992.

[44] Sarabandi K., L.E. Pierce, and F.T. Ulaby, "Calibration of a polarimetric imaging SAR," *IEEE Trans. Geosci. Remote sensing,* vol. 30, no. 3, pp. 540-549, May 1992.

[45] Sarabandi K., "Derivation of phase statistics from the Mueller matrix," *Radio Science,* vol. 27, no. 5, pp. 553-560, September-October 1992.

[46] Sarabandi K., Y. Oh, and F.T. Ulaby, "Measurement and calibration of differential Mueller matrix of distributed targets," *IEEE Trans. Antennas Propagat.,* vol. 40, pp. 1524-1532, Dec. 1992.

[47] Sarabandi, K., P.F. Polatin, and F.T. Ulaby, "Monte-Carlo simulation of scattering from a layer of vertical cylinders," *IEEE Trans. Antennas Propagat.*, vol. 41, no. 4, pp. 465-474, 1993.

[48] Sarabandi, K. and P.F. Polatin, "Electromagnetic scattering from two adjacent objects," *IEEE Trans. Antennas Propagat.*, vol. 42, no. 4, pp. 510-517, 1994.

[49] Sarabandi K., "A technique for dielectric measurement of cylindrical objects in a rectangular waveguide," *IEEE Trans. Instrum. Meas,* vol. 43, no. 6, pp. 793-798, Dec. 1994.

[50] Sarabandi K., L.E. Pierce, Y. Oh, M.C. Dobson, F.T. Ulaby, A. Freeman, and P. Dubois, "Cross-calibration experiment of JPL AIRSAR and truck-mounted polarimetric scatterometer," *IEEE Trans. Geosci. Remote sensing,* vol. 32, no. 5, pp. 975-985, Sept. 1994.

[51] Sarabandi, K., *Electromagnetic Scattering from Vegetation Canopies,* Ph.D. disertation, the University of Michigan, Ann Arbor, 1989.

[52] Sarabandi, K. and T. Chiu, "Electromagnetic scattering from slightly rough surface with inhomogeneous dielectric profiles," *IEEE Trans. Antennas Propagat.*, vol. 45, no. 9, pp. 1419-1430, Sep. 1997.

[53] Schiffer, R. and K.O. Thielheim, "Light Scattering by Dielectric Needles and Disks," *J. Appl. Phys.*, 50(4), April 1979.

[54] Seker S.S. and A. Schneider, "Electromagnetic Scattering from a dielectric cylinder of finite length," *IEEE Trans. Antennas Propagat.*, vol. 36, no. 2, pp. 303-307, Feb. 1988.

[55] Senior T.B.A., and K. Sarabandi, "Scattering Models for Point Targets." In *Radar Polarimetry for Geoscience Applications*, eds. F.T. Ulaby and C. Elachi, Artech House, Dedham MA, Chapter 3, p. 61, 1990.

[56] Sheen D.R., A. Freeman, E. S. Kasischke, "Phase calibration of polarimetric SAR images," *IEEE Trans. Geosci. Remote sensing,* vol. 27, no. 6, pp.719-731, Nov. 1989.

[57] Spencer R.C., "Optical theory of the corner reflectors," Radiation Laboratory Report 433, M.I.T., Cambridge, March 1944.

[58] Stiles J., *A coherent polarimetric microwave scattering models for grassland structures and canopies,* Ph.D. disertation, the University of Michigan, Ann Arbor, 1996.

[59] Tai C.T., "Some essential formulas in dyadic analysis and their applications," *Radio Sci.* vol. 22, no. 7, pp. 1283-1288, Dec. 1987.

[60] Tassoudji M.A., K. Sarabandi, and F.T. Ulaby, "Design consideration and implementation of the LCX polarimetric scatterometer (POLARSCAT)," Rep. 022486-T-2, Radiation Laboratory, The University of Michigan, June 1989.

[61] Tricomi F.G., *Integral Equations*, New York: Interscience Publishers, 1957.

[62] Tsang, L., J. Kong, and R.T. Shin, *Theory of Microwave Remote Sensing*, John Wiley and Sons, New York, 1985.

[63] Tsang L., C.H. Chan, J.A. Kong, and J. Joseph, "Polarimetric Signatures of a Canopy of Dielectric Cylinders Based on First and Second Order Vector Radiative Transfer Theory," *J. of Electromagnetic Waves and Applications*, vol. 1, no. 1, pp. 19-51, 1992.

[64] Tsang L., K. Ding, G. Zhang, C.C. Hsu, and J.A. Kong, "Backscattering enhancement and Clustering effects of randomly distributed dielectric cylinders overlying a dielectric half space based on Monte-Carlo simulations," *IEEE Trans. Antennas Propagat.*, vol. 43, no. 5, pp. 488-499, May 1995.

[65] Zhang G., L. Tsang, and Z. Chen, "Collective scattering effects of trees generated by stochastic Lindenmayer systems," *Microwave and Optical Technology Letters,* vol 11, no. 2, pp. 107-111, Feb. 1995.

[66] Ulaby, F.T., R.K. More, and A.K. Fung, *Microwave Remote Sensing: Active and Passive,* Norwood, MA, Artech House, 1981.

[67] Ulaby F.T. and M.A. El-Rayes, "Microwave dielectric spectrum of vegetation — part II: dual-dispersion model," *IEEE Trans. Geosci. Remote Sensing,* vol. GE-25, no. 5, pp. 550-557, September 1987.

[68] Ulaby, F.T. and C. Elachi, *Radar Polarimetry for Geoscience Applications,* Artech House, Inc., Norwood, MA, 1990.

[69] Ulaby, F.T., K. Sarabandi, K. McDonald, M. Whitt, and M.C. Dobson, "Michigan microwave canopy scattering model," *Int. J. Remote Sensing*, vol. 11, no. 7, pp. 2097-2128, 1990.

[70] Valenzuela, G.R., "Depolarization of EM waves by slightly rough surfaces," *IEEE Trans. Antennas Propagat.*, vol. AP-15, pp. 552-557, July 1967.

[71] Van Zyl J.J., "Calibration of polarimetric radar images using only image parameters and trihedral corner reflector responses," *IEEE Trans. Geosci. Remote sensing,* vol. 28, no. 3, pp. 337-348, May 1990.

[72] Winebrenner, D. and A. Ishimaru, "Investigation of a surface field phase perturbation technique for scattering from rough surfaces," *Radio Science*, vol. 20, no. 2, pp. 161-170, March-April, 1985.

[73] Whitt, M.W. and F.T. Ulaby, "Radar response of periodic vegetation canopies," *Int. J. Remote Sensing*, vol. 15, no. 9, pp. 1813-1848, 1994.

[74] Yueh, S.H., J.A. Kong, J.K. Jao, R.T. Shin, and T.L. Toan, "Branching Model for Vegetation," *IEEE Trans. Geosci. Remote Sensing,* vol. 30, no. 2, pp. 390-402, March 1992.

[75] http://www.jpl.nasa.gov/mip/airsar.html